Advanced Vehicle Power Technology Alliance Fiscal Year 2015 (FY15) Annual Report

(1 Oct 2014 – 30 Sep 2015)

Department of the Army

(RDTA-COS-EBO)

Department of Energy

29 January 2016

Mr. David Howell
Project Director (Acting), Vehicle Technologies Office, Department of Energy-Energy Efficiency and Renewable Energy (DOE-EERE).

Dr. Paul Rogers
Director, United States Army Tank Automotive Research, Development and Engineering Center (TARDEC), United States Army Research Development and Engineering Command (RDECOM), United States Army Materiel Command (AMC).

OPSEC #27457

This Page Intentionally Blank

ACKNOWLEDGEMENTS

The Advanced Vehicle Power Technology Alliance (AVPTA) between the Department of Energy (DOE) and the Department of the Army (DA) was publicly announced in July 2011. The Alliance underscores the urgency for energy security; in particular, an emphasis on developing advanced technologies that enable military ground vehicles to become significantly more energy efficient. Individually and collaboratively, the DOE and DA have a long history of successfully developing innovative vehicle technologies. The Alliance is chartered to accelerate the conceptualization and transition into deployment of inventive and creative energy-saving concepts that the Nation needs to achieve energy security.

This report summarizes the fourth year of technical effort and output of the Alliance's Technology Focus Area (TFA) working groups that were established in July 2011. The TFAs are respectively led by DOE and DA Subject Matter Experts (SMEs) that jointly recommend and oversee project portfolios in areas of interagency mutual technical interest.

We acknowledge the significant contributions of the DOE and DA administrative and technical personnel who in four years have grown the Alliance from a notional concept into a self-sustaining and highly-productive entity. Work product generated by the Alliance has migrated into commercial and military applications through industry partners. In parallel with ongoing activities, DOE and DA personnel have extended the AVPTA enterprise into new areas of engagement including the Office of the Secretary of Defense Operational Energy Plans and Programs (OSD/OEPP)-sponsored "Increasing the Fuel Efficiency of the Current Ground Tactical Fleet" (IFECGTF) Program; the project portfolio of which includes autonomy-enabled, vehicle electrification and powertrain technology-related activities.

We specifically acknowledge Mr. Patrick Davis who mid-year retired from distinguished service in the DOE Vehicle Technologies Office (VTO). Mr. Davis' contributed to the Alliance from its inception providing exceptional administrative and technical leadership as VTO Director.

Mr. David Howell
Project Director (Acting), Vehicle Technologies Office, Department of Energy-Energy Efficiency and Renewable Energy (VTO, DOE-EERE).

Dr. Paul Rogers
Director, United States Army Tank Automotive Research, Development and Engineering Center (TARDEC), United States Army Research Development and Engineering Command (RDECOM), United States Army Materiel Command (AMC).

This Page Intentionally Blank

CONTENTS

Appendix

This Page Intentionally Blank

EXECUTIVE SUMMARY

The AVPTA Mission is to leverage "resources to improve transition of technologies into both the commercial and military marketplace," and "industrial research and development (IRAD) involving commercial automotive and defense ground vehicle manufacturers to transition technologies and increase precompetitive research and development."

The following summaries document the work product of twenty-nine (29) projects contained within the AVPTA portfolio. Project performers include Automotive Industry Original Equipment Manufacturers (OEMs) and Tier 1 / 2 Suppliers, Defense Industry OEMs and Suppliers, DOE National Laboratories, DOD Research Laboratories, Contract Research Organizations, Universities and Colleges, Small and Other Category Businesses.

Some of the projects reported upon herein were among the seven (7) original projects that formed the Alliance's foundation and enabled its rapid start-up. In many instances, DOE and DA mutually leveraged respective ongoing projects by infusing personnel, contributing resources, and providing mutual experience/expertise. This quickly expanded the Alliance technical network and reach, and provided access to activities beyond those directly funded by the Alliance. An example is TARDEC SME engagement in the VTO Annual Merit Review (AMR) during which TARDEC personnel are exposed to the complete VTO project portfolio including participating/contributing as review panel members. Joint participation in the AMR helps to formulate areas of mutual technical interest (AOIs) that contain the description, scope and deliverables for future new-start projects.

Also reported upon herein are projects that were jointly selected for start-up in Fiscal Years 14 & 15. The Alliance has developed and instituted a sustainable, new-start project review and selection process based upon VTOs annual Funding Opportunities Announcements process and timeline. The process leverages DOE's National Energy Technology Laboratory Contract Office to rapidly obligate and efficiently track project funding by individual performer.

Through FY15, DOE and DA have jointly contributed to the Alliance funds totaling $101.8M. The result has been a level of effort/output that neither agency would have realized without the interagency collaboration.

AVPTA has become a reference model for interagency collaboration, and is the prototype after which the OSD/OEPP-sponsored IFECGTF Program is structured.

Report Prepared by:

Scott Schramm, Technical Advisor/Sr. Engineer, NAC/EBO/TARDEC/RDECOM/AMC

William Haris, Liaison Officer (to DOE), OGA/EBO/TARDEC/RDECOM/AMC

Gurpreet Singh, Program Manager, DOE-VTO, EERE

This Page Intentionally Blank

INTRODUCTION

There are two high level drivers that led to the development of the AVPTA. The first is the elevation of energy efficiency and security as points of emphasis throughout the Army and the Department of Defense (DOD) as a whole. For the Army, a major milestone in this was the development of the Army Energy Security Implementation Plan (AESIP) in 2009. Within the AESIP goal to Increase Energy Efficiency across Platforms and Facilities, there was an objective to increase the efficiency of tactical equipment. At the DOD level, the Operational Energy Strategy is a principle-guidance document for the Department's approach to ensure energy security for operational forces.

The second was a call by the DOD for strengthened interagency partnering. This was set forth in its 2010 Quadrennial Defense Review. Energy security was identified as an excellent opportunity area for such a partnership. To this end, the DOE and DOD worked to craft a Memorandum of Understanding (MOU) to establish a partnering framework to enhance national energy security. This MOU is included as Appendix A. The MOU calls for the Departments to work together in a wide range of technical areas; including efficient transportation and overall energy efficiency.

DA and DOE worked together under the auspices of this MOU to develop a charter for working together in a wide range of vehicle technologies. This charter describing the Alliance was signed by the Honorable Daniel B. Poneman, Deputy Secretary of Energy and the Honorable Joseph W. Westphal, Under Secretary of the Army and is included as Appendix B.

The DOE mission is to develop technologies that will reduce petroleum consumption and greenhouse gas emissions. A critical step in any new technology development is having it accepted and deployed in the marketplace. Teaming with DOD provides an attractive pathway for early utilization of the novel energy-saving ideas coming from the DOE research portfolio. These agencies strategic goals are summarized in the following table:

DOD & DOE Strategic Goals

DOD Operational Energy Strategy	DOE Vehicle Technology Program
Reduce Energy Demand: − Reduce: • Overall Operational Energy Demand • Mission Risks & Costs − Improve Energy Usage Efficiency	Reduce Petroleum Consumption
Expand & Secure Energy Supply: − Diversify Energy Sources − Protect Energy Supply Access	Reduce Green House Gas (GHG) Emissions[1]
Integrate Operational Energy Considerations Into: − Planning Activities and Force Development	

[1] Corresponds to DOD Strategic Driver

With strong support from senior leadership, the agencies collaborated at the Executive and SME Levels to identify AOIs that are the founding principles for describing each of the Alliance's Technology Focus Areas (TFAs). The respective TFA descriptions follow.

Remainder of Page Intentionally Blank

TECHNOLOGY FOCUS AREA (TFA) DESCRIPTIONS

TFA1: Advanced Combustion Engines & Transmissions

Advanced air-fuel management systems and novel combustion regimes have the potential to dramatically increase efficiency and power density, while at the same time reducing emissions. Meeting the challenge of developing and optimizing the combustion of common petroleum fuels, including Jet Propellant-8 (JP8), or biofuels in advanced engines requires a new level of the understanding of the physical and chemical phenomena of the Direct Injection (DI) diesel engine, which will be strongly affected by the different fuel properties which in turn affect fuel/air mixture preparation, combustion and emissions.

Advanced transmissions can allow the engine to operate more frequently in regions of high efficiency and transmit more torque while maintaining drivability. Of particular interest for further Research & Development (R&D) are approaches and devices to increase launch-assist device efficiency, and to increase the number of gear ratios. Among possible options for investigation are higher gear count automatic transmissions, Dual Clutch Transmissions (DCT), wet and dry clutch launch devices, multi damper torque converters, Continuously Variable Transmissions (CVTs), and binary transmissions.

TFA2: Lightweight Structures & Materials

Reduction of vehicle gross weight is an effective approach to reduce energy consumption during the vehicle usage, regardless of their energy sources (e.g., liquid fuels or electric batteries). Lightweight materials such as aluminum (Al) alloys, magnesium (Mg) alloys, high-strength steel, and carbon-polymer composites have been considered to replace low carbon steels conventionally used in automotive components. Challenges exist, however, to integrate components made of these lightweight materials into vehicle structures to achieve maximum weight reduction, while maintaining structural rigidity, crash safety, production quality and cost parity.

TFA3: Energy Recovery & Thermal Management

In current vehicles, approximately 60% of the chemical energy of fuel is lost in the form of waste heat, dissipated by the exhaust and cooling systems. The former offers high-grade heat that approaches temperatures of 800^{o}C while the latter is a considerably more modest heat source at approximately 120^{o}C. Of significant interest are exhaust heat recovery systems, including Organic Rankine cycles, as well as mechanical and electrical turbo-compounding. In addition, through the development of cost-competitive advanced second generation thermoelectric (TE) devices for vehicle applications vehicle fuel efficiency, performance, and emissions can be improved. Thermo-electric devices can convert engine waste heat to useful electrical power, to be used either assisting propulsion or for powering hotel loads. By integrating high Figure of Merit TE devices in the vehicle architecture, thermal management of vehicles can become significantly more efficient.

TFA4: Alternative Fuels & Lubricants

Alternative fuels and lubricants can facilitate or enhance conventional engine technology, as well as advanced combustion regime engine operation such as Homogeneous Charge Compression Ignition (HCCI) or Low Temperature Combustion. For alternative fuels, the focus should be on drop-in fuels or blend stocks that displace petroleum-derived fuels in vehicle applications without significant infrastructure changes or requirements. New developments in base oil and additive packages can reduce viscosity while maintaining temperature requirements, thereby improving engine and transmission efficiency.

TFA5: Electrified Propulsion Systems

Electric drive options range from mild battery-alternator systems to full parallel and series systems or all electric drive, and require engineering trade-offs between fuel consumption benefit and system complexity, reliability and cost. However, to achieve efficient solutions, electrical materials and devices will require higher conversion efficiencies and power/energy densities than are currently possible. The next generation electric drive vehicles will benefit from improved and lower cost batteries, novel electric motors, thermoelectric waste heat recovery, and power electronic devices and electrical topologies that are capable of handling increased loads and multiple combinations of sources and accessories. Activities will focus on hybrid system power electronics and electric machines.

TFA6: Energy Storage & Batteries

Stakeholders desire to improve existing battery chemistries, develop advanced battery technologies (high power and high energy systems), and conduct ultra-capacitor research. Military goals are to improve the availability of onboard power, reduce energy demand/consumption, expand the energy supply to military operations and build energy security into future forces in the specific areas of: silent watch capability, electromagnetic armor and starting/lighting/igniting (SLI). Civilian/commercial goals are to reduce the petroleum demand, reduce greenhouse gas emissions and promote US economic competitiveness in advanced hybrid electric vehicles and electric vehicles. Advanced lead-acid batteries, ultra-capacitors, lithium-ion batteries, lithium sulfur and lithium-air batteries are joint areas of interest. Both agencies are also interested in improving on-board safety, developing battery test protocols and promoting codes and standards.

TFA9: Autonomy-enabled Technologies

Autonomy-enabled technologies have the promise to significantly decrease fuel consumption through a variety of mechanisms. For example, platooning, where vehicles travel close to each other in order to reduce aerodynamic drag at high speeds, can only be achieved through connectivity and automation. A significant source of excess fuel consumption comes from vehicle operators driving in a sub-optimal manner, such as exceeding optimal speeds and accelerating and decelerating too quickly. Intelligent systems can help increase fuel efficiency by providing information to the driver to improve operational behavior, by determining more efficient routes based on topography or traffic conditions, or by taking control of certain vehicle functions. An automated traffic management system, implement through a system of autonomous vehicles connected with intelligent roadway infrastructure, could greatly reduce vehicle start/stops and slowdowns, optimizing traffic flow, and improving mobility in urban driving. Preliminary research by the National Renewable Energy Laboratory (NREL) indicates that platooning could increase fuel efficiency by 10%, eliminating driver inefficiencies another 15%, and completely automating the vehicle transportation system could yield a 40% improvement. However, these estimates are based on a limited number of experiments, which may not include the full range of variability that a real world system would experience, nor potential second-order effects, such as an increase in vehicle miles traveled. Accordingly, additional analysis and targeted experimentation are needed to more fully explore the limitations that these autonomy-enabled technologies may have in regards to increasing fuel efficiency across the transportation system.

PROJECT TECHNICAL REPORTS

(Start on Page 15)

This Page Intentionally Blank

AVPTA Technology Focus Area 1: Advanced Combustion, Engines & Transmissions

Ignition Models for Heavy Hydrocarbon Fuels

DOE-VTO TFA Lead: Gurpreet Singh
TARDEC TFA Lead: Dr. Peter Schihl

Principal Investigator(s):
Lyle Pickett and Mark Musculus

Combustion Research Facility
Sandia National Laboratory
Livermore, CA
E/M: lmpicke@sandia.gov and
mpmuscu@sandia.gov

Project Start: 2012
Project Completed: Q1 FY15

Objectives:

- Examine the ignition behavior, spray formation behavior, and evaporation characteristics of two, Army-provided military fuels of interest.
- Measure the ignition delay, liquid length penetration, and transient spray formation using an optical accessible constant volume combustion vessel and an optically accessible single cylinder engine.

Strategic Context:

- This basic research project generically supports Army ground vehicle engines by developing data and understanding that helps outline the impact of low ignition quality fuel on ignition processes in military engines which impact engine performance.

Accomplishments:

- Final reports complete and digitized data transferred to TARDEC.

Introduction:

The U.S. Army currently is using JP-8 as its primary ground vehicle fuel. This particular fuel has ‘loosely’ controlled combustion affecting parameters including the cetane number and the distillation curve. Historical sampling of various global regions that have provided fuel to the Army has shown that the ignition quality can vary between 30 and 60 (cetane index), though most of the fuel consumed by Army systems resides in the 43 to 45 range. These outlaying fuels can lead to potential reliability issues with ground system engines and thus various forms of research and testing has been underway to better understand the impact of such fuels on Army diesel engines. Such efforts have included production engine testing and also basic/applied research measurements to better understand the associated spray and ignition behavior of such fuels.

Approach:

Two measurement devices were used to acquire fundamental combustion data on the two fuels provided by the Army. One fuel was a poor ignition quality, research grade type and the second fuel was also a research grade type though with an ignition quality much higher than most military type jet fuels. Each fuel was evaluated in both a constant volume combustion vessel and a single cylinder engine in order to better understand the ignition event under representative light load operating conditions in military diesel engines using representative military relevant mean injection pressures.

Results and Discussion:

Engine experimental data showed that one of the two fuels exhibited ignition behavior sensitivity as a function of ignition duration. Subsequently, supplemental one-dimensional spray analysis was conducted to better understand non-chemistry effect on ignition behavior. Constant volume combustion vessel experimental data showed that the ultra-low ignition quality fuel required much higher initial chamber temperature in order to achieve similar ignition delays to the higher cetane number fuel.

Conclusions:

Data generated from this project will be integrated into an existing TARDEC fuel ignition delay database and provides both good comparison to past TARDEC engine experiments for one of the evaluated fuels and new ignition delay data for the ultra-low ignition quality fuel used in this project.

References:

- SAE Technical Paper Number 2015-01-1830 titled, “Influence of Injection Duration and Ambient Temperature on the Ignition Delay in a 2.34L Optical Diesel Engine” was published 1 September 2015 in the SAE International Journal of Engines. Citation: Malbec, L., Eagle, W., Musculus, M., and Schihl, P., "Influence of Injection Duration and Ambient Temperature on the Ignition Delay in a 2.34L Optical Diesel Engine," *SAE Int. J. Engines* 9(1):2016, doi:10.4271/2015-01-1830.

Remainder of Page Intentionally Blank

AVPTA Technology Focus Area 2: Lightweight Materials and Structures

Light Weight Vehicle Structure (LWVS)

DOE-VTO TFA Lead: Sarah Ollila
TARDEC TFA Lead: Martin McDonnell

Principal Investigator(s):
Dr. Richard Gerth

Affiliation:
TARDEC Ground Systems Survivability …

Project Start: October 2014
Estimated Completion: Q3 FY 2016

Objective(s):

- Design, manufacture, and evaluate lightweight, multi-material military vehicle structure that is both affordable and 30% lighter weight.
- Evaluate commercial defense barriers to lightweight material technology adoption.

Strategic Context:

- Bullet Point(s) (Connection to the TARDEC Strategy and/or a Program of Record)

Accomplishments:

- Completed turret structure detailed design and manufacture.
- Completed initial turret testing.
- Manufactured turret structure weight 527 lbs, 539 lbs (51%) less than the original turret structure (1066 lbs).

Introduction:

Vehicle lightweighting is a priority for the US. Army (Polsen, et al., 2014). Due to increased survivability requirements, additional protection measures have been added to vehicles resulting in decreased fuel economy, decreased reliability and associated vehicle availability, and in some cases, decreased swim and fording capability.

Lightweighting of ground vehicle structures, including passenger car bodies, follows a logical and predictable path (see Figure 1):

1. Single material component substitution
2. Single material subsystem substitution
3. Multi-material subsystem substitution
4. Multi-material complete structure substitution

The incumbent material in most cases is advanced high strength steel (AHSS). The alternative lightweight materials are aluminum (Al), magnesium (Mg), titanium (Ti), and fiber reinforced resin composites (FRC). Lightweight vehicle demonstrators have been built before, most notably the composite HWMV by TPI and the aluminum body by Alcoa for the Fuel Efficiency Demonstrator (Johnson, 2010). These studies were based on a single material dominant solution, i.e., the structures were constructed primarily from a single material.

But any subsystem or system made from a single material cannot be as light weight as a weight optimized system composed of multiple materials. This is the target of the industry – to effectively design, manufacture, and assemble vehicle structures and systems that are as light as possible and able to meet functional and cost requirements.

Approach:

A true multi-material structure for a military vehicle has not yet been produced for production. The FCS Aries was a hybrid monocoque / space frame architecture that was predominantly aluminum and composites (Pike & Filar, 2009). It was a multi-material structure which demonstrated the state of the art. The LWVS program is not designed to show the state of the technical art, but rather the state of the commercial art. In other words, it is not a study in how much weight can technically be eliminated through material optimization, but rather how much weight can be eliminated from a current military vehicle using commercially available and affordable technologies. The project tests the hypothesis that multi-material technologies developed for the commercial automotive industry can be adapted for military applications to significantly reduce vehicle weight for an acceptable cost. The ultimate goal of the project, if successful, is to transition the adapted technologies into a current military vehicle through a future upgrade program.

The demonstration platform for the LWVS is the Marine Light Armored Vehicle (LAV). The LWVS program is a multi-year program structured in three phases:

I. Trade study and technology development
II. Detailed design and manufacture
III. Test & evaluation

Phase I developed approximately 20 concepts and reduced the analysis to two multi-material versions: a metallic monocoque of steel and aluminum. This was a low risk approach capable of using the current armor solution and reducing the weight by approximately 25% at

$250 / lb saved. A more aggressive multi-material design resulted in over 30% weight savings at approximately $300 / lb saved. It was decided to pursue this design to determine whether the design could be produced, evaluate its performance, and quantify the barriers to adoption.

Phase II involved detailed design and manufacture of the turret. Particular aspects of the design phase were described in the FY14 report. In particular the stiffness of the turret was a concern and was redesigned to ensure an equivalent stiffness response in simulation within 95% of original steel structure. This report will discuss the manufacturing of the turret and the actual weight reduction achieved, some initial test results, as well as the path forward for the program.

Results and Discussion:

This project has a threshold weight reduction goal of 339lbs (38%) for the LAV-25 turret (see figure 2). The roof was replaced with lighter weight armor steel; the steel side walls and base plate were replaced with carbon fiber composite. The existing aluminum basket, hatches, and all other equipment were simply transferred from the existing turret to the new turret. While the trunnion was to be replaced by an aluminum-steel bi-metallic casting, the process was not successful because the trunnion dimensions could not be redesigned for the process. Hence, the existing trunnion was reused.

This project has a threshold weight reduction goal of 339lbs (38%) for the LAV-25 turret (see figure 2). The roof was replaced with lighter weight armor steel; the steel side walls and base plate were replaced with carbon fiber composite. The existing aluminum basket, hatches, and all other equipment were simply transferred from the existing turret to the new turret. While the trunnion was to be replaced by an aluminum-steel bi-metallic casting, the process was not successful because the trunnion dimensions could not be redesigned for the process. Hence, the existing trunnion was reused.

The normal challenges include meeting the structural strength requirements defined in the operating load cases, and this has been achieved with composite gages similar to the steel turret. The composite design allowable of 68 ksi tension and 33 ksi shear were more than adequate to provide healthy Margins of Safety for all FEA load cases. The material system selected was Tenax 34 MSI fiber and SAC79 epoxy resin. The composite layup is 25/50/25. The selected fabrication process is resin infusion with single side tool / vacuum bag.

Whenever a material substitution project is undertaken there are always “typical “issues to resolve such as strength, joining, and environment. For this project there were some additional challenges that had to be dealt with.

1st Challenge – Miscellaneous Design Issues:

The steel turret structure was used as a ground and EMI protection. The composite turret does not offer that protection. A simple grounding harness was created for safety reasons. However, a full electromagnetic environment effects assessment identified several other conditions, which were not addressed as part of this research project. Examples include concerns about crew exposure to high power radio frequencies and potential accidental discharge of ordnance due to radio frequencies. These risks are mitigated in a steel turret, but not in a composite turret.

Other concerns included reduced gun depression angle limits because the composite base plate was thicker. The depression angle was limited, because the ammo feed chute needed more space to flex. This resulted in a minor base plate redesign. This reduction affects how well the vehicle can shoot when it is on a grade.

Various side mounting racks were omitted because their interface mounts had changed, and it was deemed inconsequential to the research purposes of proving the basic architecture of the turret and the utility of the lightweight materials. However it elucidates the degree of engineering detail required, even on a subsystem, to ensure proper function.

2nd Challenge – Incorporating the Blast Shield:

Lastly, the lightweight design had not accounted for 600 lbs of blast shields that are usually added to the turret. To put this in perspective, the entire base turret structure is just over 1,000 lbs. Fortunately this was caught before final assembly, and was readily accommodated. It required designing a new attachment component, because the lifting points had been changed. Originally the lifting eye attachment also provided an attachment point for one of the blast shields. The composite side wall plates did not have to be modified to accommodate the additional weight from the shields.

3rd Challenge – Determining a Ballistically Equivalent Shock Test:

The existing steel turret structure is composed of high hard plates which contribute to the armor protection. In addition there is add-on armor to provide protection against more energetic threats. The new turret utilizes carbon fiber composite side walls, which while strong, are relatively brittle and contribute little to ballistic protection. Thus a new add-on armor package that combines the ballistic protection of the original steel turret with its add-on armor is required. An armor recipe was selected that defeats the specified threat, but at 20 lbs per square foot (psf) is 5 psf heavier than the current armor.

Since armor development is outside the scope of the AVPTA, the new armor was not incorporated. Yet, it is important to understand whether the composite structure is able to withstand the ballistic shock loads transferred from the armor.

A cross section of the armor attachment mechanism is shown in Figure 3. The ballistic shock generates enough force at the attachment points to require a through-thickness connection. A composite/metal appurtenance was developed primarily for the armor attachment and is used in modified form for all other major components. It uses a 12mm threaded WITTEN insert as the load carrying element and functions as a typical threaded tap pad.

It was necessary to develop a surrogate armor solution that transmitted the equivalent impulse to the composite structure. The impulse transmitted is the result of the energy quantity imparted to the armor minus the energy absorbed by the armor in plastic and elastic deformation. A measure of the energy imparted to the armor is the velocity of the threat projectile. The impulse is a strong function of the armor mass. Since the amount of energy absorbed is unknown, only the velocity and mass equivalence were used to choose between alternative surrogate armor choices.

Four options of surrogate armor were analyzed. They differ in the metallic insert within the armor matrix used to defeat the threat. Option 0 is the target armor to which the other 4 are compared. The surrogate should be as close to the target armor as possible. The table shows the mass equivalence and the relative threat speed the surrogate armor can defeat. Based on this data, option 2 was selected.

Generating the fixture and conducting the tests will be performed in Phase III of this project.

Turret Weight Results:

Manufacturing and assembly of the turret involved the following steps:

1. Receipt and characterization of the base turret
2. Creation of the lightweight turret structure components
3. Assembly of the lightweight turret structure
4. Disassembly of the base turret components and transfer to the lightweight turret structure.
5. Test and characterization of the lightweight turret.

The steel roof was cut using a waterjet process. The various composite components were formed using vacuum assisted resin transfer molding (VARTM). Figure 4 shows the assembled structure, and Figure 5 shows the final turret assembly with add-on armor panels attached. The composite protrusions for attaching the add-on armor are visible in Figure 4.

Table 2 displays the weight results. The base turret structure at 1,066 lbs was actually heavier than expected. The new structure was only 537 lbs or 51% lighter. However, the new turret structure does not have the same ballistic protection as the base turret, and thus, the weight analysis has to be conducted with the armor and attachment. As mentioned previously a new armor solution was designed, but not manufactured for this project. The estimated weight of this armor is approximately 118 lbs (28%) heavier than the current add-on armor. But the new multi-material turret armor combination is still lighter than the original steel plus add-on armor combination. The base turret with the add-on armor weighs 1,492 lbs, whereas the multi-material turret with its new add-on armor weighs 1,071 lbs. This is a weight savings of 421 lbs or 28%.

The assembled turret was evaluated separately in the GDLS turret lab. It was also integrated with the vehicle (see Figure 6), and some initial vehicle level evaluations were conducted. Additional testing will be completed in Fiscal Year 2016.

Two sets of tests were conducted. The first set were to measure and compare basic turret function with the base turret. The turret is operated under power and measurements taken on such metrics as:

- Max (Slew) Rate
- Friction
- Torque Ripple
- Stability Robustness
- Low-rate Tracking
- System Bandwidth

The measurements confirmed that that the multi-material turret did not alter basic turret speed or require software adjustments to maintain accurate control.

A major design concern was the stiffness of the turret (Davis & Rogers, 2015). The stiffness of the turret affects how quickly the turret will stop vibrating from various force inputs, such as automotive loads as well as gun firing loads. Rapid damping of automotive loads improves target acquisition on the move. Damping between successive gun firings is necessary for accurate, repeated fire.

The turret was integrated into a vehicle and driven over a bump block course at 4 different speeds to measure the gun stabilization error from automotive loads. Figure 7 shows the elevation and azimuth error as a function of vehicle speed in comparison to a baseline, steel turret (legacy). The elevation error is less at lower speeds and greater at higher speeds. Conversely the azimuth error is greater at lower speeds and less at higher speeds.

First, the errors are in the same order of magnitude as the legacy turret. So, as an engineering demonstration unit, the turret “passed” the test. However, these errors affect targeting accuracy when the vehicle is moving. Therefore, not only would additional testing be needed to estimate the variation in the error, but additional analysis would have to be conducted to better understand the root causes of the errors and the effect speed has on these causes. For example, the elevation error indicates a shift in the stiffness of the turret response at higher vehicle speeds, but it is not known why this shift occurs. Additional analysis identified specific frequencies with high error contribution. Finally, there are software modifications that can be tuned to compensate for some of the variation. In particular, the turret transient response from weapon firing would have to be improved, as well as address the various targeting errors outlined above.

Gun fire testing to measure the damping from successive fires will be measured in FY16. Other tests to be performed include corrosion tests and durability tests.

Conclusions:

The project has thus far demonstrate that it is possible to design and manufacture a multi-material turret that is significantly lighter and meets performance requirements. The turret structure itself was 51% lighter and with the proposed add-on armor 28% lighter than the current steel turret package. Initial performance test results are positive. Additional testing is planned and will be concluded in FY16. The affordability study will also be concluded in FY16.

References

- Davis, P., & Rogers, P. (2015). *Advanced Vehicle Power Technology Alliance Fiscal Year 2014 Annual Report.* Warren: Department of Army and Department of Energy.
- Gerth, R. J. (2013). Trade Study of a Lightweight, Multi-Material Military Vehicle Structure. *2013 NDIA Ground Vehicle Systems Engineering and Technology Symposium, 21-22 August 2013.* Troy, MI: NDIA.
- Johnson, C. (2010). Fuel-Saving Design and Engineering. *Accelerate Special 2010 Edition: "FED Alpha Revealed"*, pp. 4-9.
- Pike, T., & Filar, C. (2009). Advanced Reconfigurable Spaceframe (AReS). *19th US Army Ground Vehicle Survivability Symposium, 19--20 August 2009.*
- Polsen, E., Krogsrud, L., Carter, R., Oberle, W., Haines, C., & Littlefield, A. (2014). *Lightweight Combat Vehicle Science and Technology Campaign.* Warren: US Army Tank Automotive Research, Development, and Engineering Center.

Figures and Tables:

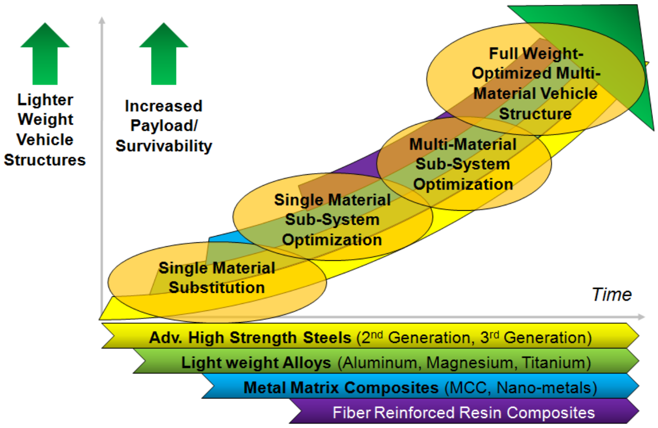

Figure 1. Lightweight Material Adoption Strategy for Structures (Gerth, 2013).

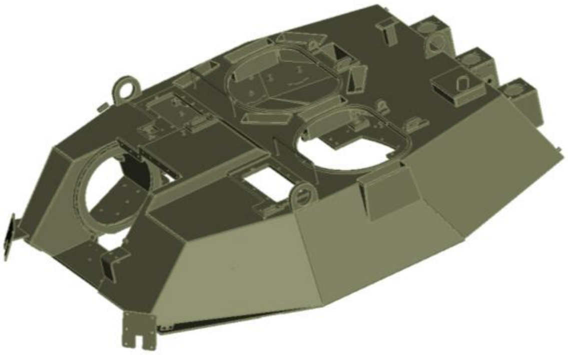

Figure 2. LAV Turret.

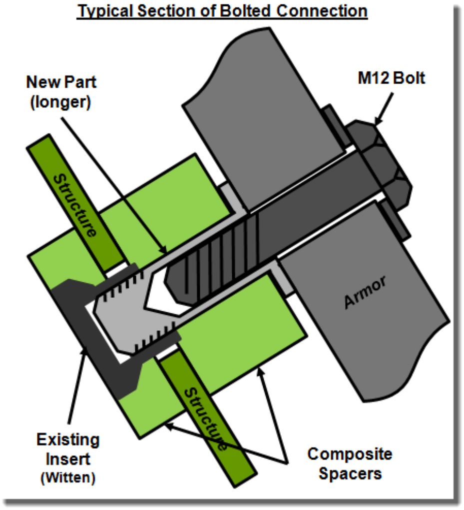

Figure 3. Cross Section View of Armor Attachment Mechanism.

Figure 4. Assembled Lightweight Turret Structure.

Figure 5. Assembled Lightweight Turret with Basket and Armor in a Turret Stand.

Figure 6. LAV-25 with turret.

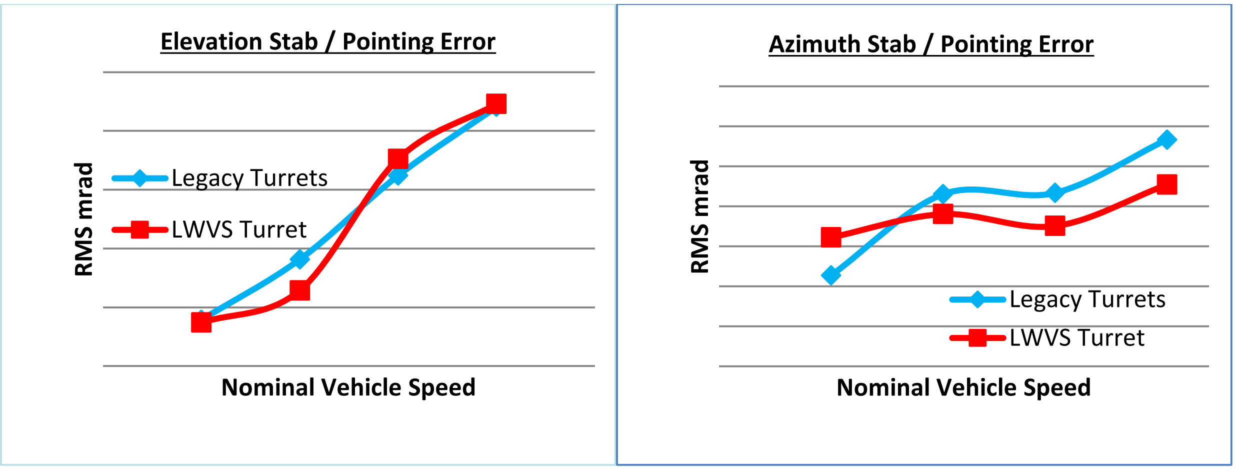

Figure 7. Elevation and Azimuth Errors vs. Vehicle Speed.

Remainder of Page Intentionally Blank

Option	Front Plate	Total Areal Density (psf)	Relative Threat Speed
0	Intended Lightweight Armor	20.0	100%
1	.750″ 6061-T651 Aluminum	18.3	100%
2	.875″ 6061-T651 Aluminum	20.1	108%
3	.300″ RHA Steel, Class 1	20.1	82%
4	.500″ RHA Steel, Class 1	28.2	100%

Table 1. Comparison of 4 Alternative Surrogate Armors.

Item	Base Turret (lbs)	LWVS Turret (lbs)	Weight Savings (lbs)	Weight Savings (%)
Structure	1066	527	539	51%
Armor	426	544	-118	-28%
Total	1492	1071	421	28%

Table 2. Turret Weight Analysis.

Remainder of Page Intentionally Blank

AVPTA Technology Focus Area 2: Lightweight Materials and Structures

Multi-Material Joining (MMJ) - Overview

DOE-VTO TFA Lead: Sarah Ollila
TARDEC TFA Lead: Martin McDonnell

Principal Investigator:
Martin McDonnell

Affiliation:
TARDEC Ground Systems Survivability

Project Start: October 2012
Estimated Completion: Ongoing

Objectives:

- Leverage DOE and DOD experience and resources to significantly impact technology development in dissimilar material joining.
- Evaluate performance and understand relative advantages of different technologies for different application and materials.

Strategic Context:

- The MMJ topics are part of TARDEC's efforts to become a Joining Center of Excellence.
- The variety of projects supports all aspects of the TARDEC Strategy, particularly CVP-related activities. The specific applications and transition plans are inclusive within each project summary.
- Both VTO and TARDEC view dissimilar materials joining as a major barrier to industry's increased adoption of advanced lightweight materials.
- Areas of future joint-agency investigation/investment include joint corrosion, adhesives and military-specific, high strain rate events such as ballistic shock.

Accomplishments:

- See individual project descriptions

Introduction:

The lightest weight structure is the one that utilizes the lightest and most cost effective material that meets the engineering design requirements, i.e., a multi-material vehicle structure. Several workshops and studies [1, 2] have documented that one of the greatest barriers to the multi-material vehicle is the lack of effective joining technologies for dissimilar materials. While there are various cost effective materials, the technology to physically join them while meeting production and engineering requirements has been lacking.

Approach:

The Multi-Material Joining effort investigates a variety of technologies to address improving joint strength for both traditional as well as novel parent materials. The technologies investigated in 2015 were:

1. Friction Stir Technologies
    a. Thermal Friction Stir Welding
2. Weld Wire Technologies
    a. Advanced High Strength Steel Weld Wire
    b. Weld Wire Characterization in Welding Armor Grade Steel
    c. High Strength Weld Wire Development Suitable for High Strength 6XXX Aluminum Alloys
3. Additive Technologies
    a. Laser Assisted Cold Spray
4. Modeling and Simulation
    a. Computation Modeling and Simulation of Metal Joints under Ballistic Impact
5. Miscellaneous
    a. Bi-Metal Brake Rotor (Formerly B-Metal Gunner Rotor Casting)
    b. Bolted Carbon Fiber Composite Joints (Note: Due to administrative issues, project technical activities were suspended during FY15, and will resume in FY16).

A technical report for each project follows this overview.

The objective is to develop these technologies to improve structural durability of existing platforms and enable lighter weight, multi-material vehicle structures in future military vehicle platforms.

References:

- AVPTA Workshop, July 2011
- National Research Council, Committee on Benchmarking the Technology and Application of Lightweighting(2012) *Application of Lightweighting Technology to Military Vehicles, Vessels, and Aircraft*.

Multi-Material Joining (MMJ) - Thermal Friction Stir Welding

DOE-VTO TFA Lead: Sarah Ollila
TARDEC TFA Lead: Martin McDonnell

Principal Investigator:
Mr. Eugene Creed

Affiliation: Focus: HOPE
1200 Oakman Blvd., Bldg C
Detroit MI 48238
Ph: 313-494-4216

Project Start: 31/03/2014
Estimated Completion: Q3FY16

Objective(s):

- Develop a production-representative manufacturing process to join high hardness armor steel with AA6061 aluminum alloy using a bimetallic friction stir welding (FSW) process.
- Demonstrate technical feasibility by producing up to 36-inch long weld samples.
- Perform process parameter experiments to optimize joint tensile strength.

Strategic Context:

- TSFW will be used by new Programs of Record (PORs) that require welding of steel to aluminum.
- The technology directly supports the TARDEC Strategy as a leap-ahead capability. It will also help ensure that newer lightweight requirements can be met without loss of performance.
- The project work product can easily transition to military stakeholders for utilization on new programs where dissimilar material joining is required. The technology also helps TARDEC's continual growth as the Joining Center of Excellence for the Department of Defense (DOD).
- Follow-on activity includes TARDEC pursuit of MANTECH support to further develop TFSW and Scribe Friction Stir Welding (SFSW).
- (Connection to the TARDEC Strategy and/or a Program of Record)

Accomplishments:

- Designed and constructed a water-cooled welding fixture capable of securing work pieces up to 40-inches long, and 36-inches wide.
- Successfully demonstrated the capability to produce up to 36-inch long bimetallic friction stir welds.
- Completed trial design of experiments (DOE) to study FSW using four different tools (A, B, C and D).
- Resulting weld quality inspection indicated that Tool A produced the best quality FSW's.
- Completed more DOE's to further check for best FSW process parameters for Tool A.
- Finalized optimal FSW process parameters for Tool A. Tool RPM = 300, Back Tilt = 2.5 degree, Traverse Speed = 30 mm/min, Tool Offset = 1 mm
- Avg. Tensile Stress observed for Tool A optimal welds= 168.9 MPa, Std. Deviation = 6.1 MPa
- Completed seven 18" long bimetallic friction stir welds using Tool A optimal parameters. Out of these seven welds, two have been reserved for post processing and delivery to TARDEC. Two will be kept at Focus: HOPE for advanced studies. And three were machined down into nine 4" x 5.5" plates for extracting mechanical test samples.
- Completed two 36" bimetallic friction stir welds using Tool A optimal parameters as well.
- A welding sub-contract was given to Brico Welding per TARDEC instructions. The subcontract work is nearing completion.

Introduction:

Weight reduction and light-weighting of ground vehicle structures has become more important as manufacturers strive to improve vehicle dynamic performance and fuel economy. From this has arisen the need for new techniques and methods to apply lightweight materials during the design of vehicle components and structures. This need serves as the motivation for this work.

Approach:

Based on a proof-of-concept project that successfully demonstrated the feasibility of joining high hardness steel to aluminum alloy using the friction stir process (TARDEC R&D Contract #W56HZV-05-C-0721), this project expands upon those results to develop the tools, equipment, and manufacturing processes required to produce extended length (up to 36- inches) production-representative bimetallic weld joints. This project has three stages.

In the first stage, the fabrication of a custom-designed FSW fixture, as shown in figure 1, was completed. This fixture was designed to hold multiple FSW samples at one time and also allowed use of thermal management techniques (as required) that were first demonstrated in the previous contract.

In the second phase, the new fixture was used to conduct a series of FSW DOE's to study tool geometries and optimize the process parameters (i.e. tool rotation speed, tool travel speed, and tool orientation). For these experiments, four different FSW tool design configurations (Tool A: 12.5 degree side tilt angle with single pass welds, Tool B: 12.5 degree side tilt angle with double pass welds, Tool C: 25 degree side tile angle single pass welds and Tool D: 36 degree side tilt angle single pass welds) were readied and used in L-9 Taguchi based DOE's. Figure 2 shows the four tools.

In the last phase, currently underway, we prepared 18" and 36" long FSW's. Select welds from this set are being analyzed further for mechanical strength and material characteristics.

Results and Discussion:

At the end of the first phase, the actual FSW fixture (as shown in figure 3) was ready and positioned on the GG1 machine table for all FSW experiments.

In the second phase, FSW's were first made using trial process parameters for all four tools. The trial process parameters were based on prior experience of staff with the FSW machine and tool combinations. Figures 4 and 5 show the side view and top view of the resulting welds.

After inspecting these test welds, it was found that Tool A produced the best welds. In order to verify the optimal FSW parameter set for Tool A, an L-9 Taguchi based DOE (as shown in Table 1) was completed and the resulting tensile test values were compared with the previously recorded best result for Tool A. The optimal process parameter set for Tool A was eventually finalized, and all 18" and 36" long FSW's (just like shown in figure 6) were completed.

Conclusions:

We investigated the use of four different W-Re FSW tool geometries for bimetallic butt welding of 0.5" thick 6061 aluminum alloy with 0.5" thick high hardness armor steel, and found that good welds of up to 36" length are doable. The observed challenges in the process are rapid tool wear and maintaining of tolerances during machining of high hardness armor steel coupons-especially as the length of the coupon increases from 18" to 36". We have also concluded that one of the four tools (Tool A), produces better welds than the others. The best observed tensile strengths (~170 MPa) are still below the target value (204 MPa) by about 15%.narrative text

In the next steps, we are making preparations to research if further tweaking of the FSW process is possible. At the same time, we are lining up activities for mechanical testing of heat treated FSW samples and advanced characterization studies of the weld material.

References:

- TARDEC R&D Contract #W56HZV-05-C-0721 reports
- TARDEC R&D Contract #W56HZV-14-C-0099 Quarterly AVPTA reports

Figures and Tables:

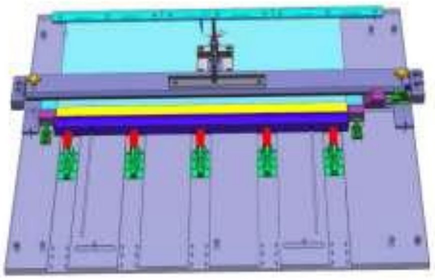

Figure 1: Design of Bimetallic FSW Fixture

Figure 2: FSW Tools

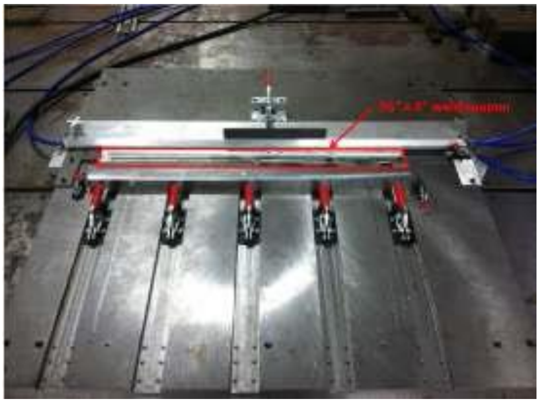

Figure 3: Bimetallic FSW Fixture with 36” Weld Coupon Mounted

Figure 4: Side view of FSW's made with Tools A, B, C and D

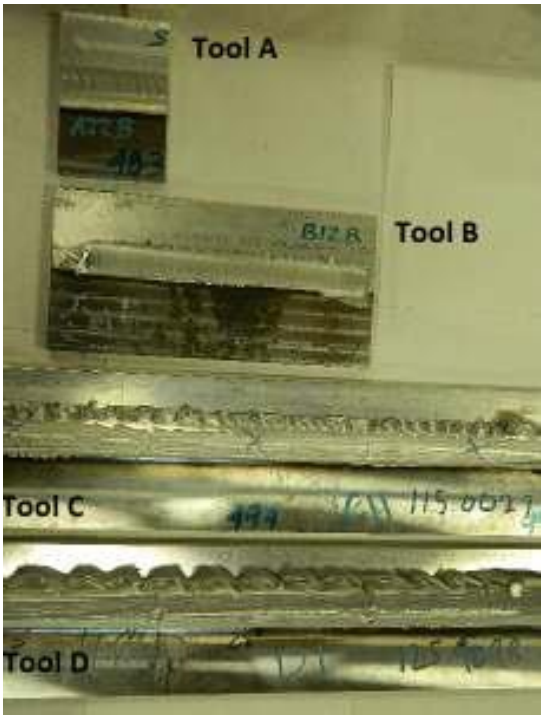

Figure 5: Top view of FSW's made with Tools A, B, C and D

Remainder of Page Intentionally Blank

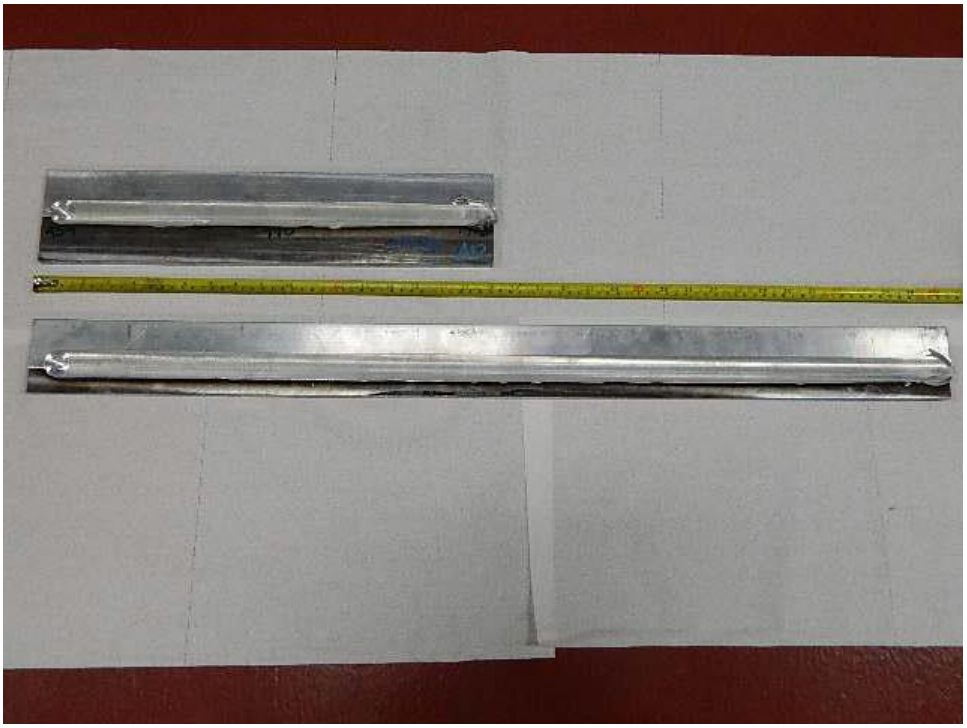

Figure 6: Sample of 18" and 36" long bimetallic FSW's

Run #	Tool (RPM)	Back Tilt (deg.)	Traverse (mm/min)	Tool Offset (mm)	Tensile Test Results (MPa)	
					Avg.	Stdev.
A24A	300	3	30	1	121	6
A24B	300	3	25	1	119	29
A24C	300	2	30	1	146	13
A25A	250	2.5	30	1	103	5
A25B	300	2.5	40	1	88	24
A25C	300	2.5	25	1	105	33
A26A	300	3	40	0.5	111	25
A26B	300	2.5	40	0.5	157	5
A26C	300	2	30	0.5	158	22
Previous best						
A20A	300	2.5	30	1	169	6

Table 1: Comparison of L-9 Taguchi based DOE and previous best result for Tool A

Remainder of Page Intentionally Blank

AVPTA Technology Focus Area 2: Lightweight Structures & Materials

Multi-Material Joining (MMJ) – Advanced High Strength Steel (AHSS) Weld Wire

DOE-VTO TFA Lead: Sarah Ollila
TARDEC TFA Lead: Martin McDonnell

Principal Investigator:
Zhilli Feng, Ph. D.II

Oak Ridge National Laboratory (ORNL)
PO Box 2008, MS6083
Oak Ridge, TN 37831
Phone: (865) 576-3797
E-mail: fengz@ornl.gov

Demetrios Tzelepis

TARDEC
Product Lifecycle Engineering

Project Start: 01/10/2013
Estimated Completion: September 2016

Objectives:

- Develop an innovative welding filler wire that can substantially reduce tensile weld residual stress and mitigate the susceptibility of hydrogen induced cracking (HIC).
- Develop residual stress measurement techniques using neutron diffraction for welded armor plates.
- Demonstrate the effectiveness of new filler wire to reduce HIC on selective welding conditions.

Strategic Context:

- The project was initiated to resolve hydrogen embrittlement during welding of armored vehicles by creating a weld wire that would produce a hydrogen embrittlement-resistance microstructure, with an added bonus that the welding process will produces compressive residual stressed, instead of tensile residual stresses at the weld toe. This would improve fatigue performance which is an interest in the automotive industry.

- The weld wire can be used across all armor steel protected military vehicles, therefore the wire will be applicable to the sustainment of legacy vehicle as well as new program of records.

Accomplishments:

- Established three experiment weld wire chemistries, and successfully produced two 0.041 in. LTPT weld wires, HV1764 and HV1766. Both weld wires were resistant hydrogen embrittlement and can be welded in ambient conditions.
- LTPT weld wire HV1766 produced compressive residual stress at the toe of the weld, and showed an overall decrease in the residual stress distribution in the weld and heat affected zone.
- With respect to tensile properties, LTPT weld wire HV1766 is over matched to MIL-DTL-12560, i.e. failure will occur in the base metal and not within the weld zone, or heat affected zone. Current commercial wires are opposite, failure occurs in the weld zone.
- Charpy testing showed a decrease in impact toughness of the weld. The decrease is thought to inclusions produced during the welding process. FY16 focus will be on increasing the fracture toughness of the weld.
- Electron Back Scatter Diffraction showed a significant decrease in retained austenite for the three pass weld vs. a single pass weld. An adjustment in the chemical composition of weld wire may be needed to stabilize the retained austenite at high temperatures.

Introduction:

Hydrogen induced cracking (HIC), or cold cracking, has been a major persistent challenge in welding of high-strength armor steels. Fabricating HIC-free welded structures can be difficult in field fabrication environment and repair. For certain types of applications, pre-heating, post-weld heat treatment, and use of low hydrogen welding practices are mandatory per code/standard specifications. These requirements are often time consuming and represent a significant cost factor in construction. There are also many other applications where it is practically impossible to consistently eliminate the presence of hydrogen, and the hardened microstructure is necessary to maintain the strength of the weld. Yet in other cases, HIC imposes undesirable limitations on the choices of high-strength steels and development of high-strength weld filler wire where the use of these steels and filler wires would be necessary for the intended applications. Therefore, there is a need and demand for new weld wire chemistry and associated welding technology that can be applied to effectively prevent HIC.

Approach:

It is well established that three essential conditions must co-exist for HIC – (i) presence/absorption of hydrogen from welding operation or environment, (ii) sensitive hardened microstructure, and (iii) high tensile residual stresses. Weld residual stresses develop in a welded structure as a result of the non-uniform thermal expansion and contraction of the base metal during welding operation. The weld region typically cools last in the entire weldment. As it cools from the melting point of the materials, the weld region shrinks. It is such on-cooling shrinkage that results in the formation of high-tensile residual stresses in the weld region that can reach or even exceed the yield strength of the base material. In principle, a volumetric expansion process that takes place during the cooling period could negate the effects of thermal shrinkage. One such volumetric expansion results from the phase transformation of austenite to a low temperature phase such as ferrite, bainite, martensite, or more likely a mixture of these low temperature phases in a steel. The effectiveness of the volumetric expansion to negate the formation of high-tensile residual stress depends on the extent of the volume expansion and temperature range in which the allotropic phase transformation takes place. The formation of martensite, especially at a temperature range close to but above the ambient temperature (or the intended service temperature of the weldments), is most effective.

This project is to develop a special welding filler wire which utilizes low temperature phase transformation (LTPT) to reduce the high-tensile residual stresses in the weldments of high-strength steels to prevent HIC. The filler wire makes it possible for "in-welding-process" HIC control, thereby eliminating the need for pre or post weld heat treatments. This reduces the fabrication cost and enables the use of high-strength steels based on the application needs without the concerns of HIC. Weld filler wire chemistries are systematically based on the LTPT principle and experimentally evaluated in the project to determine suitable weld filler wires to prevent HIC specific for armor applications.

Results and Discussion:

Based on the results from FY 14 three weld wire chemistries were cast and rolled. The weld wires are labeled by heat number HV1764, HV1765, HV1766, these weld wires were produced under contract by Special Metal in Huntington, WV. A total of 300 lbs. of each heat was produced for a total of 300 lbs. Heat number HV1765 showed cracking during the extrusion process, and no further work has been completed on these heat. Heat HV1764 and HV1766 were successfully extruded to a wire diameter of 0.041 in. Y-groove testing with No-preheat on both MIL-DTL-12560 and MIL-DTL-46100 resulted in hydrogen embrittlement free cracking. Figure 1 compares Y-Groove tests for both MIL-DTL-12560 and 46100 materials to the HV1764 and HV1766. Both the HV1764 and HV1766 showed superior resistance to hydrogen induced cracking. HV1764 and HV1766 requires no preheat (weld at room temperature), while ER100 on MIL-DTIL- 12560 and MIL-DTL-46100 requires preheat of 100 ^{o}C and 150 ^{o}C respectively.

Residual stresses were also measured at ORNL's High Flux Isotope Reactor (HFIR) using neutron diffraction for Heat HV1766 welded to MIL-DTL-12560 in a Y-Groove configuration. Figure 2 shows the results of the neutron diffraction experiments. The HV1766 weld wire showed a decrease in the residual stress distribution around the weld zone. At the toe of the weld were the stresses were compressive or near zero. This compressive stress would produce a more fatigue resistant wire and contributes to the increase in the resistance to hydrogen embrittlement over the conventional ER 100 wire.

TARDEC produce 21 in. x 14 in. mechanical test plates using the HV1766 wire and 0.5 in. MIL-DTL-12650. The weld process parameters were as follows; GMAW Pulse. 1rst pass wire feed was 220 IPM, 24.0 volts and 164 Amps. The second pass was wire feed of 205 IPM, Volts 24 and Amps 150. The third pass was 200 IPM, 23 Volts and 155 Amps. 95-5 Argon-CO_2 gas mixture was used. The atmospheric conditions were at TARDEC 23 ^{o}C and 69 % relative humidity. No pre heat was used, and the maximum interpass temperature was 260 ^{o}C. Figure

3 shows micro-hardness traverses near the start and stop of the weld. The micro- hardness in the weld zone ranged from 350 to 425 HV the HAZ ranged from 250-325 HAZ. Base metal hardness per the specification ranges from 382-423 HV. Based on hardness the weld wire produced a weld zone that is equivalent in strength to the base metal, and the HAZ would be slightly lower than base-metal. This result is significantly different than what is seen with the ER100 wire for the same base metal. Figure 4 compares the micro hardness of HV1766 and ER 100. The ER100 wire produces a significantly under matched (in strength) weld wire when compared to the base metal while the HV1766 produces a matched (in strength) as the weld wire.

The Tensile properties were measured for the HV1766 and compared to the ER100. Table 1 compares the two weld wires. As predict by the hardness values the HV1766 wire produced weldments with higher tensile strengths but lower elongation. The failure location between the two wires did change from base metal failure to weld zone failure, i.e., HV1766 wire failed in the bae metal but the ER100 failed in the weld zone. In effect the HV1766 tensile properties are measure the tensile properties of the base metal and not the actual weld wire strength.

Charpy Impact properties for the HV1766 wire were also measured and compared to base metal properties. Figure 6 summarizes the results of the charpy impact testing. Although the failure modes for all the temperature were ductile, a significant drop in toughness when compared to the base metal is seen. Analysis of the fracture surfaces of the impact specimens showed excessive inclusions on the fracture surface, Figures 7 and 8. It is believed the inclusions are a result of excessive heating during the welding process, and impurities in the weld wire itself. Further work will be conducted to increase the impact toughness weldments produced with this weld wire.

Since austenite has a high solubility of hydrogen, it acts as a hydrogen “trap” when it presence in the weld. As a result, it is critical to understand the fraction of retained austenite in the weld. Retained austenite in the weld made by HV 1766 were characterized using electron backscattering diffraction (EBSD) technique. The result was shown in Figure 9. Retained austenite was seen in between martensitic substructures. The amount of retained austenite in the weld detected by EBSD is less than 1%.

Conclusions:

Our current approach has shown the feasibility of a new HIC resistant-high strength welding filler wires. The weld wire HV1766 produce weldments with favorable residual stress distributions with respect to hydrogen embrittlement and fatigue performance. Furthermore at least one of the weld wires produced weldment that was stronger than the base metal. The following work will be conducted in FY16. Develop welding process to increase the toughness of the HV1766 weld wire. Complete the characterization of the HV1766 weld wire and the HV1764 weld wires.

Figures and Tables Begin on Next Page

Figures and Tables:

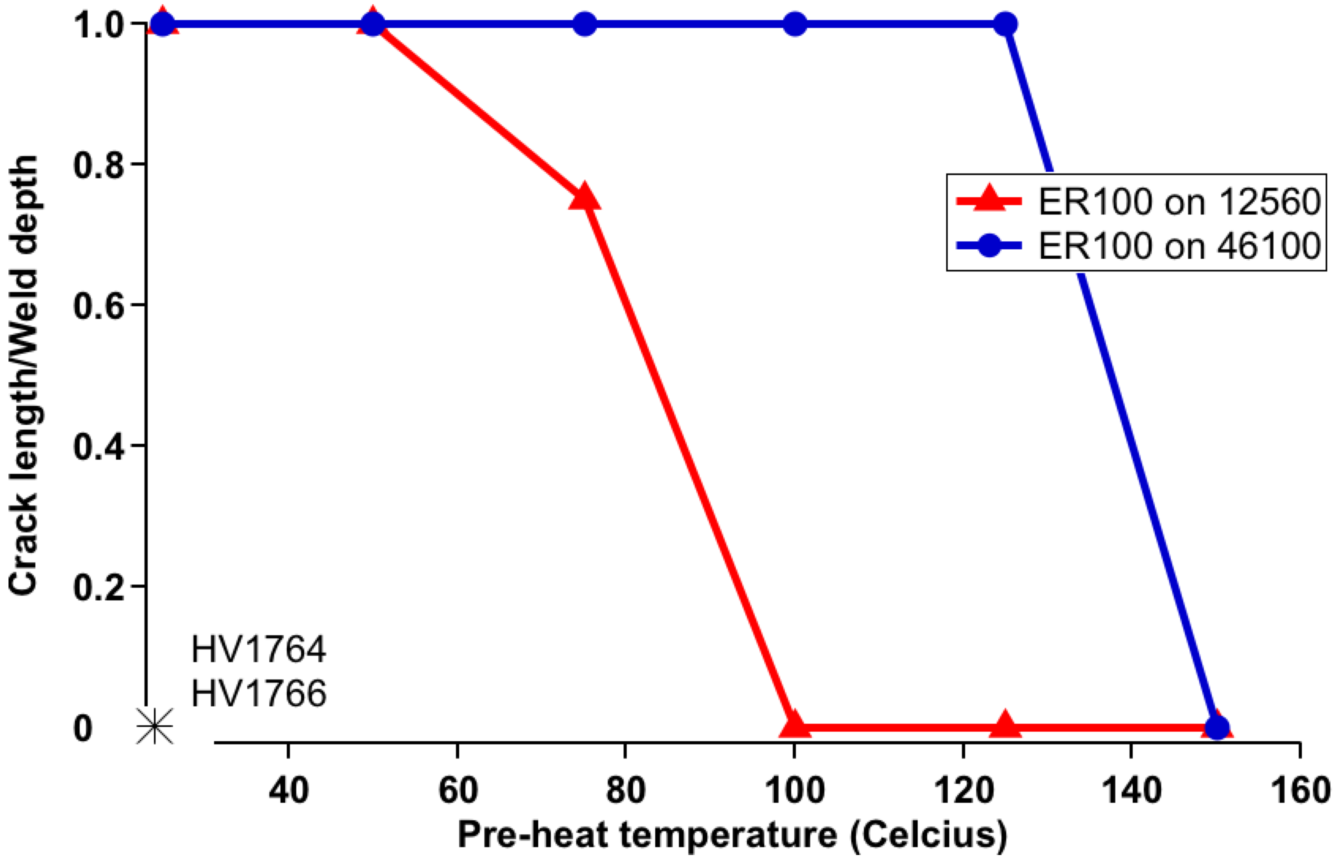

Figure 1. Comparison of Pre-heating requirement to weld ultra-high strength armored steels. Based on Y-groove testing.

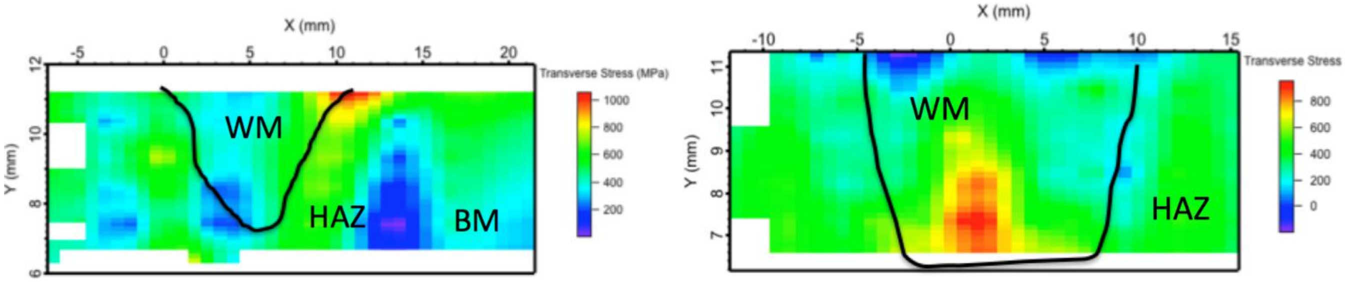

Figure 2. Transverse stress distribution in the weld of (a) conventional ER100 filler wire (left) and (b) of the HV1766 weld wire showing reduced tensile residual stresses in the HV1766 wire weldment.

Remainder of Page Intentionally Blank

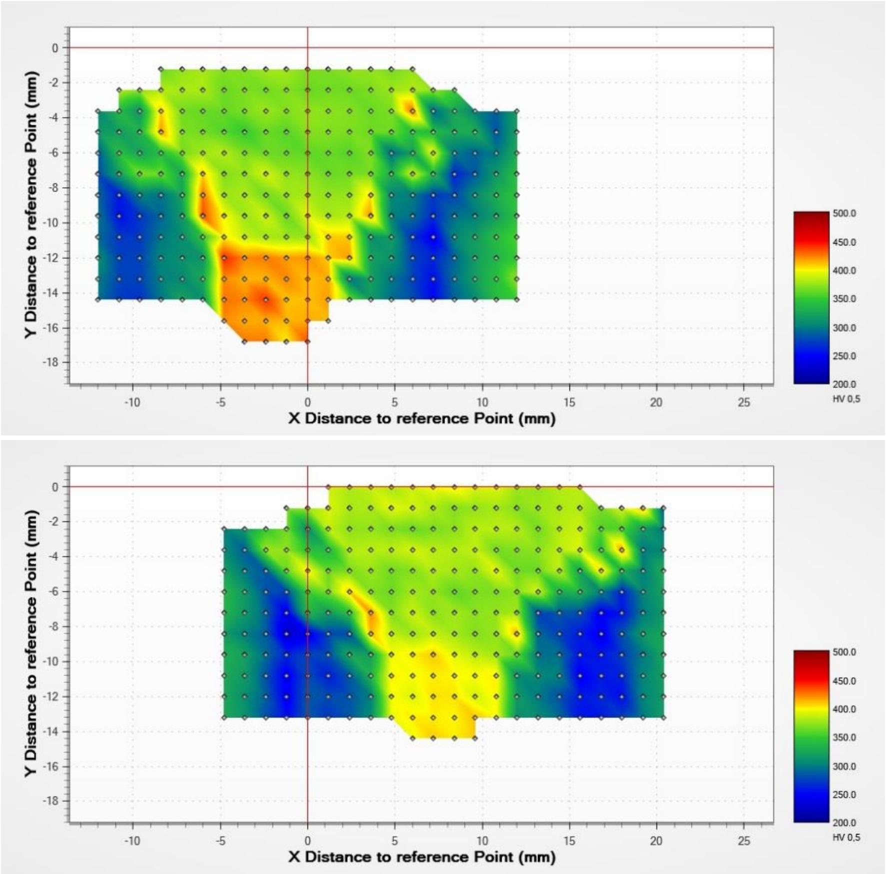

Figure 3. Micro hardness profile near the start (top picture) and stop (bottom picture) of a three pass weld showing that the weld zone has a higher hardness than the base metal of the HAZ.

Remainder of Page Intentionally Blank

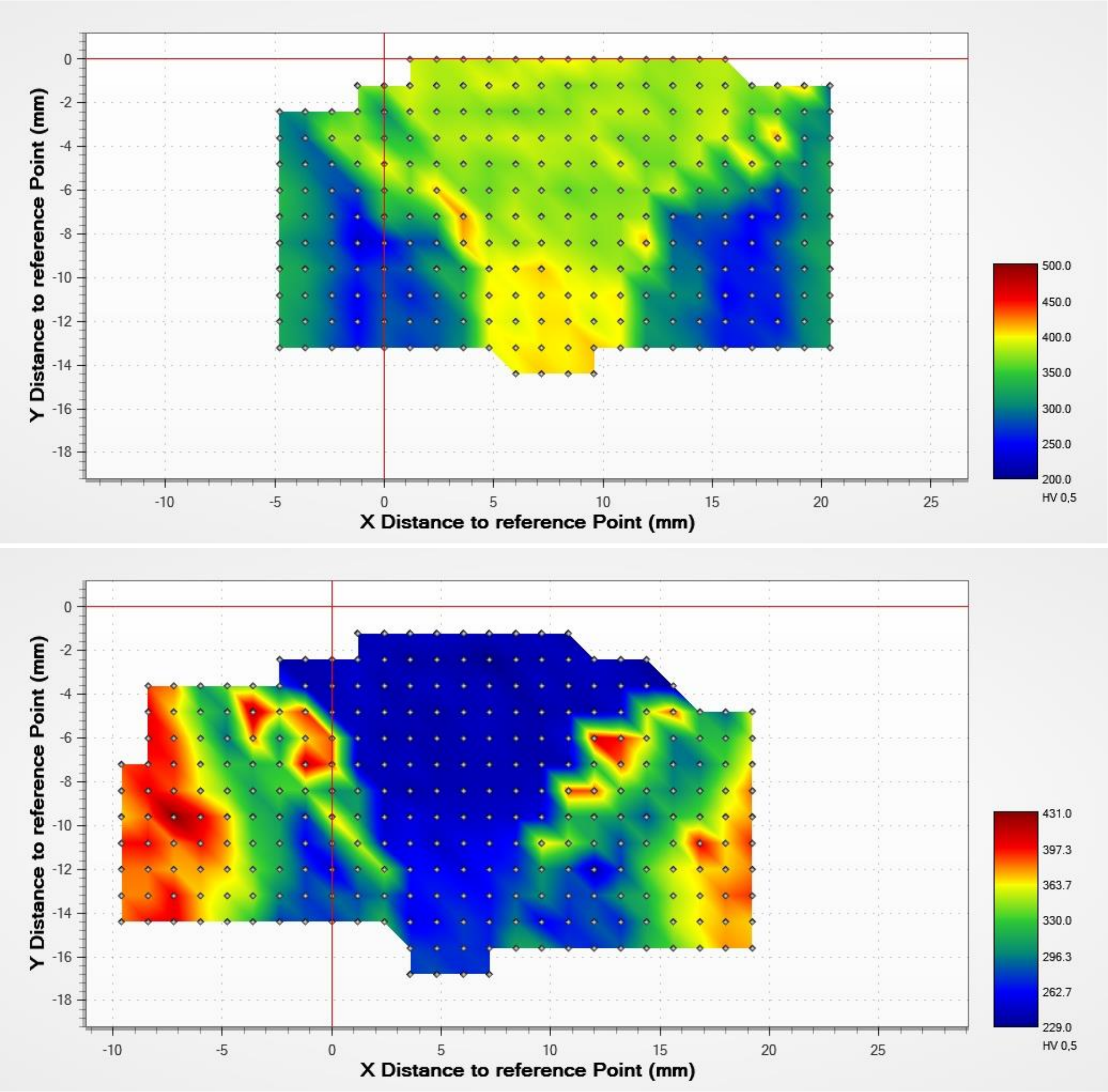

Figure 4. A comparison of the HV1766 wire to the conventional ER100 wire. The HV1766 is in the overmatched condition while the conventional is under matched when compare to the base metal.

Remainder of Page Intentionally Blank

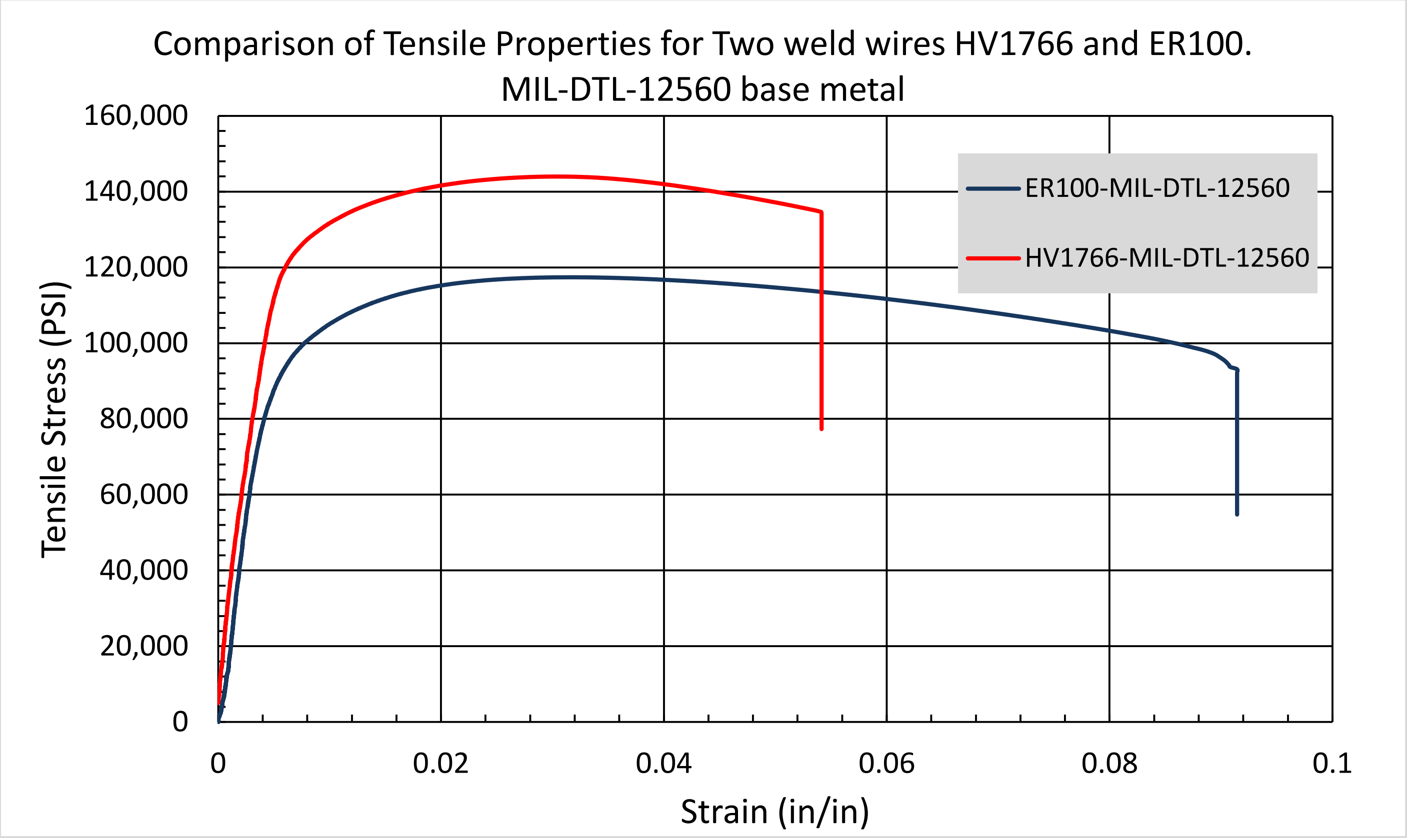

Figure 5. Tensile properties of the HV1766 wire compared to the ER100 wire. The failure location for the HV1766 wire is in the base metal, while for the conventional ER100 wire is in the weld zone.

Weld Wire	Tensile Strength (ksi)	Yield Strength (ksi)	% Elongation	Failure Location
HV1766	142.3	119.3	6.7	Base Metal
ER100	120.1	98.7	9.6	Weld Zone

Table 3. Comparison of mechanical properties of HV1766 to ER100.

Remainder of Page Intentionally Blank

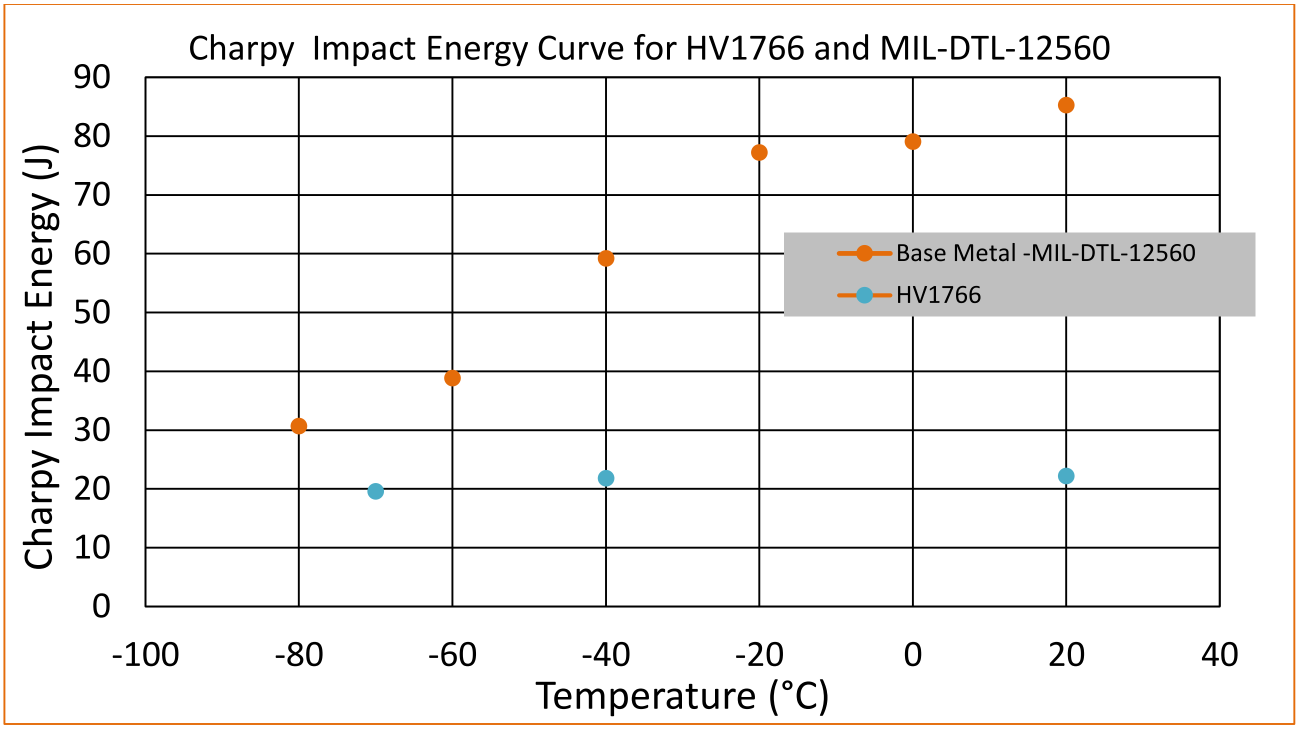

Figure 6. Charpy Impact Energy Curve for HV1766 and the MIL-DTL-12560 base metal.

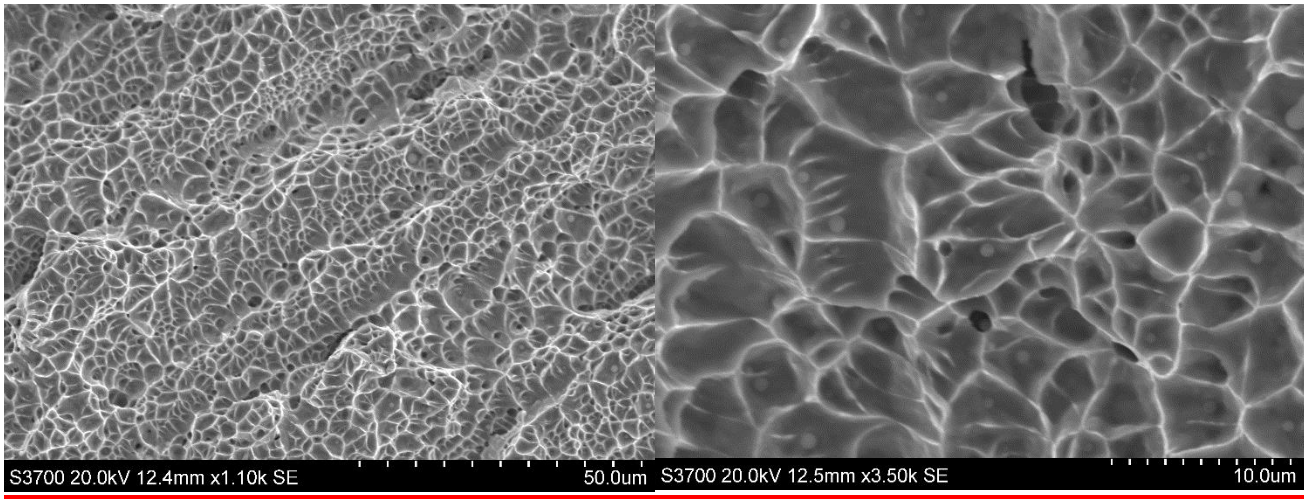

Figure 7. Photograph showing the fracture surface of the charpy impact sample at room temperature. The failure mode is ductile (left). I fine dispersion of Mn, Si, O inclusions were found in the fracture surface. See Figure 8. It is believed that these inclusions contributed to the lower than expected charpy values.

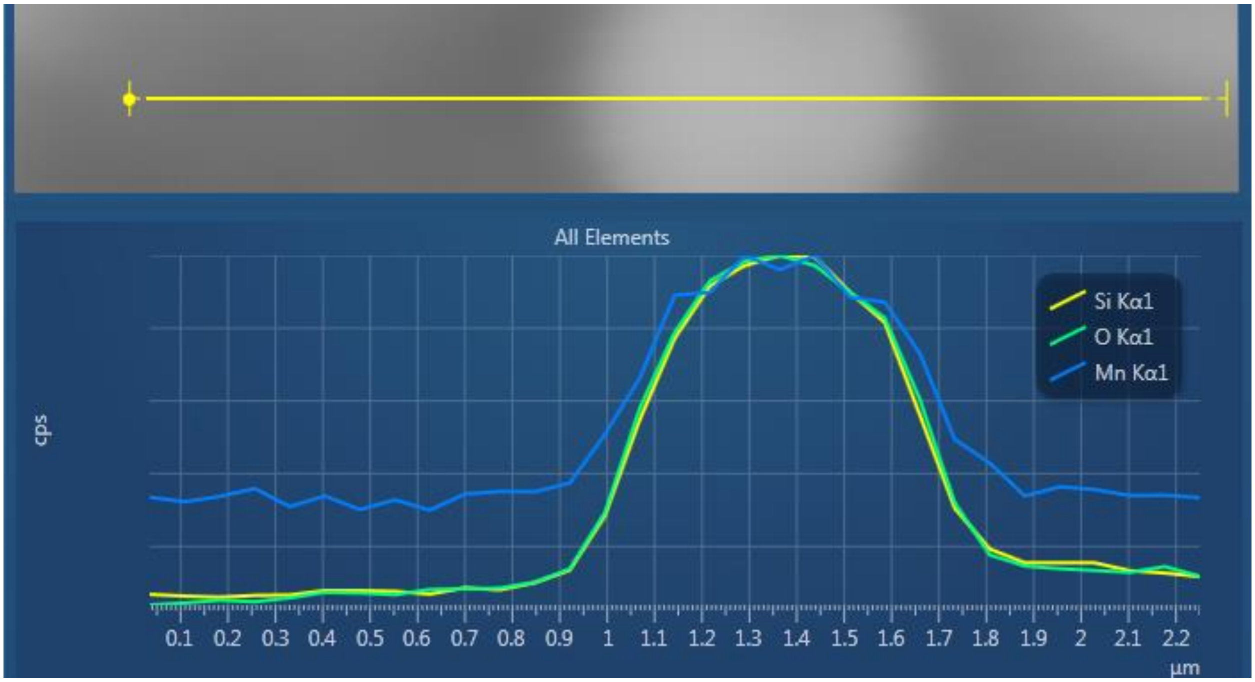

Figure 8. EDS line scan of the inclusions on the fracture surface of the charpy samples, Figure 7. The composition of the inclusions are Si, O, and Mn.

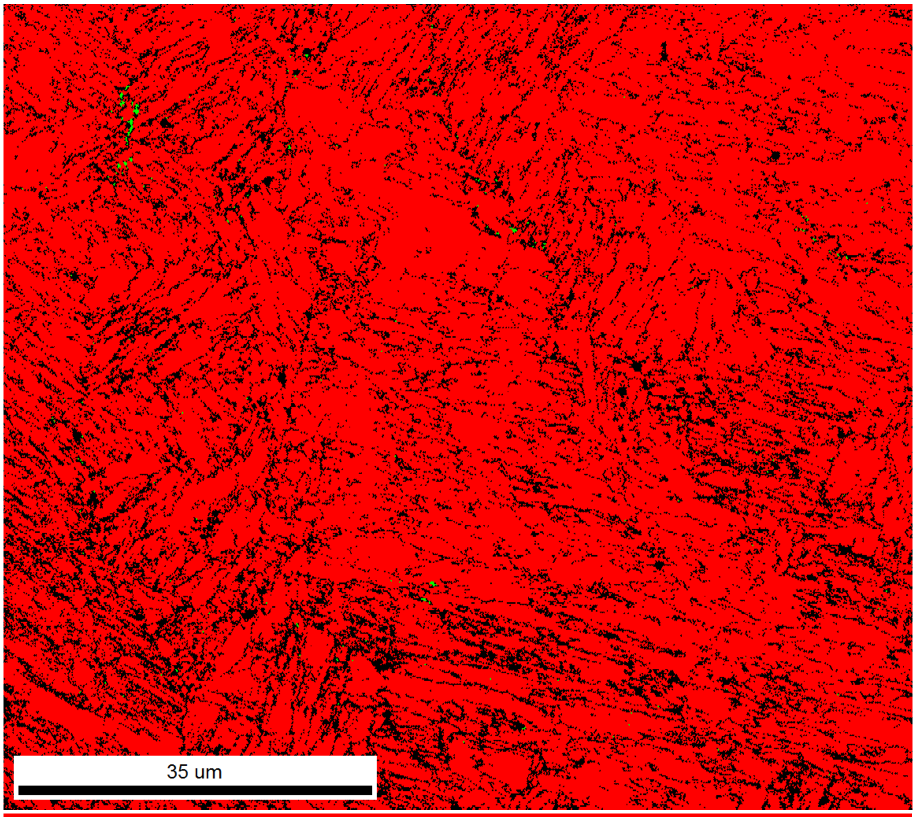

Figure 9 Electron backscatter diffraction of a three pass weld made by HV 1766 wire showing small fraction of austenite (<1%). Red is Martensite and green is retained austenite.

AVPTA Technology Focus Area 2: Lightweight Structures & Materials

Multi-Material Joining (MMJ) – Weld Wire Characterization in Welding Armor Grade Steel

DOE-VTO TFA Lead: Sarah Ollila
TARDEC TFA Lead: Martin McDonnell

Principal Investigator(s):
Mr. Matthew Rogers

Affiliation: TARDEC
Ground Systems Survivability

Project Start: October 2013
Estimated Completion: July 2016

Objectives:

- Understand the joint quality and welding process efficiency of welded armor steels.
- Establish weld wire selection criteria for the new MIL-Standard on the welding of armored steel.
- Provide practitioners a point of comparison between current joining practices and future welding practices.
- Create validation data for ballistic and blast models of welded armor plates.

Strategic Context:

The project data will transition and be used by both TARDEC engineers and vehicle manufactures to further optimize vehicle designs. The data will identify optimal weld wire / material combinations to maximize weld filler material properties. The information will be transitioned to OEMS and suppliers through the MIL weld Standard.

The project supports TARDEC's Value Stream 2 by providing PM's with data and standards for improving weld quality for all steel vehicles. The same data and standards can be transitioned to the automotive industry.

The project continues to build on the AVPTA MMJ investments in making TARDEC a joining center of excellence. The level of detail and fidelity of study speaks to TARDEC's in-depth expertise in welding.

Future plans are to expand the study to include aluminum materials (2xxx, 5xxx, 6xxx, and 7xxx).

Accomplishments:

- Welding of Phase 1-3 Completed
- Phase 1 Hardness Testing- Complete, Tensile Testing- 25%, Charpy Testing-10%, Bend Testing- 5%. Analysis of Hardness testing is currently being compiled.
- Phase 2: 90 plates have gone through testing 30 plates remain. Analysis is currently being compiled for completed plates.
- Phase 3: Testing of samples is schedule for January 2016.

Introduction:

The chemical and mechanical properties of armor steel used by the US Army are similar to advanced high strength steels used in the automotive industry. The ultimate tensile strength ranges from 150 ksi to 300 ksi depending on the armor grade selected. The last MIL standard for welding armor was canceled in 1998 and replaced with the Ground Combat Vehicle Welding Code (GCVWC)-Steel, which has never been updated and has no engineering guidance for the selection of weld wire. Additionally, neither the old MIL standard nor the GCVWC-Steel include any recommendations based on newer armor grades and new welding techniques. There are also no published industry guidelines for welding of advanced high strength steels, which the government could use to weld armor. This has led to a proliferation of welding techniques by the defense contractors, which in turn has led to a general decrease in weld quality and the proliferation of defects, such as cracks induced by hydrogen embrittlement.

Performance of welded joints is critical to the performance and reliability of ground vehicles. The performance depends on many factors associated with the welding. One key factor is the type of weld wire, of which there are many. A weld wire is classified by weld process and tensile strength. The preferred process for welding plate armor in ground vehicles is Gas Metal Arc Welding (GMAW) pulse. Weld wire tensile strength ranges from 70 ksi to 140 ksi; some ground vehicle manufactures have even used austenitic stainless steel filler metals. Unfortunately, the weldments made from these wires in combination with modern armor materials have not been characterized. There is also a general lack of knowledge of the mechanical and ballistic performance, in terms of joint efficiency, of these wires. Joint efficiency is defined as the ratio of the properties of the welded armor to the properties of the base metal armor. If the joint efficiency of each weld wire is known, then proper filler metal selection criteria can be established and implemented through a the new weld standard.

In addition to establishing selection criteria for the welding of armor steel, the data obtained in this study will be used to validate material models for ballistic and blast modeling and simulation. This data can be used by both TARDEC engineers and vehicle manufactures to further optimize vehicle designs.

Approach:

The project is divided into three phases:

Phase 1: Investigate the mechanical and metallurgical properties of welded armor using various weld wires:

This phase involves robotically welding MIL-DTL-12560 class 1, MIL-DTL-46100 class 1, and ASTM A514 Grade A to themselves in 14" x 21" x 1/2" single V-groove sample. Filler materials are solid wire, stainless steel, and metal core filler. Various tensile strengths ranging from approximately 70ksi-140ksi will be used. All samples will be welded internally at Center for System Integration (CSI). The samples will then undergo tensile, hardness, fatigue, charpy impact, hydrogen embrittlement (see Table 1). Once this is complete the samples will be ranked for performance. The highest performers will move to Phase 2.

Phase 2: Perform high strain rate events using a ballistic shock test with a welded H-Plate.

This phase will involve taking the highest filler performers from Phase 1 and robotically welding them into a 3' x 3' x 1/2" H-plate configuration. The same single V-Groove configuration will be used throughout this test as well. Once the plates are welded and radiographically tested they will be sent over to the TARDEC SABL lab for Ballistic Shock testing (see Table 2). Digital imaging correlation (DIC Figure 7) software will be used on these samples to calculate deformation response. If the samples pass they will be used for Phase 3.

Phase 3: Perform penetration testing to determine magnitude of vulnerability.

This phase will involve taking the performers from Phase 2 and robotically welding 2' x 2' x 1/2" single V-groove plates. Penetration testing will be conducted to determine the joint efficiency as defined by the magnitude vulnerability (see Table 3). These tests will be performed with a high speed camera and flash x-ray to record the dynamic deformation during the ballistic shock test. Understanding the dynamic deformation response is crucial to improving our understanding of weld responses to high strain rate events.

Results and Discussion:

In the first year the overall study plan was completed and the welding material and weld wires procured. In addition, it was necessary to develop an automated manner to weld standard I plates and H plates for testing. Figure 1 shows the hardware fixture that was developed to robotically weld the large sample of I and H plates. Figure 2 shows a completed I-plate weld, and Figure 3 shows how an H-Plate looks by comparison.

One issue that was not anticipated was that the MIL-DTL-46100 (high hard) material became highly magnetic from the shoot penning cleaning process. This required adding the additional step of demagnetizing the material before welding to prevent arc blow (see Figure 4). The phase 1 I plates welding has been completed. Figure 5 shows a sample hardness scan of a completed weld zone. Figure 6 shows how all the weld characterization samples are cut from a single plate. Three samples will be cut from different plates for each weld wire / parent material combination to obtain statistical validity of the results.

As of September 2015 90 H-plates from Phase 2 have gone through testing. 30 H-plates remain and will be tested in May of 2016. The results of the test are currently being put into a report. This information will need to be compared to the data being collected from the Phase 1 samples to determine if the the data is correlating. Phase 3 plates have completely welded as of November 2, 2015 and have been schedule to be tested in January of 2016.

Conclusions:

The Phase 1 will need to finish samples preparation, then test, and finally be analyzed. Phase 2 will need to have the final 30 H-plates completed and analyzed. Phase 3 will need to be tested and analyze. Once the data is collected, it will be statistically analyzed and provide input to the development of a new MIL-STD for welding. MIL-STD will utilize the data and testing criteria to develop mechanical acceptance criteria.

This data will transition and be used by both TARDEC engineers and vehicle manufactures to further optimize vehicle designs. This data will transition to Industry, PM's, Depot's, and Arsenals through the new welding mil standard, by creating filler metal selection charts. The data from this project will also be easily transitioned to help industry, such as the automotive and heavy equipment companies, in the selection of weld filler materials for their types of AHSS due to the similarities in properties. The data obtained in this study will also be used to refine material models for modeling and simulation.

References:

- N/A

Figures and Tables:

Test	Locations	Time Frame
Robotically welded samples	TARDEC CSI weld area	FY14/FY15
Tensile Testing	TARDEC Metallurgical Lab	FY14/FY15
Hardness Testing	TARDEC Metallurgical Lab	FY15
Charpy Impact	TARDEC Metallurgical Lab	FY16
Hydrogen Embrittlement Test	Oak Ridge National Lab	FY15/FY16

Table 1. Phase 1 Test, Test Location, and Time Frame.

Test	Locations	Time Frame
Robotically welded samples	TARDEC CSI weld area	FY15
Radiographic Test	ANAD	FY15
Ballistic Shock Test	TARDEC GSS SABL	FY15

Table 2. Phase 2 Test, Test Location, and Time Frame.

Test	Locations	Time Frame
Robotically welded samples	TARDEC CSI weld area	FY15
Penetration Test	TARDEC GSS SABL	FY15/FY16

Table 3. Phase 3 Test, Test Location, and Time Frame

Figure 1. Fixture for Robotic Welding of Phase 1 plate.

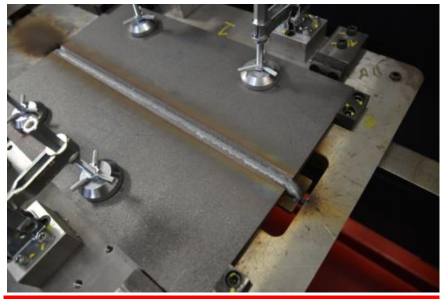

Figure 2. Completed Phase 1 Weld.

Figure 3. Phase 2 H-Plate Clamped and Ready for Welding.

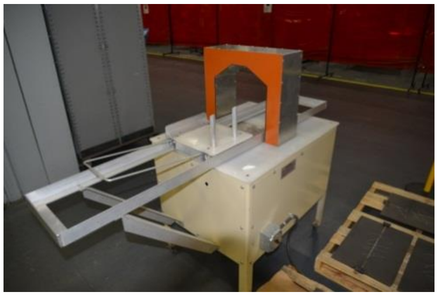

Figure 4. Demagnetizing Process.

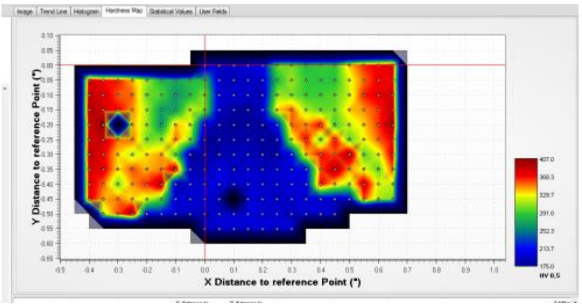

Figure 5. Sample of Micro hardness profile.

Figure 6. Phase 1-Plate Marked Samples for Standardized Weld Characterization Tests.

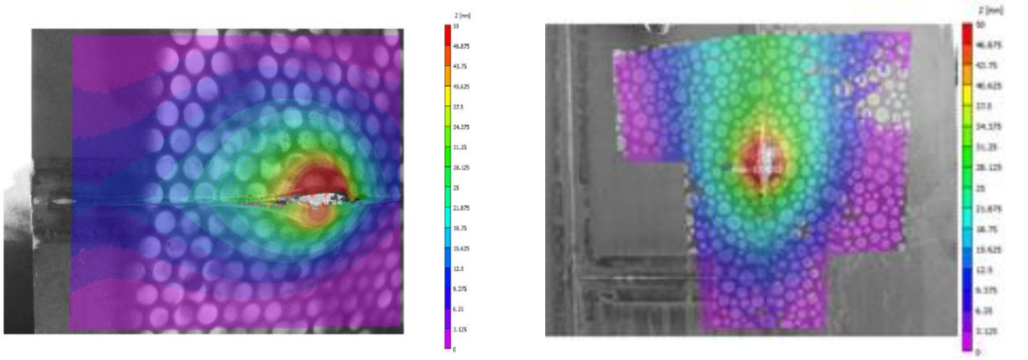

Figure 7. DIC of Phase 2 H-plate

Remainder of Page Intentionally Blank

This Page Intentionally Blank

AVPTA Technology Focus Area 2: Lightweight Structures & Materials

Multi-Material Joining (MMJ) – High Strength Weld Wire Development Suitable for High Strength 6XXX Aluminum Alloys

DOE-VTO TFA Lead: Ms. Sarah Ollila
TARDEC TFA Lead: Mr. Martin McDonnell

Principal Investigator:
Mr. Matthew Watson

Affiliation:
Alcoa Defense, Inc.
Alcoa Technical Center
100 Technical Drive
Alcoa Center, PA 15069-0001

Project Start: May 2014
Estimated Completion: Q2 FY16

Objectives:

- Develop a weld wire for welding high strength aluminum plate, particularly 6055; such that the weld joints exhibit improved mechanical properties and corrosion resistance over the incumbent weld wire material.
- Refine the chemistry of the weld wire in an effort to optimize the corrosion and mechanical properties of the resulting weld joint.
- Fusion weld aluminum alloy materials (5083 and 6055) with the newly developed high strength filler wire.

Strategic Context:

- Permits the light weighting and improved performance of new vehicles, as well as increased protection for the Warfighter, due to a 20% strength increase in 6xxx alloys
- Improves the maintainability and repairability of legacy vehicles.
- Provides a cost effective solution and enables design flexibility in material choices for high performance combat and heavy transport vehicles.
- Attractive for commercial transportation applications to cost effectively save weight.

Accomplishments:

- Eleven (11) new chemistries were developed for welding the 6055 alloy and book molds were used to create gas tungsten arc (GTA) welding rods. Two (2) of the chemistries (C138H and C139H) performed very well in restrained-T tests and were selected for further development.
- Crack-free GTA butt welds were produced in 0.5” thick 6055 using both C138H and C139H
- Tensile tests were performed with encouraging results. C138H provided ~19% improvement in tensile strength vs. the current MIL-DTL-32262A minimum (6055 Welded with 4943) and C139H provided ~26% improvement
- Crack-free restrained-tee welds were produced when GTA welding 6055 to 5083 with both C138H and C139H fillers
- 5083-5083 restrained -T weld tests were successful performed using the developed C139H filler wire. No cracking was observed visually or with die penetrant.
- ASTM G67, Nitric Acid Mass Loss Tests were completed for 6055-6055 butt welds using both the C138H and C139H. Results were slightly higher than a traditional 5xxx alloy, which was expected since C138H/C139H alloys have more copper than these alloys, but were within expectations. ASTM G110 tests were also initiated.
- 2, 100 lb billets each of C138H and C139H were successfully cast to provide material for gas metal arc (GMA) welding evaluations.
- Alternative suppliers for extruding the prototype billets were explored to address slower than desired turnaround times, which has led to delays in receiving the wire needed for evaluation. In particular, extrusion trials were conducted at 2 alternative suppliers. Of particular note, C139H was extruded at Milward, Inc. to ¾” with a good turnaround but with mixed results.

Introduction:

High strength 6XXX aluminum alloys, such as 6055, have approximately 20% higher strength than currently used aluminum alloys. They offer the potential to significantly improve performance and reduce weight and cost. However, when welding 6XXX high strength alloys, the only commercially available filler wires that can be used to weld these alloys without cracking (4043, 4047 and 4145) produce welds with limited shear strength and ductility, which in turn limit their capability to withstand blast type of loads. Because the joints produced with these filler wires are so much weaker than the parent material, the full benefits of the high strength 6xxx alloys cannot be realized. As such, the thickness of the components must be designed to compensate for the weakness of the joining method used, resulting in parasitic materials and increased weight. The increase in weight results in an increase in fuel consumption, an increase in drive train and suspension requirements, and a loss in performance. In addition, when welding these high strength alloys to 5XXX (e.g. 5083) parts, the use of 4XXX type filler leads to formation of brittle MgSi2 at the fusion zones of the welds with the 5XXX parent metals. On the other hand, when welding such high strength 6XXX/5XXX alloy combinations with Mg based 5XXX filler alloys (e.g. 5556, 5356, 5183), the formation of Mg/Cu low melting eutectics at the fusion zones of the welds leads to their cracking. Improved joining methods are therefore needed so that these high strength materials can be joined in a fashion that optimizes the vehicle manufacturing system. To address this need, the Alcoa Technical Center (ATC) is developing a number of weld wires that would result in higher strength weld joints over the incumbent weld wires. Specifically, ATC is developing new high Mg weld filler alloys with the following benefit attributes:

- Enables joining high strength 6xxx alloys (e.g. 6055) to each other and 5xxx alloys (e.g. 5083).
- Enables fusion welds with high shear strength, ductility and blast resistance.
- Features a chemistry optimized to minimize corrosion susceptibility.
- Solves MgSi2 brittle effects of using 4043 in high strength 6xxx alloys.

This effort will contribute directly to developing welding parameters for each of the subsequent alloy sets and weld wire combinations. The mechanical properties and corrosion performance of the weld joints are also being evaluated for each of the combinations to determine strength and joint characteristics.

Approach:

In Phase I of the High Strength Filler Wire Program a filler wire was developed, to bench scale levels, which could join 6013 plates while maintaining high strength and ductile weld joints.

In Phase II of the program, the chemistry of the weld wire is being refined in an effort to optimize the corrosion and mechanical properties of the resulting weld joint. Additionally, other aluminum alloy materials (5083 and 6055) are being fusion welded with the newly developed high strength filler wire. The corrosion resistance of the weld joints and their mechanical properties are also being evaluated. The following approach has been established for this evaluation.

- Develop Candidate Chemistries
- Cast Book Molds
- Machine, Homoginize, Roll Candidate Chemistries
- Bench Scale Test and Evaluate – GTA
    - Weldability Evaluation
    - Corrosion Evaluation
    - Macrographs
    - Microscopy
    - Mechanical Property Evaluations
- Repeat if Necessary or Down-select
- Cast Pilot Scale Ingots - 100#
- Extrude Ingots to Rod
- Draw, Shave and Clean Wire to 0.062”
- Test and Evaluate – GMA
    - Weldability Evaluation
    - Corrosion Evaluation
    - Macrographs
    - Microscopy

- Mechanical Property Evaluations

Repeat if Necessary

Results and Discussion:

Weld Trials for Initial Chemistries:

At the beginning of the year, seven (7) new weld filler chemistries (W01-W07) for the welding of aluminum alloy 6055 were developed. Book molds were cast of the 7 new chemistries, rolled into plate, and TIG rods were created from the rolled plate stock. Weldability tests were then conducing using restrained T samples and the chemistries were ranked based on weld quality, dye penetrant tests, and optical metallographic results (Table 1). Unfortunately, some level of bottom member, under bead cracking was observed in all specimens, including welds with 4943 weld filler (Figure). Two additional restrained T specimens were then welded with 4043 and 4145 weld fillers. The 4043 weld filler cracked under the bottom weld similar to the 7 new chemistries, however there was no cracking observed with the 4145 weld filler. As a result of this analysis, it was concluded that all of the new chemistries failed the evaluations and that the chemistries needed to be refined.

Welding Trials and Performance of Refined Chemistries:

Based upon the unfavorable results of the previous chemistries, four (4) new chemistries (W08-W10) were developed for welding the 6055 alloy. Book molds were cast of the four (4) new chemistries and the molds were rolled into plate. Gas tungsten arc welding (GTAW) rods were created and weldability tests were performed using restrained-T samples. Two (2) of the chemistries (W09 & W10) performed very well based on weld quality and dye penetrant tests (Figure) and were selected for continued development. These chemistries were given new designations C138H and C139H and further evaluated.

Next, crack-free GTA butt welds were produced in 0.5” thick 6055 using both C138H and C139H. The tests were repeated 4 times for each chemistry with no cracking. Each weld was evaluated with micrographs (Figure and Figure) and die penetrant inspections (Figure and Figure), with favorable results. Slightly more porosity was noted in the C138H GTA welds as compared to C139H but neither was concerning. Tensile tests were performed with encouraging results. C138H provided ~19% improvement in tensile strength vs. the current MIL-DTL-32262A minimum (6055 Welded with 4943) and C139H provided ~26% improvement (Figure).

In addition, crack-free restrained-tee welds were produced when GTA welding 6055 to 5083 with both C138H and C139H fillers (Figure). The tests were performed using 5083 as the base of the tee and 6055 in the vertical (Figure). Die penetrant inspection was performed with favorable results (Figure and Figure).

The ability to weld 5083-5083 was also evaluated using a crack prediction model. The model suggested that there is a slight risk of cracking but overall the results were not too alarming. Based on these results, 5083-5083 restrained-T weld tests were performed using the developed C139H filler wire. No cracking was observed visually or with die penetrant and the test was deemed successful (Figure).

ASTM G67, Nitric Acid Mass Loss Tests were completed for 6055-6055 butt welds using both the C138H and C139H. Results were slightly higher than a traditional 5xxx alloy, which was expected since C138H/C139H alloys have more copper than these alloys, but were within expectations. Optical MET is currently being performed to further evaluate the results. ASTM G110 (immersion in sodium chloride + hydrogen peroxide) tests were also initiated.

Casting and Extrusion Trials

Four (4) casting trials were conducted in order to produce material for gas metal arc (GMA) welding evaluations. As an initial step, ~100 lb billets were desired for the evaluations. Given the relatively small size of the billets, Alcoa contracted Milward Alloys, Inc. to cast the material. A total of seven (7) ~100 lb billets were cast during this time, with four (4) of the billets being useable for further evaluation (Table 2). Of the remaining 3, 1 was an unsuccessful cast and 2 others tested outside of composition limits. Hydrogen results were generally high for all billets but not too alarming. As a result, ~200 lbs each of C138H and C139H material is available for further processing and weld trials.

In addition, alternative suppliers for extruding the prototype billets were explored to address slower than desired turnaround times, which has led to delays in receiving the wire needed for evaluation. In particular, extrusion trials were conducted at 2 alternative suppliers. Of particular note, C139H was extruded at Milward, Inc. to ¾” with a good turnaround but with mixed results (Figure).

Conclusions:

Two weld wire chemistries (C138H and C139H) have been developed and successfully used to weld 6055-6055, 6055-5083, and 5083-5083 using GTA welds, including crack free butt welds in 0.5” thick alloy 6055, crack free restrained-Tee welds when welding 6055 to 5083, and crack free restrained-Tee welds when welding 5083 to 5083 with C139H filler. These wires have been demonstrated to provide a ~19% and 26% improvement in tensile strength vs. the current MIL-DTL-32262A minimum (6055 Welded with 4943) and initial corrosion testing has demonstrated acceptable performance. Although a number of challenges have been faced while trying to produce material for additional GMA welding trials, solutions have been identified and this testing is expected to resume once the material is drawn down into wire.

References:

- **MIL-DTL-32262A (MR):** Aromor Plate, Aluminum Alloy 6055 Weldable & Alloy 6061, Unweldable Appliqué, 16 March 2015

Figures and Tables Start on Next Page

Figures and Tables:

Rankings	
Weld Quality	Micrographic Analysis
Best	Best
4145	4145
4943	4943
4043	4043
W6	W6
W5	W5
W2	W2
W1	W4
W4	C56U
C56U	W3
W3	W1
W7	W7
Worst	Worst

Table 1. Initial Ranking of the Seven New Filler Chemistries

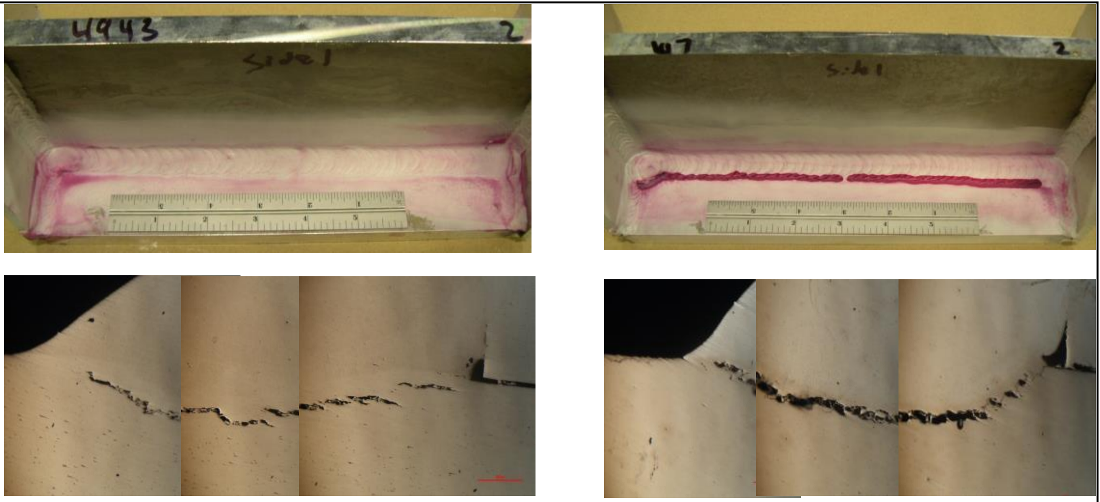

6055-T6 GTA Welded With TARDEC Blast Approved 4943 Filler – Baseline Best Case

6055-T6 GTA Welded With Candidate Filler (W7) Filler

Figure 1. Restrained "T" Weldability Samples with Polished Cross Sections

Remainder of Page Intentionally Blank

Figure 2. Initial restrained-T results for W09 (left) and W10 (right)

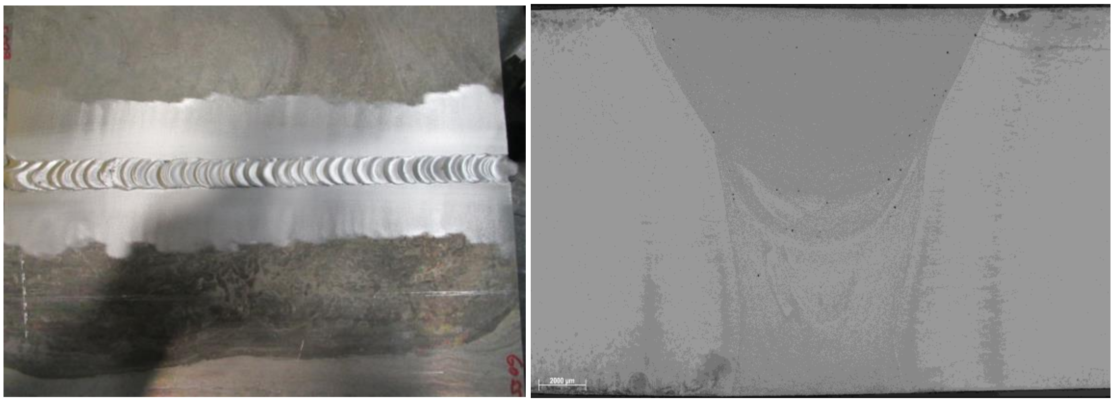

Figure 3. Example 6055-T6 GTA weld using C138H Filler (left) and example macro/micro section results (right).

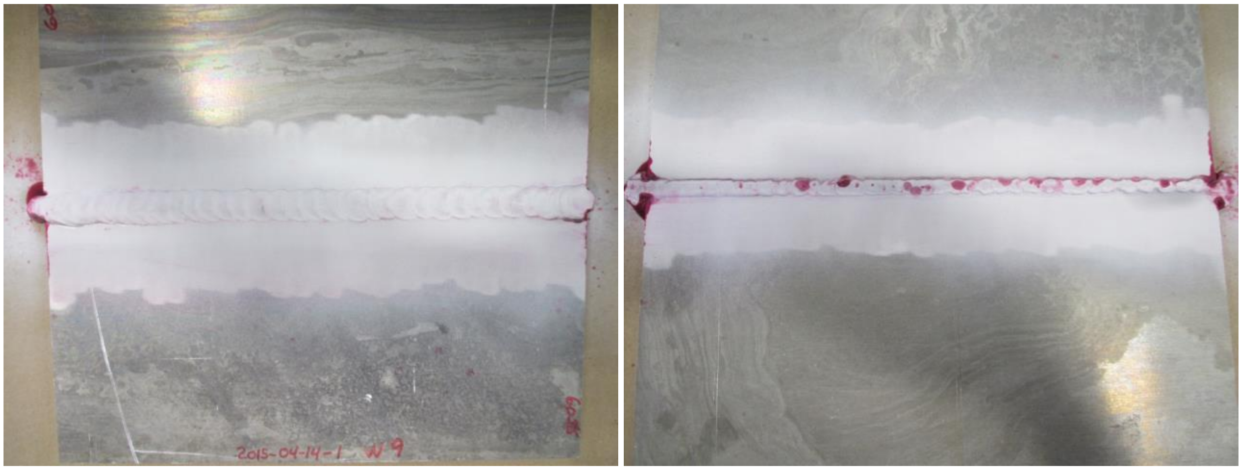

Figure 4. Example face (left) and root side (right) penetrant inspection for 6055-T6 GTA welded with C138H

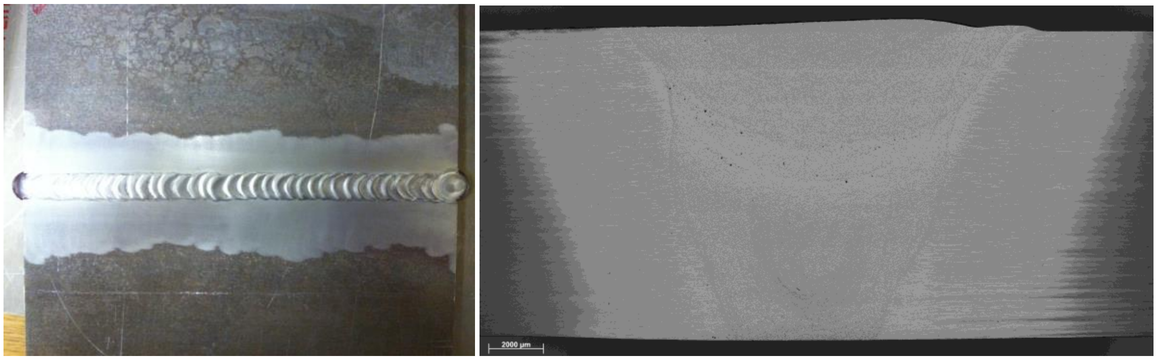

Figure 5. Example 6055-T6 GTA weld using C139H filler (left) and example macro/micro section results (right)

Figure 6. Example face (left) and root side (right) penetrant inspection for 6055-T6 GTA welded with C139H

Remainder of Page Intentionally Blank

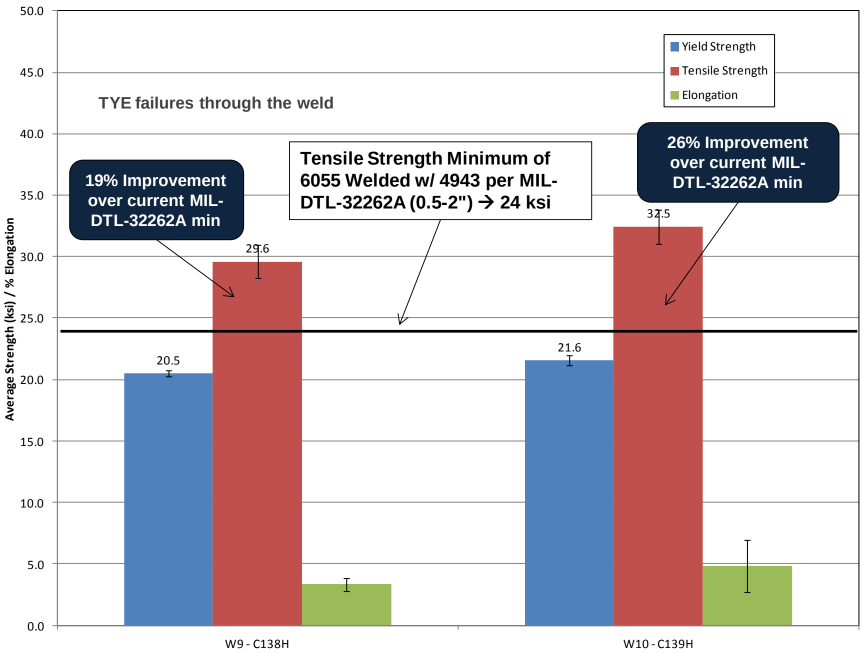

Figure 7. Initial tensile results for 6055-T6 GTA welded with C138H and C139H fillers

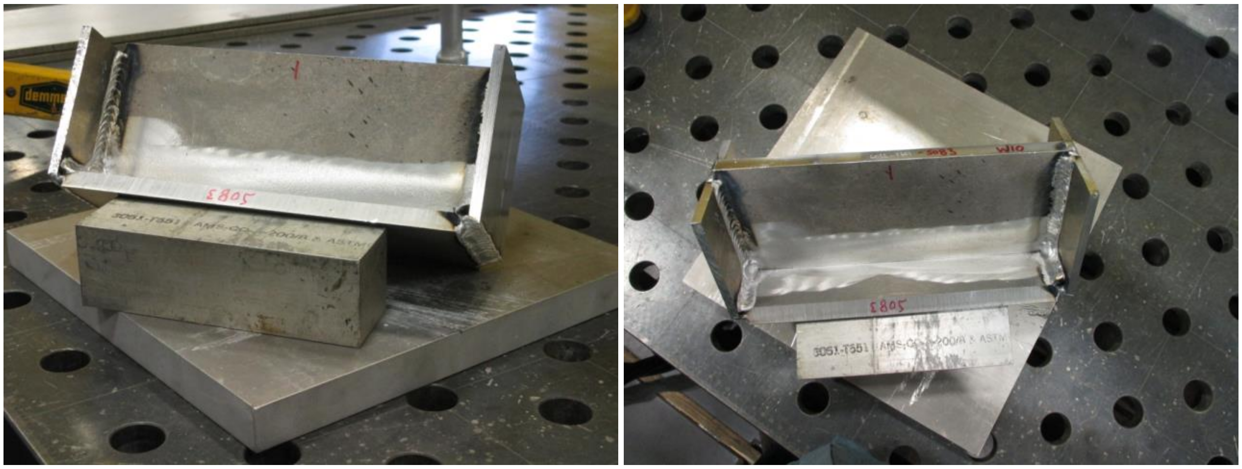

Figure 8. Sample setup for 6055-5083 restrained-tee evaluations

Remainder of Page Intentionally Blank

Figure 9. Example 6055-5083 restrained-tee welds using C138H (left) and C139H (right)

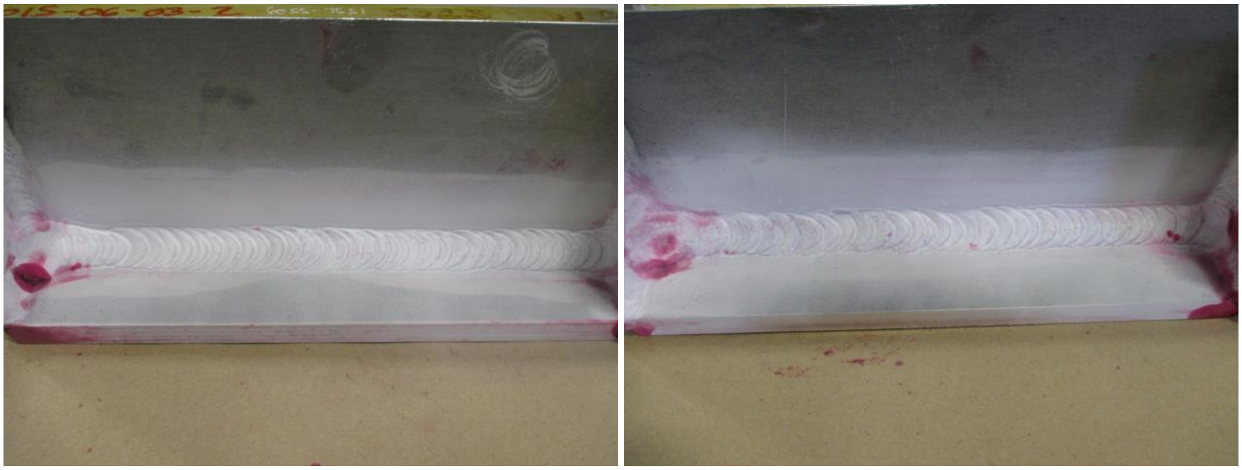

Figure 10. Example side 1 (left) and 2 (right) die penetrant results from 6055-5083 restrained-tee welds using C138H

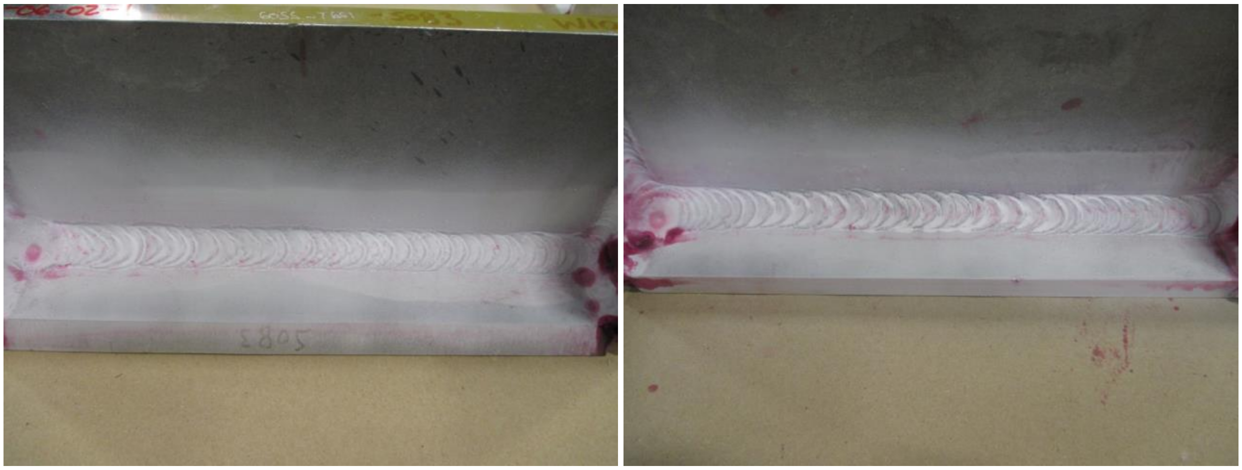

Figure 11. Example side 1 (left) and 2 (right) die penetrant results from 6055-5083 restrained-tee welds using C139H

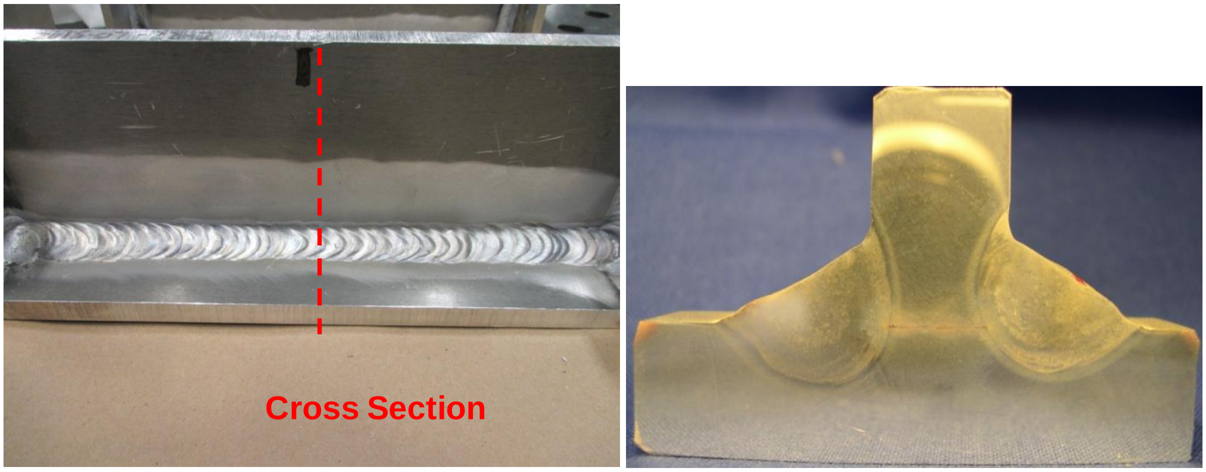

Figure 12. Example 5083-5083 restrained-tee welds using C139H

Chemistry	Trial #1 (4/29/15)	Trial #2 (5/6/15)	Trial #3 (5/13/15)	Trial #4 (9/10/15)
C138H (W9)	Chemistry tested outside of limits - billet not used	Successful cast	Successful cast	------
C139H (W10)	Successful cast	Billet bled out - unsuccessful cast	Chemistry tested outside of limits + high hydrogen measured - billet not used	Successful cast

Table 2. Summary of Casting Trials

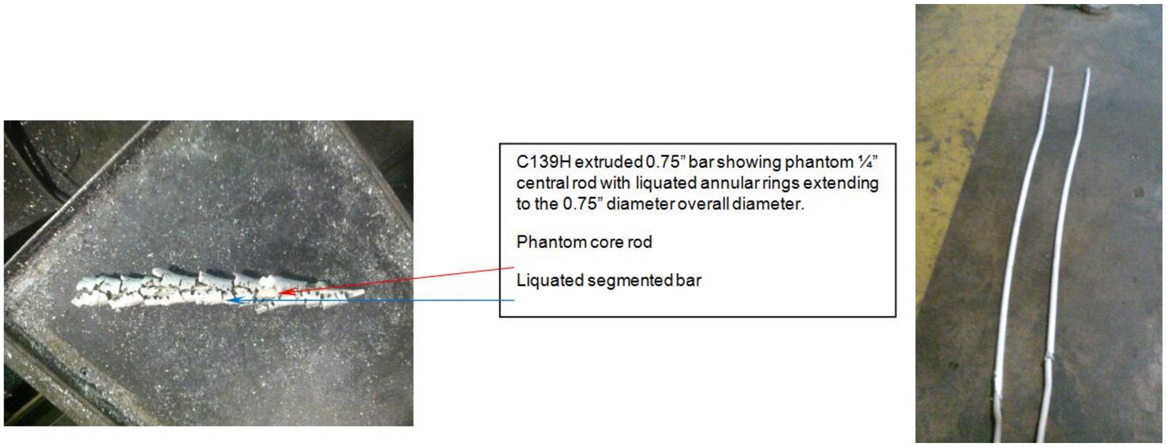
C139H extruded 0.75" bar showing phantom ¼" central rod with liquated annular rings extending to the 0.75" diameter overall diameter.

Phantom core rod

Liquated segmented bar

Figure 13. Failed (left) and successful (right) extrusion trials conducted at Milward Alloys, Inc.

This Page Intentionally Blank

AVPTA Technology Focus Area 2: Lightweight Structures & Materials

Multi-Material Joining (MMJ) – Laser-Assisted Cold Spray

DOE-VTO TFA Lead: Ms. Sarah Ollila
TARDEC TFA Lead: Mr. Martin McDonnell

Principal Investigator:
Dr. Pravansu Mohanty

Affiliation:
University of Michigan
1058 WOLVERINE TOWER
3003 S. STATE ST
ANN ARBOR MI 48109-1274

Project Start: 09/10/2014
Estimated Completion: Q2 FY 16

Objectives:

- Vehicle weight reduction via coated Aluminum brake rotor.
- Exploration of alternative alloys to reduce brake fading.

Strategic Context:

- Coated aluminum brake rotors will support sustainment of existing Programs of Record (PORs) and be available as an option for next generation vehicles.
- The technology directly supports the TARDEC Strategy for the sustainment and light-weighting of legacy and next generation POR vehicles.
- TARDEC Ground Systems Survivability (GSS) will be able to utilize the new light-weight armor applicable to legacy and next generation POR vehicles.
- Follow-on activity is conditional to results of pending testing and evaluation.

Accomplishments:

- Design and fabrication of cast G dot rotor with wear resistant coating
- Optimization of Fe-Mn alloy
    - Reduction in brake pad wear
    - Improved deposition efficiency
- Development of new wear resistant Nitronic 60 alloy

Introduction:

The focus of this investigation is to enable effective use of multi-material components to achieve weight reduction in military vehicles. This can increase mission lengths or payload. Optimization of two components; brake rotor discs and renewed search for alternative alloys are addressed in this investigation. Brake rotors are a heavy unsprung vehicle mass that serves to act a heat sink to dissipate the kinetic energy of the vehicle in order to decelerate or stop. In addition the rotor surface provides stable friction across its operating regime. Weight reduction in rotors can increase mission lengths (via fuel efficiency) but also ride and maneuverability. Coated Aluminum brake rotors present a viable light weighting solution. The coating withstands the grunt braking action while the aluminum serves an efficient heat sink and keeps temperatures low. Key issue with this concept is the lack of feasible joining process and compatible material system. The present investigation will develop a potential coating material and deposition process to fabricate coated aluminum brake rotors.

Approach:

Process:

The University of Michigan has developed a novel Co-axial laser assisted supersonic sintering process (CLASS). This solid –state deposition technology overcomes the hurdles of multi-material joining process: - melting point, formation of intermetallics and thermal degradation. Akin to cold spray technology, powders of desired materials are accelerated to target area at supersonic velocities. At these conditions, the powder undergoes adiabatic shear straining to create micro jets at the interface to create metallurgical bonds. A coaxial laser beam irradiates this foot print to relieve excessive stresses to prepare for next layer of deposition. The novelty of the process lies in the ability to switch the laser beam as primary deposition source. Here at significantly lower particle velocity; the process can create finer deposited features. The CLASS process has been utilized for this investigation. (Figures 1 A&B).

Choice of Aluminum Alloy:

The Silverado rotors were reversed engineered (Figure 3) to match GDOT requirement. Al356 rotors were cast (Figure 4) and manufactured according to the GDOT rotor specification. While Al398 alloy has better high temperature characteristics (Figure 2), porosity in the casting is a big issue and hence was avoided.

Coating Material:

The Fe-Mn-Al system has been thoroughly investigated to replace conventional Ni-Cr based stainless steel and is considered as a potential coating material for brake rotor application [1]. The work hardening property of the Mn based ferrous alloy system results in plastic deformation under impact loading with abrasion or erosion. This mechanism obviates the possibility of brittle fracture and spalling [2]. Manganese is an austenite former and a cost effective replacement Nickel. Disadvantages of manganese are the tendency to segregate forming beta manganese and its high affinity for oxygen at higher temperature [3]. This often results in the alloy with depleted Mn content. This alters the stacking fault energy leading to formation of martensitic phases which could be unwarranted and detrimental. Aluminum also helps increase the SFE. Therefore it stabilizes the austenitic phase and prevents formation e martensite phases. At Higher levels of aluminum, the formation of a continuous passive layer has been shown [4,5]. Silicon is known to reduce SFE and promotes Y to e transformation. Silicon is often added as it improves fluidity during casting and also increases strength by solid solution alloying. Chromium Additions to Fe-Mn Alloys have been widely studied as means to improve the corrosion properties of this alloy [6,7]. Chromium also increases the yield strength or the flow stress thus enhancing wear property [6]. There is discrepancy on the effect of the stacking fault energy by Chromium. Some prove that it increases while the others prove otherwise. Carbon and Nitrogen are two other important elements widely researched in Ni-free austenitic alloys. Both these elements have higher solubility in austenite matrix. The disadvantage of these interstitials is precipitation. The maximum amount of carbon that can be added was limited to 1.2% [7] Nitrogen up to .22wt% has shown to reduce work-hardenability [8]. Carbon has been shown to precipitate at 450^0C [9].Carbon was however added as it affects the critical resolved shear stress which is necessary for twinning [7, 9].

Thus Fe-Mn-Al-Cr-C Alloy system forms a suitable framework for wear resistant alloy for a brake rotor application. The role of manganese will be to ensure the stability of austenitic phase at all temperatures and compensate for its affinity to oxidize. By Varying Aluminum and Chromium the galvanic potential of the alloy will be brought to match that of aluminum. The role of carbon will be to enhance twinning tendency. Its precipitation will result in strengthening of the alloy and lubrication preventing galling. High temperature wear tests will be conducted to ensure stable wear resistance at upper limits of typical braking surface temperature.

Optimization of Fe-Mn Alloy Composition:

The Fe-Mn alloy (B95 rockwell hardness) was modified from previous compositions to improve the overall deposition efficiency of the powder while also meeting target brake performance. Different variations of the Fe-Mn alloy can be seen in Table 1.

Development of Alternative Alloy for Fe-Mn Steel:

Austenitic steel alloys have several advantages from a metallurgical standpoint. Their FCC structure is very tough and ductile down to absolute zero. These steels also do not lose their strength during high temperatures which can occur during severe braking conditions [10]. Two alloys from the Nitronic series N50 and N60 were chosen based on the higher hardness when compared to high Mn alloy. Due to this these alloys can be used for wear resistant coatings. Metal to metal galling resistance for N50 and N60 are typically higher than the 316SS. Due to this reason they can be used for brake rotor applications. These alloys also have a higher hardness and are more corrosion resistant than the typical 316 and 317 stainless steel. Their yield strength is also much higher than 316SS. Unlike many of the typical austenitic steel these do not become magnetic when cold worked. Much of all this is attributed to the composition of both these alloys [11].

The typical compositions of the Nitronic 50 and 60 can be seen in Table 2. The Nitronic N50 is harder than N60 due to the small additions of Niobium and vanadium. While chromium and molybdenum are added to improve the corrosion resistance, nickel and manganese are added to preserve the austenitic structure. Unfortunately more addition of nickel would increase the cost of the alloy itself. For applications requiring higher galling, wear and cavitation resistance coupled with enhanced corrosion resistance N60 is considered [11, 12].

Results and Discussion:

Fe-Mn:

A newer alloy formulation was developed for the brake rotor coatings, in parallel during the design and production phase of the Al356 rotor castings. The objective was to increase the deposition rate of the Fe-Mn alloy by reducing overall alloying content to enhance deformation. The newer FeMn3 and previously used FeMn1 and FeMn2 compositions are shown in Table. The deposition rate of all three Fe-Mn alloys is shown in (Figure 5). A significant increase in deposition rate was observed with Fe-Mn3. The wear depth tracks and wear results of these alloys can be seen in Figures 5 and 7. The change in alloying also improved galvanic coupling with the Al356 alloy (Figure 6).

Influence of Laser Power on Tribology and Coating Thickness:

Dense coatings were obtained from FeMn4 powders with varying laser power. Even though the secondary electron images appear similar, as the laser power increased there was a reduction in coating weight (Figure 8). Increase in coating hardness is attributed to this slight reduction in weight (Figure 9). Previous results have shown that despite this reduction in weight, the coating quality is significantly superior with the laser assisted process. Consequently laser irradiated coatings exhibit lower wear rates as shown in worn track depth profile (Figure 10) and weight loss of the coatings after wear testing (Figure 11).

Effect of Nozzle Geometry on Deposition Weight:

To further improve the deposition efficiency, the nozzle throat geometry was modified to counterpart the increase in powder feed rate. The nozzle throat diameter was increased from 0.109 to 0.136. With this higher powder rates (3rpm) depositions were run successfully. Nozzle geometry and feed rate go hand in hand. Feed rate determines the particle loading inside the nozzle. Excessive feed rate would result in significant reduction in particle velocity resulting in poor coating quality. Deposition at lower feed rates on the other hand could result in insufficient utilization of the high velocity gas jet. In addition to, deposition at higher federate also enables an increased tamping/shot peening action that increases the fatigue strength of the coating. Gun pressure and powder feed rate were varied with different nozzle geometries and their respective deposition weights can be observed from Fig 12. The modified nozzle throat with 3rpm powder feed rate yielded highest deposition weight.

Alloy FeMn4 was deposited onto full scale Gdot rotor with higher powder federate (3 RPM) thereby reducing deposition time significantly which can be seen in Figure 13.

Nitronic 50 and Nitronic 60 Deposition:

Gas atomized N50 and N60 powders with -22 micron powders (d90) were used in coating development. Cold spraying parameters were optimized based on the standoff, gas temperature, pressure, powder federate and laser power. 15mm and 10mm standoff for N50 and N60 yielded maximum deposition weight respectively (Figure 14A). Dense coatings were achieved for both N50 and N60 powders but N60 deposited twice as much as N50 powder at both lower and higher feed rates (Figure 14B).

The hardness of N50 is higher than the N60 at both 0.75rpm and also at 1.5rpm (Fig 15) but the wear rate of N60 is lower than N50 which can be seen from the wear test and wear profile in Figures 16 and 17. Material consolidation post deposition was superior for N60 than N50 which resulted in better tribology results. The coefficient of friction of N60 is comparable to that of cast iron making this a very good wear resistant material. The addition of laser didn't have much effect on the coefficient of friction.

Coating thickness decreases as the laser power intensity increases. This occurs due to the increase in coating hardness. Despite the reduction in weight, the coating quality is significantly better with the addition of laser. The laser irradiated coating at 200W showed a reduction in weight loss of the coating after the wear test (Figure 18).

Conclusions:

An improved and optimized FeMn alloy and deposition process resulted in improved deposition efficiency while meeting target performance. Newer wear resistant alloys were investigated and Nitronic 60 was deposited onto a full scale brake rotor in the process. Advancing from here is to enhance production parameters for best brake performance via brake testing.

References:

[1] H. H. Huang, T. H. Chuang, *Materials Science and Engineering: A* **2000**, *292*, 90.
[2] A. Ball, *Wear* **1983**, *91*, 201.
[3] Y. F. Gong, B. C. De Cooman, *steel research international* **2011**.
[4] A. Grajcar, S. Ko+éodziej, W. Krukiewicz, *Archives of Materials Science* **2010**, *78*, 78.
[5] I. El-Mahallawi, R. Abdel-Karim, A. Naguib, *Materials science and technology* **2001**, *17*, 1385.
[6] A. S. Hamada, *Acta Universitatis Ouluensis C* **2007**, *281*, 1.
[7] O. Bouaziz, S. Allain, C. P. Scott, P. Cugy, D. Barbier, *Current Opinion in Solid State and Materials Science* **2011**.
[8] Y. N. Dastur, W. C. Leslie, *Metallurgical and Materials Transactions A* **1981**, *12*, 749.
[9] L. Remy, A. Pineau, *Materials Science and Engineering* **1977**, *28*, 99.
[10] Stainless Steel for Design Engineers, Michael F.McGuire, Chapter 6,pg 69.
[11] Specialitysteelsupply.com
[12] Smt.Sandvik.com

Figures and Tables:

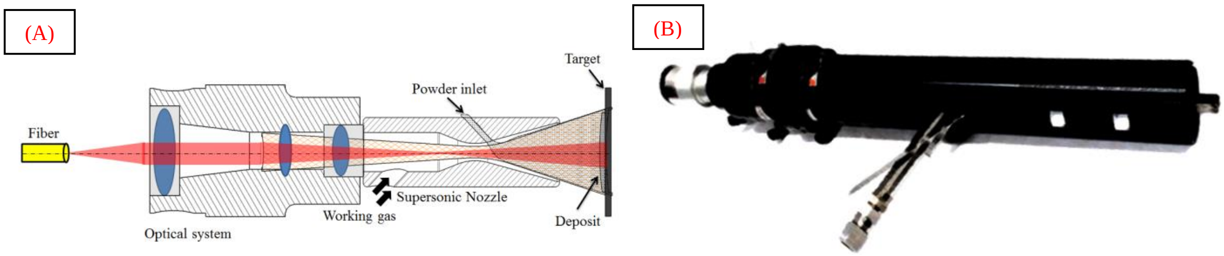

Figure 1. (A) Schematic of CLASS process (B) CLASS Prototype.

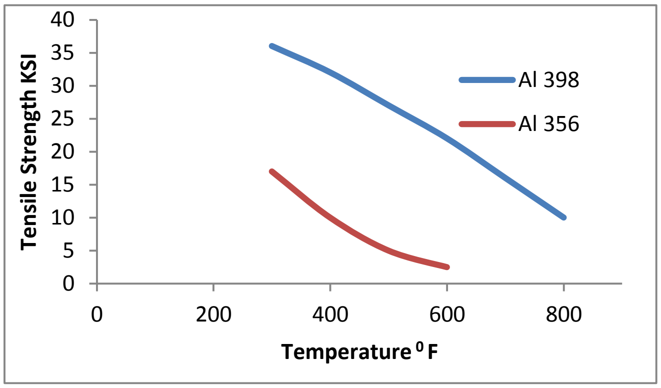

Figure 2. Elevated Temperature property Aluminum Alloy

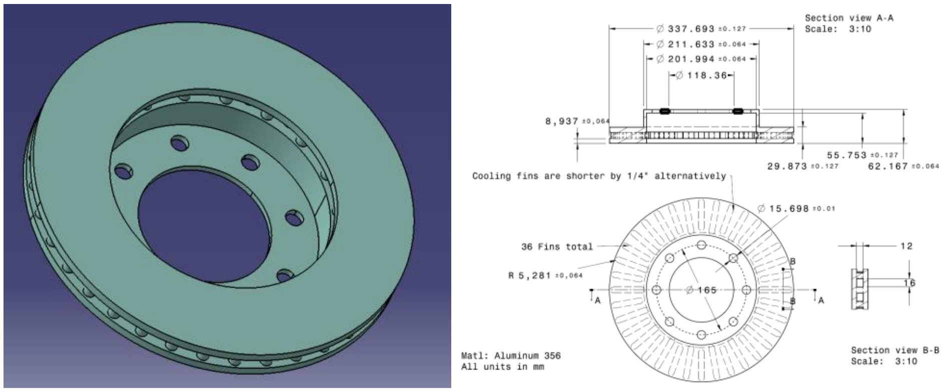

Figure 3. Al356 Brake Rotor Casting Specification.

Remainder of Page Intentionally Blank

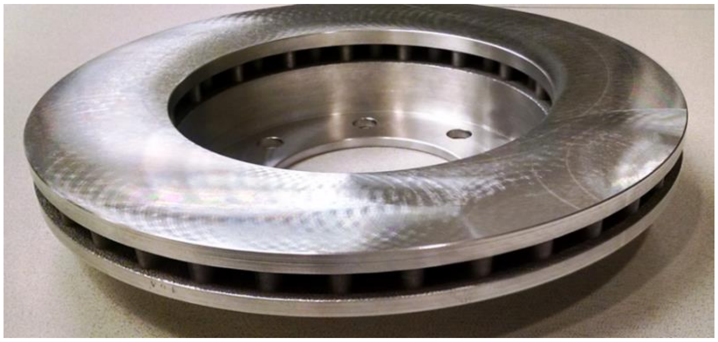

Figure 4. Al356 Cast Brake Rotor

%wt	Mn	Al	Cr	C
Fe-Mn1	25	6	4	-
Fe-Mn2	35	4	2	0.2
Fe-Mn3	25	2	2	0.1
Fe-Mn4	35	4	2	0.1

Table 1. Fe-Mn Alloy Compositions

Material	C	Cr	Ni	Mo	Si	Mn	N	Nb	V	Hardness
Nitronic 50	0.017 max	(21-25)	(11-14)	(2-3.5)	1 max	(5-6)	(0.35-0.5)	0.3	(0.15-0.35)	(C28)
Nitronic 60	0.1	(16-18)	(8-9)	-	(3.5-4.5)	(7-9)	(0.08-0.18)	-	-	(B98)

Table 2. Composition of Nitronic 50 and Nitronic 60

Remainder of Page Intentionally Blank

Figure 5. Deposition Weights for Various FeMn Alloys.

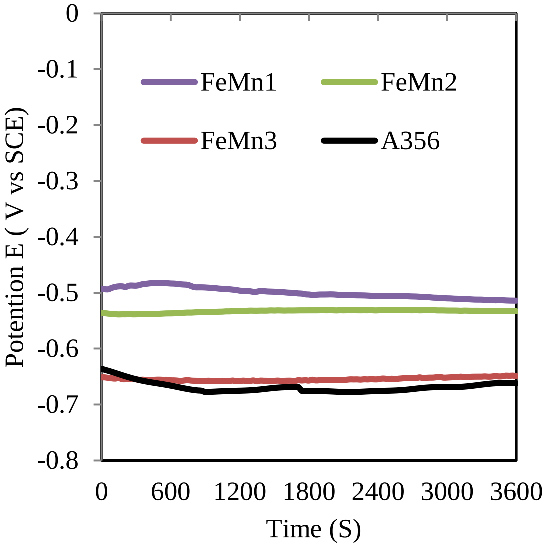

Figure 6. Electrochemical Open Circuit Voltage (0.5%NaCl solution) of Various FeMn Coatings.

Remainder of Page Intentionally Blank

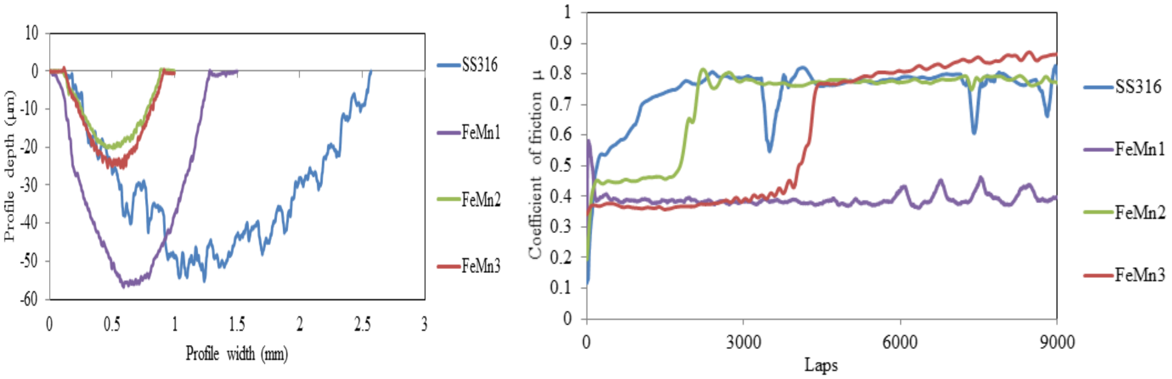

Figure 7. Profile Wear Depth and Wear Test Results for Different FeMn Alloys.

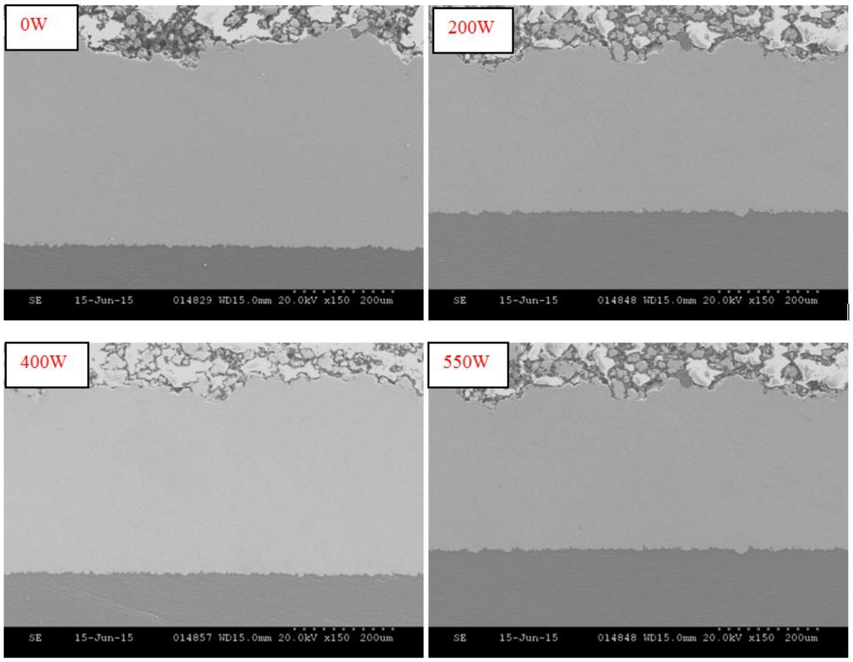

Figure 8. SEM Images of FeMn4 Coatings at Different Laser Powers

Remainder of Page Intentionally Blank

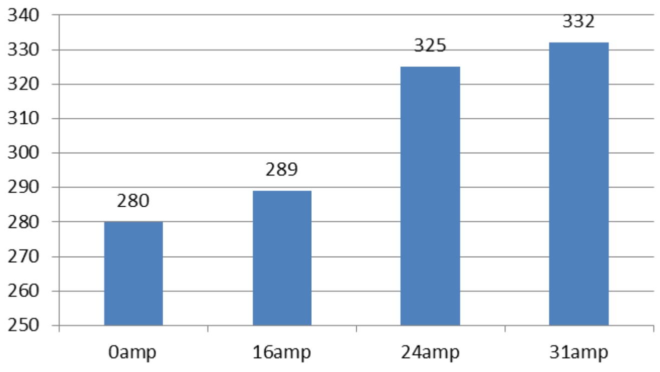

Figure 9. Hardness of FeMn4 Coatings Deposited at Different Laser Powers.

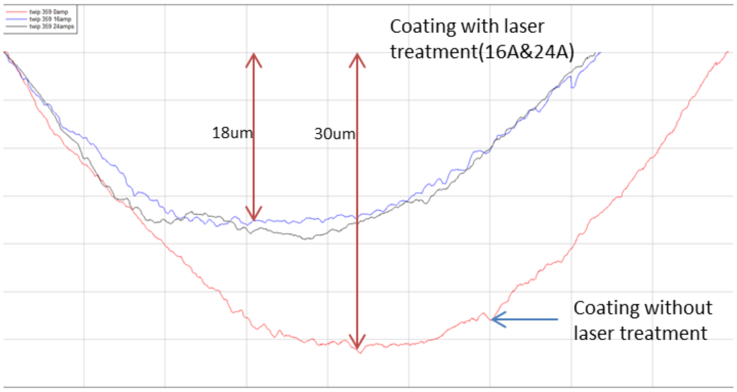

Figure 10. Wear Depth Track Profile with and without Laser Irradiation.

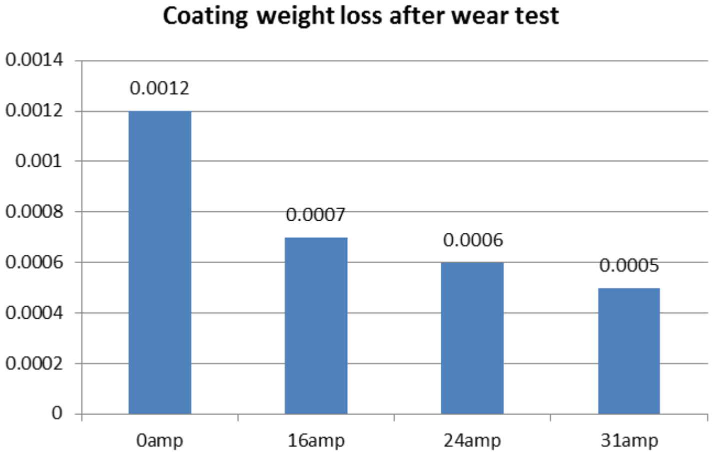

Figure 11. Effect of Laser Power on Weight Loss after Wear Test

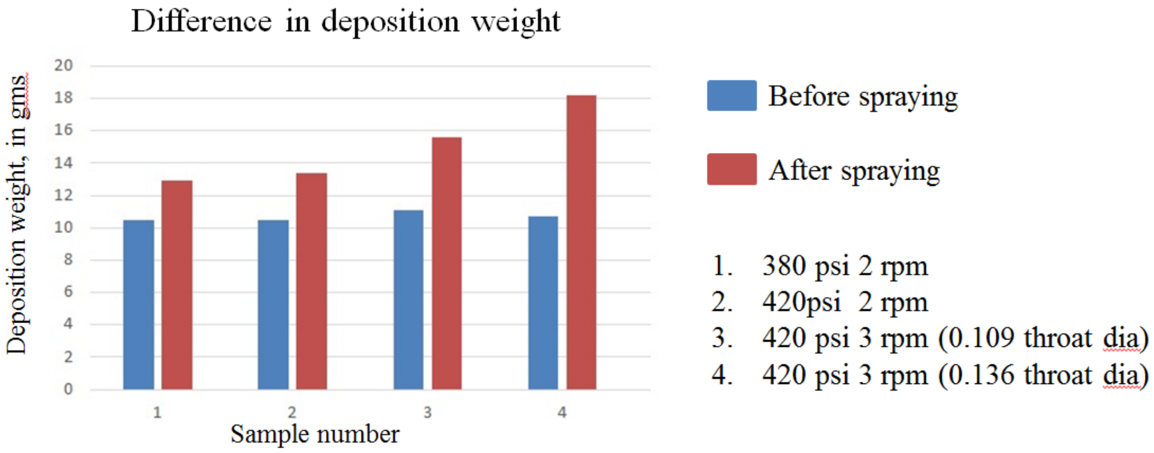

Figure 12. Difference in Deposition Weight at Different Feed Rates with Varying Nozzle Geometry.

Figure 13. FeMn4 Brake Rotor Coating on GDOT Rotor.

Remainder of Page Intentionally Blank

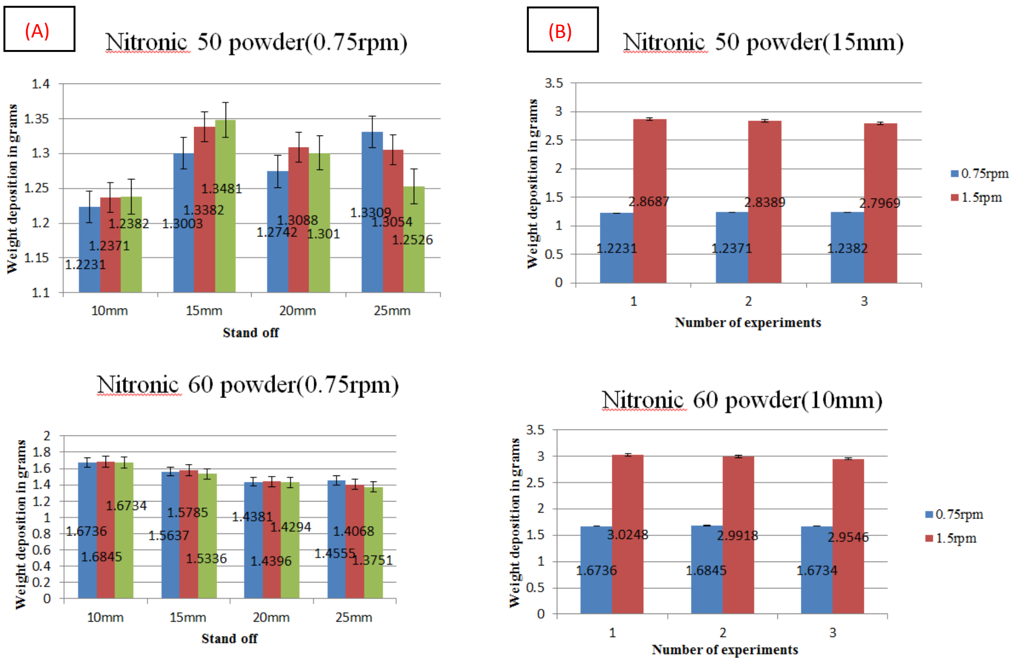

Figure 14. (A) Weight Comparison between N50 and N60 at Different Standoffs (B) Weight Difference between N50 and N60 at 0.75 RPM and 1.5 RPM.

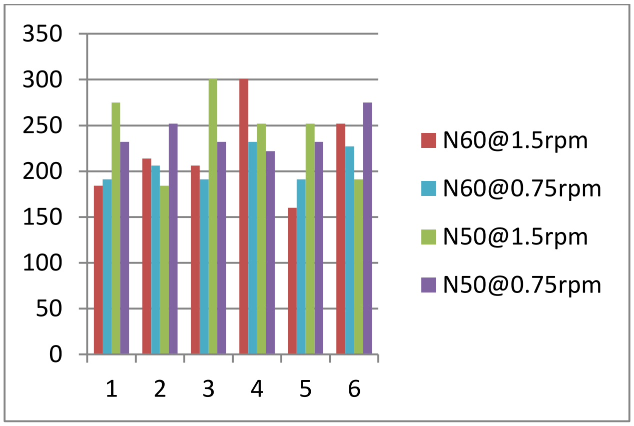

Figure 15. Hardness Measurements of N50 and N60 at Different Powder Feed Rates.

Remainder of Page Intentionally Blank

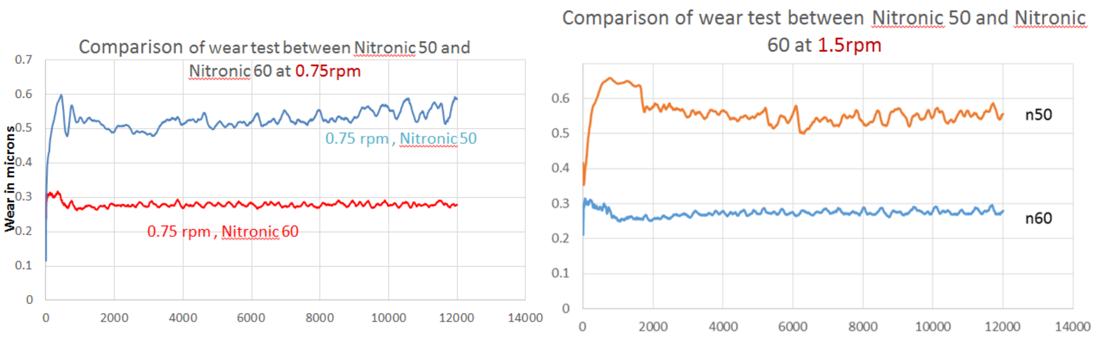

Figure 16. Wear Test Results of N50 and N60 at different at 0.75 RPM and 1.5 RPM.

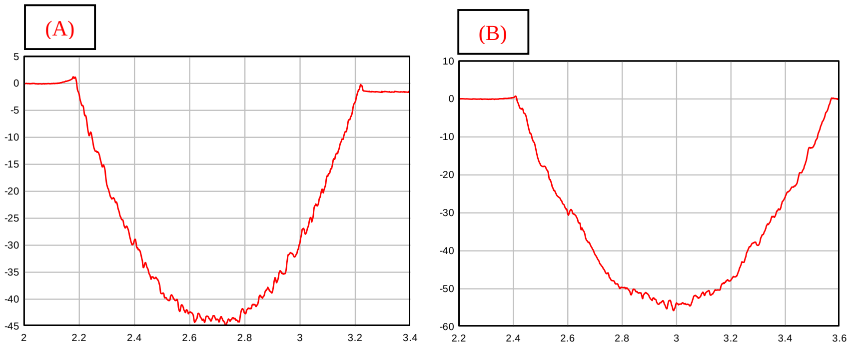

Figure 17. Wear Track Depth Profile (A) N60 (B) N50.

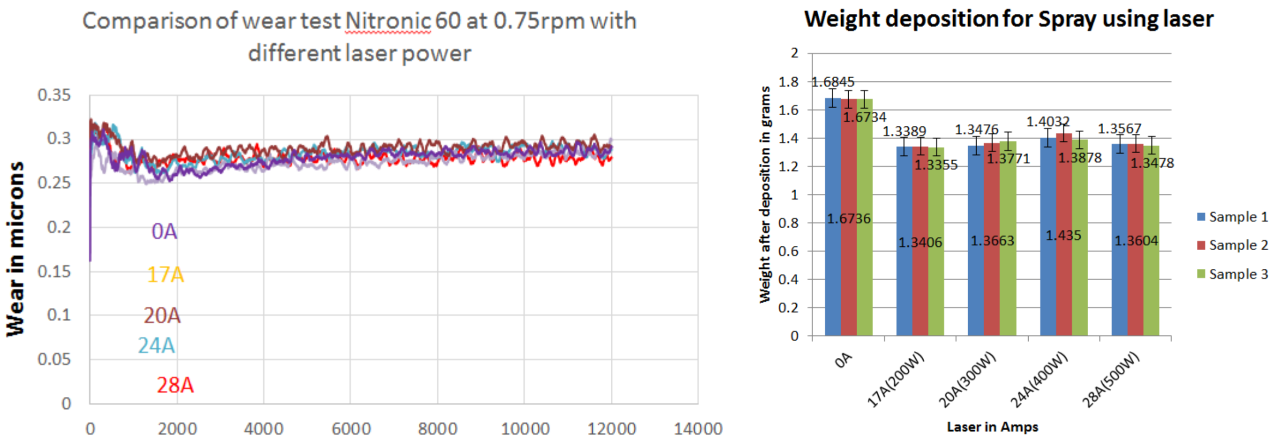

Figure 18. Nitronic 60 Wear Results at Different Laser Powers and Corresponding Deposition Weights

Remainder of Page Intentionally Blank

This Page Intentionally Blank

Multi-Material Joining (MMJ) – Computational Modeling and Simulation of Metal Joints under Ballistic Impact

DOE-VTO TFA Lead: Ms. Sarah Ollila
TARDEC TFA Lead: Mr. Martin McDonnell

Principal Investigator(s):
Dr. James Sheng with Ron Renke and Shabbir Hussain

Affiliation:
TARDEC Analytics

Project Start: FY12
Estimated Completion: FY15

Objectives:

- Characterize armor materials and weld filler materials for utilization in computational modeling and simulation of ballistic impact.
- Develop an analytical simulation capability of an armor plate weld seam under high speed impact loading (ballistic impact).
- Use the analytical capability to design and fabricate a test set up to test armor plates and weld seams subjected to a ballistic impact.
- Validate the computational finite element models by using physical ballistics impact test measurement
- Develop a central repository to store all material data in an organized way with easy and controllable access.
- Develop a tool set for engineers to easily analyze, access and use the material characterizations in ground vehicle system design and development.

Strategic Context:

- The modelling developed / assessed within the project will assist to develop techniques to simulate ballistic impacts, design test fixture structures, and reduce testing with resultant cost and time decreases.
- This project provides TARDEC with new capabilities for Finite Element Analysis (FEA) of H-Plate weld joints.
- The technology will be applied to supplement physical testing and identify / develop areas identify as potentially susceptible to physical testing.

- The technology will be directly support the TARDEC Strategy providing modeling support to the Combat Vehicle Prototype (CVP) and other Program of Record (POR) vehicles requiring ballistic impact analysis of welded joints.

Accomplishments:

- The final report for this Work Directive has been successfully received and reviewed by TARDEC Analytics.
- Successfully tested 14 materials (with 3 samples each) and fitted the measured properties to the internal state variable (ISV) material models.
- Analytical methodology was successfully utilized to verify the test fixture design for conducting the ballistic impact tests.
- Validated analytical models of ballistic impacts on armor material and weld seam within 11% of physical test data.
- Successfully acquired, tested, and installed Matereality for TARDEC repository center for all material characterization datasets.

Introduction:

Vehicle modeling and blast simulation analyses requires high fidelity in the material characterizations, to improve accuracy of predicting material failure/rupture and to design a vehicle system with better survivability performance. This is especially true when it comes to characterizing the weld filler material in armor plates because the welding process usually reduces the material strength and is therefore the weak spot of the structure under ballistic loading.

TARDEC has developed a finite element modeling capability to simulate a ballistic projectile impact on an armor plate and weld seam. This analytical methodology was used to verify the structural integrity of the test fixture before fabricating the hardware and to predict the performance of armor plate along with welding seam under ballistic impacting. However, detailed models that capture the material changes in the heat affected zone (HAZ) post weld are a complex function of the parent materials, the weld wire, and the welding process used. Accurate material characterization is crucial to the prediction improvement of the armor plate impacting. These material models developed in this project is integrated into developed FEA models to predict the weld seam integrity when subjected to the effects of a ballistic projectile impact.

The models developed in this project will help reduce the number of tests needed in the lab by using simulation and also identify the areas that need to be targeted for hitting the projectile on the plate. If the analytical models can be validated to accurately predict weld seam failures with the ballistic shock data, it is believed that the FEA techniques can be extended to blast events.

TARDEC Analytics has acquired a material data analyzer and database (Matereality) deployed on the TDREN computer network.

This database consists of advanced material models that will aid in developing M&S models for simulation of metallic joints under ballistic impact. This will also create a central repository for all the material models used for multi material joining modeling and simulation. Different material model properties can also be compared using the material database. The material database will also build material models for different CAE packages and for ease of collaboration between different TARDEC Analytics teams.

Approach:

The multiple objectives of this project are an attempt to get more accurate performance predictions of various hull structural configurations when subjected to blast events.

Material Characterization:

Material test samples were cut from armor plate weld samples and subjected to high strain rate testing and fatigue testing. The results of these tests were used to define the necessary material parameters and coefficients for the analytical material models. (see Figure 1)

Test Configuration Design:

A series of H-plate tests were designed to measure the ballistic impact performance of these welded joints. The H-Plate consists of four rectangular shaped metal plates that were joined by weld seams. The plates were used for ballistic impact tests with projectiles, to determine their structural integrity during the impact. Total six impact tests have been conducted, and 2 of the impact locations are illustrated in Figure 2.

A test fixture was also designed to hold the H-plate for the impact tests, as shown in Fig. 3. The fixture will support both sides of the H-plate (cyan). The H-plate can be positioned from either side or top into the holding slot. Once the testing plate is in position, a 2x4 wood block is wedged in the slot to hold the h-plate in position for impacting.

Analytical Methodology Development:

A finite element model of the test fixture and sample (H-Plate) was created to replicate the test fixture, armor plate, and ballistic projectile. Multiple iterations of the finite element model were run to achieve a stable solution and deformation modes in the plate and projectile that reasonably predicted the results from the hardware testing. The structural integrity of the test fixture was also verified during this process.

Results and Discussion:

The test fixture used to conduct ballistic impacts on weld plates was modeled to develop the process for ballistic impact testing in the lab. The fixture shown in Figure 3 below was first modeled and analyzed to make sure it can withhold the impact of the projectile, before the fixture was built. The FEA simulation model for the fixture with the projectile hitting it at a certain velocity was modeled as shown in Figure 4. The armor plate material properties were assigned and the fixture material and thicknesses were modeled using simulation.

The displacement contour plot from the FE simulation, showing the maximum displacement due to the impact of the projectile is shown in Figure 5. As expected, the displacements are the highest at the point of projectile contact with the test specimen plate.

The plastic strain plot for the simulation, showing the plastic strain on the plate due to the impact of the projectile, is shown in Figure 6. Both the plastic strain and the displacement plots were used to help guide the design of the test fixture.

The test fixture setup for the H-plate to withstand ballistic projectile impact is shown in Figure 7. The results of the simulation are based on actual test material properties of the filler material and armor plate due to heat affected zones of the armor contact plate material. This simulation will help optimize and reduce the actual projectile shots needed to assess the impact on the H-plate because the validated computational modeling and simulation can be used to substitute many intermediate tests in design welding seam and patterns.

Figure 8 shows the plate after impacting at the welding corner with an impacting speed of 1352 ft/s by a steel projectile. The predicted weld cracking length is 12.19 inches compared with 13.5 inches of measured cracking length, i.e., the prediction was within 11% of the actual measurement. The crater diameter estimated in the computational simulation is 9.7 inches compared with the measured 9.5 inches, i.e., the prediction was within 2.2% of the actual measurement. The results of the developed welding seam models show good agreement with the ballistics impacting test measurement.

In the simulation shown in Figure 9, the impact of the projectile with the H-weld plate does not lead to any separation of the weld or failure of the weld.

Conclusions:

In this project, more than 40 material sample tests have been conducted, and about 14 material ISV models have been developed. These models have been used in computational modeling and simulation of the H-Plate welds to predict ballistic impact performance. The modeling methodology and procedures developed at TARDEC, as part of this effort, provide reasonably good prediction of the physical ballistic impact test measurement.

Analytics plan in the future is to apply these developed material model, methodology and procedures to support other PM and technology development programs.

References:

- N/A

Figures and Tables Begin on Next Page

Figures and Tables:

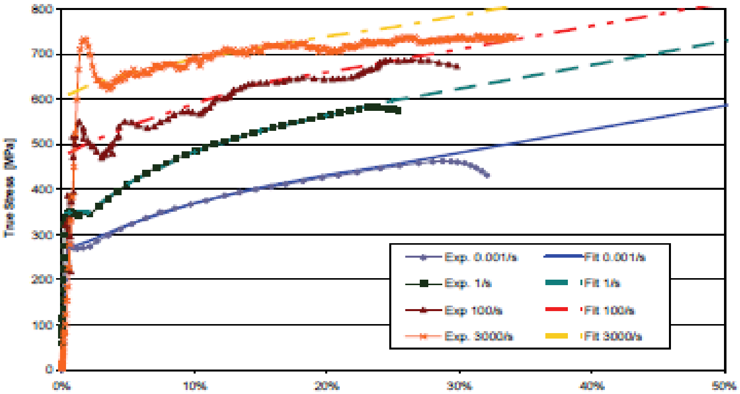

Figure 1. True Stress for different Strain Rates.

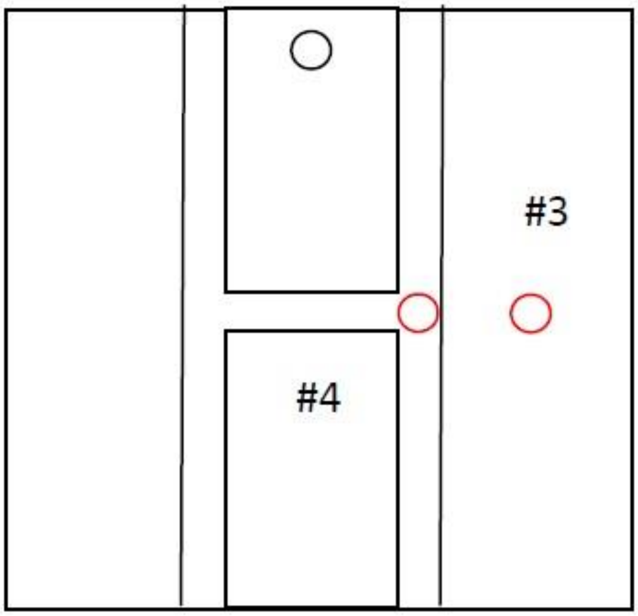

Figure 2. H-Plate design with 2 impact locations.

Remainder of Page Intentionally Blank

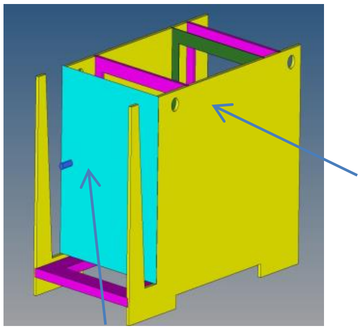

A36 Structural Steel

MIL-A-46100
steel plate ½
in. Thick

Figure 3. Finite Element Model of Ballistic Test Fixture.

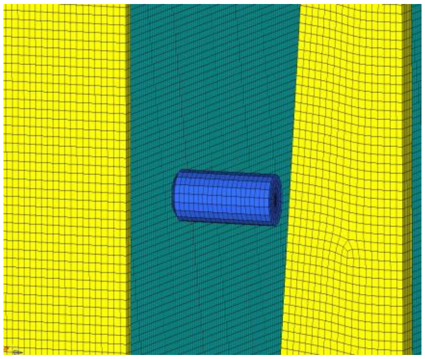

Figure 4. Finite Element Model of Projectile.

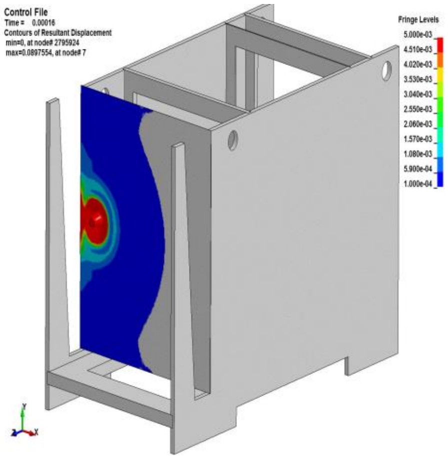

Figure 5. Displacement Contour Plot.

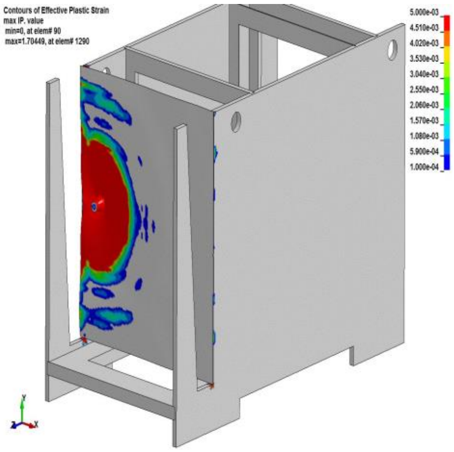

Figure 6. Plastic Strain Contours.

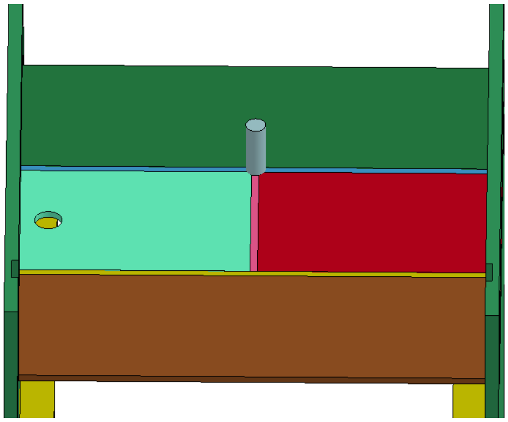

Figure 7.Armor H-Plate Weld Test Configuration.

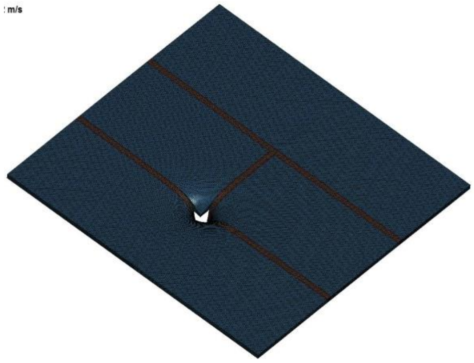

Figure 8. Finite Element Model of shot 14309-4-C with penetration.

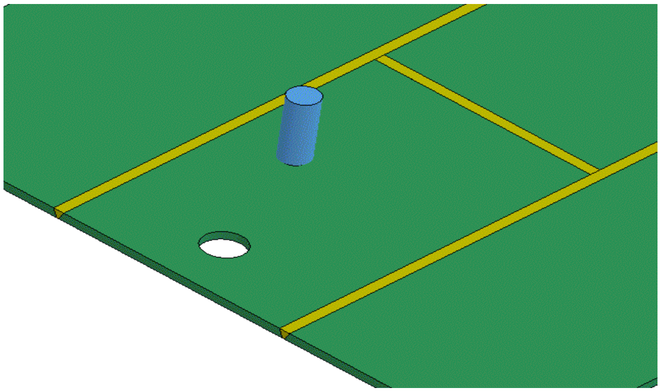

Figure 9. H-Plate Weld with no separation.

Remainder of Page Intentionally Blank

AVPTA Technology Focus Area 2: Lightweight Structures & Materials

Multi-Material Joining – Bi-Metal Brake Rotor (Formerly B-Metal Gunner Rotor Casting

DOE-VTO TFA Lead: Sarah Ollila
TARDEC TFA Lead: Martin McDonnell

Principal Investigator:
Dr. Adam Loukus

Affiliation:
REL Inc.
57640 North 11th St.
Calumet, MI 49913
Phone: (906) 337-3018
Email: adam@relinc.net

Project Start: 14/11/2015
Estimated Completion: Q4FY16

Objectives:

- Develop lightweight bimetal rotors for the HMMWV platform which shall provide comparable weight, but increased durability and performance.
- Determine whether new advanced materials, advanced manufacturing techniques and thorough testing of prototype units shall improve the performance of the HMMWV.

Strategic Context:

- The bi-metal cast brake rotor has the same weight with increased durability and performance compared to the brake rotor currently used in the High Mobility Multipurpose Wheeled Vehicle (HMMWV) system.
- The project directly supports the TARDEC Strategy by enabling a better performing brake rotor availability for legacy and future Program of Record (POR) vehicles.
- Bi-metallic casting is a commercial process.
- Increasing durability and performance of components is an area of interest for military and commercial vehicles. Determining the best material for optimal performance, cost and weight is an area of mutual technical interest and ongoing research.

Accomplishments:

- Start of Work for Bi-Metal Brake Development initialized.
- Realization of applicable existing REL technologies for bi-metal rotor development.

Introduction:

REL's Bi-Metal technology combined with Functional Reinforcement Gradient technology will be employed to overcome the previous limitations of brake materials. REL has vertically integrated the MMC rotor process, and is now delivering MMC brake rotors to the motorcycle market and is expanding the deployment of this technology into automotive markets. REL is leveraging their knowledge obtained in developing MMC brake products to develop rotors for the HMMWV application.

The goal of the Bi-Metal Brake Development is to rapidly modify a HMMWV braking system to improve stopping performance, handling, safety, and durability throughout the range of vehicle weights.

This bi-metal brake development project is the second of two proposed ideas. The aim of the original project was to produce a bi-metal upright (Figure 2) which is bonded to a steel spindle via the bimetal casting process as a means to improve durability and reduce component weight. Lack of technical support from OEM's and withholding of technical data led to REL's inability to move past the initial stages of the project. Although it was initiated, this project was delayed and ultimately transformed into the current Bi-Metal Brake Development.

Approach:

REL will aim to produce a bi-metal aluminum metal matrix composite rotor that can be used in the current configuration of the HMMWV braking system. Merging MMC technology with REL's bi-metal developments will allow for the production of a bi-metal lightweight brake rotor. An in-house dynamometer allows REL to test brake rotors and brake friction materials while evaluating performance of the baseline HMMWV rotor against the bi-metal option. The relationship between standard friction materials and bi-metal braking surfaces will be explored in detail.

Many of the tasks needed to develop a bi-metal brake system will be accomplished concurrently, with their results being combined following completion. Key tasks are as follows:

- Define geometry of bi-metal rotor
- Analysis of rotor design
- Develop and optimize manufacturing methods for HMMWV MMC rotor casting
- Adapt current rotor bi-metal surface technology to HMMWV MMC rotor
- Manufacture molds and support tooling for rotor casting
- Cast, machine, and surface initial rotors to prove out manufacturing process
- Performance testing and analysis on initial rotors
- Manufacture final prototypes

- An overview and background of REL’s bi-metal and MMC technologies that can be adapted to the Lightweight Bi-Metal Brake System are detailed below.

REL’s Lightweight Brake Rotor Technology:

REL has developed lightweight aluminum metal matrix composite brake rotors for both motorcycle and automotive applications. The aluminum MMC rotors are differentiated from others by their Functional Reinforcement Gradient (FRG). A FRG in a MMC rotor can be tailored to optimize performance based on a braking heat cycle.

REL’s MMC brake technology in motorcycle rotors has a proven record to minimize brake fade and increase braking performance in addition to the benefits below.

- High Load/High Temperature Application - Minimize Fade during High Energy Braking Events with High Thermal Conductivity (K) & Heat Dissipation
- High Torque at Low Temperature- “Hill-Load”.
- FRG Technology to Maintain Rotor Uniformity/Superior Flatness –> less brake drag
- Quieter Braking - MMC has High Damping Compared to Iron Rotors
- Effective Thermal Management
- Increased Life Expectancy & 50% Weight Reduction
- Longer Life - High Wear Resistance, Toughness, Fatigue Strength, and Corrosion Resistance
- Lowers un-sprung weight for better handling and fuel savings
- Overall lower life cycle cost

REL’s unique method of manufacturing aluminum MMC brake rotors is done through high pressure indirect squeeze casting in REL’s UBE 900 squeeze casting press. The process of motorcycle rotor manufacturing is shown in figures 4 and 5.

Casting preforms are made from a ceramic slurry mix. The preforms are dried out in an oven and degassed in a high temperature kiln. Once the preforms are at their final thickness, they are ready to be cast. The squeeze casting process involves the placement of a preform in the casting die, filling the die with molten aluminum, then using the casting press to squeeze the molten aluminum to high pressure. Through this the process the ceramic preforms are infiltrated by the surrounding molten aluminum, creating an aluminum ceramic composite material. After being removed from the squeeze casting press and cooled, the gating is removed and the casting begins heat treatment. In the final manufacturing task, the casting is machined to the dimensions required by the rotor.

REL has developed a single-piece, externally vented, aluminum metal matrix composite rotor (figure 6) has been developed and put into practical application on a Mazda 6. The rotors were installed and were driven for 5000 miles. The total weight savings resulting from the replacement was ~40 lbs. The rotors performed well in this test and provided substantial evidence of the viability of MMC rotors.

Further development on a one-piece internally vented rotor is currently ongoing and will able to be adapted to the Lightweight Bi-Metal Brake Development. Prototypes have been developed with manufacturing methods which are still under development. (Figure 7) Analysis of the MMC rotor has been done, with the results of the stress and temperature distributions shown in figures 8 and 9.

REL's Friction Material Testing:

Brake friction and rotor testing on REL's in-house brake dynamometer (figure 10) has created an inventory of data regarding MMC compatible brake material, MMC rotor surface friction, and rotor temperature performance (figure 11). REL can easily compare and baseline brake pads and rotors using the brake dynamometer, data collection equipment, data analysis tools, and testing procedures.

REL's capability and capacity to test and analyze brake friction and brake rotors enables the quick turnaround for evaluating a lightweight bi-metal HMMVW rotor.

REL's Bi-Metal Technology:

A successful bimetal gunner rotor casting has been manufactured at the initial prototype stage shown in Figure 13. The aluminum gunner rotor with four high strength steel armor inserts which was cast at REL produced a weight savings of 23 percent over original mild steel version (Figure 12). Produced was a high integrity casting that was tested to withstand the required load cases. The finished component has been delivered and is awaiting fit up on the vehicle.

Results and Discussion:

REL's previous and current research and technologies will allow for quick progress in the initial stage of rotor development. Concepts for a lightweight bi-metal HMMWV rotor are based on REL's MMC technology with integration of REL's bi-metal and rotor cladding developments.

The concept for an internally vented, aluminum metal matrix composite, bi-metal cored and skinned rotor has been investigated (figure 14). Geometry of the rotor will be based on utilizing the existing packaging of HMMWV braking system (figure 15). Rotor blades will be composed of aluminum MMC material, while the rotor surface and internal venting core will be bi-metal. Although there may be deviations to this general concept, it gives the best chance at developing the necessary performance for the HMMWV braking system. A matrix of materials and rotor designs will be vetted this month.

Conclusions:

REL has begun the start of work on the Lightweight Bi-Metal Braking System Development. The original project, lightweight bi-metal uprights, was delayed and ultimately canceled due to a lack of data and support from OEM's. REL has developed an approach to apply current bi-metal technologies to brake rotors. REL's existing technologies, MMC rotors, brake testing, surface friction improvement, and bi-metal casting, can be adapted and merged to develop a high performance brake system. An internally vented, aluminum metal matrix composite, bi-metal cored and skinned rotor has been developed as a concept and will be the guide to development as the project moves forward.

References:

- N/A

Figures and Tables:

Figure 1. HMMWV Bi-Metal Brake Development.

Figure 2. Uprights to be replace in first Bi-Metal Development.

Remainder of Page Intentionally Blank

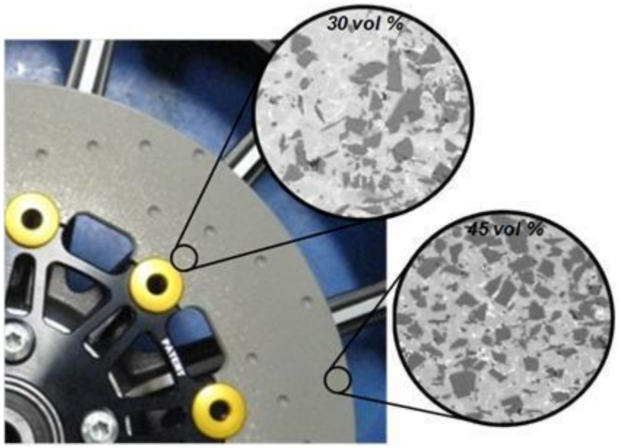

Figure 3. REL Motorcycle Rotor Showing FRG

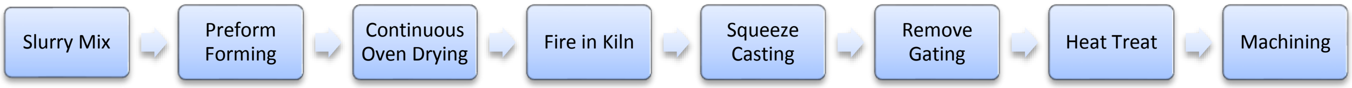

Figure 4. REL's motorcycle rotor manufacturing process.

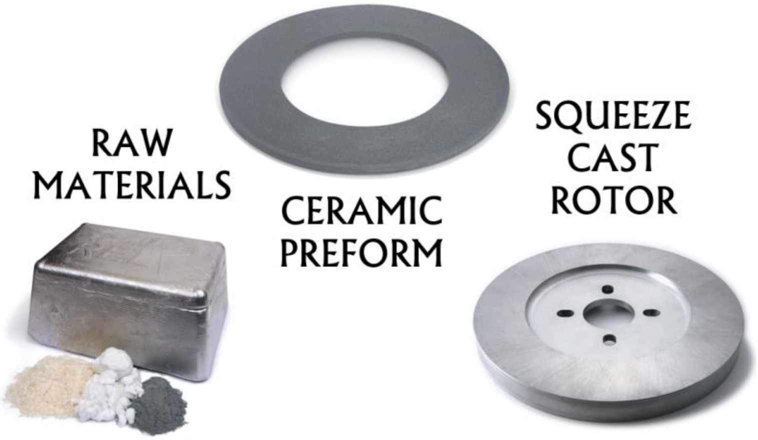

Figure 5. REL Brake Rotor Process.

Figure 6. REL MMC Automotive Rotor.

Figure 7. Prototype Internally Vented MMC Rotor.

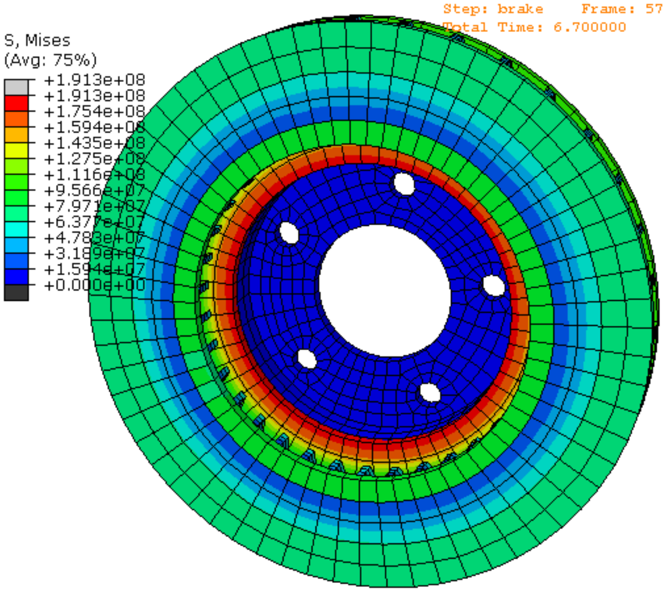

Figure 8. Internally Vented MMC Rotor Stress Distribution.

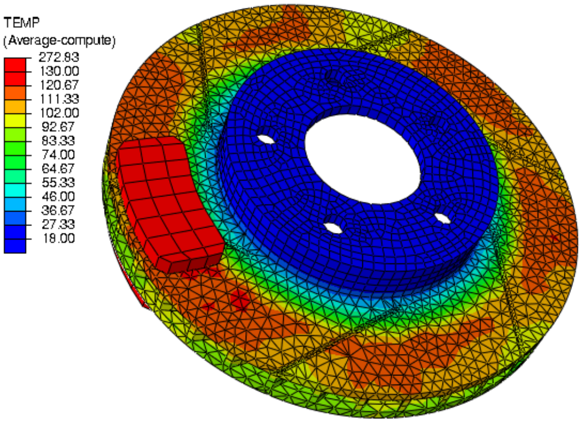

Figure 9. Prototype Internally Vented MMC Rotor.

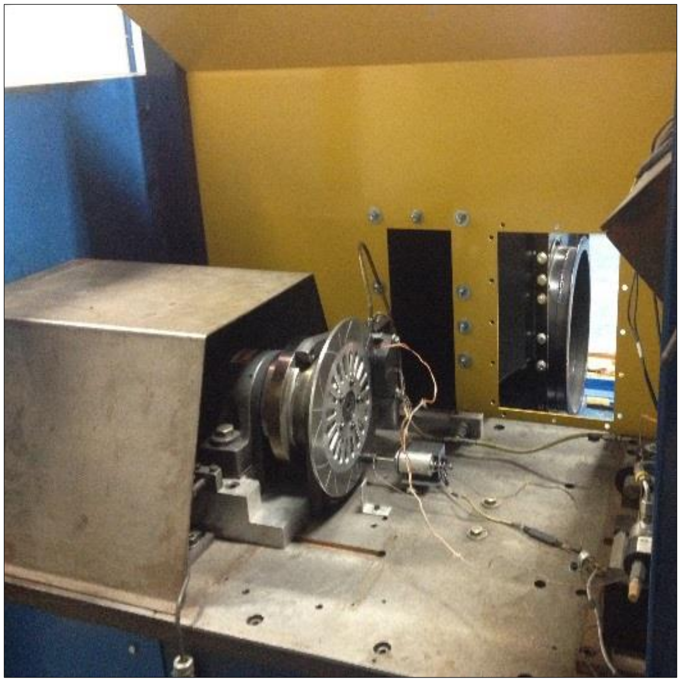

Figure 10. REL’s Brake Dynamometer.

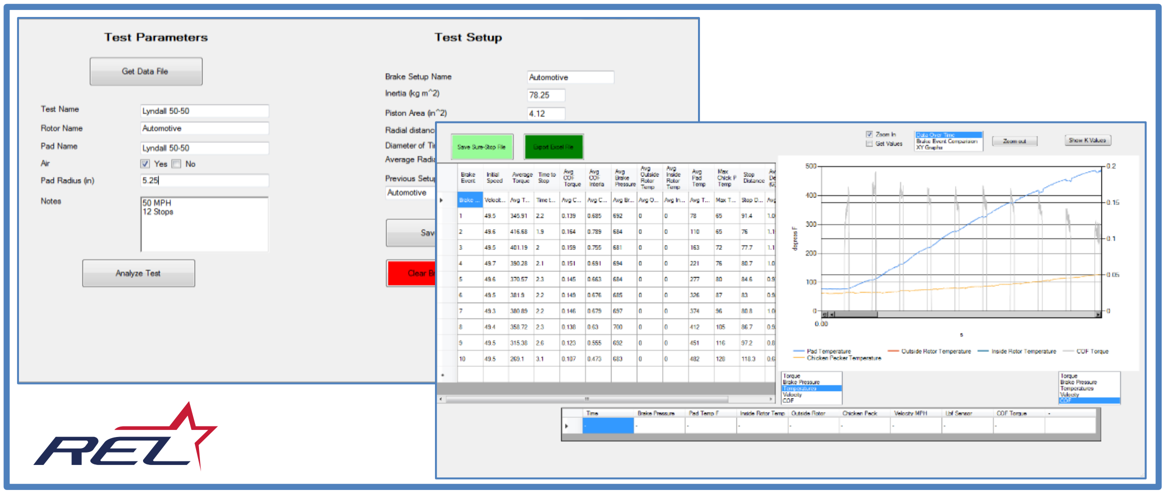

Test Name: Lyndall 50-50
Rotor Name: Automotive
Pad Name: Lyndall 50-50
Air: ☑ Yes ☐ No
Pad Radius (in): 5.25
Notes: 50 MPH
12 Stops

Brake Setup Name: Automotive
Inertia (kg m^2): 78.25
Piston Area (in^2): 4.12
Previous Setup: Automotive

Brake Event	Initial Speed	Average Torque	Time to Stop	Avg COF Torque	Avg COF Interia	Avg Brake Pressure	Avg Outside Rotor Temp	Avg Inside Rotor Temp	Avg Pad Temp	Max Chick P Temp	Stop Distance
Brake ...	Velocit...	Avg T...	Time t...	Avg C...	Avg C...	Avg Br...	Avg O...	Avg In...	Avg T...	Max T...	Stop D...
1	49.5	345.91	2.2	0.139	0.685	692	0	0	78	65	91.4
2	49.6	416.68	1.9	0.164	0.789	684	0	0	110	65	76
3	49.5	401.19	2	0.159	0.755	681	0	0	163	72	77.7
4	49.7	390.28	2.1	0.151	0.691	694	0	0	221	76	80.7
5	49.6	370.57	2.3	0.145	0.663	684	0	0	277	80	84.6
6	49.5	381.9	2.2	0.149	0.676	685	0	0	326	87	83
7	49.3	380.89	2.2	0.146	0.679	697	0	0	374	96	80.8
8	49.4	358.72	2.3	0.138	0.63	700	0	0	412	105	86.7
9	49.5	315.38	2.6	0.123	0.555	692	0	0	451	116	97.2
10	49.5	269.1	3.1	0.107	0.473	683	0	0	482	120	118.3

Time	Brake Pressure	Pad Temp F	Inside Rotor Temp	Outside Rotor	Chicken Peck	Velocity MPH	Lbf Sensor	COF Torque	-
-	-	-	-	-	-	-	-	-	

Figure 11. REL’s Brake Testing Data Analysis Software.

Remainder of Page Intentionally Blank

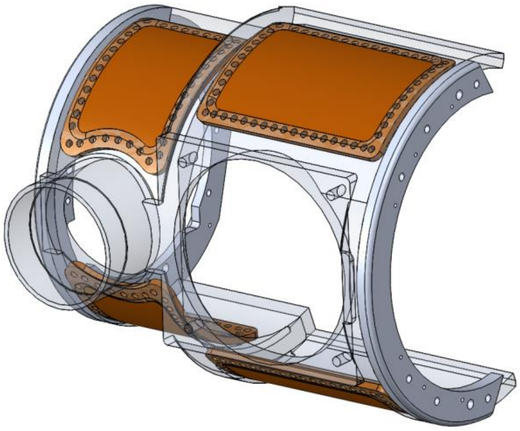

Figure 12. REL Bimetal Gunner Rotor Design with Steel Inserts.

Figure 13. Gunner Rotor assembly casting and welding.

Remainder of Page Intentionally Blank

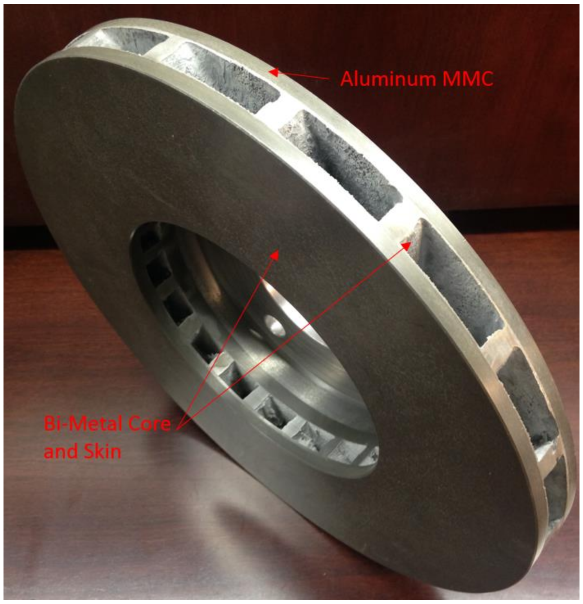

Figure 14. Lightweight Bi-Metal Rotor Concept.

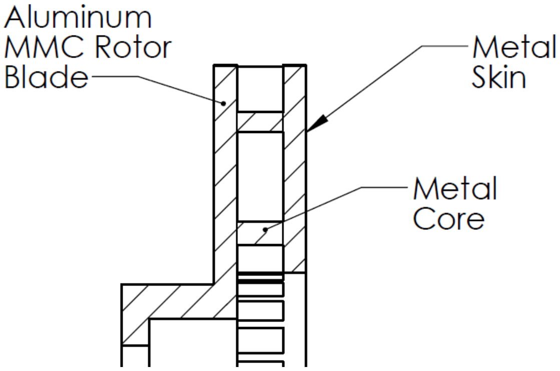

Figure 15. Lightweight Bi-Metal Rotor Concept Diagram.

Remainder of Page Intentionally Blank

Breakthrough Techniques for Dissimilar Material Joining - Overview

DOE-VTO TFA Lead: Sarah Ollila
TARDEC TFA Lead: Martin McDonnell

Principal Investigator:
Martin McDonnell

Affiliation:
TARDEC Ground Systems Survivability

Project Start: October 2013
Estimated Completion: Ongoing

Objective:

- To establish new techniques for producing dissimilar material joints in vehicle structures.

Strategic Context:

- These are investigations into Technology Readiness Level (TRL) 2 & 3 technologies for which the performance and scalable applicability are unknown.
- The technologies directionally support the TARDEC Strategy because they are both early TRL and because they focus on dissimilar material joining that enables multiple benefits to future Programs of Record (PORs).
- Depending upon the success of the projects, they may create new technology investment areas increasing performance (e.g., higher strength joints), reducing cost and / or applicability to other materials and joint designs.
- Follow-on direction / opportunities will be based upon project success.

Accomplishments:

- See individual project descriptions.

Introduction:

The lightest weight structure is the one that utilizes the lightest and most cost effective material that meets the engineering design requirements, i.e., a multi-material vehicle structure. Several workshops and studies [1, 2] have documented that one of the greatest barriers to the multi-material vehicle is the lack of effective joining technologies for dissimilar materials. While there are various cost effective materials, the technology to physically join them while meeting production and engineering requirements has been lacking.

Approach:

The five breakthrough techniques (and their performers) are:

- Brazing Dissimilar Metals with a Novel Composite Foil (Johns Hopkins University) – development of a foil that will braze two steel to aluminum and magnesium without pre-wetting through a self-propagating chemical process.
- Collision Welding of Dissimilar Materials (Ohio State University) – develop a process that applies current to a suitable metallic foil (e.g. aluminum) and vaporizes the foil to create a rapidly expanding plasma gas. The expanding gas moves one material with rapid force to explosively bond with the dissimilar mating material.
- Upset Protrusion Joining Techniques (Chrysler Corporation) – develop a fast and economical process to “squash” cast protrusions from a precision casting that can fit through holes in a composite (or other dissimilar material) thereby creating a bond similar to rivets.
- Active, Tailorable Adhesives for Dissimilar Material Bonding, Repair and Assembly (Michigan State University) – Development of a nano-platelet doped adhesive that can be cured (assembly) and “uncured” (disassembly) using magnetic fields.
- Advanced carbon fiber to aluminum joining (Oak Ridge National Laboratory) – Develop rapid process to use a laser to burn a surface pattern into carbon fiber composite parts to increase adhesion to aluminum components.

References:

- AVPTA Workshop, July 2011
- National Research Council, Committee on Benchmarking the Technology and Application of Lightweighting (2012) *Application of Lightweighting Technology to Military Vehicles, Vessels, and Aircraft*.

Remainder of Page Intentionally Blank

AVPTA Technology Focus Area 2: Lightweight Structures & Materials

Breakthrough Techniques for Dissimilar Material Joining – Brazing Dissimilar Metals with a Novel Composite Foil

DOE-VTO TFA Lead: Sarah Ollila
TARDEC TFA Lead: Martin McDonnell

Principal Investigator:
Dr. Timothy P. Weihs

Affiliation:
Johns Hopkins University (JHU)
3400 North Charles St.
Baltimore, MD 21218
Phone: (410) 516-4071
E-mail: weihs@jhu.edu

Project Start: Q1FY14
Estimated Completion: Q4FY17

Objective:

- To develop, characterize, and assess novel reactive foils that are based on reduction-oxidation (redox) chemical reactions for use in dissimilar alloy bonding applications.

Strategic Context:

- This technology will be applied to future Programs of record (PORs) requiring dissimilar material lap joints.
- The technology supports the TARDEC Strategy enabling new capability in the design and application of dissimilar material lap joints.
- A patent application has been submitted with the intent of licensing the technology to a materials manufacturer, who will then sell to the automobile industry.
- Follow-on activities may include further AVPTA interest to investigate increasing joint strength, reducing cost and / or developing foils for other material combinations. TARDEC-specific follow-on may include lap joint ballistic shock evaluations.

Accomplishments:

- Processed ball-milled, composite powders into diluted Redox Foil with higher reactivity using conventional swaging and rolling techniques
- Performed studies to identify set of ball-milling parameters that maximizes heat of reaction in Al:Cu_2O and Al:NiO composite powders
- Characterized stresses in Al:NiO multilayer films fabricated via magnetron sputtering as a function of three sputtering pressures and two distinct bilayer spacings
- Increased amount of diluent that can be added to Redox Foils before self-propagating reaction quenches in bond interface using ball-milled powders
- Achieved dissimilar bond strengths as high as 10 MPa.

Introduction:

The last two decades have seen the development and commercialization of reactive, self-propagating multilayer foils as local heat sources for joining materials [1-2]. When used in conjunction with solder or braze, these foils can join dissimilar materials without heating either component significantly, as only the area near the interface is heated [3-4]. The standard NanoBond practice of pre-wetting components with solder, however, adds cost, slows dissemination of the technology, and limits bond strength to the strength of the solder being used within the joining process. Ideally, no pre-wetting would be required and stronger braze bonds would be enabled.

The aim of this project is to develop, characterize, and assess novel reactive foils that are based on reduction-oxidation chemical reactions. Many redox reactions are noted for their exothermic heats of reaction and molten metallic products, making them intriguing candidates for solder-free bonding applications. These are typically known as thermite reactions. Figure 1 gives a schematic of a possible bonding configuration using a Redox Foil. In addition, the reactive properties of thermite foils may be tailored in a controllable manner by altering the chemistry of the reactants and refining the foil microstructure. We seek to understand the relationships between foil properties and bond characteristics for several thermite systems and dissimilar alloys, including Al 3003, Mg AZ31, and HSBS. Of particular interest are the shear strengths of the bond, mass ejection (gas and particle) during the reaction, wettability of braze materials, and extent of joint corrosion.

Approach:

Diluting Redox Foils with excess metal has been shown to decrease gas production and increase the amount of braze present in the joint interface [5]. However, the presence of diluent also reduces the heat generated in the reaction because the total amount of reactants decreases and the average reactant spacing increases. When highly-diluted Redox Foils are ignited in a joining configuration, the resulting self-propagating reaction tends to quench in the bond interface because the rate of heat loss exceeds the rate of heat generation. One way to preserve small reactant spacings while diluting the reaction is to create composite thermite powders that are comprised of small oxide inclusions embedded in softer aluminum powders. Figure 2 and Figure 3 provide a schematic and micrograph, respectively, showing how these powders change during ball milling. These two-phase powders are then mixed with diluent powders and processed via swaging and rolling.

Ball milling was used to create thermite composite powders with average reactant spacings of less than 1 µm. Initials experiments were performed using Al and NiO powders to explore the effect of changing various ball-milling parameters, particularly the ball-to-powder mass ratio (BPR), ball size, and milling time. Once these variables were better understood, we generated several batches of ball-milled powders, varying ball size and milling time in an effort to maximize the heat of reaction. Heats of the composite powders were measured using differential scanning calorimetry (DSC) and compared to Redox Foils prepared from single-phase powders. After the best milling parameters were identified, we diluted the ball-milled powders and packed them into steel tubes to be swaged and rolled into Redox Foils.

We have also begun to prepare thermite-based multilayer films via physical layer deposition. A magnetron sputtering system was used to sputter fully-dense films with controllable layer spacings. Multilayer films produced in this manner provide an ideal basis for comparison to mechanically-processed Redox Foils, which are nearly fully-dense and whose reactant spacings are less uniform. NiO and Cu_2O targets were diluted with 20 wt% Ni/Cu and Cu, respectively, to increase the conductivity of the targets for direct current (DC) sputtering. The NiO target was doped with a $Ni_{60}Cu_{40}$ alloy (by wt%) to make the diluent non-magnetic at room temperature. To generate the multilayer structure, substrates were rotated past aluminum and oxide targets in an alternating fashion.

Stresses that evolve during the deposition process represent a significant obstacle in the effort to produce thick, free-standing multilayer films. If the magnitude of these stresses is significant, the film tends to crack or delaminate from the substrate, depending on whether the stress is tensile or compressive. The focus of FY2015 was to understand how these stresses develop in Al:NiO films as a function of layer spacing, sputtering pressure, and substrate-film interaction. Films with a total thickness of ~1 µm and varying layer spacings were deposited on silicon wafer substrates at different sputtering pressures. A wafer curvature rig was used to measure the change in wafer curvature that occurred due to the deposition of the film. The change in substrate curvature was related to the biaxial stress of the film using the Stoney equation. The orientation of each wafer was tracked throughout the experiment in order to measure the stresses in two orthogonal directions, one of which corresponds to the direction of rotation in the sputtering chamber.

Results and Discussion:

We attempted to dilute Al:NiO Redox Foils produced from single-phase powders with copper instead of nickel. We have empirically observed that copper wets the base metals better than nickel, and the Al:NiO system produces less gas than the Al:CuO and Al:Cu_2O systems, as displayed in Figure 4b.

Changing the diluent of the Al:NiO system from nickel to copper increased the velocity of Redox Foils by a factor of 2-3 across the range of dilutions. We attribute this increase in velocity, in part, to increased thermal conductivity along the length of the Redox Foil due to the presence of copper. In addition, DSC experiments indicate that the onset of the reaction occurs at a lower temperature when the Al:NiO system is diluted with copper. Figure 5 gives DSC traces for Al:NiO Redox Foil diluted with copper and nickel. A shift of the second exotherm from 650 C to ~550-560 C is evident for both copper-diluted samples. This exotherm corresponds to the melting of aluminum; since these reactions are diffusion-limited, we expect the rate of diffusion to increase upon melting of the reactant. The melting point of aluminum is lowered due to alloying with copper. These phenomena explain the observed increase in velocity.

A focus in FY2015 was on the fabrication, testing, and application of Redox Foils produced from ball-milled, composite powders. Initials experiments were performed using Al and NiO powders to explore the effect of changing various ball-milling parameters, particularly the ball-to-powder mass ratio (BPR), ball size, and milling time, on heat of reaction. Samples were tested using DSC. The BPR was fixed at 10 for this set of experiments. The results are shown in Figure 6.

At comparable milling times, the 5mm diameter balls generated powders with higher heats of reaction. This is attributed to the nature of the interactions between the milling media and the powders. For instance, 9mm diameter balls are more massive, but the velocities and mean free paths between collisions are different than those seen in 5mm diameter balls. In general, collisions which minimize the reactant spacing between aluminum and the metal oxide without leading to significant reaction will maximize the heat of reaction. The highest heats of reaction was measured in powders that were milled with 5mm diameter balls and were generally found to be higher than heats observed in fully-processed Redox Foils prepared with single-phase powders. Thus, the reduction in reactant spacing induced by the milling process is likely larger than that induced by the swaging and rolling processes.

A similar study was performed using Al:Cu_2O composite powders, as the Al:Cu_2O system is predicted to produce more braze by volume than either the Al:CuO or Al:NiO systems. Heat of reaction data was collected using DSC and is shown in Figure 7. In this case, the highest heat of reaction was observed in powders milled with 8mm diameter balls for 30 minutes. X-ray diffraction (XRD) experiments were also performed before thermal analysis to correlate the heats of reaction with the relative amounts of Al and Cu_2O present. The XRD traces are shown in Figure 8. The extent of reaction was assessed by searching for Cu peaks, which indicate that some of the reaction had occurred given the samples were undiluted. The Al:Cu_2O powders with the highest heat of reaction (8mm-30min) yielded the highest peak intensities of reactant phases, with insignificant Cu peaks. Conversely, the 5mm-60min sample yielded the highest peak intensities for Cu, indicating significant reaction had occurred. This sample produced the lowest measured heat of reaction.

In order to assess reactivity in Redox Foils fabricated from ball-milled powders, we compared reaction propagation velocities to those measured for Redox Foils prepared from single-phase powders. The velocity data is shown in Figure 9 as a function of braze volume. For the Al:Cu_2O system, we found that ball milling increases the average propagation velocity by a factor of 3 in 20 wt% diluted foils and a factor of nearly 7 in 40 wt% diluted foils. This is a promising finding, as it suggests we can significantly increase the reactivity of Redox Foils that approach 75% braze content by volume. All ball-milled powder Redox Foils propagated faster than their single-phase counterparts.

We also tested ball-milled Redox Foils in a joining configuration to determine whether the reactions would quench in the bonding interface. Quenching tests were performed in bonds where similar alloys were joined together (Mg AZ31 to Mg AZ31 and Al 6061 to Al 6061) using conventional and ball-milled Redox Foils. The results are shown in Figure 10. In all cases, the highest dilution that could be fully propagated through a bond interface was increased by at least 20 wt% when bonding with ball-milled Redox Foils.

Experiments to determine the nature and magnitude of stresses in thermite films that are deposited via magnetron sputtering were performed. Stresses were calculated as functions of three deposition parameters: the first deposited layer (Al or NiO), sputtering pressure, and film bilayer thickness. The calculated stresses are shown in Figure 11 and Figure 12. For each figure, x-stress refers to the film stress acting in direction of rotation (horizontal), while y-stress refers to the film stress acting in vertical direction. For the regime of sputter pressures tested, film stress becomes increasingly compressive as sputter pressure increases for all first layer and direction combinations, as shown in Figure 11. Stresses in the rotation direction decrease in a linear fashion, while y-stresses tend to level off. The trends suggest that stresses in both directions can be minimized at a sputter pressure of about 2.5 mtorr. Figure 12 shows film stress as a function of bilayer spacing. For the regime of bilayer spacings tested, the film stress gradually decreases in magnitude as the bilayer spacing increases from 53 nm to 106 nm.

Per the discussion above, we have attempted to deposit 20 µm thick Al:NiO multilayer films using a bilayer spacing of 106 nm and a sputter pressure of 2.5 mtorr. Large aluminum and brass substrates were included in the stress experiments to assess the viability of using these substrates for large-scale film deposition. For particularly thick multilayer films, we have deposited on both thermal oxide Si wafers (with 500 nm thick silicon oxide layer) and large aluminum substrates. In the event that films cannot be pulled from aluminum substrates, measurements of velocity can be performed on films deposited on thermal oxide wafers. Unfortunately, issues with various components of our sputtering system prevented a successful deposition of this film. We have purchased larger, rectangular oxide targets to help control film stress and give us better control of our sputtering rates.

Technology Transition Path:

A provisional patent for this technology has been submitted and other possible embodiments of the Redox Foil. In the future, Johns Hopkins University plans to license the technology to a materials manufacturer, who will then sell to the automobile industry.

Conclusions:

In FY2015, we have focused on the fabrication and characterization of Redox Foils prepared with ball-milled composite powders. Micrographs confirm that the ball-milling process reduces the average distance between the aluminum and oxide phases when compared to Redox Foils prepared with single-phase powders. The decrease in reactant spacing is expected to increase reactivity in diffusion-limited reactions, which is supported by the observed increase in average propagation velocity and the shift in exothermic activity to lower temperatures. In addition, we have successfully identified ball-milling parameters for which heats of reaction are maximized in undiluted Al:NiO and Al:Cu_2O ball-milled powders. Quench test data indicates that ball milling can be used to enable bonding at higher dilutions for Al:NiO and Al:Cu_2O Redox Foils. This is essential in reducing porosity caused by gas production and increasing the amount of braze available for bonding. We have characterized stresses in Al:NiO-Ni/Cu multilayer films produced by magnetron sputtering and identified a set of sputtering parameters that reduces the magnitude of the stress to an acceptable level. Understanding how these stresses evolve during deposition is critical for scaling up the film thickness to produce free-standing films.

References:

(1) Ma, E.; Thompson, C. V.; Clevenger, L. A.; Tu, K. N. *Appl. Phys. Lett.* **1990**, *57*, 1262.
(2) Duckham, A.; Newson, J. E.; Brown, M. V.; Rude, T. R.; Knio, O.; Heian, E. M.; Subramanian, J. S. Method For Fabricating Large Dimension Bonds Using Reactive Multilayer Joining, 2008.
(3) Wang, J.; Besnoin, E.; Duckham, a.; Spey, S. J.; Reiss, M. E.; Knio, O. M.; Powers, M.; Whitener, M.; Weihs, T. P. *Appl. Phys. Lett.* **2003**, *83*, 3987.
(4) Swiston, A. J.; Hufnagel, T. C.; Weihs, T. P. *Scr. Mater.* **2003**, *48*, 1575–1580.
(5) Woll, K.; Gibbins, J. D.; Slusarski, K. A.; Kinsey, A. H.; Weihs, T. P. In review for publication in *Combustion and Flame*

Figures and Tables:

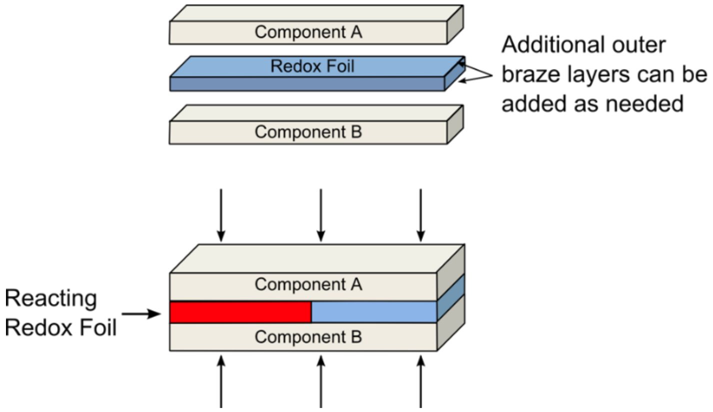

Figure 1. A Schematic Representation of Bonding with a Redox Foil. After Ignition, a Reaction within the Foil Self-propagates through the Bond Interface.

Remainder of Page Intentionally Blank

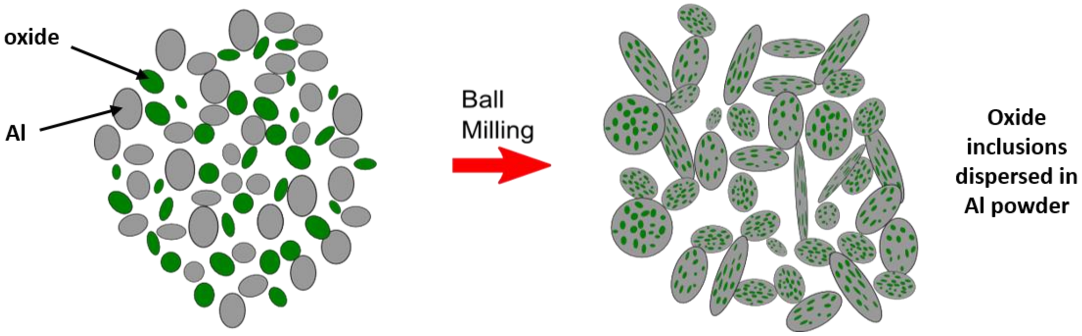

Figure 2. Schematic of Powder Evolution during Ball Milling Process. Collisions between the Milling Media and Single-phase Powders Create Composite Powders containing Oxide Fragments dispersed in Softer Aluminum Powders.

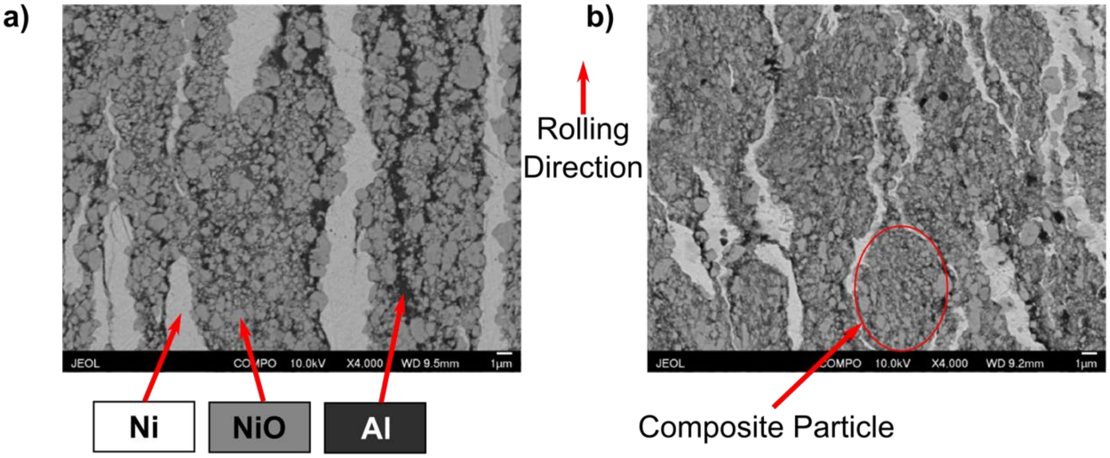

Figure 3. Scanning electron micrographs of Al:NiO:Ni Redox Foil fabricated from (a) single-phase powders, and (b) ball-milled composite powders.

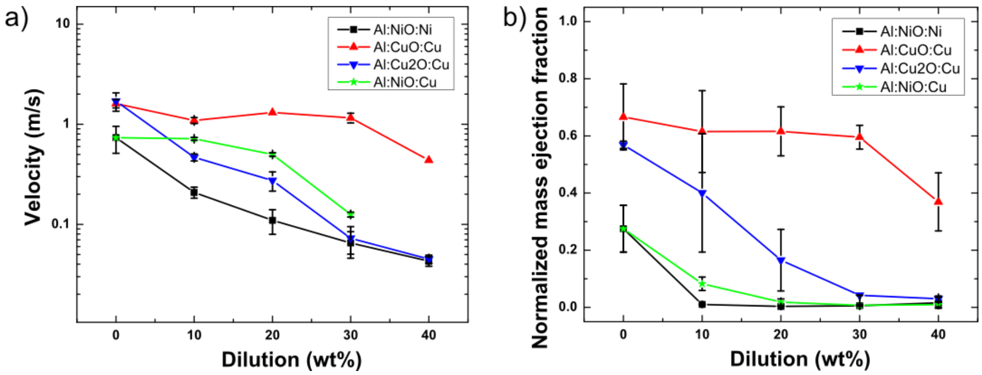

Figure 4. (a) Velocity of selected thermite systems as a function of dilution. When changing the diluent of the Al:NiO system from nickel to copper, the velocity increases by a factor of 2-3. (b) Mass ejection fraction of selected thermite systems as a function of dilution. The Al:NiO:Cu system produces slightly more gas at lower dilutions, but the mass ejection fraction plateaus near zero at 20 wt% dilution.

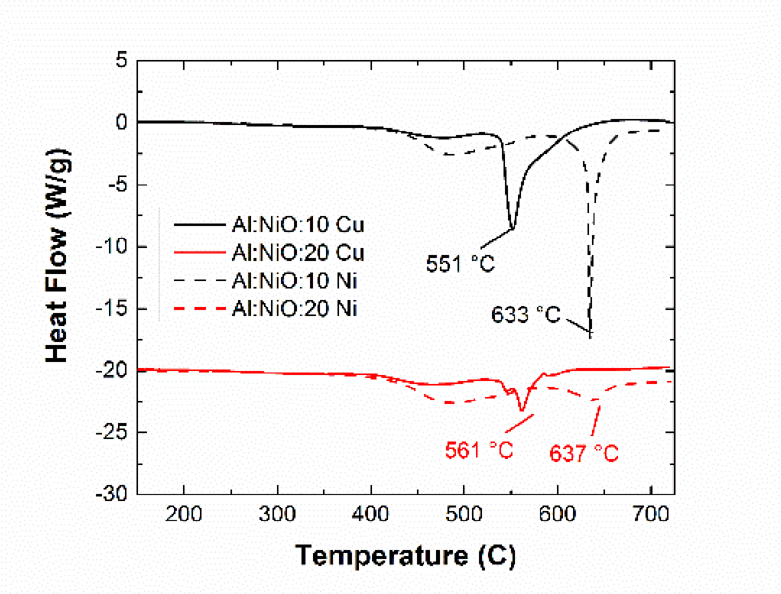

Figure 5. DSC traces of Al:NiO Redox Foil diluted with copper (solid lines) and nickel (dashed lines), for both 10 wt% and 20 wt% dilutions. There is a shift of the second exotherm to lower temperatures, indicating that the onset of the reaction occurs at a lower temperature. This shift offers one explanation as to why we see enhanced velocity when diluting with copper as opposed to nickel.

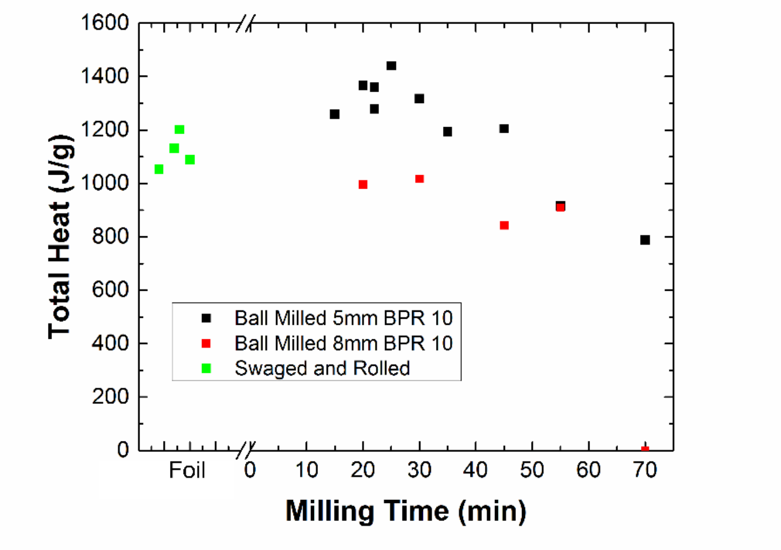

Figure 6. Heats of reaction of ball-milled, composite Al:NiO powders as a function of ball diameter and milling time compared to conventionally processed, undiluted Redox Foil. Heats of reaction are maximized at a ball diameter of 5mm and milling time of 25 min.

Remainder of Page Intentionally Blank

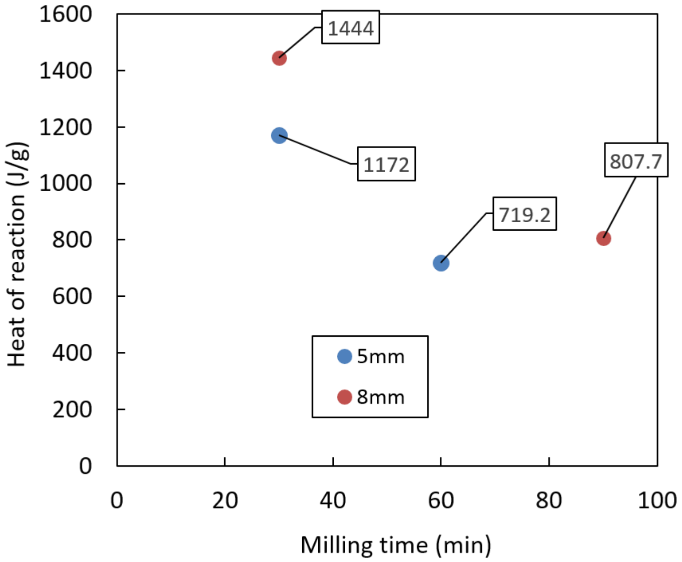

Figure 7. Measured heats of reaction of Al:Cu_2O ball-milled powders as functions of ball diameter and milling time. The highest heat of reaction was measured in powders milled with 5mm diameter balls for 30 min.

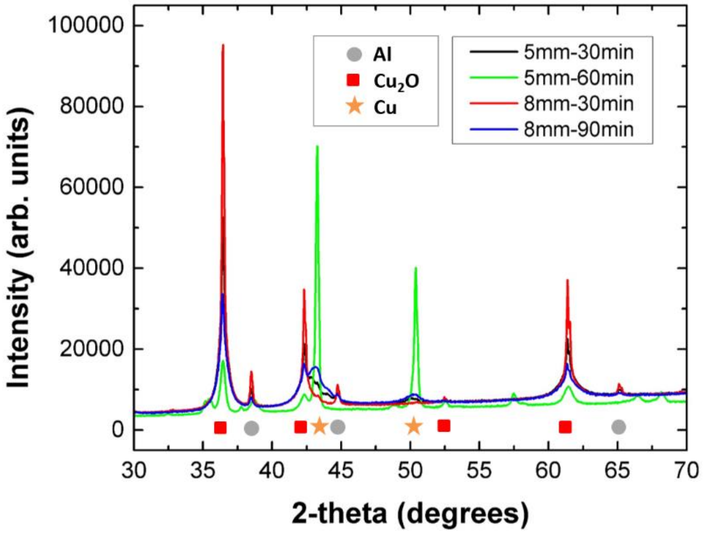

Figure 8. XRD traces of undiluted Al:Cu_2O ball-milled powders at various ball diameters and milling times. Small/absent Cu peaks suggest that little or no reaction has taken place and correlate with large reactant (Al, Cu_2O) peak intensities.

Remainder of Page Intentionally Blank

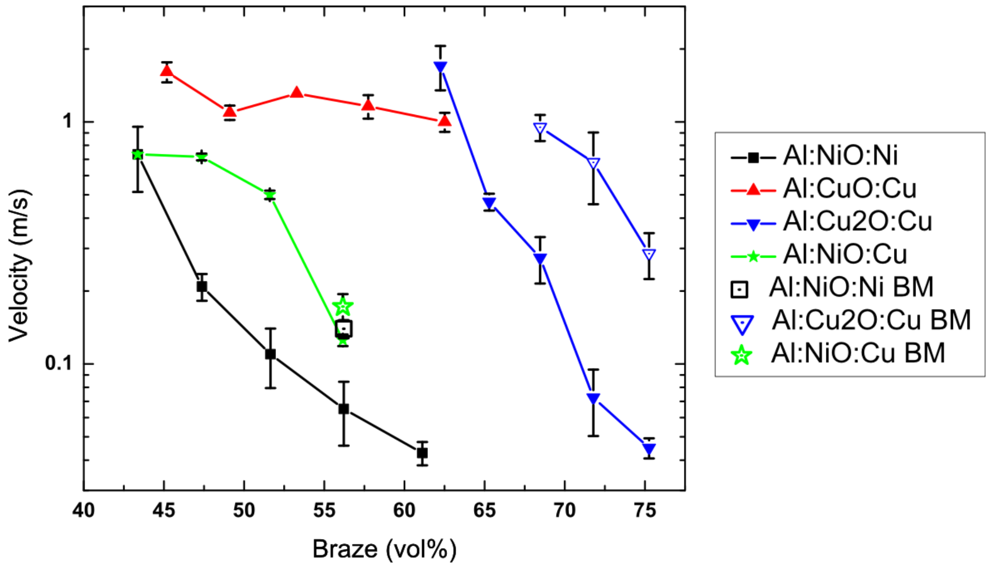

Figure 9. A comparison of propagation velocities for thermite systems produced from single-phase powders and ball-milled (BM) composite powders. Velocities are plotted as a function of expected braze percent by volume, where the balance is the expected alumina content. Diluent increases from moving left to right.

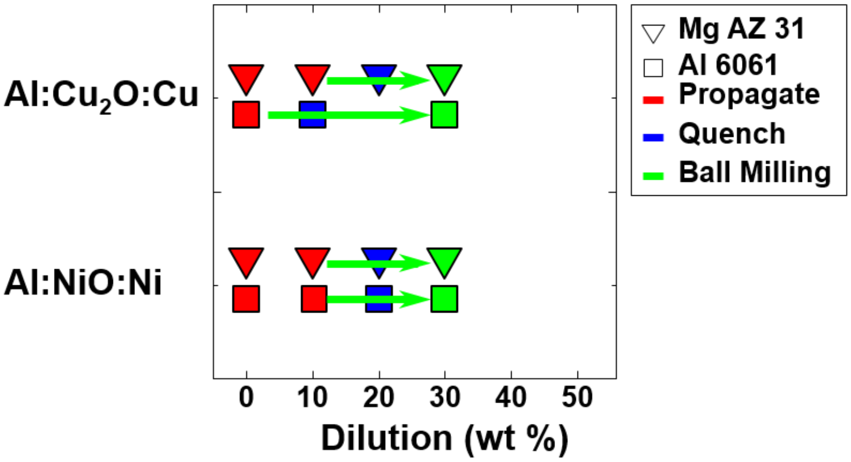

Figure 10. Quenching limits for Al:Cu$_2$O:Cu and Al:NiO:Ni systems using conventional and ball-milled powders. Foils created from ball-milled powders could be subjected to higher levels of dilution before quenching in the bond interface.

Remainder of Page Intentionally Blank

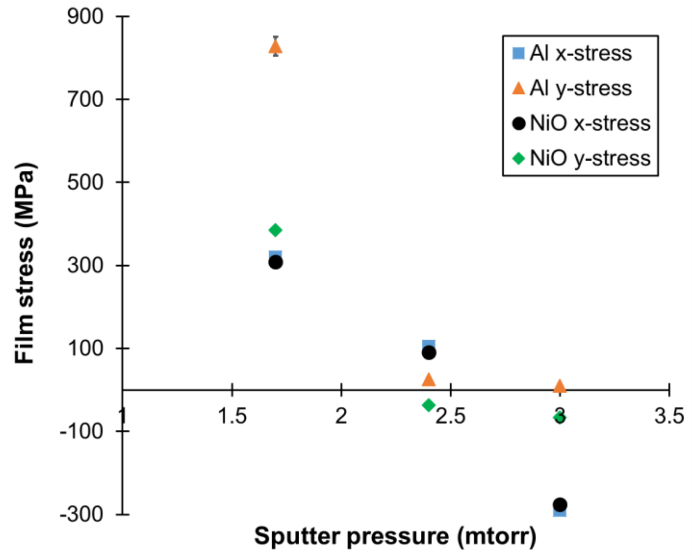

Figure 11: Biaxial stresses in Al:NiO-Ni/Cu multilayer films as a function of sputter pressure. Total film thickness is ~1 μm and bilayer thickness is 106 nm. Positive values indicate tensile stresses. The legend indicates which layer was deposited first.

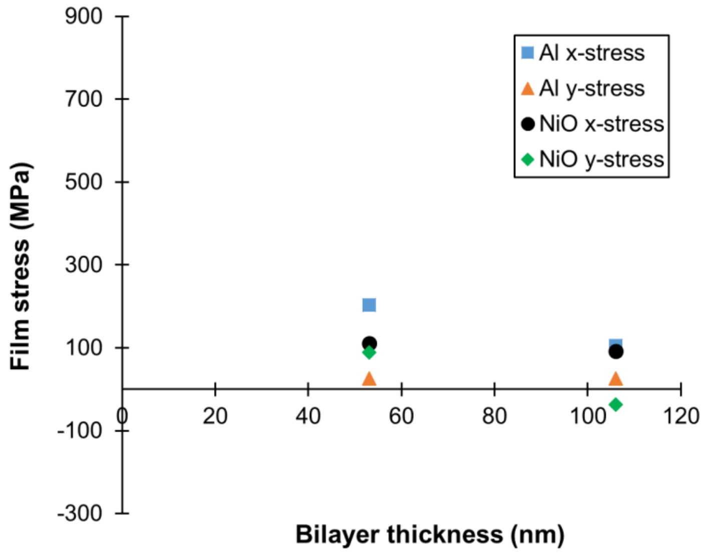

Figure 12. Biaxial stresses in Al:NiO-Ni/Cu multilayer films as a function of bilayer thickness. Total film thickness is ~1 μm and sputter pressure is 2.4 mtorr. Positive values indicate tensile stresses. The legend indicates which layer was deposited first.

This Page Intentionally Blank

AVPTA Technology Focus Area 2: Lightweight Structures & Materials

Breakthrough Techniques for Dissimilar Material Joining – Collision Welding of Dissimilar Materials by Vaporizing Foil Actuator

DOE-VTO TFA Lead: Sarah Ollila
TARDEC TFA Lead: Martin McDonnell

Principal Investigator:
Glenn Daehn

Affiliation:
Ohio State University
141 Fontana Labs, 116 W 19th
Columbus, OH
Phone: (614) 292-6779;
E-mail: daehn.1@osu.edu

Co-Principal Investigator:
Anupam Vivek

348 McQuigg Labs, 105 W Woodruff Avenue
Columbus, OH
Phone: (608) 332-4892
E-mail: vivek.4@osu.edu

Project Start: Q1FY14
Estimated Completion: Q4FY16

Objective:

- To meet the challenge of effectively welding starkly dissimilar materials, namely, steel, aluminum, and magnesium for creating multi-material automotive body structures.

Strategic Context:

- This technology will be applied to future Programs of record (PORs) requiring dissimilar material lap joints.
- The technology supports the TARDEC Strategy enabling new capability in the design and application of dissimilar material lap joints.

- Follow-on activities may include further AVPTA interest to investigate increasing joint strength, reducing cost and / or developing foils for other material combinations. TARDEC-specific follow-on may include lap joint ballistic shock evaluations.
- In addition to discussions with an automotive industry Original Equipment Manufacturer (OEM) and major automotive industry material supplier on material selection and corrosion inhibition strategies, OSU developed a close working relationship with an OEM Tier 1 supplier which is looking to integrate VFAW into its manufacturing process to enable creation of multi-material, lightweight automotive seating structures.

Accomplishments:

- (Since FY 2014) Screened 21 dissimilar metal combinations consisting of magnesium, steel, and aluminum alloys for welding using vaporizing foil actuator welding (VFAW). More than 14 combinations successfully welded.
- Selected seven combinations for corrosion testing and mechanical testing.
- Made six weld coupons for each selected material combination, for testing under three conditions: as-welded, coated and corroded, and uncoated and corroded. Each coupon yielded two or three lap-shear test samples.
- Lap-shear tested about 90 samples, in various material combinations and conditions
- Welded 2mm thick AA6061-T4 flyer sheets to DP780 steel.
- Successfully welded JSC1500 boron steel with tensile strength of 1500 MPa, with AA5052 and AA6111-T4 flyers.
- E-coated samples of DP780/AA6061-T4, JAC270F/AA6061T4, and JAC980/AA5052 retained >90% lap-shear strength after 30 cycles of ASTM B-117 salt-spray testing. In most cases, failure was in base metal away from the weld. Strength decreases were due to reduction in material thickness due to corrosion.
- Studied fracture surfaces of peeled weld interfaces using scanning electron microscopy (SEM) and energy dispersive x-ray spectroscopy (EDS) mapping. Both ductile and brittle regions were identified.
- Obtained larger weld area using a pre-formed tent-shape target.

Introduction:

This report is a continuation to the FY2014 annual report. This project aims to meet the challenge of effectively welding starkly dissimilar materials, namely, steel, aluminum, and magnesium for creating multi-material automotive body structure. Traditional fusion-based welding between dissimilar combination of aluminum, steel, or magnesium always leads to formation of intermetallic compounds (IMCs), which are brittle. Upon mechanical testing, failure in such weld samples tends to happen within the weld. For instance, Al-Fe welds made by resistance spot welding often contain IMCs and are not tough enough to be applied in the body in white. Solid-state welding techniques, like friction stir and impact welding, offer ways to avoid or reduce the formation of IMCs.

This project used VFAW [1], a solid-state impact welding technique developed at the Ohio State University. A schematic of the progress of a weld interface is shown in Figure 1a. The main driver of these experiments is a 0.0762mm thick aluminum foil, which is a consumable, replaced after every experiment. When a high, short-duration current pulse, driven by a capacitor discharge, passes through the foil, the foil vaporizes rapidly due to Joule heating. The rapidly expanding gas drives the flyer sheet to high velocities toward the target plate. Standoff sheets between the flyer sheet and target plate provide the distance over which the flyer accelerates. Additionally, the height of the standoff sheets and the horizontal distance between them help create an oblique collision, which is necessary for weld creation. As shown in Figure 1b, a good weld, represented by a wavy interface with no continuous layer of IMCs, is obtained when the impact angle and velocity are within the process window.

The flyer sheet is chosen based on density, strength, and ductility of the joining members. Ideally, the flyer materials should be one that is lighter, weaker, and more ductile between the two metals. However, in some cases where not all three criteria can be met simultaneously, the more ductile material is chosen. Flyer sheet thickness ranges from 0.5 mm to 2.0 mm. Target plates can be as thick as needed, since they are stationary. Many alternate flyer and target configurations are now under examination in separate investigations.

During FY2015, we focused on corrosion behavior and its effect on mechanical performance, since corrosion due to disparate electrochemical potentials is a major issue with dissimilar material joining. Corrosion mitigation by using e-coating was pursued. In addition, we also studied electrochemical properties of some base materials, fracture surfaces, and some new welding configurations.

Approach:

The following seven material combinations were studied during FY2015 (target/flyer sheet):

- JAC270F/AA6061-T4
- AM60B/AA6061-T4
- DP780/AA6061-T4
- JAC980/AA5052
- JAC980/AA6111-T4
- JSC1500/AA5052
- JSC1500/AA6111-T4

JAC270F and JAC980 are galvannealed steels with nominal tensile strengths of 270 and 980 MPa, respectively. The Zn coating was surface ground prior to welding by either belt-sanding or surface grinding. JSC1500 was also surface ground to remove its dull-colored surface layer. Since aluminum is light and ductile, it was a fitting flyer material in every test.

The main body of this work consists of mechanical testing of as-welded, corrosion-protected, and corroded samples. Six weld coupons were made for each material combination (Figure 2). All samples were welded in the lap configuration, using 10 kJ input energy and 1.7-mm standoff distance. With these input parameters and a 1mm thick aluminum flyer sheet, the impact velocity was found to be approximately 700 m/s. Of the six samples, two were e-coated and then corrosion-tested, and two were left uncoated and then corrosion-tested (Figure 3). All six samples then were sectioned by abrasive water jet machining and lap-shear tested. Each weld coupon yields either two or three useable 12.7-mm wide lap-shear test samples, depending on the dimensions of available materials.

E-coating was performed by Electro Prime, using POWERCRON 6000CX cationic epoxy electrocoat. Corrosion testing was done according to ASTM B-117 (35°C, spray of 5% NaCl solution, 24 hours/cycle), for 30 cycles. Lap-shearing testing was done in an MTS Systems Corporation mechanical testing frame, at a rate of 0.1 mm/s.

Electrochemical characterization of the base metals was conducted for AA5052, AA6111-T4, JAC980, and JSC 1500, by polarization scans. Figure 4 shows the corrosion cell. Since aluminum is typically anodic and Fe, cathodic, anodic polarization scan was done on AA5052 and AA6111-T4, and cathodic polarization scan was done on JAC980 and JSC1500 with current density measured.

The research analyzed fracture surfaces of AM60B/AA6061-T4, DP780/AA6061-T6 welds (from FY14) were studied using SEM and EDS mapping.

A new welding configuration involved a pre-formed, tent-shaped target sheet, with the intention of maximizing the area of oblique impact. Successful impact welding requires an oblique impact, but in the typical flat-on-flat configuration, the center of the impact area experiences a non-oblique impact and therefore is not welded. Furthermore, such a flat impact may cause the flyer sheet to rebound away from the target, which could put the weld under tensile stress. Therefore we pre-formed the target sheet into a tent shape, so to maximize the area where oblique impact occurs (Figure 5). Only the AA6061-T4/DP780 combination used this configuration with flyer thicknesses of 1.5mm and 2mm.

Results and Discussion:

Mechanical Testing:

Figure 6 shows a sectioned sample of each test condition. In most cases, no clear sign of galvanic corrosion was observed, but rather general corrosion, especially with Fe/Al welds. More discussion on corrosion will follow in a later section.

Figure 7 summarizes the mechanical testing data and reports the average lap-shear failure loads. For comparison, the chart also shows the expected failure loads calculated, based on reported tensile strength values.

Most of the welds failed in the base aluminum during mechanical testing, for both uncorroded and corroded samples. Furthermore, in the as-welded condition, the average measured failure loads are generally quite close to the expected failure loads calculated based on reported ultimate tensile strength (UTS) values. This indicates that the mechanical knock-down due to the welding process is minimal. In other words, the welds are at least as strong as one of the base metals, indicating nearly 100% joint efficiency.

In the uncoated, corroded condition, two material pairs (DP780/AA6061-T4 and AM60B/AA6061-T4) delaminated along the weld during corrosion testing. On the positive side, the remaining five material combinations retained more than 50% of their strength after corrosion testing in the uncoated condition. Failure still mostly occurred in the base aluminum, indicating a retained joint efficiency of 100%, but the failure load was reduced due to the reduction in cross-section of the aluminum.

E-coating was fairly effective in protecting the materials from corrosion. Again, in most cases, e-coated, corroded samples failed in the base aluminum. The e-coated samples of DP780/AA6061-T4, JAC270F/AA6061T4, and JAC980/AA5052 experienced strength degradations of less than 7% through corrosion testing. The most severe strength reduction of e-coated samples occurred with AM60B/AA6061-T4, where all samples delaminated along the weld during corrosion testing. This is largely because the e-coating used here was not appropriate for Mg alloys. Application of an intermediate conversion coating should result in better compatibility. A more appropriate corrosion test as well as coating method for that combination will need development in collaboration with the industry experts.

Electrochemical Properties of Base Metals:

Figure 8 shows the polarization curves, and open cell potentials (OCP) in volts (V) for a saturated calomel electrode (SCE), in Table 1.

The driving force for galvanic corrosion between two adjacent metals has to do with the difference in OCP between the two metals. In this case, the largest potential difference is the one between JAC980 and AA6111-T4, with a magnitude of 0.060 V, which is not very large. In other words, the propensity for galvanic corrosion is not very high. This is consistent with the fact that we mainly observed general corrosion during corrosion testing. JAC980 turned out to be more anodic than both aluminum alloys at hand, which is quite surprising, since aluminum alloys are typically more anodic than Fe alloys. In any case, the potential differences are small enough that galvanic corrosion is not a major concern for the aluminum-steel joint combinations above. The microanalysis discussed below concerns only pre-corrosion aluminum-steel and aluminum-magnesium weld samples.

Microanalysis - Interfacial Structure and Fracture Surfaces:

Figure 9 shows the weld interface of a DP780/AA6061-T6 sample welded at 8kJ input energy and illustrates some features of a typical weld interface. Along the direction of weld progress initially, there are cracks or unwelded regions followed by wavy regions that contain intermittent layers of IMCs. A continuous layer of brittle IMCs provides an unhindered crack path, and is therefore not desirable. Regions with discontinuous IMCs are expected to be tougher.

The weld interface of a sample created with 8kJ input energy is shown in Figure 9. Along the direction of weld progress it can be seen that initially there are cracks or unwelded regions followed by wavy regions that contain intermittent layers of IMCs.

In addition to lap-shear testing, where most of the samples failed in the base material, we have also performed some peel testing, which had a higher tendency to cause failure along the weld, thus revealing the weld interface. DP780/AA6061-T6 and AM60B/AA6061-T4 were peeled in this fashion. SEM images and EDS maps of their peeled fracture surfaces of are shown in Figures 10 and 11.

A scanning electron fractograph of the Fe side of DP780/AA6061-T4 is shown in Figure 10 and the corresponding EDS map of the fracture surface is shown in Figure 10b. As noted in FY 2014 annual report, several samples created with T6 temper flyer sheets failed within the weld during mechanical testing. However, Figure 7 illustrates that, even though the overall failure of such sample seemed brittle, there were regions where ductile failure in the parent aluminum occurred. Since interfacial IMCs are usually brittle, one can infer that the areas where ductile fractures occurred were free of interfacial IMCs. Further microanalysis could validate this reasoning. Furthermore, based on past studies on the impact-welding window, the joint toughness can be improved by tailoring the welding conditions to minimize the formation of interfacial IMCs [3].

AM60B is a cast Mg alloy and AA6061 is an age-hardenable aluminum alloy. This particular weld sample yielded an exceptionally large weld area and a peel strength of 32.5 N/mm. The fracture surface (Figure 11) showed very pronounced and regular wavy features. The fracture surface appears to be primarily ductile, which corresponds with the high toughness of the joint in peel.

Both the peaks and valleys of the waves contain continuous lines of residual aluminum, which were transferred over to the Mg side by ductile fracture, which occurred within the base material. Such material transfer by ductile fracture indicates areas where the bond strength exceeds the strength of one of the base materials. In this case, areas of material transfer are continuous and regular, which are good for joint strength and toughness.

Figure 12 shows SEM micrographs from the AA5052/JAC980 and AA6111/JSC1500depicting slightly wavy interfaces. Regions with no IMCs were found at both welds, and these areas are expected to be tougher than welds with large amounts of IMCs.

Pre-Formed Tent-shape Target:

The peeled fracture surface of the tent-shape-target weld shows distinct bands welded regions (Figure 13). A significant welded area is near the centerline. This is in contrast to the flat-on-flat weld, where the unwelded area near the centerline. Since the area near the centerline experiences the highest driving pressure, obtaining welding in this area may be a more efficient way of creating good welds, even though the overall welded area does not seem much larger in this particular case.

Mechanical testing employed samples of two flyer thicknesses (1.5 and 2.0 mm) and two welding configurations (flat target with 1.6 mm standoff and tent target with 3.67 mm standoff). Table 2 gives results for both peel and lap-shear tests and the data indicate that tent-shape targets achieved higher peak failure loads, but there was much scatter in the data and the trend was not all consistent. Nevertheless, the tent configuration provides one workaround for the flat-impact problem and can be pursued further during industrial implementation.

Technology Transition Path:

From the work performed under the auspices this project, VFAW is a flexible process for welding a variety of material combinations in patch as well as spot configurations. Due to the lack of heat-affected zones, the welds have nearly 100% joint efficiency even for advanced high strength materials. With these value propositions at its core, a customer alignment process was initiated under the I-Corps@Ohio program wherein 80 customer interviews were conducted within the automotive industry. Besides providing the research team with key insights on industry pain points, supply chain and ways to implement new processes in the industry, this program also enabled wider dissemination of the knowledge gained from this project. A few Original Equipment Manufacturers, Tier 1 and Tier 2 parts, systems and material suppliers have expressed interest in conducting validation studies with the aim of ultimately implementing the VFAW process on their production floors.

A major breakthrough in process innovation has been further miniaturization of the weld apparatus as well as the reduction in the electrical energy requirement (Figure 14). An impact spot welding head that weighs less than 20lbs was used to create a weld between two sheets of 1 mm thick AA6111-T4 material with a spot size of 10mm at an energy level of 1kJ. Figure 14c shows the experimental apparatus. Demonstration of an impact spot weld with such low input energies is encouraging. As much lower energies are used, noise and gas generation are also dramatically reduced.

Conclusions:

During FY2015, six combinations of aluminum/steel and one combination of aluminum/magnesium alloys were impact welded using VFAW. These combinations were down-selected for prototype build based on the screening tests of FY2014 and suggestions from our industrial collaborators. Multiple coupons of each combination were created in order to subject them to various post-weld treatments. In lap shear, most of the as-welded specimens failed outside the welded region at nearly 100% theoretical strength of one of the base metals. Based on that result, the base material properties are not degraded due to heat or from plastic work. Furthermore, all samples used the same input parameters of energy and standoff distances.. This illustrates the wide process window and flexibility of the method for welding a variety of material combinations. Post corrosion mechanical testing of the e-coated samples revealed that the aluminum/steel samples retained most of their un-corroded strength, which indicated that e-coating was successful in mitigating galvanic or other forms of corrosion. Aluminum/magnesium samples, however, did not survive 30 days of the corrosion treatment chosen for these tests. The low-energy spot welding results are particularly encouraging with regard to the feasibility of the technology and the Ohio State University team is committed to collaborating with equipment builders, system integrators, tier suppliers and Original Equipment Manufacturers to bring this process to market.

PRESENTATIONS/PUBLICATIONS/PATENTS:

- Liu, B. C., Vivek, A., Daehn, G. S., (2015), “Use of Vaporizing Foil Actuator for Impact Welding of Aluminum Alloy Sheets with Steel and Magnesium Alloys”, Light Metals, pp 463-468.

- Vivek, A., Liu, B., Sakkinen, D., Harris, M., & Daehn, G. (2015), Impact Welding of Aluminum Alloy 6061 to Dual Phase 780 Steel Using Vaporizing Foil Actuator (No. 2015-01-0701). SAE Technical Paper.
- Daehn, G. S., Vivek, A., Liu, B. C., et al., (2015), “Novel joining and process design”, Global Automotive Lighweight Manufacturing Summit (Novi, Michigan)
- Daehn, G. S., Vivek, A., Liu, B. C., et al., (2015), “Keynote: Application of impulse for dissimilar metal joining”, MS&T (Columbus, Ohio)
- Vivek, A., Hansen, S., Benzing, J., He, M., & Daehn, G.S., 2014, Impact Welding of Aluminum to Copper and Stainless Steel by Vaporizing Foil Actuator: Effect of Heat Treatment Cycles on Mechanical Properties and Microstructure. In Metallurgical and Materials Transactions A, 1-11.
- Vivek, A.,Daehn, G.S., Liu, B.C., et al., 2014, Impulse Manufacturing: Multi-material Joining, presented at Global Lightweight Vehicle Manufacturing Congress (Troy, Michigan).
- Vivek, A., Daehn, G.S., 2014, Welding in Lap and Spot Configurations with Vaporizing Foil Actuator, provisional patent application, The Ohio State University.

REFERENCES:

[1] Findik, F., 2011, Recent developments in explosive welding. In *Materials & Design*, *32*(3), 1081-1093.
[2] Psyk, V., Risch, D., Kinsey, B. L., Tekkaya, A. E., & Kleiner, M., 2011, Electromagnetic forming—A review. In *Journal of Materials Processing Technology*, *211*(5), 787-829.
[3] Vivek, A., Hansen, S. R., Liu, B. C., & Daehn, G. S., 2013, Vaporizing foil actuator: a tool for collision welding. *Journal of Materials Processing Technology*.
[4] Chace, W. and Moore, H., 1959, *Exploding Wires*, 4 vols. Plenum Press.
[5] Vivek, A., Liu, B. C., Hansen, S. R., & Daehn, G. S., 2014, Accessing collision welding process window for titanium/copper welds with vaporizing foil actuators and grooved targets. In *Journal of Materials Processing Technology*,*214*(8), 1583-1589.

Figures and Tables Start on Next Page

Figures and Tables:

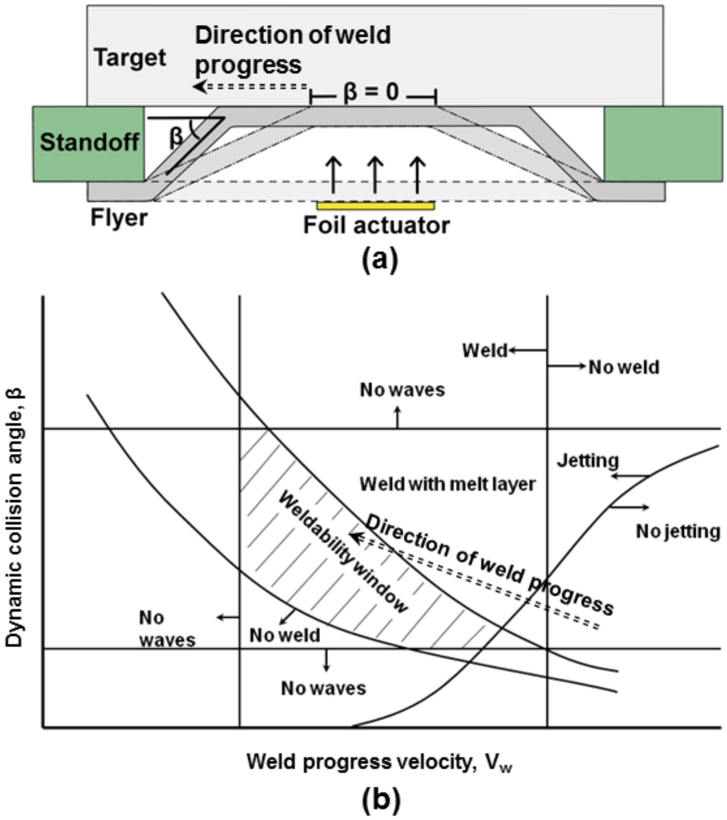

Figure 1. (a) Mechanism of weld progress during current VFAW implementation, (b) A generic impact welding window depicting conditions that lead to different compositions and structure of the weld interface [15]. The dotted arrow labeled as the direction of weld progress (single column)

Remainder of Page Intentionally Blank

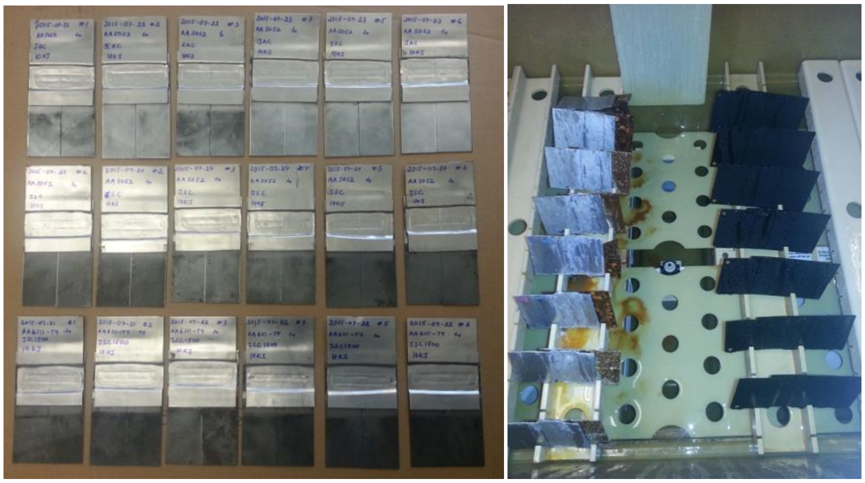

(a) (b)

Figure 2. (a) Al/Fe weld coupons.
Six of the coupons are not shown,
(b) corrosion testing in progress (double column).

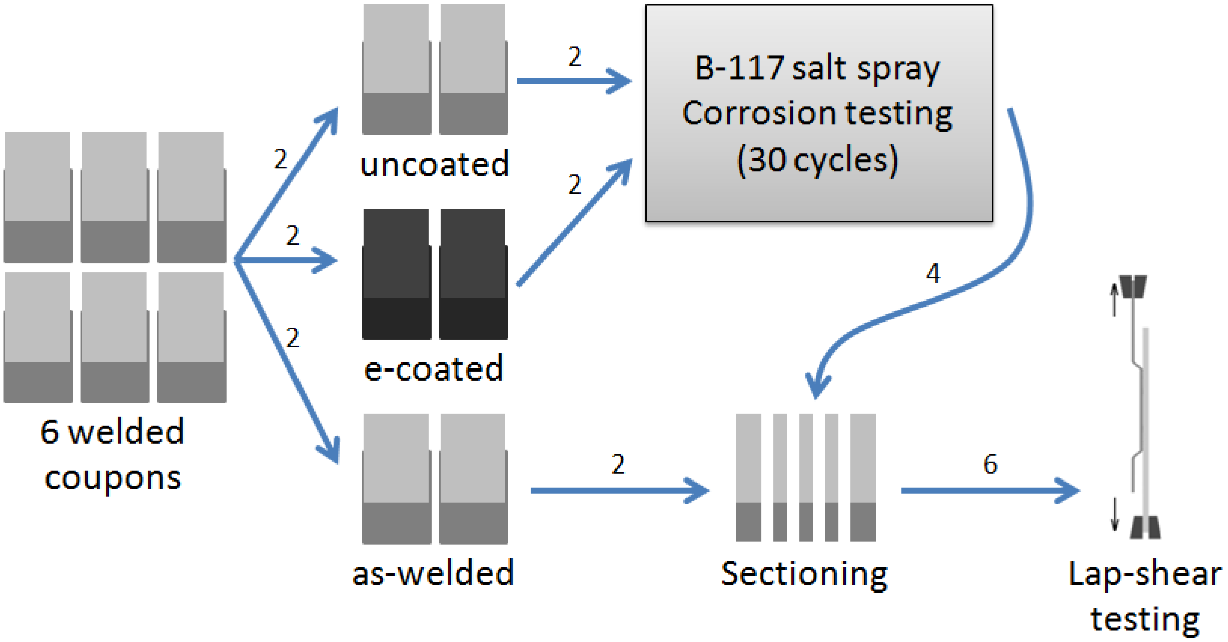

Figure 3: Schematic of experiment plan (double column).

Remainder of Page Intentionally Blank

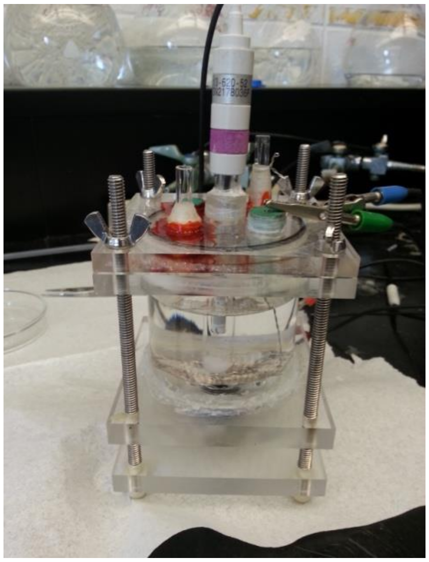

Figure 4. Corrosion testing cell (single column)

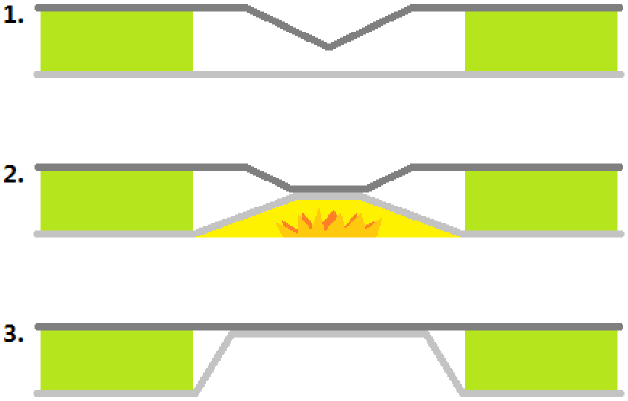

Fig. 5. Side-view Schematic of Welding Process using a Tent-Shape-Target (single column)

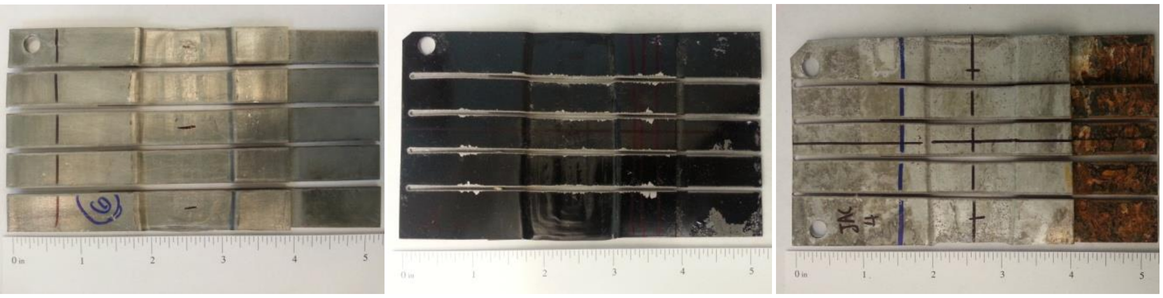

(a) (b) (c)

Figure 6. Sectioned samples in the (a) as-welded, (b) e-coated and corroded, and (c) uncoated and corroded conditions. (double column)

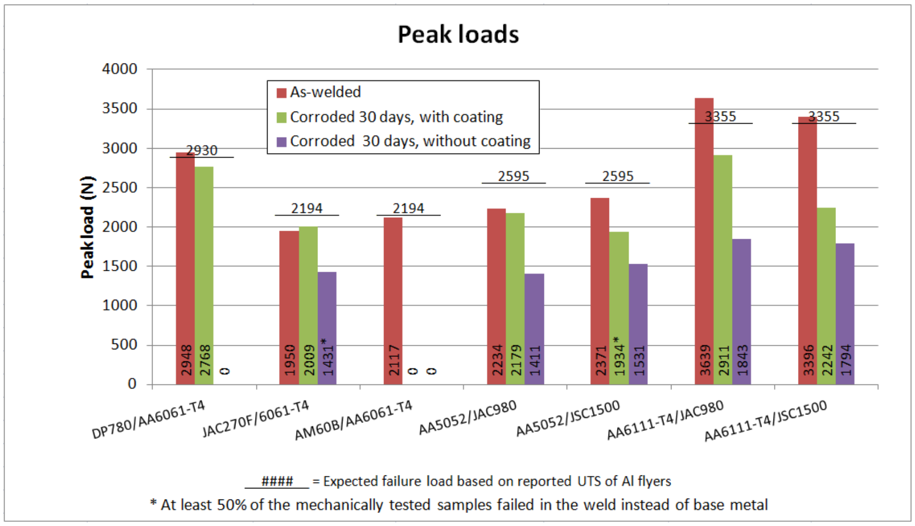

____####____ = Expected failure load based on reported UTS of Al flyers

* At least 50% of the mechanically tested samples failed in the weld instead of base metal

Figure 7. Lap-shear data of various material combinations and conditions.

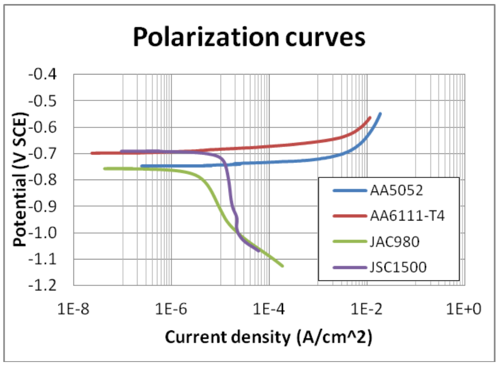

Figure 8. Polarization curves of base metals.

Metal	OCP (V SCE)
AA5052	-0.746
AA6111-T4	-0.698
JAC980	-0.758
JSC1500	-0.690

Table 1. Open cell potentials of base metal

Remainder of Page Intentionally Blank

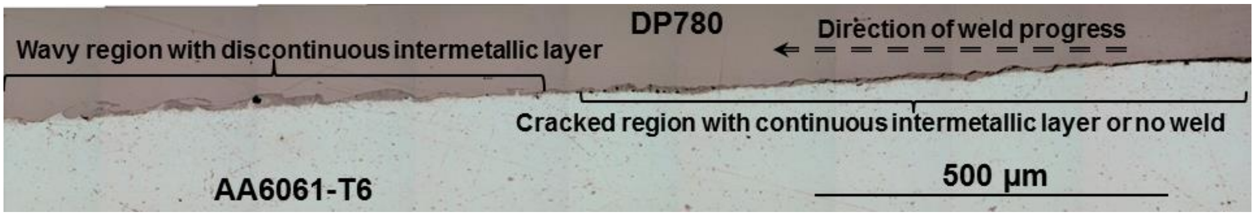

Figure 9. DP780/AA6061-T6 weld interface showing wavy and cracked regions. The interfacial waves were formed by gross material flow due to the severe shearing action of the collision process.

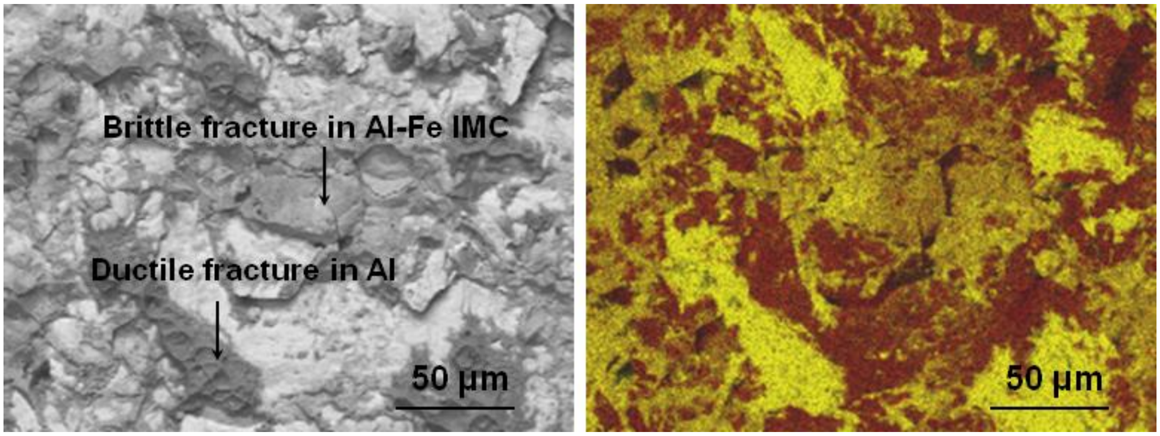

Figure 10. Peeled fracture surface (left) and the corresponding EDS map (right) of a DP780/AA6061-T6 weld. Yellow = Al, red = iron.

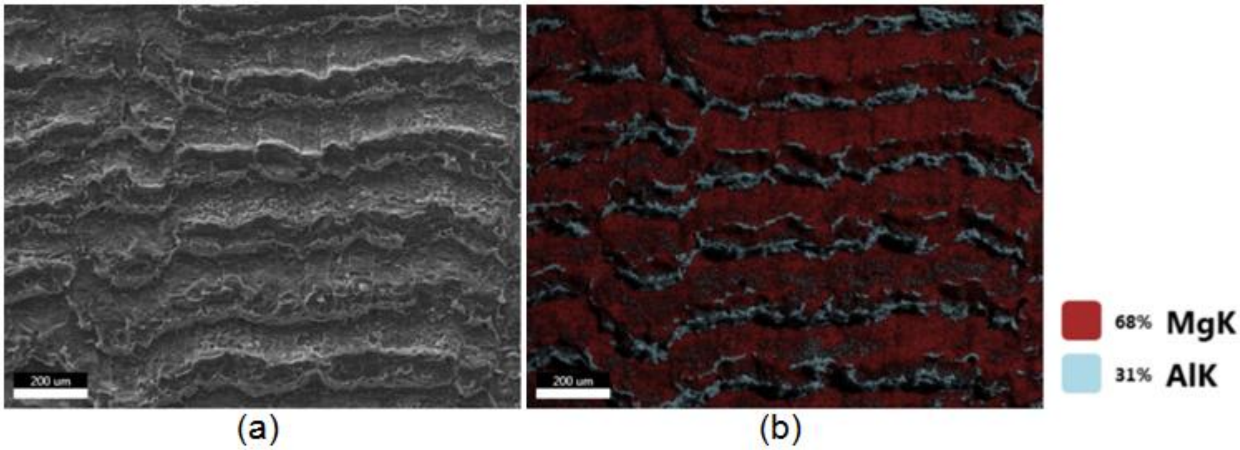

Figure 11. Peeled fracture surface (left) and the corresponding EDS map (right) of an AM60B/AA6061-T4 weld.

<u>Remainder of Page Intentionally Blank</u>

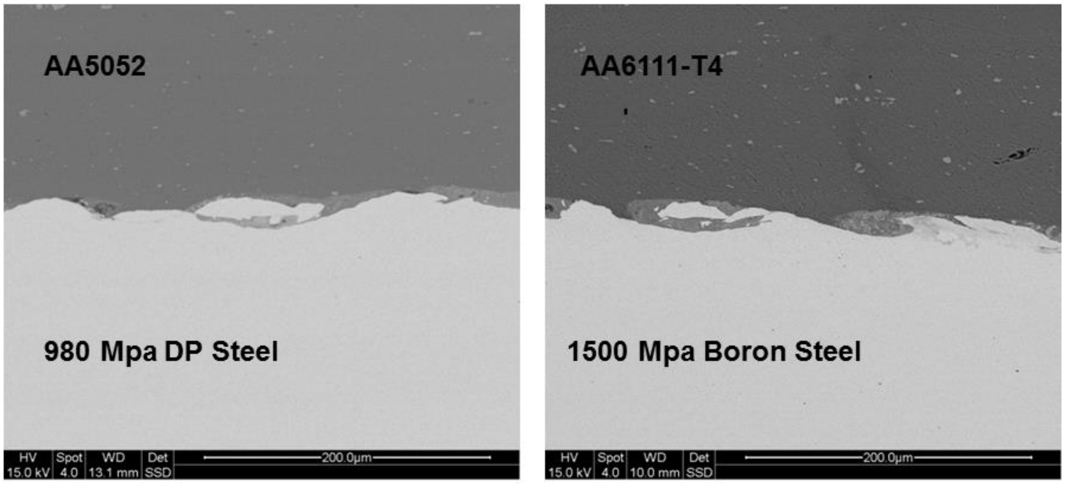

Figure 12. Backscattered electron SEM images of the AA5052/JAC980 (left)) and AA6111/JSC1500 (right) weld interfaces.

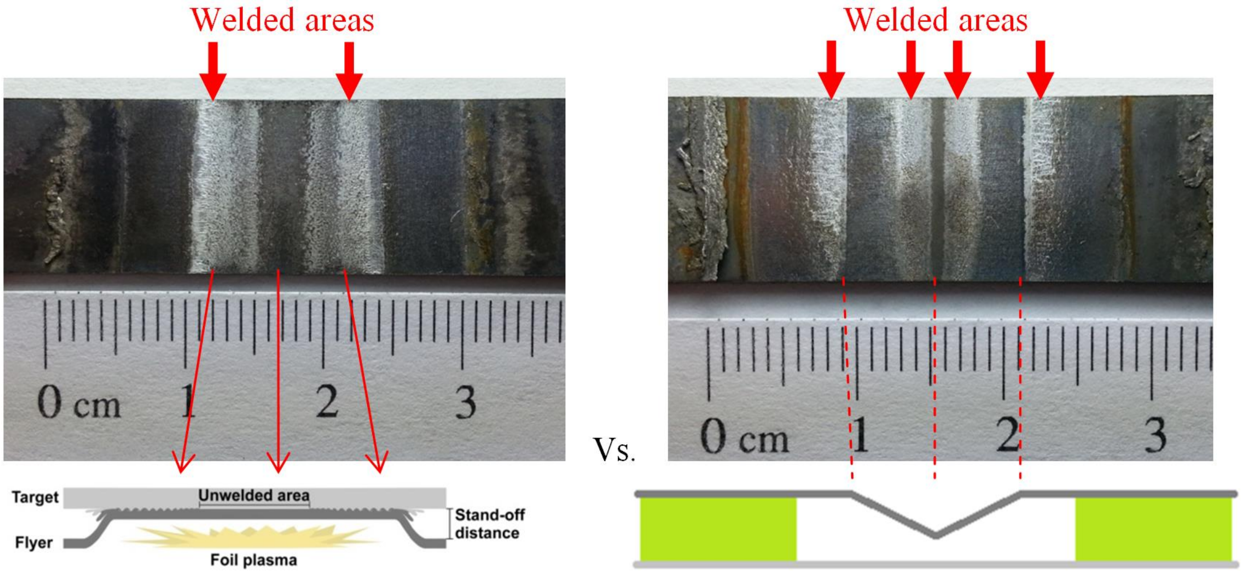

Figure 13. Peeled fracture surfaces of a flat-on-flat weld (left) and a tent-shape-target weld (right)

Peel test		
	Flat target	Tent target
1.5 mm flyer	9.1	23.9
2.0 mm flyer	21.7	23.5

Lap-shear test		
	Flat target	Tent target
1.5 mm flyer	317.1	376.4
2.0 mm flyer	420.5	423.4

Unit: N/mm (failure load normalized by sample width)

Table 2. Mechanical testing results of welds done with flat targets and with tent targets.

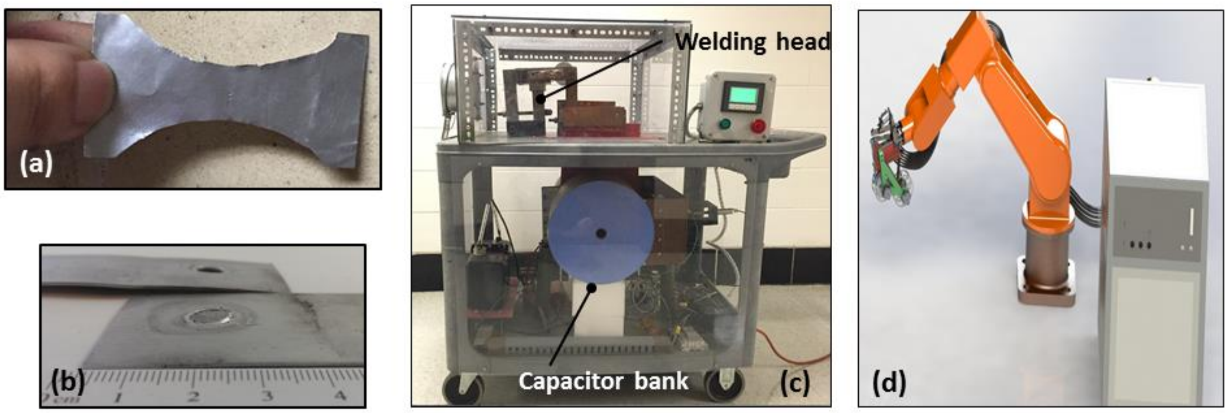

Figure 14: low-energy welding (a) 2 inch long "spot welding" foil,
(b) a mechanically-tested AA6111-T4 weld specimen,
(c) lab-built apparatus with a small spot welding head and a fast, low-energy capacitor bank,
(d) schematic of possible robotic implementation.

Remainder of Page Intentionally Blank

This Page Intentionally Blank

AVPTA Technology Focus Area 2: Lightweight Structures & Materials

Breakthrough Techniques for Dissimilar Material Joining – Upset Protrusion Joining Techniques for Joining Dissimilar Metals

DOE-VTO TFA Lead: Sarah Ollila
TARDEC TFA Lead: Martin McDonnell

Principal Investigator:
Stephen Logan

FCA US LLC
800 Chrysler Drive
Auburn Hills, MI 48326
CIMS #482-00-13
Phone: (248) 512-9485
E-mail: stephen.logan@fcagroup.com

Start: Q1FY14
Projected Completion: Q4FY16

Objective:

- To develop and demonstrate a robust, cost effective, and versatile joining technique, known as Upset Protrusion Joining (UPJ), for joining challenging dissimilar metal combinations, especially those where one of the metals is a die cast magnesium (Mg) component.

Strategic Context:

- The project goal is to join magnesium castings to resin composite structures. The technology and research methodology will be used to develop similar processes for steel or aluminum castings.
- The technology supports the TARDEC Strategy enabling new capability in cost and technically effective joining of metals and composites.
- Follow-on activities may include further AVPTA interest to investigate increasing joint strength, reducing cost and/or developing foils for other casting materials.
- TARDEC-specific follow-on will depend upon project success.
- FCA, a U.S. automotive manufacturer, is leading this project. Since two of the key obstacles preventing more widespread use of light metals in high volume automotive applications are lack of robust joining techniques (especially for dissimilar metal joining) and susceptibility to galvanic corrosion, successful completion of this project will provide a key enabler to high volume application of lightweight materials, allowing FCA (and

ultimately other manufacturers) to accelerate the development of new lightweight vehicle designs that utilize multiple lightweight materials in order to aggressively reduce mass on future vehicle programs.

Accomplishments:

- Pretreated appropriate Mg die castings for round boss UPJ joining. (FY14 & FY15)
- Optimized boss geometry for oval boss configurations using computer-aided engineering simulation tools. (FY14 & FY15)
- Produced over 650 round boss UPJ joints from eleven unique material/coating configurations to support mechanical/structural and corrosion evaluation. (FY15)
- Completed initial (pre-corrosion) mechanical/structural evaluation of round boss UPJ joints, including microstructure evaluations, joining-induced defect characterization, and quasi-static, impact, and fatigue tests of shear and cross-tension joint configurations of 355 Mg to Al and Mg to steel joints. (FY15)
- Commenced twelve weeks of round boss UPJ accelerated corrosion exposure and post-corrosion evaluation of 350 round boss UPJ joints in eleven unique material/coating configurations of shear and cross-tension joint configurations. (FY15)
- Obtained 1,200 oval boss test coupons (each including two bosses for a total of 2,400 bosses) to support oval boss UPJ joining process development, modeling correlation work, and the assembly of joining test coupons in later tasks. (FY15)
- Machined and polished final optimized round boss electrode geometries to support process optimization and production of joined assemblies. (FY15)
- Conducted numerous simulations and physical experiments of oval boss UPJ joints to compare the effects on joint development performance of varying force and current rates throughout the process. This information was utilized in the final process optimization used to produce joints for evaluation. (FY15)
- Produced over 400 oval boss UPJ joints including process development and optimization as well as 220 joints intended for mechanical/structural evaluation. (FY15)
- Completed initial (pre-corrosion) mechanical/structural evaluation including microstructure evaluations, joining-induced defect characterization, and quasi-static, impact, and fatigue tests of shear and cross-tension joint configurations of 220 Mg to Al and Mg to steel oval boss joints. (FY15)
- Developed and optimized UCR geometry using computer-aided engineering simulation tools. (FY15)
- Obtained 1,000 UCR rivets for process development and test coupon production. (FY15)
- Optimized UCR joint electrode shapes and process parameters using a combination of extensive simulation and actual physical experiments in order to develop optimum robust head shapes. (FY15)
- Machined and polished final optimized UCR electrode geometries to support process optimization and production of joined assemblies. (FY15)
- Conducted numerous simulations and physical experiments of UCR joints comparing the effects on joint development performance of varying force and current rates throughout the process. This information was utilized in the final process optimization used to produce UCR joints for evaluation. (FY15)
- Pretreated appropriate Mg die castings for UCR joining. (FY15)

- Produced over 500 UCR joints during process development and test assembly production, including 384 test assemblies. (FY15)
- Initiated pre-corrosion mechanical/structural evaluation including microstructure evaluations, joining-induced defect characterization, and quasi-static, impact, and fatigue tests of shear and cross-tension joint configurations of 384 steel to Al and Al to steel UCR joints. Sixty tests were completed at this writing. The remaining tests are expected be completed by the end of December, 2015. (FY15)

Introduction:

The UPJ process, shown conceptually in Figure 1, is similar to heat staking of plastic components. The simplest form of the process uses a cast-in protrusion on a die cast component, which is aligned with a clearance hole in a mating component. An application of force and heat are used to upset forge the protrusion into a larger diameter boss that fills the clearance hole and forms a mushroom-shaped head that solidly locks the two components together.

Die casting is the most common and cost-effective process for producing lightweight Mg components. The UPJ process was conceived primarily for joining Mg die-castings to each other and for joining Mg die-castings to dissimilar metals. However, prior to this study there has been relatively little work, other than bolting, aimed at joining components produced from this process.

Alternative dissimilar metal joining processes have been investigated with varying levels of success, however galvanic corrosion has consistently been demonstrated to be a key challenge. Particularly:

- Metallic bonding such as fusion or solid state welding processes, which require a clean (either no coatings, or a specific coating designed to improve intermetallic bonding rather than corrosion performance) surface on both metals and does not allow for any isolation between the two metals.
- Fasteners (e.g., rivets or bolts), which are typically made of steel for high strength and low cost tend to promote galvanic corrosion in Al and aggressively promote galvanic corrosion in Mg. The galvanic activity is increased if one of the two light metals is joined to a steel component. Coatings intended for corrosion protection on steel fasteners tend to get damaged during the installation process. Fasteners also typically damage coatings on the components being joined. One result is that the preliminary coatings are rendered useless since the galvanic isolation has been broken. Another result is that the galvanic attack on the anode can be magnified if a small defect is created in the anode coating. Figure 2 shows an example of this magnified galvanic attack where coated steel screws were driven into a coated magnesium component and then exposed to a corrosive environment.

The UPJ process, by contrast, relies on a robust mechanical joint rather than intermetallic bonding, so the more cathodic material can be coated prior to joining to protect against galvanic attack on the more anodic material. Additionally, since the UPJ protrusion is going through a hole that can be pre-drilled or pre-punched prior to coating, the UPJ process is much less likely to damage the coating when the joint is being made. Furthermore, there is no joining-induced galvanic activity beyond that between the two parent materials since no additional cathodic material (such as a steel fastener) is used to create the joint.

Approach:

The project technical approach is summarized as follows:

- Establish the benchmark performance of magnesium to aluminum joints produced through SPR, a currently available commercial process, for comparison purposes only.
- Obtain additional knowledge and understanding of thermo-mechanical behavior of magnesium alloys through Gleeble® testing conducted in Canada at no cost to the U.S. Department of Energy (DOE).
- Supplement existing FCA UPJ process knowledge with computer-aided engineering forming simulation results based on knowledge gained through the Gleeble® testing. Use this information to develop optimized cast protrusion and welding electrode shapes to reduce electrical current requirements and provide more robust, repeatable forming performance for each of the joint configurations being considered.
- Evaluate all material configurations (e.g., AM60B to Al6022, Al6013, and high-strength steel [HSS] materials in bare, pretreated, and coated conditions for round and oval shaped joints). For each configuration, produce tensile shear and cross-tension test coupons. Apply additional coating layers to select joint configurations prior to the mechanical/structural and corrosion evaluations.
- Subject five samples of each configuration to the initial mechanical/structural tests described above.
- Subject a substantial number of samples to FCA's accelerated corrosion tests, reviewing visually every two weeks and removing three samples of each configuration at four week intervals for quasi-static testing.
- Finally, at the end of the twelve-week accelerated corrosion exposure, subject select configurations to fatigue and impact testing for comparison to pre-corrosion performance.

Validate the joint performance through:

- Characterization of material microstructure in the joint region.
- Characterization of joining-induced defects in the joint region.
- Quasi-static tensile shear tests.
- Quasi-static cross-tension tests.
- Drop tower impact tests of select tensile shear and cross-tension samples.
- Cyclic fatigue testing of select tensile shear and cross-tension samples.
- FCA's twelve-week accelerated corrosion test (ASTM G85-A2) with quasi-static lap shear failure and cross-tension failure being evaluated after each 4-week increment, and fatigue testing and impact testing to be re-evaluated on select samples at the end of corrosion exposure.
- Characterization of failure mechanisms for each of the mechanical tests described above.

Results and Discussion:

This report focuses on results of UPJ and UCR joint process development and joint performance testing. A comparison of round boss UPJ joint performance to the benchmark SPR joint performance (reported in the FY 2014 annual report) is also included.

The team developed optimized round boss UPJ boss and head geometries. The team also developed process parameters to facilitate production and testing of a substantial number of unique joint configurations. The configurations discussed in this report are defined below in Table 1.

Figure 3 shows several round boss head formations produced with Al, Mg and steel top sheets in bare, pre-treated, and coated configurations. It can be seen that well-formed, crack-free head formations were produced for all of these material and coating configurations.

Figure 4 shows two examples of round boss UPJ joint cross-sections. Figure 4(a) shows a section through a Mg to steel joint while Figure 4(b) shows a section through a Mg to Al joint. There is no evidence of cracking or porosity in either of these joints. The boss expanded to completely fill the clearance hole in the top sheet while the head shape is well-formed and provides a substantial overlap to the joined sheet material to produce high cross-tension joint strength.

Figure 5 shows quasi-static and impact lap shear tension testing results of samples using seven different coating configurations. The different coating configurations were not expected to show any substantial performance difference in these pre-corrosion mechanical/structural tests. However, it should be noted that UPJ8-1 and UPJ8-3 are Mg-steel joints and are expected to show slightly higher strength than Mg-Al joints. UPJ8-6 is a powder coated assembly, which may have experienced an increase in joint strength as a result of the paint bake temperature cure of the Al-6013 material. The three impact configurations performed as expected with UPJ8-1 (Mg-steel) displaying higher strength than UPJ8-2 (Mg-Al), which is in turn higher than UPJ8-7 (Mg-Mg).

Figure 6 shows the quasi-static and impact cross-tension testing results. There are no unexpected results in this study. The Mg-steel joints (UPJ8-1 and UPJ8-3) again show slightly higher joint strength levels than the Mg-Al and Mg-Mg joints.

Figures 7 and 8 show lap shear tension and cross-tension fatigue testing results of 8 mm round boss joints for Mg-steel, Mg-Al, and Mg-Mg joints. The Mg-steel joints are shown in red, the Mg-Al joints are shown in blue, and the Mg-Mg joints are shown in green. It is notable that the Mg-steel joints showed greater high cycle fatigue strength than the Mg-Al and Mg-Mg joints despite the fact that all high cycle joint failures occurred in the die cast Mg bottom plate. This result shows that the high-cycle fatigue strength could be affected by the overall joint stiffness.

Figure 9 shows results of bare Mg to bare Al6013 joints that separated after 8 weeks (~1,350 hours) of exposure to FCA's ASTM G85-A2 accelerated corrosion procedure. This is a cyclic salt spray test with the addition of acetic acid. Although galvanic attack of the Mg sheet by the Al sheet was expected to be the source of failure for this combination, the actual source of failure turned out to be exfoliation corrosion of the Al6013 alloy. This alloy contains more copper than most conventional automotive Al alloys, so it is very sensitive to acidic environments such as that experienced in the FCA corrosion procedure. Figure 10 shows more extensive exfoliation corrosion and more extensive joint damage of Mg-Al 6013 joints after 12 weeks (~2,000 hours) of exposure.

Figure 11 shows results of Mg-steel joints that separated after less than eight weeks of accelerated exposure. In this case, the failure mode was as expected (galvanic attack from the steel to the Mg sheets) but slightly more severe. The photos show that crevice corrosion around the edges of the joints is the biggest challenge. Even the combination of galvanizing, e-coating, and sealing around the edges was not sufficient to prevent the corrosion damage. Although this is a very severe test and may not be reflective of performance in the field, these results do indicate that a complete top coating of the steel panel (prior to joining to Mg), followed by extensive precautionary sealing and coating of the full assembly may be advisable.

Quasi-static lap shear test results for round boss UPJ joints are shown in Figure 12 both prior to corrosion testing and after four-, eight-, and twelve-weeks of accelerated corrosion exposure. For reasons cited in the previous paragraph, none of the Mg-steel joints (UPJ8-1 and UPJ8-3) remained intact after 8-weeks. All of the coated Mg-Al configurations (UPJ8-4, UPJ8-5, and UPJ8-6) maintained good joint strength performance even after 12-weeks of accelerated corrosion testing exposure. For comparison, the uncoated (bare) Mg-Al configuration (UPJ8-2) remained intact but exhibited lower overall joint strength. Cross-tension test results showed similar performance retention to the lap shear tension tests after corrosion testing.

Comparisons of quasi-static lap shear tensile test and cross-tension test results for round boss UPJ joints and benchmark SPR joints are shown in Figures 13 and 14 prior to accelerated corrosion exposure, and after four-wks, eight-wks, and twelve-weeks of exposure. The benchmark SPR data was presented in the previous annual report but is repeated here to facilitate a comparison with the round boss UPJ joints. When viewing these figures, note that UPJ8-2 and SPR1 are both bare Mg to bare Al joints; UPJ8-4 and SPR2 are pretreated Mg to pretreated Al with the whole assembly being powder-coated; UPJ8-5 and SPR3 are pretreated Mg to powder-coated Al; and finally UPJ8-6 and SPR4 are pretreated Mg to powder-coated Al with the whole assembly being powder-coated after assembly.

The figures indicate substantially higher levels of joint strength were achieved for all UPJ configurations (primarily a function of geometry in this case). However, the real purpose of this comparison was to evaluate the performance retention after corrosion exposure. Both SPR and UPJ joints performed reasonably well when the Mg was pretreated and the Al was powder-coated (SPR3, SPR4, UPJ-5, and UPJ-6). Even so, there were two rivet fractures in the SPR3 configuration. Both the SPR and UPJ joints failed to survive twelve-weeks of exposure in the bare Mg to bare Al configurations (SPR1 and UPJ2). The configurations with the greatest distinction between similar UPJ and SPR configurations were SPR2 and UPJ8-4, where both the Mg and Al samples were pretreated and the assembly was powder-coated after assembly. In this configuration, there were multiple rivet fractures in the SPR joints at eight-weeks. This resulted in no SPR samples surviving to twelve-weeks of exposure. Only two UPJ joints of this configuration failed before reaching twelve-weeks exposure.

The team also developed optimized joint geometries and process parameters for oval boss configurations. Figure 15 shows three oval boss UPJ head formations that resulted from increasing temperature and force. The superimposed yellow oval indicates the top sheet clearance-hole shape. As the head formation was squeezed harder to improve the coverage over the clearance hole, the head shape deviated further from the original oval proportions and began to approach a circular shape. While this did not significantly affect joint strength, it did limit the ability of the oval boss joint design to enable the use of narrower joint flanges.

Figure 16 shows metallurgical cross sections for oval boss Mg-Al UPJ joints. The sections shown along the top row are cut through the transverse axis while the sections along the bottom row are cut through the longitudinal axis. These sections illustrate the substantial difference in overlap to a clearance hole in the top sheet in longitudinal and transverse directions resulting from the tendency of the oval joints to tend closer to round as they are deformed.

Figure 17 shows quasi-static joint performance comparisons between oval boss joints and 8-mm round boss Mg to steel joints. Lap shear tension joint strength is significantly higher for the oval boss joints than the round boss joints, primarily as a result of the shear area of the oval boss joints being substantially larger than the round boss joints. In the case of cross tension testing, the strength of these joints is known to be highly correlated to the stiffness of the top sheet and the strength of the UPJ head, so the cross sectional area of the boss does not have such a great effect as it does for lap shear tension.

Finally the team optimized electrode geometry and force/current application for UCR joints for steel to Al joints using CAE simulation tools and physical experimentation. After evaluating over twenty unique rivet and electrode concepts through computer simulations, the ultimate rivet and electrode geometry wound up being very similar to the optimized UPJ boss and electrode geometry. Figure 18 shows the head form of four unique material/coating configurations while Figure 19 shows the metallographic cross sections of five samples of one of these configurations, which was typical for all four configurations. Clearly all of these configurations can be produced with good quality head formations with very little cracking. The figure also shows that the rivet expands to fill the clearance holes even when they are misaligned.

Figure 20 shows initial lap shear and cross tension test performance of four UCR Al-steel joint configurations (the rivet is Mg AM60B). The red bars indicate lap shear performance while the blue bars indicate cross-tension performance. The chart on the left shows results for joints of 1.4 mm thick steel sheet to 1.3 mm thick Al6016 sheet. The chart on the right shows results for joints of 1.0 mm thick steel sheet to 1.3 mm thick Al6016. The results are quite interesting in that the lap shear tension results for the joints with the thicker steel sheet are slightly lower than those for the joints with the thinner steel sheet. A review of the failure modes shown in Figure 21 indicates that the reason for this unusual result may be related to the fact that bending of the thinner steel sheet results in an entirely different failure mode.

Technology Transition Path:

Two of the key obstacles preventing more widespread use of light metals in high volume automotive applications are lack of robust joining techniques (especially for dissimilar metal joining) and susceptibility to galvanic corrosion. Successful completion of this project will provide a key enabler to high volume application of lightweight materials. This will allow FCA (and ultimately other manufacturers) to accelerate the development of new lightweight vehicle designs that utilize multiple lightweight materials in order to aggressively reduce mass on future vehicle programs.

Conclusions:

During FY15, the team has demonstrated UPJ to be capable of providing good, repeatable joints in several material/coating configurations and boss geometry configurations. Extensive thermo-mechanical material characterization, modeling/simulation, and physical experimentation were used to optimize the process parameters for round boss UPJ joints. A full test matrix of over 350 round boss UPJ joints were produced and evaluated for mechanical/structural performance, and were subjected to FCA's accelerated corrosion exposure, and were compared to the benchmark SPR process. Neither UPJ or SPR passed the full corrosion test in the bare Mg to bare Al combination. However, UPJ showed significant improvement over SPR for at least one of the coated joint configurations. It also had improved lap shear strength and dramatically improved cross-tension strength in all configurations.

Additionally, oval joint UPJ joining processes were developed for use on narrow flange applications. These joints displayed improved joint strength over round boss UPJ due to increased boss shear area, but did not offer quite the level of reduced flange width capability as anticipated due to a tendency of the head formations to veer away from oval and toward round.

UCR joining processes have also been developed for joining dissimilar metals where neither metal is cast Mg. These joints have shown exceptionally good formation with very little to no cracking tendencies.

References:

- None

Remainder of Page Intentionally Blank

Figures and Tables:

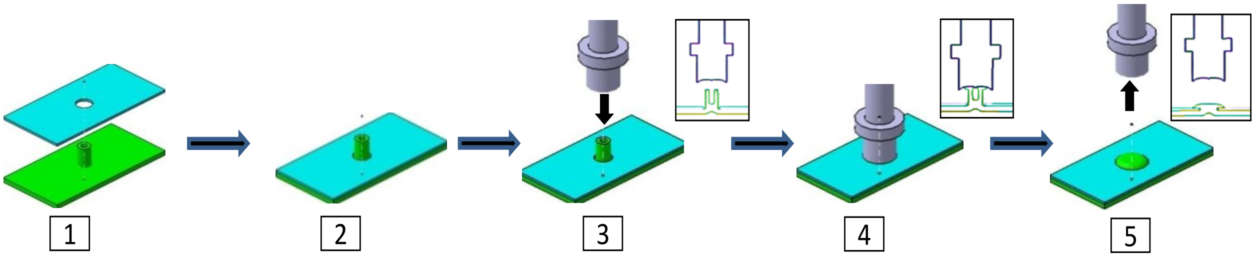

Figure 1. Initial conceptual schematic of UPJ process – assembling parts, applying heat and force, assembly complete.

Figure 2. Galvanic corrosion effects of steel screws in a magnesium component exposed to 240 hours of ASTM B117 salt spray testing.

Configu-ration Number	Upper Sheet			Bottom Sheet			Assembly Coating Configuration
	Material	Thickness (mm)	Coating	Material	Thickness (mm)	Coating	
UPJ8-1	HSS DP-590	2.0	Galvanized	Mg AM60B	4.0	Pretreated	Uncoated
UPJ8-2	Al 6013-T4	2.2	Bare	Mg AM60B	4.0	Bare	Uncoated
UPJ8-3	HSS DP-590	2.0	Galvanized	Mg AM60B	4.0	Pretreated	Powdercoated
UPJ8-4	Al 6013-T4	2.2	Pretreated	Mg AM60B	4.0	Pretreated	Powdercoated
UPJ8-5	Al 6013-T4	2.2	Powdercoated	Mg AM60B	4.0	Pretreated	Uncoated
UPJ8-6	Al 6013-T4	2.2	Powdercoated	Mg AM60B	4.0	Pretreated	Powdercoated
UPJ8-7	Mg AM60B	2.0	Bare	Mg AM60B	4.0	Bare	Uncoated

Table 1: Round Boss UPJ material and coating configurations

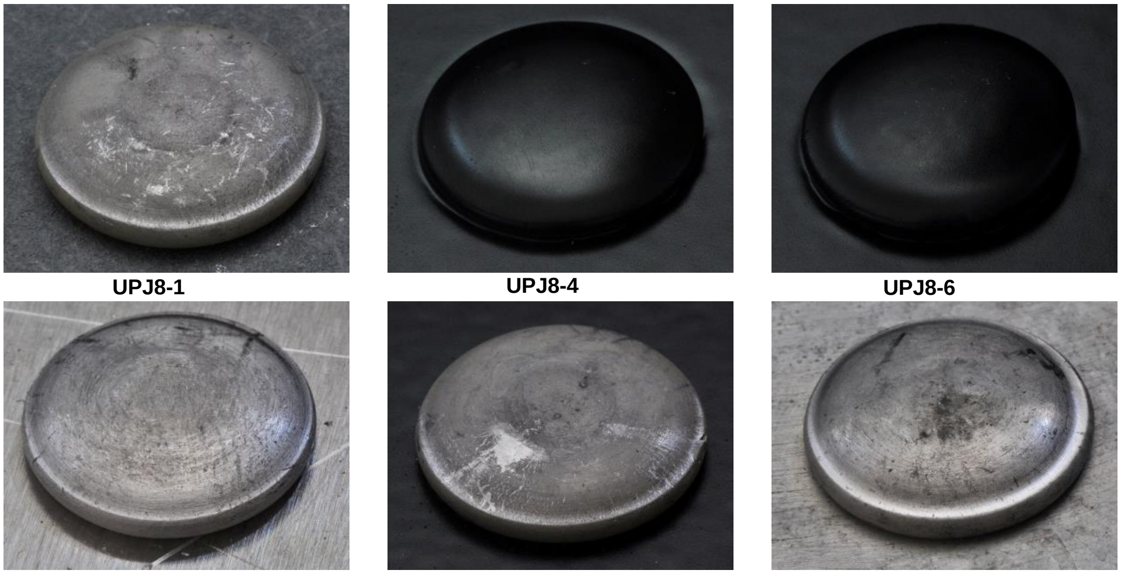

UPJ8-1 **UPJ8-4** **UPJ8-6**

UPJ8-2 **UPJ8-5** **UPJ8-7**

Figure 3. Round boss UPJ head formations.

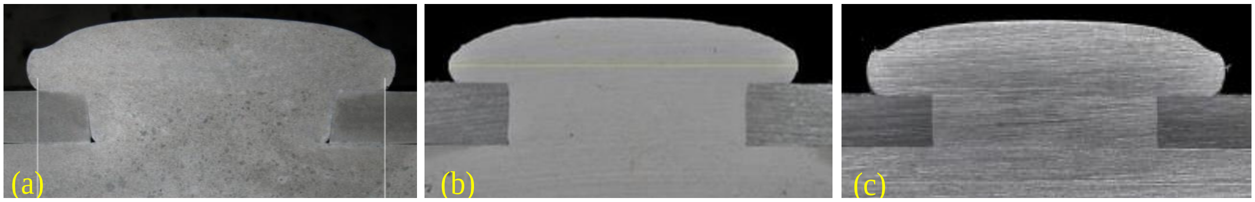

Figure 4. Metallurgical cross-sections of round boss UPJ joints.

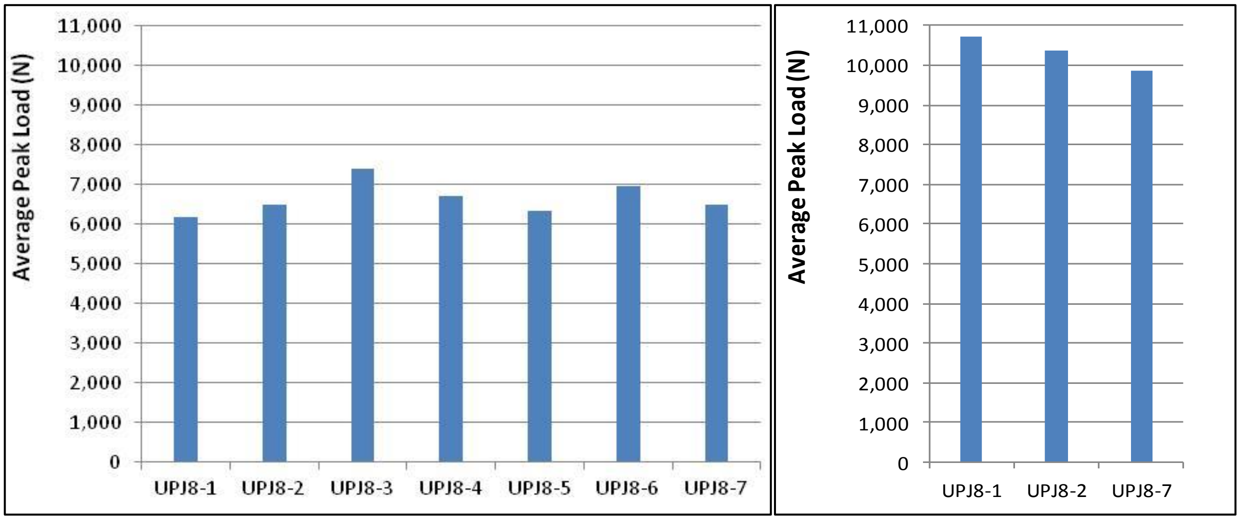

Figure 5. Round boss UPJ quasi-static (left) and impact (right) lap shear test results.

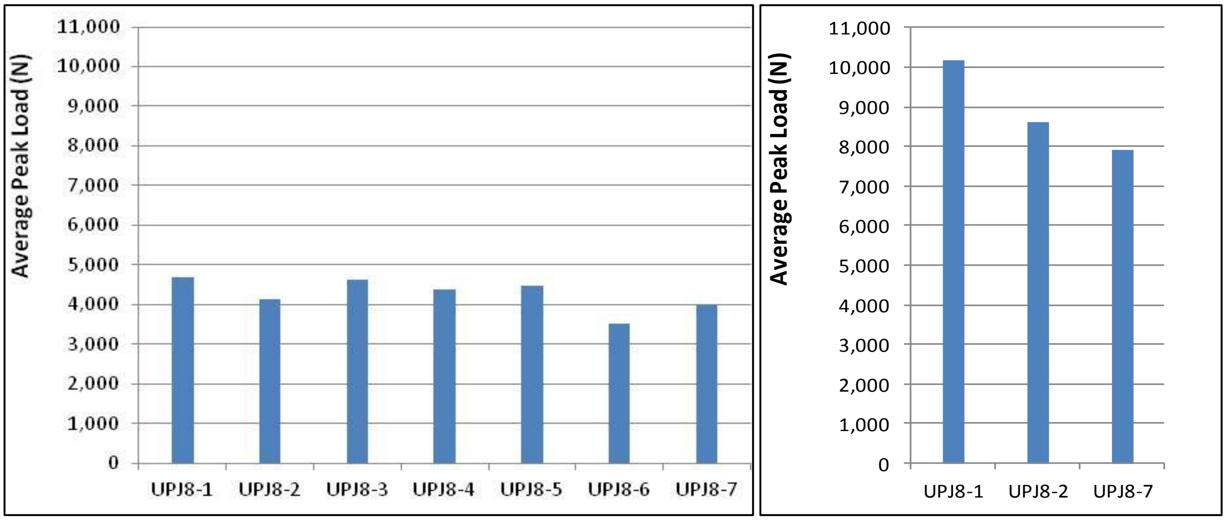

Figure 6. Round boss UPJ quasi-static (left) and impact (right) cross tension test results.

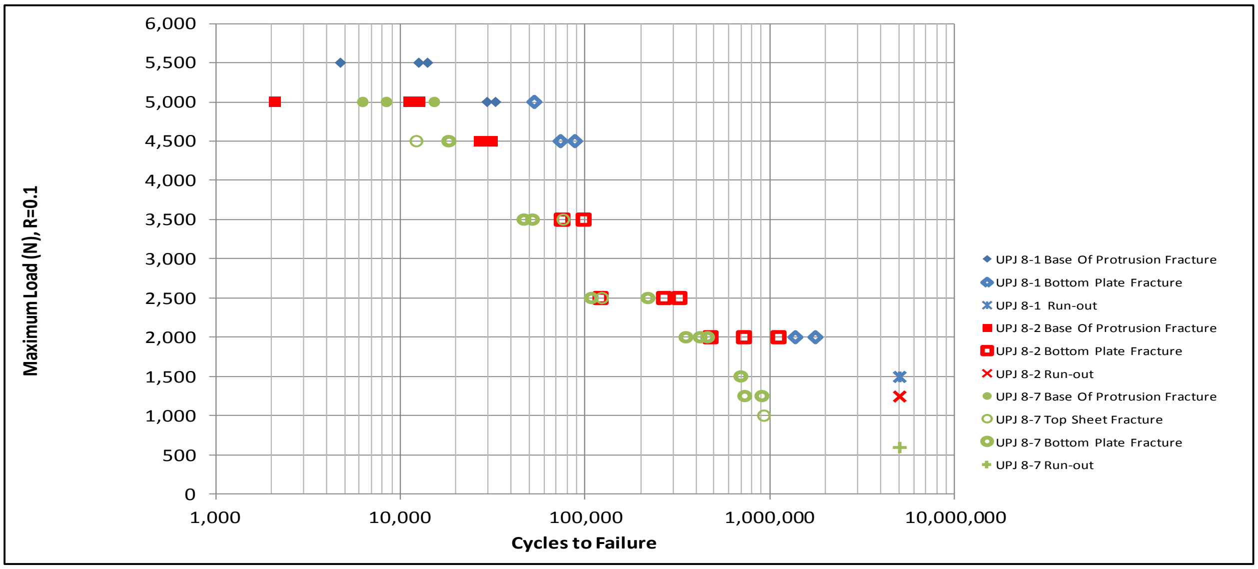

Figure 7. Round boss UPJ lap shear fatigue curves.

Remainder of Page Intentionally Blank

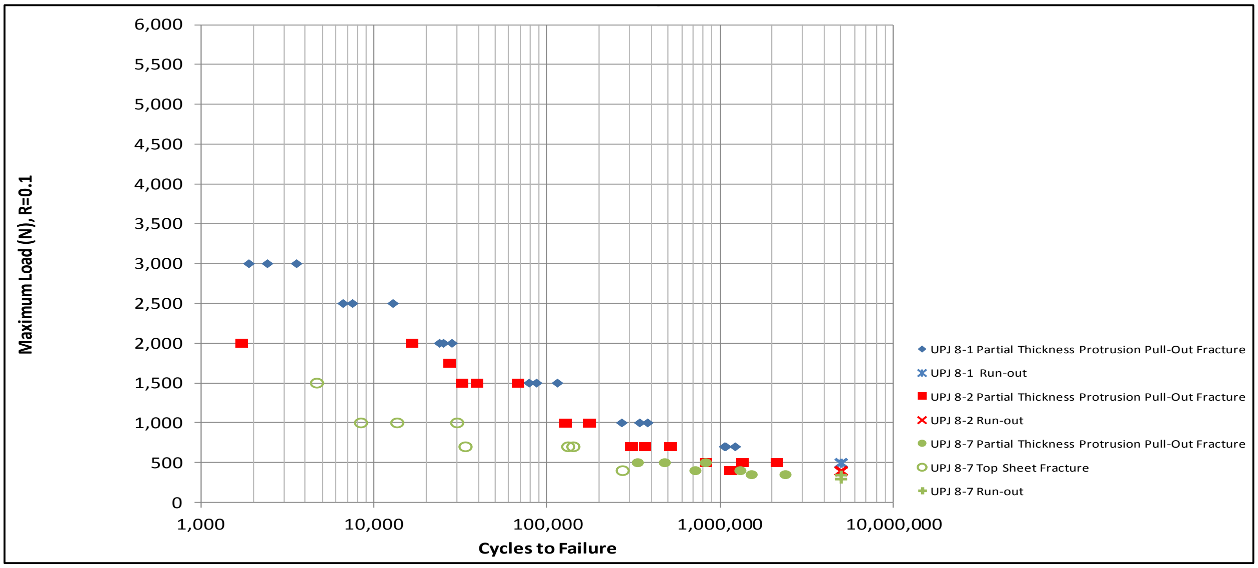

Figure 8. Round boss UPJ cross-tension fatigue curves.

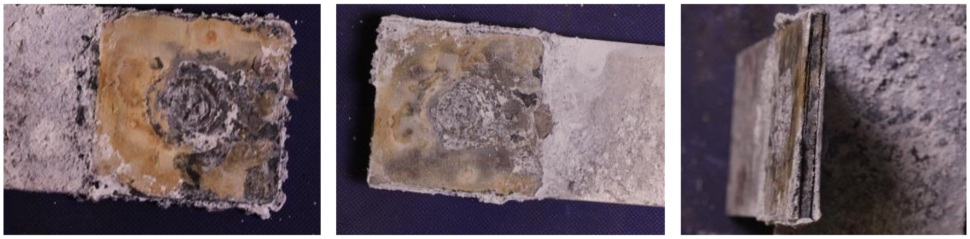

Figure 9. UPJ8-2 (bare Mg to bare Al6013) after eight-weeks of accelerated corrosion exposure.

Figure 10. UPJ8-2 (bare Mg to bare Al6013) after twelve-weeks of accelerated corrosion exposure.

Remainder of Page Intentionally Blank

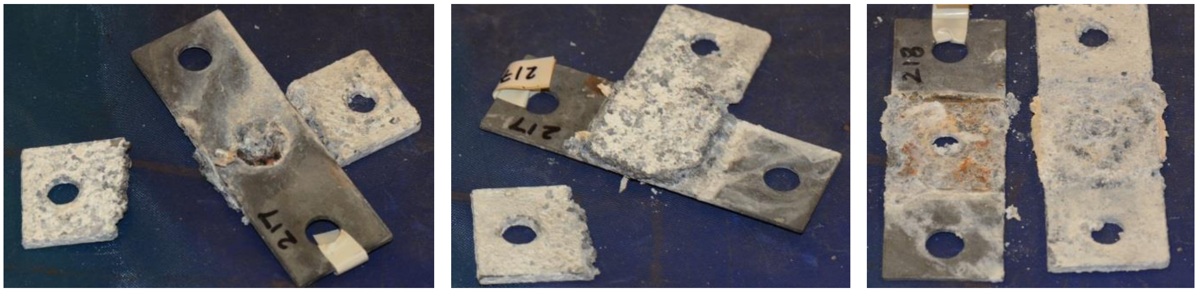

Figure 11. UPJ8-1 (Mg-steel) after eight-weeks of accelerated corrosion exposure.

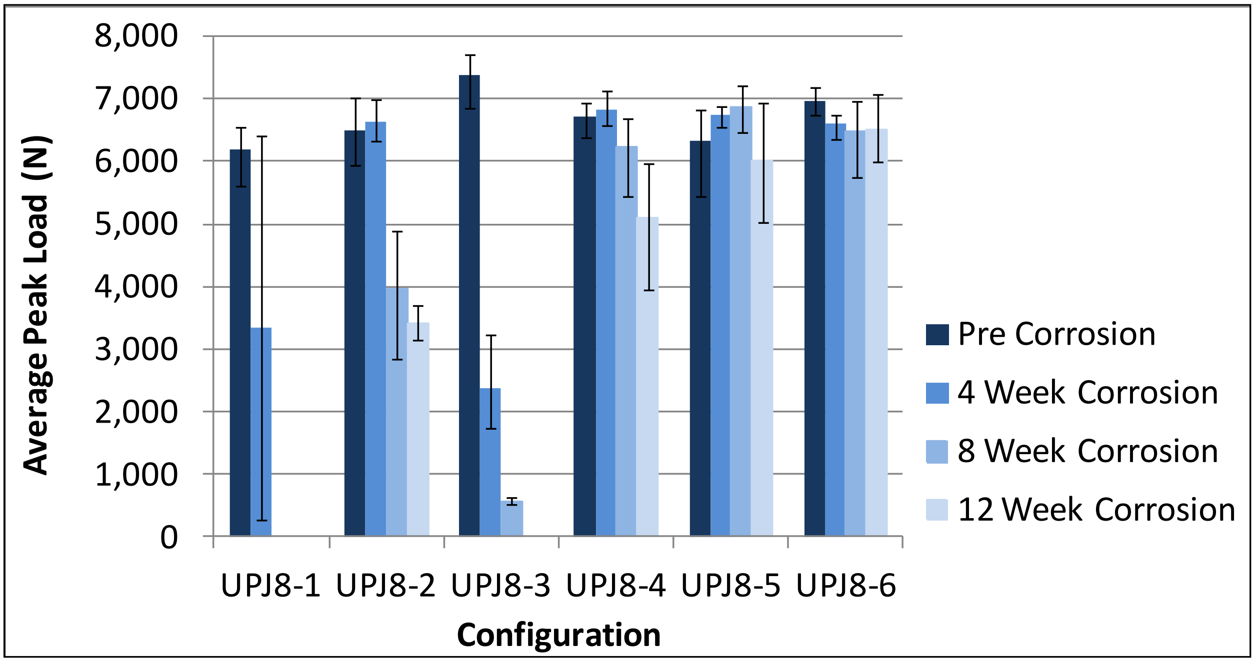

Figure 12. Round boss UPJ lap shear tension performance prior to corrosion testing and at four, eight, and twelve-weeks of accelerated corrosion exposure.

Remainder of Page Intentionally Blank

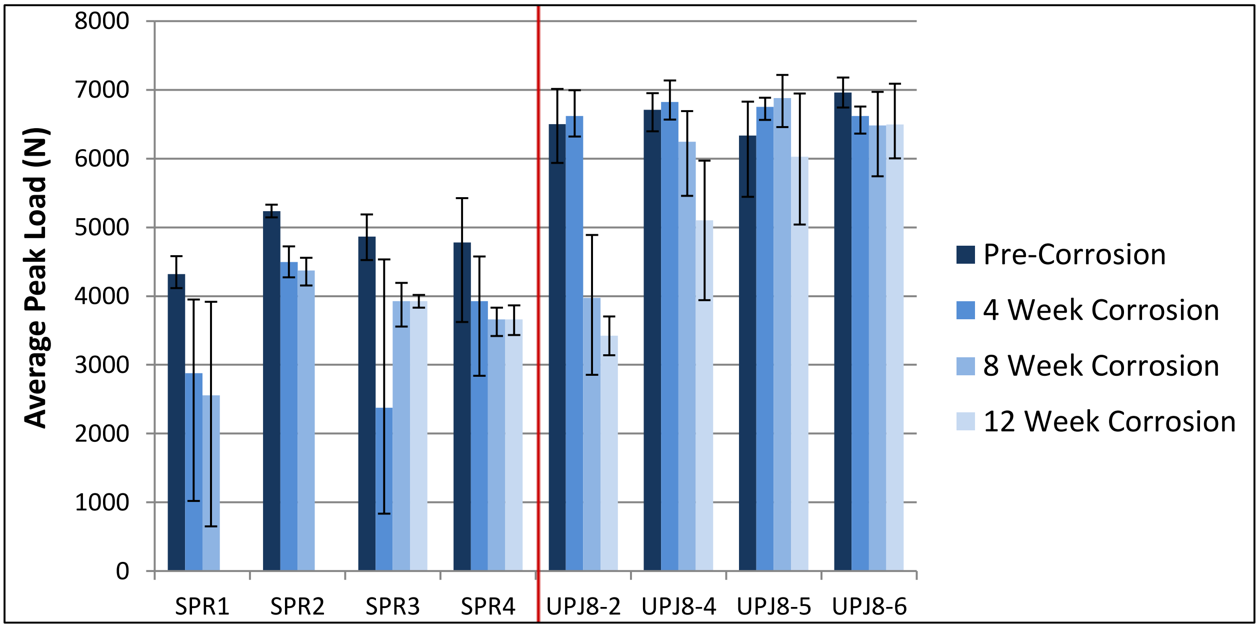

Figure 13. Round boss UPJ lap shear tension performance comparison to benchmark SPR joints prior to corrosion testing and at four, eight, and twelve-weeks of accelerated corrosion exposure.

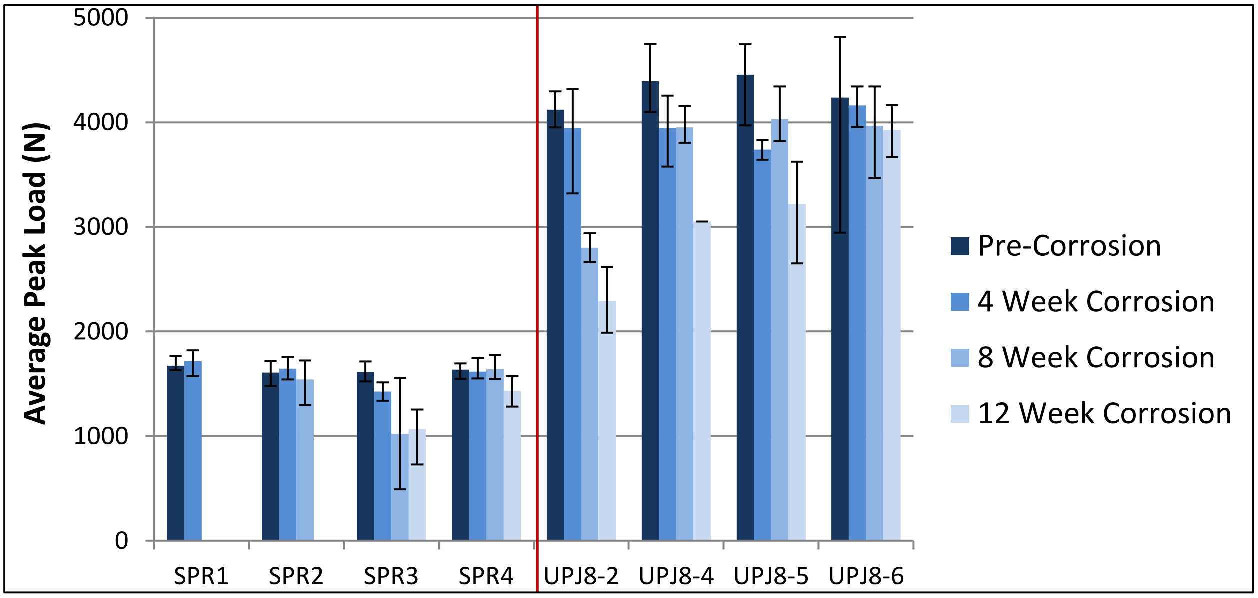

Figure 14. Round boss UPJ cross tension performance comparison to benchmark SPR joints prior to corrosion testing and at four, eight, and twelve-weeks of accelerated corrosion exposure.

Remainder of Page Intentionally Blank

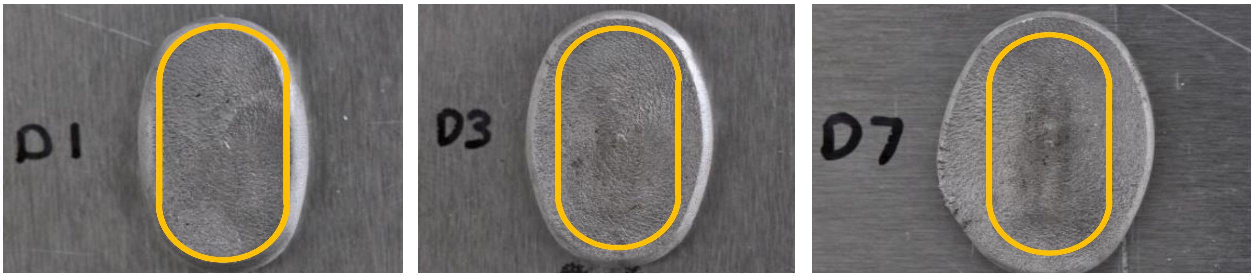

Figure 15. Effect of increasing force and temperature on oval boss UPJ head shape and size.

Figure 16. Metallurgical cross-sections of oval boss UPJ joints through the transverse axis (top) and the longitudinal axis (bottom).

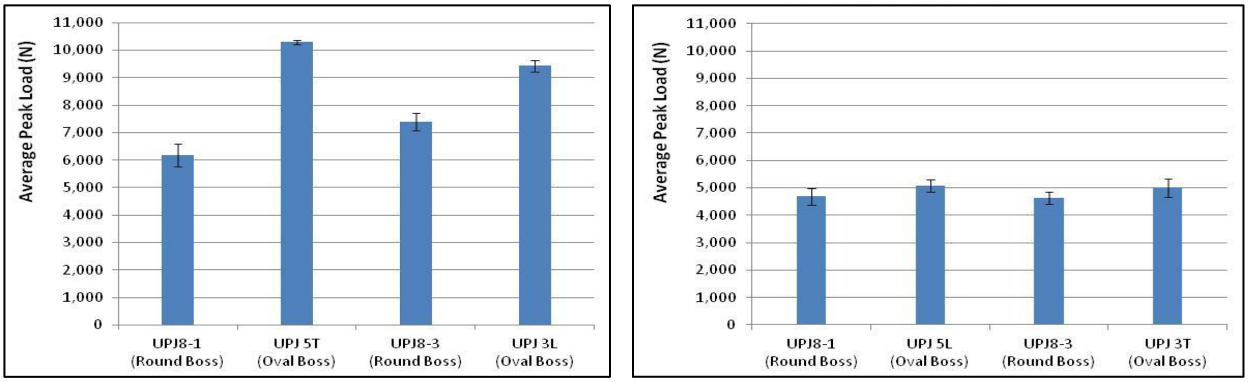

Figure 17. Comparison of oval boss joints to 8-mm round boss Mg-steel joints in quasi-static lap shear tension (left) and cross tension testing (right).

Remainder of Page Intentionally Blank

Figure 18. UCR head formations for four unique material/coating configurations.

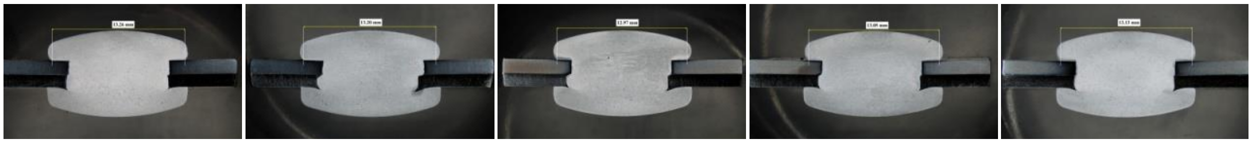

Figure 19. Metallographic cross-sections for a typical UCR material/coating configuration.

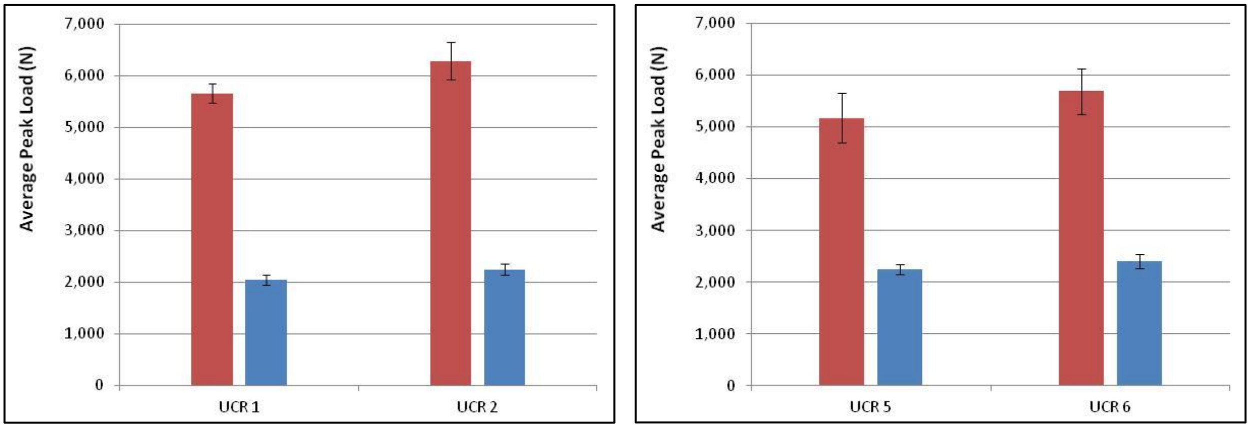

Figure 20. UCR initial quasi-static lap shear and cross tension test results for 1.4 mm steel to 1.3 mm Al (left) and 1.0 mm steel to 1.3 mm Al (right).

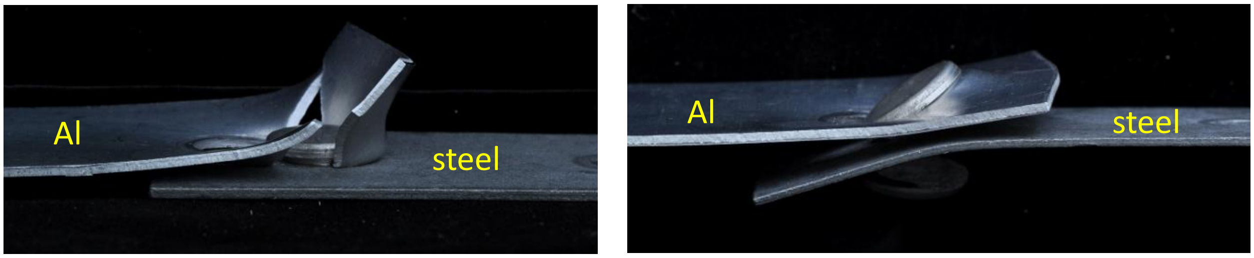

Figure 21: UCR initial quasi-static lap shear and cross-tension failure modes for 1.4 mm steel to 1.3 mm Al (left) and 1.0 mm steel to 1.3 mm Al (right).

AVPTA Technology Focus Area 2: Lightweight Structures & Materials

Breakthrough Techniques for Dissimilar Material Joining – Active, Tailorable Adhesives for Dissimilar Material Bonding, Repair and Reassembly

DOE-VTO TFA Lead: Sarah Ollila
TARDEC TFA Lead: Martin McDonnell

Principal Investigator:
Mahmoodul Haq

Michigan State University (MSU)
428 S. Shaw Lane, Room 3569
Engineering Building,
East Lansing, MI 48824.
Phone: (517) 402-3409
E-mail: haqmahmo@egr.msu.edu

with
Lawrence T. Drzal
428 S. Shaw Lane, Room 3569
Engineering Building,
East Lansing, MI 48824.
Phone: (517) 353-5466
E-mail: drzal@egr.msu.edu

Start: Q1FY14
Projected Completion: Q4FY16

Objective:

- To demonstrate the feasibility of ‘active adhesive’ technology for structural joining of dissimilar materials, with the ability to dis-assemble/re-assemble and repair while in-service cast magnesium (Mg) component.

Strategic Context:

- The immediate application target is the Combat Vehicle Prototype (CVP).
- The technology supports the TARDEC Strategy enabling new capability in cost and technically effective joining of dissimilar materials including the potential for joint disassembly.

- Follow-on activities may include further AVPTA interest to investigate increasing joint strength, reducing cost and / or developing adhesives for other material combinations.
- TARDEC-specific follow-on will depend upon project success but is expected to include joint ballistic shock evaluation.

Accomplishments:

- Successful development of ‘active adhesives’ films comprising of pristine (non-functionalized) and functionalized graphene nanoplatelets (FY15).
- Experimental characterization of tensile properties of functionalized active adhesive completed (FY15)
- Successful proof-of-concept of ‘activation’, i.e. effective bonding and debonding of composite adherends using variable frequency microwave (VFM). (FY15)
- Evaluated the tensile behavior of active adhesives under varying temperature conditions; room temperature 25^{o}C (75^{o}F), 100^{o}C (212^{o}F) and 177^{o}C (350^{o}F). (FY15)
- Developed numerical simulations to obtain effective properties of novel adhesives and structural behavior of resulting joints. (FY15)

Introduction:

The objective of the project is to demonstrate the feasibility of the proposed active adhesive technology for structural joining of dissimilar materials, with the ability to dis-assemble/re-assemble and perform in-service repair. The outcomes of this work will accelerate the development of efficient active adhesive technology to join multi-material lightweight structures in different sectors, such as automotive, aerospace, and marine applications.

Thermoplastic adhesives modified by the incorporation of electrically conductive graphene nanoplatelets at a concentration above the percolation point provide a unique synergy of mechanical, thermal and electrical properties. While the choice of the thermoplastic is governed by the desired application, the addition of the graphene nanoplatelets allows energy to be deposited primarily in the adhesive. The percolated network of graphene particles in the adhesive at less than 2 wt% can quickly couple to ultra-high frequency (UHF) microwave (□W) radiation via non-contact methods and increase the adhesive temperature to above the required processing temperatures. The adhesive melts and flows over the adherends and, upon cooling, forms a structural adhesive bond. Furthermore, the process can be used to disassemble the adhesive joint if repair or reworking is required. A schematic of the proposed technology and the overall approach is provided in Figure 1. To the best of the investigators’ knowledge, such active adhesives with repeatable healing/repair and facile disassembly are unique and have not been used in structural joining, and offer a possibility in a wide range of applications.

Approach:

Thermoplastic adhesives modified by the incorporation of electrically conductive graphene nanoplatelets at a concentration above the percolation point provide a unique synergy of mechanical, thermal and electrical properties. While the choice of the thermoplastic is governed by the desired application the addition of the graphene nanoplatelets allows energy to be deposited primarily in the adhesive. The percolated network of graphene particles in the adhesive at less than 2 wt% can quickly couple to Ultra-High Frequency (UHF) Microwave (MW) radiation via non-contact methods and increase the adhesive temperature to above the required processing temperatures. The adhesive melts and flows over the adherends and upon cooling forms a structural adhesive bond. Furthermore, the process can be used to disassemble the adhesive joint if repair or reworking is required. A schematic of the proposed technology and the overall approach is provided in Figure 1. To the best of the investigators knowledge, such active adhesives with repeatable healing/repair and facile disassembly are unique and have not been used in structural joining, and offer a possibility in a wide range of applications.

Most structural joints development studies focus solely on in-plane behavior. This work evaluates the feasibility of proposed technique in: a) in-plane (lap-joints), (b) out-of-plane (3D-woven Pi/T-joints), and c) torsional/rotatory (super-charger) joints. Measurement techniques such as embedded fiber-Bragg optic sensors and infrared thermography will be used to accurately measure the in-service performance and observe the repair efficiency of resulting dissimilar material joints. Such a thorough study is directed to cover all possible automotive and ground vehicle applications.

The above mentioned approach of developing ‘active adhesives’ will be achieved through the following sub-objectives/tasks:

A. Processing, Material Development and Optimization of the Active Adhesives:
B. Lab-Scale Evaluation & Detailed Material Characterization:
C. Design, Testing and Applications:

The detailed sub-tasks for the aforementioned categories were provided in FY14 annual report [1] and for brevity not included in this report.

Processing of ‘Active’ (GnP modified) Adhesives:

In this work, nylon-6 was selected as the thermoplastic material. The choice of thermoplastic depends on the desired application, and instead of studying multiple thermoplastics a single adhesive was selected. The processing of thermoplastics with GnP and associated experimental characterization can be directly extended to other thermoplastics. In this work, a melt extrusion process was used to blend GnP into nylon-6. The nylon-6 pellets were exposed to 70°C for four hours to eliminate any presence of moisture. Then, melt extrusion of pristine and GnP-modified nylon-6 was carried out in a DSM Micro 15 cc Compounder, (vertical, co-rotating, twin-screws micro-extruder) operating at 260°C for 3 min at a screw speed of 100 rpm. The melted material was then directly transferred in to a Daca Micro-injector with the $T_{barrier}$=260°C and T_{mold}=100°C. The injection pressure applied for injection molding of tensile, impact, flexural coupons and discs was around 0.97 MPa. The resulting injection molded samples were used for experimental testing and the discs were used for adhesive film production.

The discs from the injection molded specimens were placed between stainless steel plates covered by a high-temperature resistant polyimide film, Kapton® (DuPont®) to enable ease of adhesive film removal. To control/maintain the adhesive film thickness, 0.09 mm thick aluminum spacers were placed between the top and bottom plates. To eliminate/reduce entrapped air, the entire setup was covered by a vacuum bag and subjected to vacuum pressure of one atmosphere. While maintaining the vacuum pressure, the plates were heated at a rate of 5°C/min up to 260°C, followed by an isothermal process for 5 min. In order to obtain the desired film thickness, successive pressures of 30, 60, and 90 MPa were applied to the plates with a time interval of 3-5 min. Additional spacers were placed in the center of the plates to ensure uniform adhesive thickness. The overall process is shown schematically in Figure 2.

Functionalization of GnP:

The enhancements in mechanical thermal and damage resistance properties offered by addition of GnP in polymers can be further enhanced by proper chemical functionalization, i.e., creating compatibility between the host polymer and GnP. In this work, three types of GnP functionalization were studied; aliphatic epoxy (AE), phase-separated carboxyl-terminated acrylonitrile butadiene rubber (CTBN), and styrene-butadiene-methyl-methacrylate (SBM) triblock. The grafting of the aforementioned functional groups to epoxy has found considerable enhancements in toughness and fracture resistance [2][3]. Similar work on thermoplastics is not explored elsewhere and hence studied in this work.

Material Characterization of 'Pristine' and 'GnP-modified Nylon-6:

Tensile and flexural tests were performed using a universal testing system (UTS) electro-mechanical equipment. A minimum of five specimens per case were tested and only the average values are reported. The tensile tests were performed according to ASTM D638. A 1000 lb. (454 kg) standard load cell attached to the UTS frame and external laser extensometer were used to measure applied force and resulting longitudinal strain, respectively. On the other hand, flexural tests (three-point bending mode) were performed according to the ASTM D770-10 on the same machine with a load cell of 100 lb. (45.4 kg). The dimensions of the samples for flexural tests were 62.7 mm ×12.24 mm×3.2 mm. The span length was set at 50.8 mm. The crosshead speed was calculated based on specimen geometry, according to ASTM standard, and was set at 1.27 mm/min. A linear variable differential transformer (LVDT) was used to measure the deflection in flexural tests. Impact resistance tests (Izod type) were carried out according to ASTM D256 standard test. The dimensions of the samples for impact resistance tests were 62.7 mm x 10.72 mm×3.91 mm cross-sectional area at the mid-notch.

Results and Discussion:

Tensile Behavior of GnP-modified Adhesives:

The enhancements in tensile, flexure and impact behavior due to pristine (non-functionalized) GnP in nylon-6 were reported in FY2014 [1]. For 5 wt.% GnP content, the flexural strengths and modulus improved by 10% and 30% respectively, while the tensile strengths reduce by ~15%. [1]. Figure 3 and Figure 4 provide the effect of functionalization on tensile modulus and strengths respectively. The experimental characterization of AE functionalized GnP was still in progress at time of the submission of this report and hence not included. The effect of functionalization is very clear from the observations of Figure 3 and Figure 4. CTBN modifications had adverse effects on both tensile modulus and strengths, while SBM modification showed enhancements in tensile modulus and minimal drop in strengths. The biggest advantage (and need) of functionalization is the improvements in toughness and resistance to fracture without sacrificing stiffness. Experimental characterization on toughness is in progress. Nevertheless, the enhancement in tensile stiffness along with equal or better tensile strengths (as seen in Figure 3 and Figure 4, for 3 wt.% and 5 wt.% SBM) shows that stiffness-toughness balance can be achieved using functionalized GnP. From earlier evidence in thermosets as seen by the authors [2,3], the fracture toughness should considerably increase due to the improved functionalization.

Temperature-dependent Tensile Behavior of GnP-modified Adhesives:

In order to understand the behavior of GnP modified adhesives at high temperatures, tensile tests were performed at three temperature states: a) room temperature 25 ^{o}C (75 ^{o}F), b) 100 ^{o}C (212 ^{o}F), and c) 177^{o}C (350 ^{o}F). All tests were performed in displacement control at a rate of 2 mm/min in a universal testing machine equipped with an environmental chamber at EATON research facility.

Figure 5 shows representative plots of high temperature tensile behavior corresponding to pristine nylon-6 (0 wt.%) and 3 wt.% GnP contents. The 1 wt.% and 5 wt.% GnP contents are not shown for clarity, plus the 3 wt.% response was found to be intermediate and bounded by the 1 wt.% and 5 wt.% responses. Figure 5a shows the entire tensile response while Figure 5b shows the linear regime depicting the stiffness variations. The pristine case (0 wt.%) for each temperature is shown in a solid line while the 3 wt.% is shown with a dotted line. As expected, the embedment of non-functionalized GnP in nylon-6 reduces the ductility while increasing the stiffness. As the temperature increased, the stiffness dropped considerably and the ductility increased. The increase in ductility is attributed to the increased ability of the polymer chains to move at higher temperatures. While considerable reduction in ductility was observed due to GnP reinforcement at room temperature, such a drastic reduction was not observed at higher temperatures. Instead a balance in stiffness-toughness was observed relative to pristine nylon for similar temperature.

Microwave-activated Joining: Assembly and Dis-assembly:

To demonstrate the concept of ‘selective activation’ of the GnP modified nylon-6 adhesive, the joints were exposed to microwave radiations using a variable frequency microwave (VFMW), model MC2100 supplied by Lambda Technologies, Inc. NC, USA. For bonding, the two adherends and GnP modified nylon-6 film were placed inside the VFMW cavity with quartz rods as dead-weights. Additionally, Teflon spacers were placed to maintain uniform adhesive thickness as the adhesive heats and flows during VFMW activation. Figure 6a and 6b show the schematics of the assembly and dis-assembly setup prior to microwave activation. Figure 7 describes the entire assembly/bonding procedure.

A fiber optic contact probe was attached to the bond-line region of assembly. An aluminum/quartz block weighing ≈200 g was used to provide hold down weight, the desired load balance that allows to bond (see Figure 7) and debond (see Figure 8) the joint. For bonding of the joint, three and four-step processes were used. For brevity, only the four-step process is described here: (1) ramp at 2 ^{o}C/s to 100^{o}C and hold for 1 min; (2) ramp at 1.5 ^{o}C/s to 115^{o}C and hold for 1 min; (3) ramp at 1 ^{o}C/s to 150 ^{o}C and hold for 2 min, and (4) ramp at 0.5 ^{o}C/s to 230 ^{o}C and hold for 4 min. For the de-bonding process a two-step VFM process was used: (1) ramp at 2 ^{o}C/s to 200 ^{o}C and hold for 1 s followed by (2) a ramp of 0.5^{o}C/s to 240^{o}C and hold for 1 min. The quartz rods were placed such that they create a cantilever/lift-off mechanism to de-bond the joint. Figure 8 shows the de-bonding setup and the actual test sample.

Quality Control and Measurement of Temperature in the Bond-line during Bonding and Debonding:

The temperature profiles of the substrate and the adhesive were recorded using both infrared and thermocouple sensors. Additionally, fiber-optic sensors were embedded in the adhesive to measure the temperature in the bond-line. Figures 8a and 8b show the temperature profiles of the adhesive during the bonding and debonding process for varying GnP contents in the adhesive film. As expected, the temperature profile within the bond-line changed with varying GnP content during both bonding and debonding. Specifically, as the GnP content increases, the higher the change in adhesive temperature was expected. This was clearly observed in the bonding process (Figure 9a) and not so distinct in the debonding process. This discrepancy is primarily attributed to the differences in the location of the temperature sensor as the opening gap increases during debonding and changes in the length of the cantilever portion in the current setup (Figure 8). Experiments currently in progress address this issue by carefully maintaining the location of the cantilever portion along with embedment of sensors in the adhesive at similar location for all samples.

Another expected observation was that the substrate would also heat up due to the interactions with microwave, but the hypotheses was to selectively heat just the adhesive. Figure 10 shows the increase in temperature of the substrates during the bonding process. The concentration shown in Figure 10 corresponds to the adhesive and not the substrate. As a result, the substrates seem to heat up more uniformly, independent of GnP content. Another observation is that the maximum temperature reached by the substrate was 200^{o}C whereas the adhesives reached higher than 200^{o}C (see figure 9a), indicating relatively better interaction of adhesives to microwaves. In all the above mentioned experiments, the microwave applicator was controlled by the temperature of the adhesive over a constant duration, and the power applied varied based on the feedback from the temperature probe. In this process, the substrate and the adhesive both heated up according to their dielectric properties. In order to better understand the selective heating of just the adhesive, instead of using temperature control, ‘constant power’ was selected to control the applicatior, and the temperature of the adhesive and substrate was measured, as shown in Figure 11. It was observed that at a power of 350 Watts or more, the adhesive heated up much rapidly than the substrate for the same duration. This indicates the possibility of selective activation of just the adhesive. Statistically significant experiments are in progress to validate this observation for a wide range of substrates.

Comparison of Lap-shear Properties: “Thermally bonded – convection oven” VS. “Microwave Assisted Bonding”:

In order to understand the efficacy of ‘active adhesives,’ lap-shear joints were tested from both the microwave assisted bonding process and the conventional thermally bonded process.

All parameters (processing, film thickness, GnP content, batch, testing conditions, etc.) were the same, except the bonding process. Figure 12 shows the comparison of the lap-shear strengths for varying GnP contents from the microwave –assisted and thermally bonded joints.

The lap-shear tests from both the microwave assisted and thermally bonded joints were expected to be similar. Interestingly, the microwave assisted joints showed much better performance. This could be due to several reasons. Firstly, the adhesive heats up relatively uniformly as it is activated by the microwave. In thermal systems, the heat is transferred via conduction from the substrates to the adhesives, and via convection through the edges of the adhesives. This leads to non-uniform heating of the adhesives and may be degrading the adhesive near the edges. Unfortunately, the edges are locations where the stress concentrations are maximum and this could affect the joint behavior significantly. Secondly, in microwave assisted heating, the substrate does not degrade as the adhesive is heated rapidly. This in-turn should increases the stiffness of the substrate and the joint, thereby increasing the load-transfer rate, and resulting strength of the joint. Statistically significant testing along with embedded sensors and NDE tests are currently in progress to further validate the observed results. Overall, the results are very promising and further prove the concept and the possibility of a wide range of applications.

Numerical Solutions:

Finite element (FE) based numerical simulations were performed to obtain the effective properties of novel adhesives and to study the structural behavior of resulting joints. The effective properties of the adhesives such as modulus taking into account due to variation in GnP content, its morphology and random distribution was obtained through numerical homogenization using FE based unit cells as reported in FY2014 report [1]. The structural simulation of a lap-joint was performed using a commercial finite element software ABAQUS. The material properties of the substrate and the adhesives input in the software were experimentally obtained. Figure 13 shows a typical peel stress distribution in a lap-joint. As expected the stress concentrations occur at the ends of the joints (Figure 13b). An interesting possibility is to develop active adhesive films with oriented GnP platelets and place these films along the direction of the loads (Figure 13a) to reduce stress concentrations, delay the onset of failure, therby increase the load carrying capacities and fully exploit the benefits offered by GnP,. While this has not yet been attempted in this work, it shows the possibility of tailoring the adhesives to enhance the structural performance while taking advantage of reversible bonding.

Technology Transfer Path:

The deliverables (procedures and results) of this project will be transferred to the industry through the collaboration with EATON. EATON is an industrial partner as a part of this project. Additionally, the results and findings will be shared with U.S. Army Tank Automotive Research Development and Engineering (TARDEC) to facilitate applications on ground vehicles.

Conclusions:

During the past year considerable progress was made to develop active adhesive technology for multi-material joints in lightweight structures. Microwave-activated assembly and dis-assembly was successfully performed on joints with a wide-range of GnP contents. The process was found to be repeatable and efficient. Microwave-activated joints had improved lap-shear strengths than those of conventional thermally-bonded joints. This is attributed to uniform heating throughout the bondline due to microwave-activation rather than non-uniform heating from the conventional thermal bonding. Work is in progress additional joints in out-of-plane and torsional configurations along with improved modeling and simulations.

GnP were chemically functionalized to increase the compatibility between the host polymer and GnP. Three types of GnP functionalization were studied;AE) CTBN), and SBM triblock. Successful processing and tensile property characterization were completed. SBM based functionalization showed enhancements in tensile modulus with minimal drop in strengths. The biggest advantage (and need) of functionalization is the improvements in toughness and resistance to fracture without sacrificing stiffness. Impact resistance and toughness characterization is in progress and will be reported in following communications.

Overall, the progress and results from this work show great promise in use of GnP reinforced thermoplastics as active adhesives for dissimilar material joining.

PRESENTATIONS/PUBLICATIONS/PATENTS:

- Haq M, Koricho EG, Drzal LT, Gerth RJ. “Tailorable Adhesives for Multi-material Joining, Facile Repair and Re-assembly,” American Society of Composites (ASC2015) conference, September 28-30, 2015, Michigan.
- Haq, M, “Examining Novel, Tailorable Reversible Bonded Joints For Multi-material Joining,” Invited lecture -4th Annual Global Automotive Lightweight Materials Detroit 2015, Symposium, August 18-20, 2015.
- Haq M, Drzal LT, Koricho., “Reversible Adhesive Compositions and Related Methods,” U.S Prov. Patent App. No. 62/137,023.

REFERENCES:

1. http://energy.gov/eere/vehicles/downloads/vehicle-technologies-office-merit-review-2014-active-tailorable-adhesives, Accessed Nov., 10, 2015.
2. Downey MA., Drzal LT., “Toughening of aromatic epoxy via aliphatic epoxy copolymers,” Polymer, 6658-6663, 2014.
3. Kamar NK, Drzal LT., “Micron and Nanostructured Rubber Toughened Epoxy: A Direct Comparison of Mechanical, Thermomechanical and Fracture Properties,” Polymer (in review)
4. Haq M, Drzal LT, Patterson EA. “Adhesively Bonded Structural Composite Pi-Joints: Damage-induced Behavior, Modeling and Experiments,” ASME 2011 Applied Mechanics and Materials Conference, Chicago, USA, May 31-June 2, 2011.

Figures and Tables Start on Next Page

Figures and Tables:

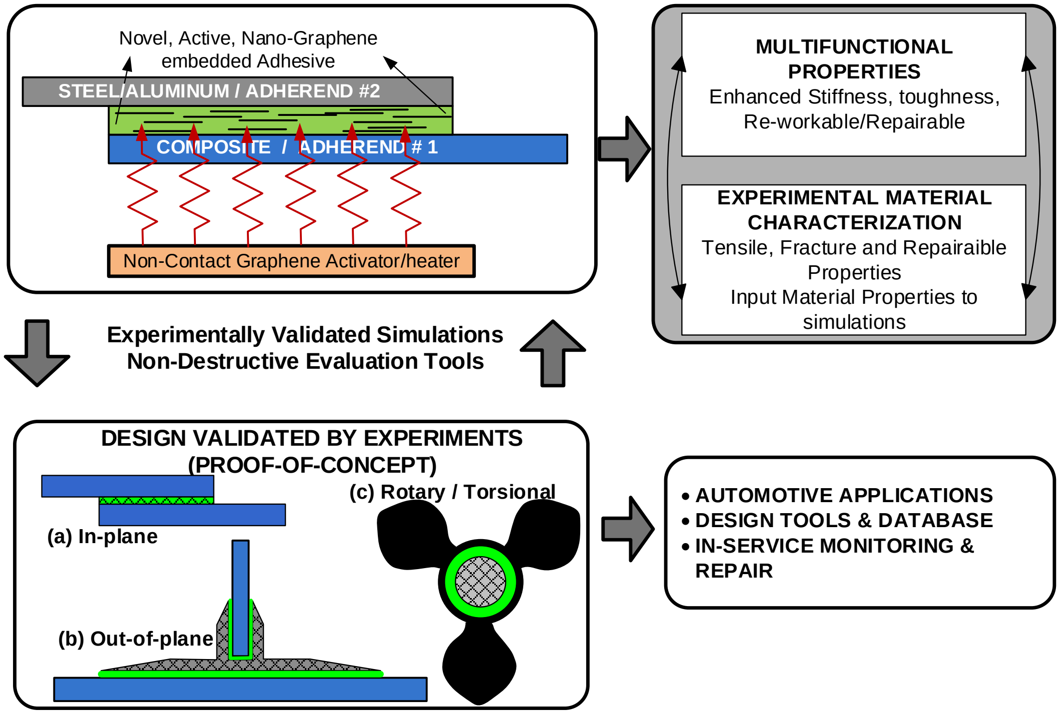

Figure 1. Schematic of the concept and overall approach.

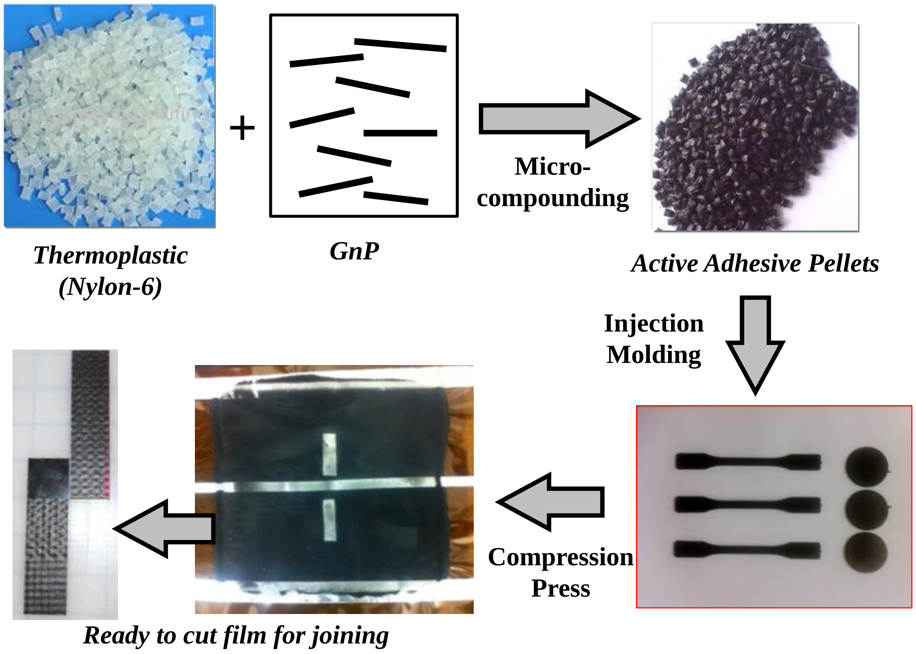

Figure 2. Production of active adhesives.

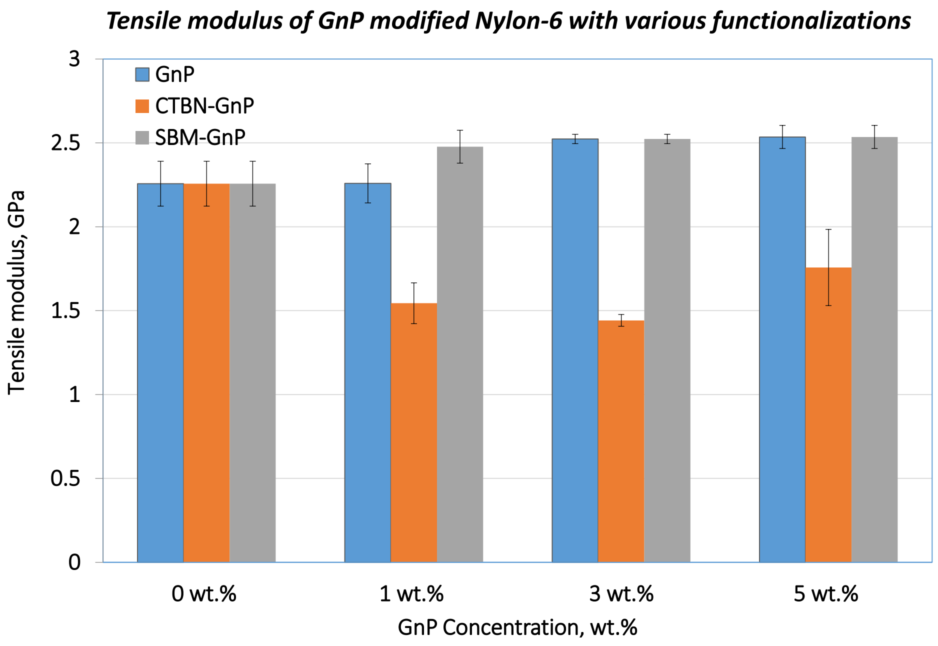

Figure 3. Effect of Functionalization on Tensile Modulus of GnP-modified Nylon-6.

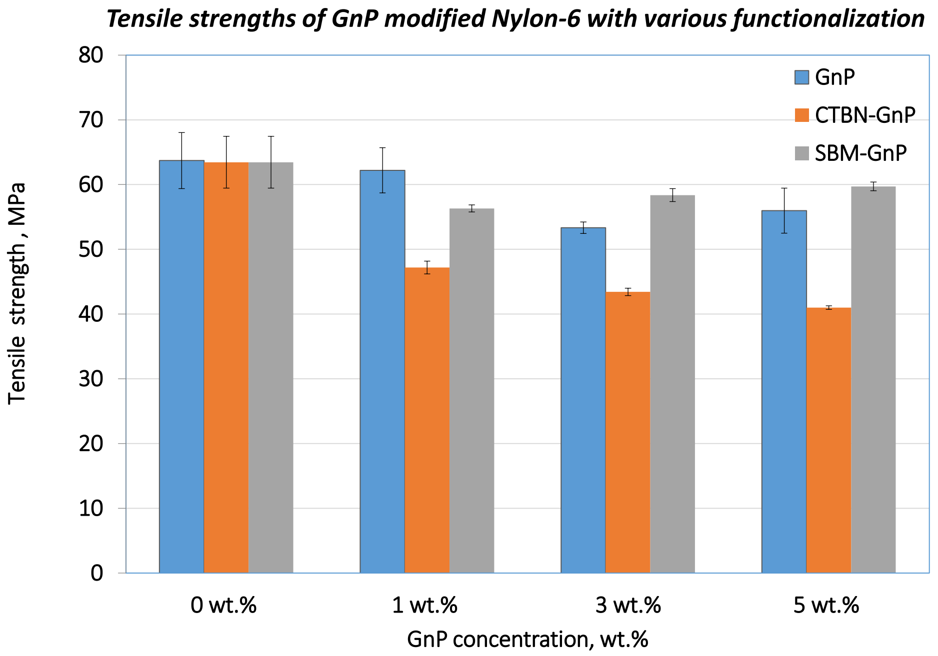

Figure 4. Effect of Functionalization on Tensile Strengths of GnP-modified Nylon-6.

Remainder of Page Intentionally Blank

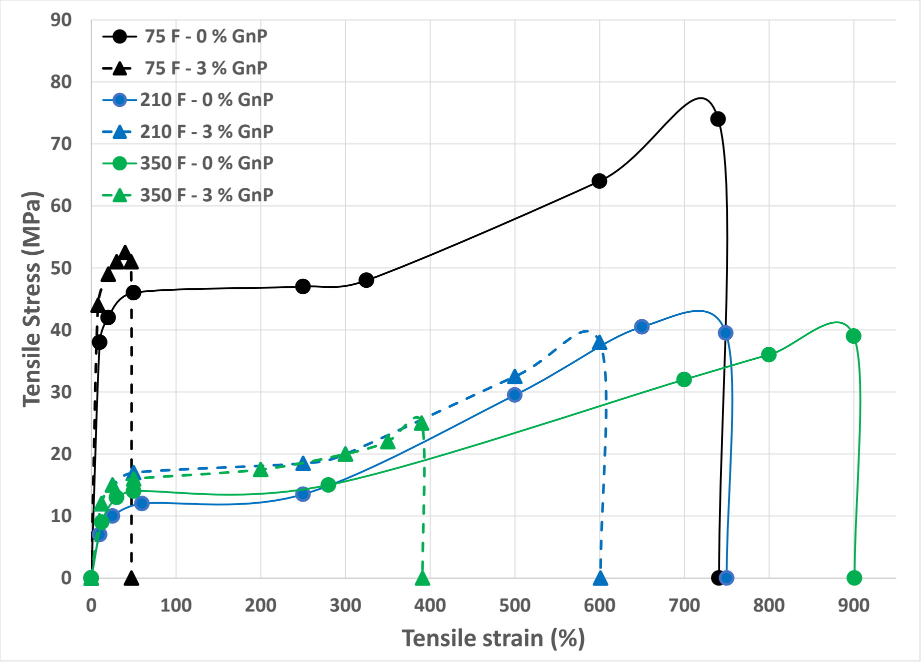

(a)

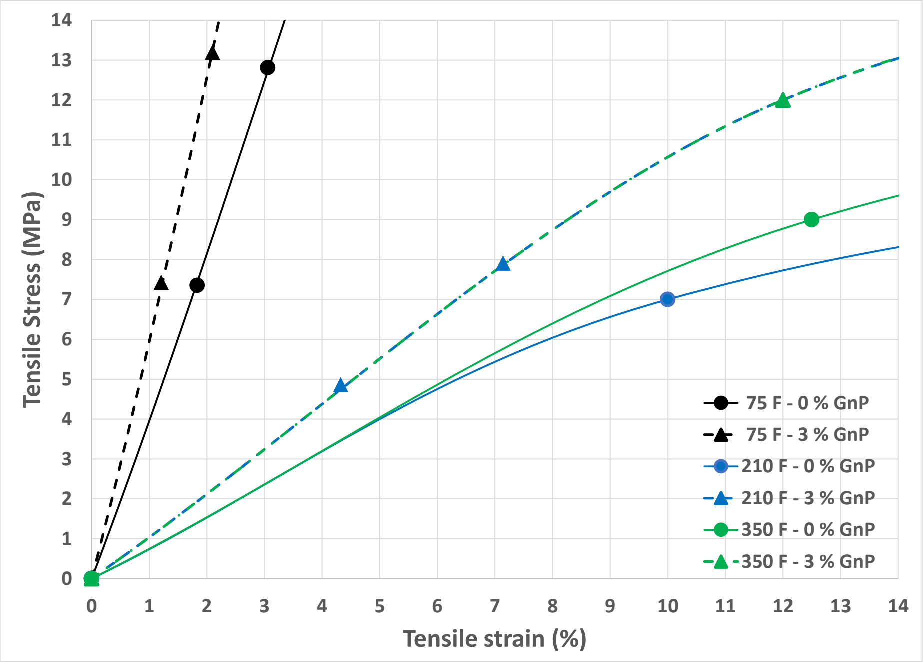

(b)

Figure 5. Tensile behavior of GnP reinforced nylon-6 with varying temperature, a) entire response, and b) linear regime.

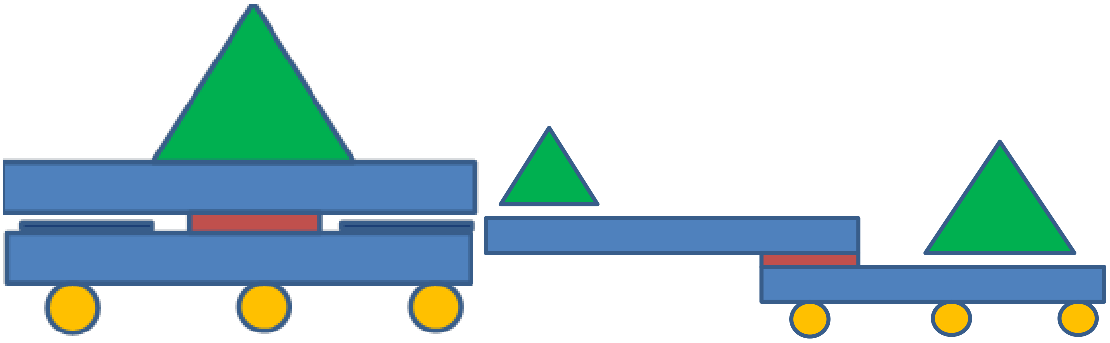

(a) (b)

Figure 6. Schematics of microwave setup: a) assembly/bonding, b) dis-assembly. The green triangles are dead-weight and the red rectangle represents the active adhesive.

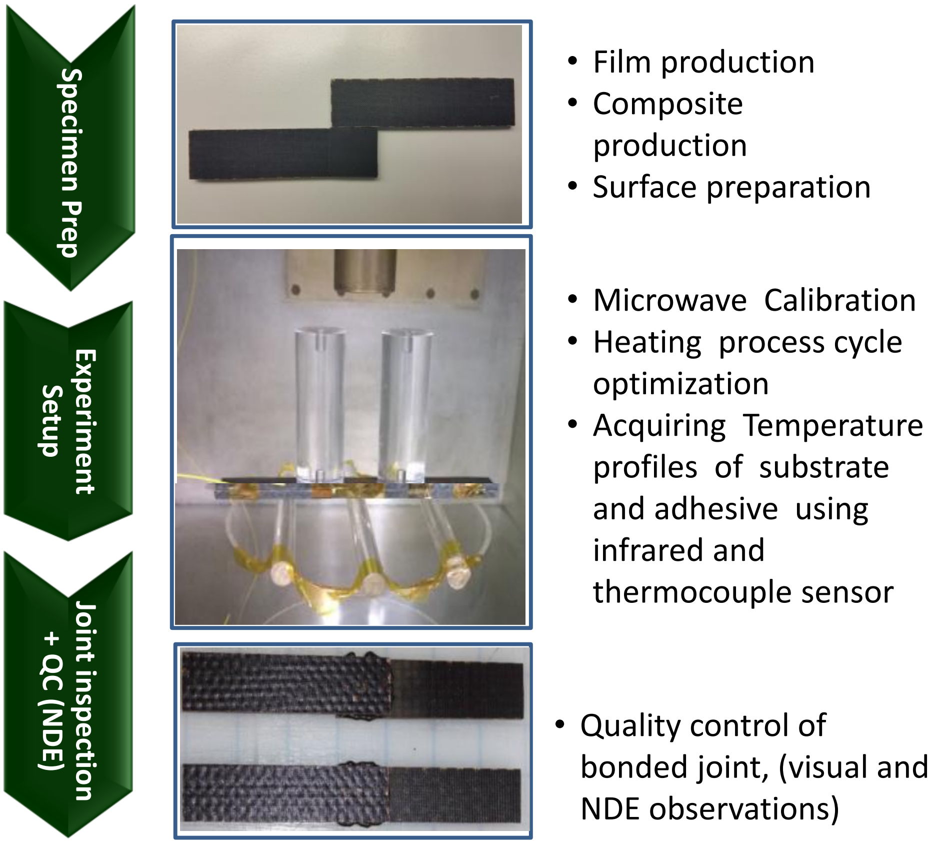

- Film production
- Composite production
- Surface preparation

- Microwave Calibration
- Heating process cycle optimization
- Acquiring Temperature profiles of substrate and adhesive using infrared and thermocouple sensor

- Quality control of bonded joint, (visual and NDE observations)

Figure 7. Process of Microwave-Activated Assembly/Bonding.

Remainder of Page Intentionally Blank

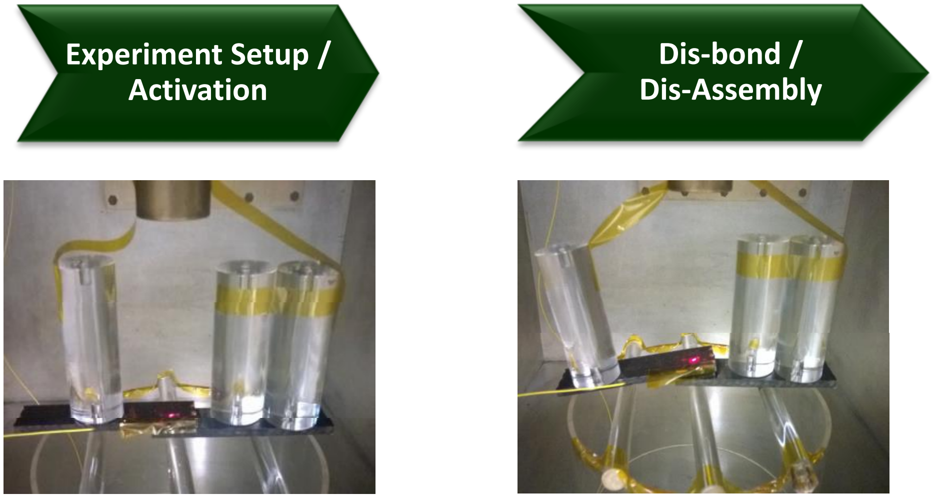

- Heating process cycle optimization for debonding.
- Optimizing debonding force verses temperature required .

Figure 8. Process Setup and Actual Test Sample of Microwave-Activated Dis-Assembly.

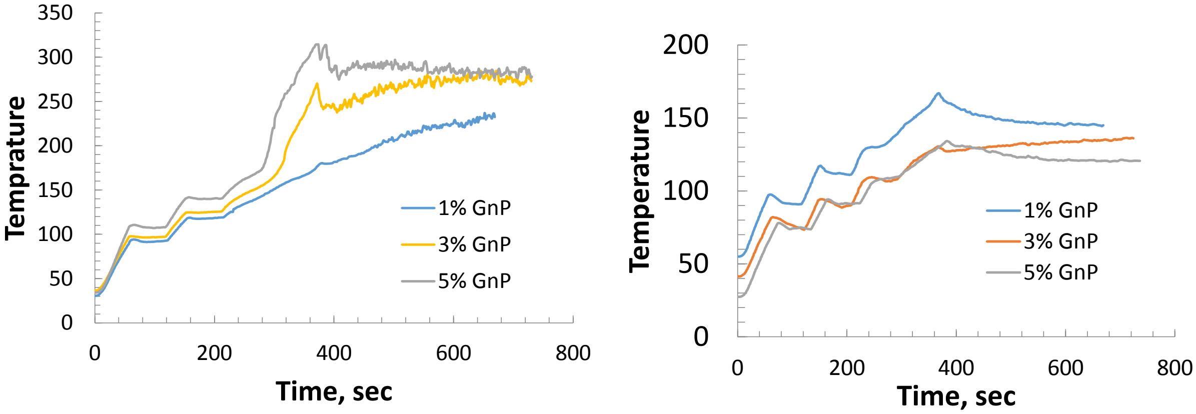

Figure 8. Adhesive temperature profile during a) bonding, b) debonding.

Remainder of Page Intentionally Blank

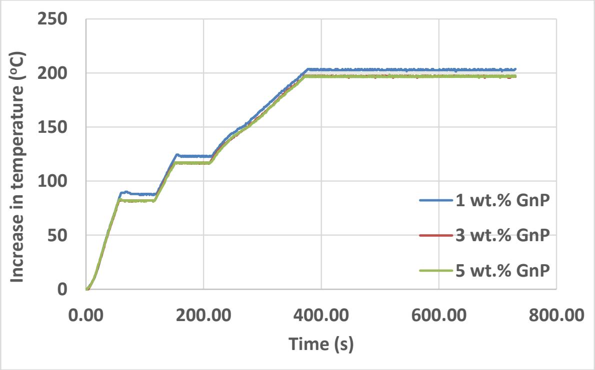

Figure 10. Substrate Temperature Profile during Bonding.

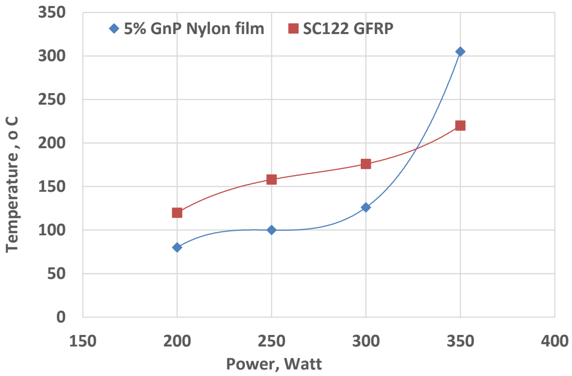

Figure 11. Temperature Profile of Adhesive and Substrate with Varying Applied Power

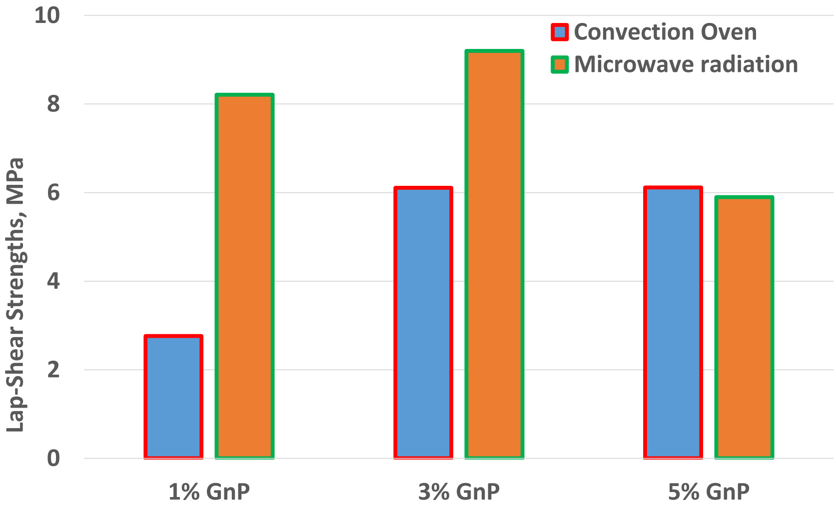

Figure 12. Comparison of Lap-shear Joints Strengths for ‘Conventional Thermal-bonded’ and Microwave-activated Assembled Joints.

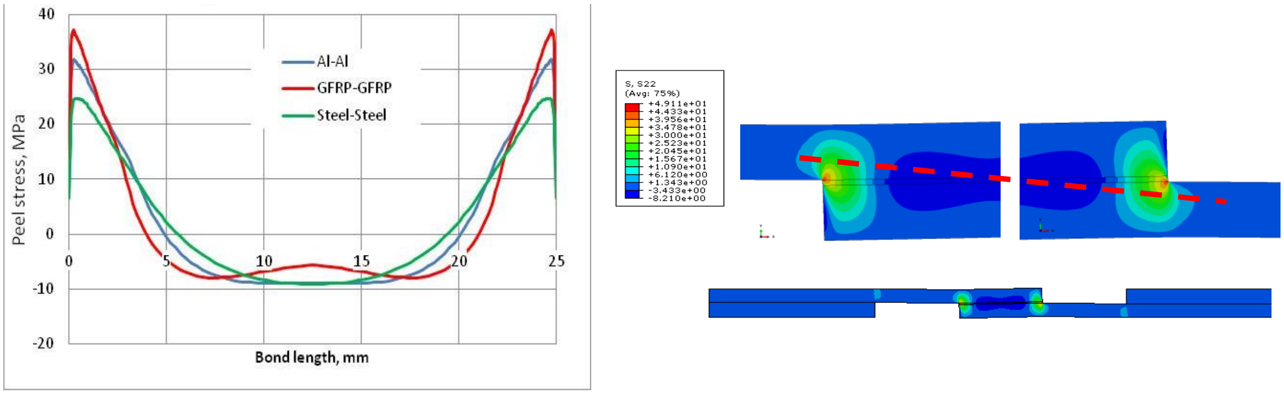

Figure 13. Variation of Peel Stresses (S_{22}) along the Adhesive Mid-plane in aLap-joint; (a) along the Length of the Bonded Area, b) S_{22} Stress Contours showing Stress Contours in the Two Ends.

Remainder of Page Intentionally Blank

This Page Intentionally Blank

AVPTA Technology Focus Area 2: Lightweight Structures & Materials

Breakthrough Techniques for Dissimilar Material Joining – Laser-Assisted Joining Process for Aluminum and Carbon Fiber Composites

DOE-VTO TFA Lead: Ms. Sarah Ollila
TARDEC TFA Lead: Mr. Martin McDonnell

Principal Investigators:
Dr. Adrian S. Sabau and David C. Warren

Oak Ridge National Laboratory (ORNL)
1 Bethel Valley Road; Oak Ridge, TN 37831

Project Start: 01/10/2013
Estimated Completion: Q1 FY 16

Objective:

- To demonstrate a breakthrough laser structuring technology for joining carbon fiber polymer composites (CFPC) and aluminum (Al) components.

Strategic Context:

- The immediate application target for this technology is the Combat Vehicle Prototype (CVP) because it can join thick aluminum with composite resins. No specific CVP design application has yet to be identified.
- The technology supports the TARDEC Strategy enabling new capability in cost and technically effective adhesively bonded composite joints.
- Follow-on activities may include further AVPTA interest to investigate increasing joint strength, reducing cost and/or developing adhesives for other material combinations.
- TARDEC-specific follow-on will depend upon project success but is expected to include joint ballistic shock evaluation.
- Two US-based automotive Original Equipment Manufacturer (OEM) Tier I suppliers that are project participants have the ability to commercialize this technology. This technology is attractive because the use of lighter weight, adhesively joined materials in automotive applications would reduce fuel consumption and the production of greenhouse gasses. Enabling the joining of these lightweight substrates in the process being developed in this work would give credibility to incorporating them in a larger structure for automotive testing. Issues related to the process scale-up will be addressed by the industrial partners. Several steps toward commercialization include:
  -

Tier 1 supplier identified materials that are commonly used in the automotive industry and reviewed industrial needs to ensure that the materials used in this project would ensure a straightforward pathway to dissemination of the joining technology developed in this project.

Accomplishments:

- A minimum of six specimens were used per each condition to obtain range, mean, and standard deviation data on quality indicators for characterization of joint performance such as shear-lap strength, maximum load, displacement at which the maximum load was recorded, and mode of failure.
- Demonstrated increases in the measured lap-shear strength up to 40% compared to the “the abraded and ethanol cleaned” baseline.
- Demonstrated up to 35% increases in the maximum load for single-lap Al-CFPC joints.
- Demonstrated 90% increases in the elongation, or displacement at failure, of Al-CFPC joints.
- Demonstrated a 100% increase in the total energy absorbed during tensile testing of double-lap Al-CFPC joints.
- Attained the maximum possible mechanical strength of the double-lap Al-CFPC joints with 50% of double-lap Al-CFPC joints failed in the Al away from the joint.

Introduction:

This technology will enable the increased use of both Al and carbon fiber composites in primary automotive structures. Body structures make up a significant fraction of the weight of a vehicle and therefore represent a significant opportunity to reduce the weight of a vehicle. According to multiple analyses by the United States Council for Automotive Research, the U.S. Department of Energy, and Oak Ridge National Laboratory, Al alloys have the potential to reduce component weight by 30%–60%, and carbon fiber composites have the potential to reduce component weight by 40%–70%.

To date, CFPC and Al 5000, 6000, or 7000 series components are joined by simply overwrapping the Al with the CFPC or using specially formulated adhesives coupled with extensive surface preparation techniques. Traditional industrial techniques used to prepare Al surfaces for bonding include grit blasting, solvent wiping followed by abrading, and anodizing. The results from grit blasting and abrasion techniques are inconsistent; a more controlled process would be an improvement. In addition, these processes are empirical, use multiple steps, and are labor-intensive surface preparation methods that are incompatible with the degree of automation required in automotive applications.

Approach:

Cosma supplied Al 5182 samples that were 1.5 mm gauge, 100 mm width, and 300 mm long. Plasan supplied CFPC specimens made from the T70 prepreg (T700S carbon fiber and an epoxy resin); the samples were 12 inches (in.) × 12 in., four plies thick, and 0/90 lay-up plaques. Three adhesives were selected for this project based on their compatibility with the Al alloy and the CFPC. The selection process took place at 3M. These structural adhesives were selected:

DP460 (an epoxy), DP620 (a polyurethane), and DP810 (a low-odor acrylic). By using a laser-structuring technique [1] before the adhesive bonding operation, the untreated, smooth adhesive–composite interface was replaced with a rough fiber-reinforced interface, which was expected to increase the bond strength of the CFPC-AL joint.

A 10 hertz (Hz), Q-switched neodymium-doped yttrium aluminum garnet (Nd:YAG) laser (Quanta-Ray PRO 230, Spectra Physics) was used in this study. With only 10 nanoseconds (ns), the laser pulse duration is very short, creating an extremely high power above 100 megawatts (MW) and resulting in greater than 1,012 degree Kelvin per second (^{o}K/s) heating rates. The beam diameter was 8 mm. The fundamental emission with the wavelength of 1,064 nm was transformed to 355 nm and 266 nm using nonlinear crystals. The maximum laser energy per pulse was 0.15 Joules (J) at 355 nm and 0.038 J at 266 nm. Patterns could be dot-, line-, and ring-shaped [2–6]; however, only dot patterns were used in this work.

Two types of laser structuring were used: (1) rastering, in which the laser beam was translated over the sample surface while the laser was on, and (2) spot-by-spot, in which the laser beam was held over each spot for a certain amount of time to allow multiple laser shots over the same area. Conditions for the laser rastering and laser spot-by-spot processing modes were selected based on a sensitivity study for DP810 adhesive conducted in the last quarter of FY 2015. Surface preparation conditions were as follows.

Baseline Surface Preparation:

Surfaces of Al and composite samples were abraded using Scotch-Brite^{TM} and ultrasonically cleaned using ethanol.

Laser-structured Surfaces:

Both carbon fiber polymer composites (CFPC) and Al specimens, in the as-received condition, were laser structured using the interference technique, without any additional surface preparation steps. The laser-structured samples were not cleaned with ethanol before joining.

Results and Discussion:

Adhesive Effect on Single-lap Joint Strength for 0.25mm Thick Bond Line:

To assess the adhesive effect on the joint strength, a total of 60 Al and CFPC joints were bonded using the three adhesives provided by 3M, as follows: 24 joints with DP810, 18 joints with DP460, and 18 joints with DP620 (Table 1).

Figure 1 shows the baseline shear-lap strengths with each of the three adhesives compared to samples with laser-structured surfaces. Table 2 shows the increase in mean lap shear strength as a percentage for the laser-structured joints with respect to their corresponding baselines for the three adhesives considered. The results show that the shear-lap strength of Al-CFPC joints increased by 12%–35% using laser-interference structuring.

To identify an optimum adhesive, several criteria have to be reviewed, including curing temperature and curing time. Depending on the actual production line, a cost analysis that would include the impact of curing time and temperature would have to be performed. This cost analysis is not presented. The laser assisted technique will both increase the joint strength and eliminate the sanding and solvent cleaning steps. The largest impact of the laser structuring was seen in the no heat-cure adhesive (DP620) which attained strength increases 35% higher than its baseline. This allowed the DP620 adhesive to attain strength comparable to the 810 adhesive that requires a 10-minute curing at 66°C. Based on the data shown in Figure 1, adhesives DP810 and DP620NS are recommended for use, as the joint strength of the baseline and laser-structured samples of the DP460NS falls between these two adhesives and requires a much longer curing time.

Dynamic Single-lap Shear Strength Properties for 0.25mm Thick Bond Line:

To assess the effect of the loading rate on the lap-shear strength, a total of 48 Al-CFPC joints were bonded using the DP810 adhesive. Six specimens each were used for loading rates of 0.02, 0.2, 2, 20, and 200 inches per second (in/s). The results from the lap-shear-strength mechanical testing are shown in Tables 3 and 4 for the mean and minimum and maximum values, respectively. The results show that, at loading rates of 0.2, 2, and 20 in/s, the dynamic shear-lap strength has improved for the laser-structured specimens with respect to the baseline. The improvement is evidenced by the large mean shear lap strength, which was obtained by averaging the data for six specimens, as well as by the data range, i.e., from minimum to maximum. The data for the slowest loading rate showed the greatest improvement indicating that the fiber reinforcement of the interface is load rate dependent. The data at 2 in/s showed the least improvement in both the mean shear-lap strength and range. At 200 in/s the mean values for both the baseline and laser-structured joints were very close. Another quality indicator is the minimum-to-maximum range variation of the shear-lap strength. Table 4 shows the minimum-to-maximum data range for both the baseline and laser-structured joints. The range of shear strength variation for the laser-structured specimens was just a fraction of that for the baseline at loading rates of 0.2, 2, and 20 in/s.

Single-lap Joint Strength for 0.85mm Thick Bond Line:

The results from the mechanical testing of the lap-shear strength are shown in Figure 2 for the minimum, mean, and maximum values when surface structuring was conducted using a laser beam size of 6 mm and the adhesive bond line thickness was 0.85 mm. In Table 5, the increase in mean shear-lap strength [Figure 2] is shown as a percentage for the laser-structured joints with respect to the corresponding baselines. The results show that the shear-lap strength of Al-CFPC joints increased more than 30% when Al and CFPC surfaces were interference structured, with one condition showing shear-lap strengths slightly greater than 40%. The load increase was about 20% to 28% of the mean baseline.

Remainder of Page Intentionally Blank

Displacement at Failure for Single-lap and Double-lap Joints with a Bond Line Thickness of 0.25mm:

The displacement at maximum load in Newtons (N) is an indication of the elongation and is a direct measure of the energy absorbed by the joint during the shear-lap test. Figure 3(a) shows the evolution of the shear-lap stress during mechanical testing for three single-lap joint specimens: baseline (no laser structuring), laser-structured spot-by-spot, and laser structured by rastering with a 4 mm laser beam. These data indicate that the laser-structured joints are much more ductile than that without laser structuring. The displacement at failure increases from 0.145 in. for the baseline joint to more than 0.26 in. for the laser-structured joints. This behavior indicates an enhanced bonding of adhesive to both Al and CFPC. Laser-structured joints can absorb almost double the energy of the baseline joints (area under the stress-strain curve).

The results for the evolution of the load during mechanical testing are shown in Figure 3(b) for two representative double-lap joint specimens, a baseline specimen and another one using laser-structured surfaces. The double-lap joint was made with laser-structured surfaces using a laser beam size of 6 mm. These results show that the elongation has increased by about 83% (0.77 in. for the laser-structured specimen and 0.42 in. for the baseline joint). By integrating the load with respect to the displacement, the total energy absorbed by the joint with laser-structured surfaces showed an increase of about 100% over that for the baseline joint (202.03 J for the laser-structured specimen and 101.18 J for the baseline joint).

Mode of Failure - Single-lap and Double-lap Joints with a Bond Lline Thickness of 0.25mm:

The failure mode was changed as a result of laser structuring for Al and CFPC surfaces. Pictures taken after mechanical testing of single-lap joints bonded with adhesive DP620 and a bond line thickness of 0.25 mm were used to identify fracture surfaces and/or failure modes for the single-lap joints (Figure 4). For the baseline joints, the large, clean fracture surfaces indicate an adhesive failure mode where there is poor adhesion to either substrate [Figure 4(a)]. The joints made with laser-structured surfaces exhibit residual adhesive on both surfaces, demonstrating a cohesive failure mode.

Figure 5 shows pictures of baseline joints and joints made with laser-structured surfaces taken after mechanical testing of double-lap joints bonded with adhesive DP810 and a bond line thickness of 0.25 mm. Figures 5(a) and 5(b) indicate that none of the baseline joints failed in the component Al or CFPC, while 50% of the joints made with laser-structured surfaces were found to fail in the Al component [Figure 5(c)]. The fact that 50% of the joints made with laser-structured surfaces were found to fail in the Al component indicates that the maximum performance (load, shear-lap strength) for the joint was attained and that no further improvement could be attained irrespective of surface treatment.

Technology Transition Path:

Two project participants, Cosma and Plasan, are tier I suppliers and have the ability to commercialize this technology. Issues related to the process scale-up will be addressed by the industrial partners.

The following steps are being taken to ensure the commercialization potential of the joining technology developed in this project.

- Cosma, Plasan, and 3M identified materials that are commonly used in the automotive industry and reviewed industrial needs to ensure that the materials used in this project were the same or comparable.
- 3M selected the adhesives based on the commercialization plans of the two tier I suppliers participating in the project, Cosma (Al structures) and Plasan (carbon fiber composites structures).
- The project team has engaged a supplier of high-speed industrial laser systems that currently supplies the automotive industry as a future scale-up partner.

Conclusions:

The project has demonstrated significant improvement in the mechanical properties of shear-lap joints made with laser-structured surfaces compared to those of baseline joints, demonstrating the proof of concept for laser structuring and/or laser ablation for surface preparation of both CFPC and Al coupons before adhesive joining. The joints demonstrated higher loads to break and a significant increase in energy absorption during failure. This was due to the failure mode shifting from being an adhesive-to-adherend interfacial failure to a failure cohesively through the bulk of the adherend, either in the region of the joint or in regions away from the joint.

The data indicate that mechanical properties of the joints can be significantly increased by laser structuring the Al and CFPC. This method can be robotically controlled, eliminating the need for labor intensive and variable manual processes.

This technology is attractive because the use of lighter weight, adhesively joined materials in automotive applications would reduce gas consumption and production of greenhouse gasses. The proof of concept for laser structuring to enable joining of these lightweight substrates this work gives credibility to incorporating them in a larger structure for automotive testing.

References:

- Daniel, C.; Mücklich, F.; Liu, Z. Periodical micro-nano-structuring of metallic surfaces by interfering laser beams. *Appl. Surf. Sci.* **2003,** *208–209*, pp. 317–321.
- Daniel, C.; Mücklich, F. Quantification of periodical surface structures by white light interferometry. *Prakt. Metallogr*. **2004**, *41* (6), pp. 277–285.
- Mücklich, F.; Daniel, C.; Lasagni, A.; Yu, F. Direct Surface Patterning Induced by Interfering Laser Beams. *Mat. Res. Soc. Symp. Proc.* **2004,** Vol. EXS-2, M11.1.
- Mücklich, F.; Lasagni, A.; Daniel, C. Laser Interference Metallurgy—Periodic Surface Patterning and Formation of Intermetallics, *Intermetallics* **2005,** *13* (3–4), pp. 437–442.
- Mücklich, F.; Lasagni, A.; Daniel, C. Laser Interference Metallurgy—using interference as a tool for micro/nano structuring. *Int. J. Mater. Res.* **2006**, *97* (10), pp. 1337–1344.
- Daniel, C. Biomimetic structures for mechanical applications by interfering laser beams—more than only holographic gratings. *J. Mater. Res.* **2006,** *21*, pp. 2098–2105.

Figures and Tables:

Adhesive	Joint Type	Preparation of CFPC	Preparation of Al
DP810	Baseline	Abraded and ethanol cleaned	Abraded and ethanol cleaned
DP460NS	Baseline	Abraded and ethanol cleaned	Abraded and ethanol cleaned
DP620NS	Baseline	Abraded and ethanol cleaned	Abraded and ethanol cleaned
DP810	2B-raster	Laser raster #2	Laser raster B
DP810	3B-raster	Laser raster #3	Laser raster B
DP810	3C-spot	Laser spot-by-spot #3	Laser spot-by-spot C
DP460NS	2B-raster	Laser raster #2	Laser raster B
DP460NS	2B-spot	Laser spot-by-spot #2	Laser spot-by-spot B
DP620NS	2B-raster	Laser raster #2	Laser raster B
DP620NS	2B-spot	Laser spot-by-spot #2	Laser spot-by-spot B

Table 1. Six joint specimens made for each joint type to assess the effect of adhesive for laser structured surface preparation over conventional surface preparation.

Remainder of Page Intentionally Blank

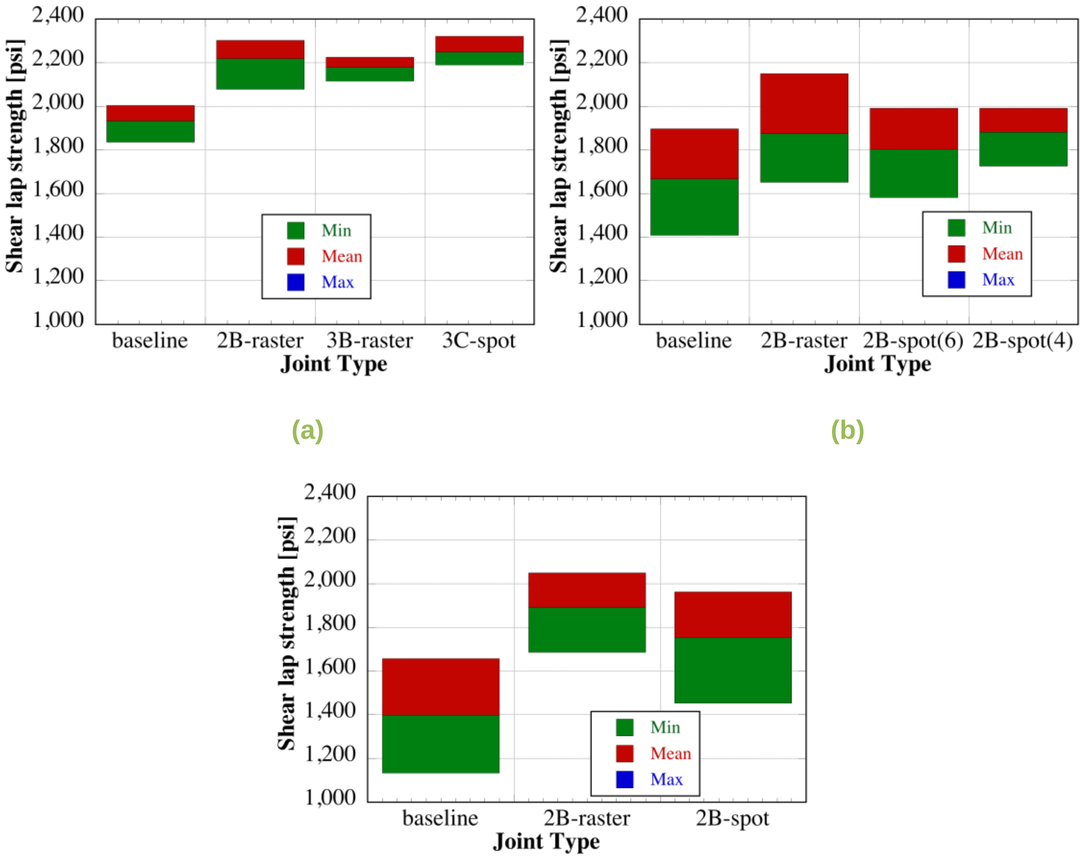

(a)

(b)

(c)

Figure 1. The single-lap shear strength (in pounds per square inch (psi)) results for minimum, mean, and maximum values for baseline and laser-interference structured surfaces for both CFPC and Al for the following adhesives: (a) DP810, (b) DP460NS, and (c) DP620Ns.

Adhesive	% increase by laser-raster	% increase by laser spot-by-spot
DP810	12.7-14.8	16.3
DP460NS	12.8	8.2-12.8
DP620NS	35.3	25.4

Table 2. Increase in mean shear-lap strength shown in percentage for the laser structured joints with respect with their corresponding baselines.

Remainder of Page Intentionally Blank

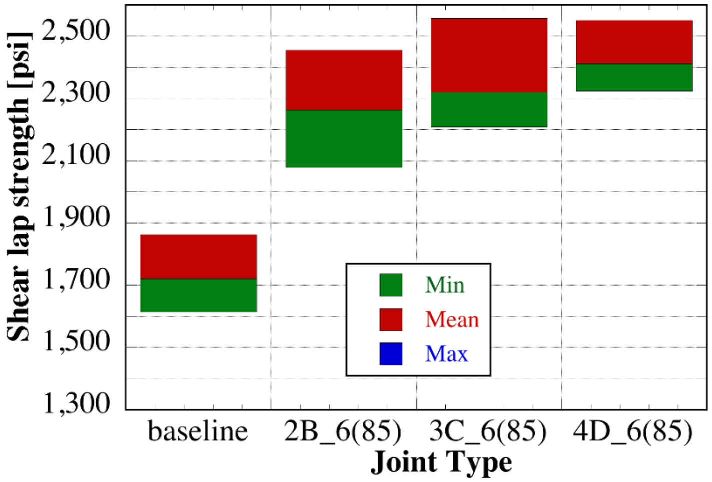

Figure 2. The single-lap shear strength results for minimum, mean, and maximum values for baseline and laser-interference-structured surfaces for both CFPC and Al for a bond line thickness of 0.85 mm and a laser beam size of 6 mm.

Loading rate [in/s]	τ(psi) Baseline joints	τ (psi) Laser raster-structured joints	% increase by laser-raster
0.02	1,933.7	2,219.6	14.78
0.2	2,203.7	2,374.2	7.74
2	2,228.3	2,236.7	0.37
20	2,220.8	2,316.2	4.67
200	3,980.6	3,970.8	-0.24

Table 3. Increase in mean lap shear strength (psi), for the laser-structured joints with respect to their corresponding baselines.

Loading rate (in/s)	τ_{min} (psi) Baseline joints	τ_{max} (psi) Baseline joints	$\Delta\tau$ (psi) Baseline joints	τ_{min} (psi) LS joints	τ_{max} (psi) LS joints	$\Delta\tau$ (psi) LS joints	$\Delta\tau_{base}/\Delta\tau_{LS}$
0.02	1,835.5	2,005	169.7	2,078.6	2,303.1	224.5	1.32
0.2	1,784.4	2,370	585.9	2,306.5	2,424.2	117.7	0.2
2	1,959.6	2,330	370.9	2,071.2	2,328.1	256.9	0.69
20	1,992.1	2,349	356.6	2,300.0	2,346.2	46.2	0.13
200	3,661.5	4,204	543.1	3,609.0	4,437.6	828.6	1.53

Table 4: Minimum shear-lap strength, τ_{min} (psi), maximum shear-lap strength, τ_{max} (psi), and range $\Delta\tau=\tau_{min}-\tau_{max}$ (psi) for baseline and laser-structured (LS) joints.

Remainder of Page Intentionally Blank

Joint type	% shear-lap increase (of mean)	% load increase (of mean)
2B_6	31.5	19.9
3C_6	34.8	23.3
4D_6	40.1	28

Table 5. Increase in mean shear-lap strength shown as a percentage for the laser-structured joints with respect to the baseline for a bond line thickness of 0.85mm (the laser beam size was 6 mm).

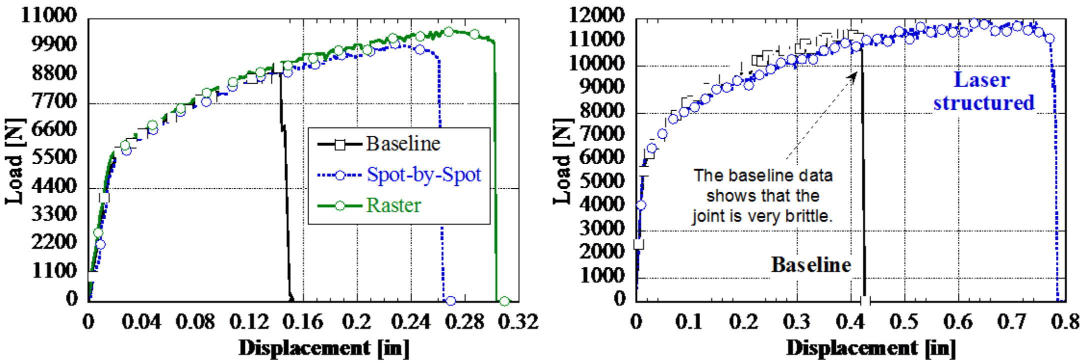

Figure 3: Load evolution during mechanical testing as a function of displacement for (a) single-lap joints and (b) double-lap joints.

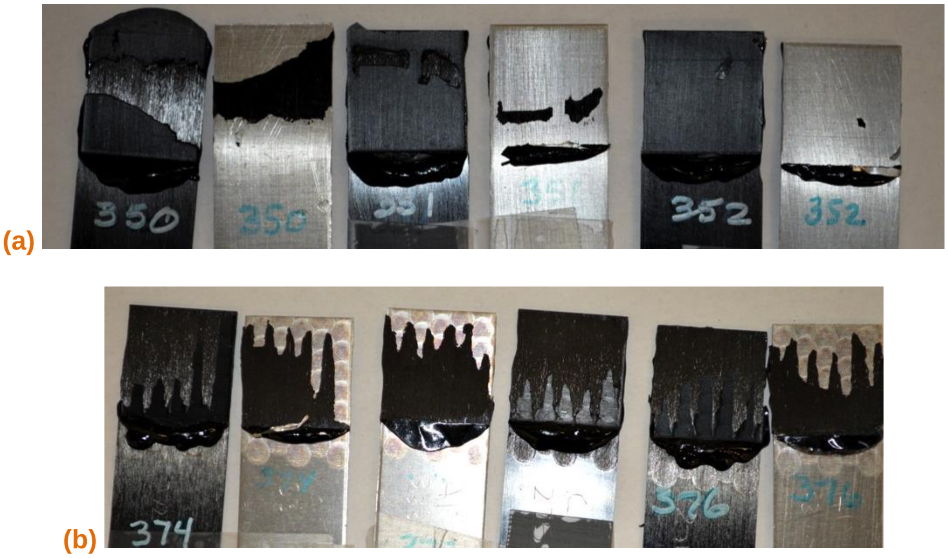

Figure 4. Pictures taken after mechanical testing of single-lap joints bonded with adhesive DP620 and a bond line thickness of 0.25 mm showing fracture surfaces and failure modes: (a) baseline joint (b) joints with laser-structured surfaces using a laser beam size of 6 mm.

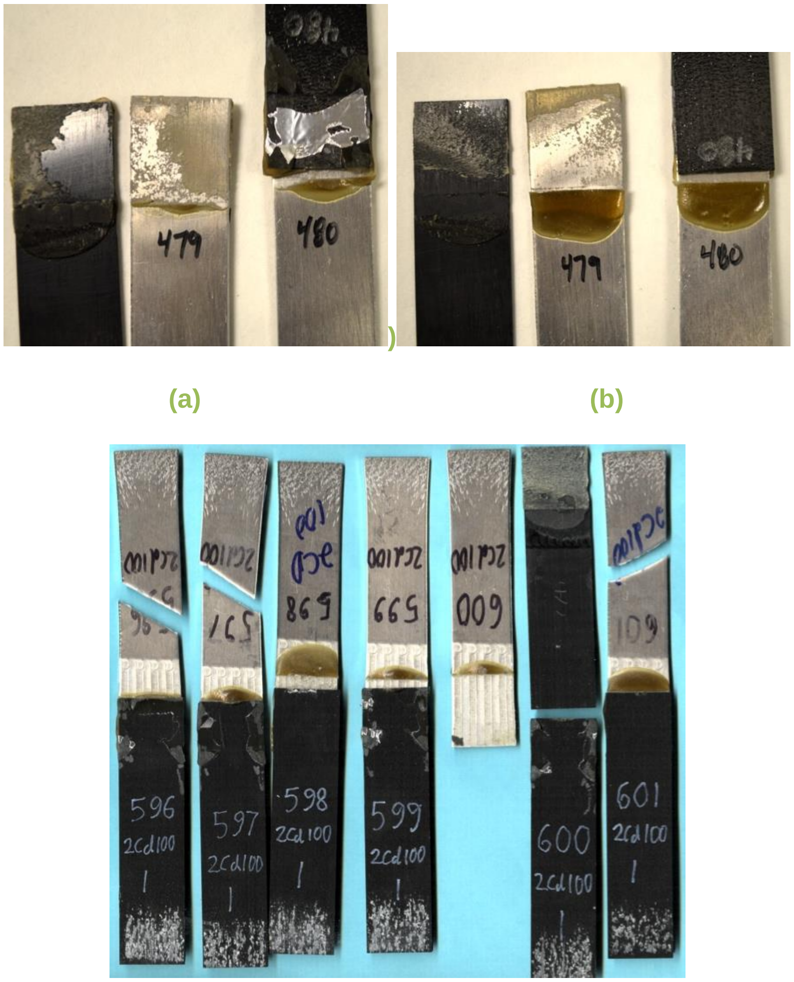

(a) (b)

(c)

Figure 5. Pictures taken after mechanical testing of double-lap joints bonded with adhesive DP810 showing fracture surfaces and/or failure mode: (a, b) baseline joints (c) joints with laser structured surfaces using a laser beam size of 6mm.

Remainder of Page Intentionally Blank

This Page Intentionally Blank

AVPTA Technology Focus Area 3: Energy Recovery & Thermal Management

Thermoelectric Generator (TEG) Enabled Waste Heat Recovery (Gentherm)

DOE-VTO TFA Lead: Gurpreet Singh
TARDEC TFA Lead: Mary Goryca

V.Jovovuc (Principal Investigator)[1], D. Lock[1], C. Haefele[2], M. Miersch[3], and A. Gurdogan[4].

[1] Gentherm, Inc.
5462 Irwindale Ave.
Irwindale, CA 91706
Phone: (626) 593 – 4532
E/M: vladimir.jovovic@gentherm.com

[2] BMW AG
Research & Innovation Center
Knorstrasse 147
80788 Munich, Germany

[3] Tenneco GmbH
Luitpoldstrasse 83
67480 Edenkoben, Germany

[4] Tenneco, Inc.
3901 Willis Road
Grass Lake, MI 49240

Start: Q3 2011
Completion: Q3 2015

Objectives

- A detailed production cost analysis for TEG for passenger vehicle volumes of 100,000 units per year and a discussion of how costs will be reduced in manufacturing.
- A five (5) percent fuel economy improvement by direct conversion of engine waste heat to useful electric power for light-duty vehicle application. For light duty passenger vehicles, the fuel economy improvement must be measured over the US06 cycle.
- Confirmatory testing of the hardware to verify its performance in terms of fuel economy improvement.
- Build scaled-up thermoelectric generator (TEG) for TARDEC Bradley Fighting Vehicle (BFV).

Strategic Context:

- Reducing fuel consumption of military vehicles.
- Increasing onboard electricity generation.
- Reducing thermal visibility of vehicles.

Accomplishments:

- Developed equipment for manufacturing of TE materials.
- Designed, built and tested thermoelectric power generator for Bradley fighting vehicle.
- Designed, built and tested thermoelectric power generator for passenger vehicle.
- Experimentally confirmed device performance model.
- Performed vehicles for vehicle tests.

Introduction:

The focus of this project is the development of a simple and reliable device that would enable recovery of otherwise wasted exhaust gas energy. Recovered thermal energy is directly converted into electricity using a solid state device – a Thermoelectric Power Generator (TEG). The primary objective of this program is to design and implement TEG devices which demonstrate 5% FEI for passenger or light duty vehicles (LDV). In FY2015 we have demonstrated a device design for both Light Duty Vehicles (LDV) and Heavy Duty Vehicles (HDV). The HDV device was developed for Bradley Fighting Vehicle application was tested at Tenneco’s R&D center and showed the potential to generate up to 1.8kW of electricity and provide FEI of up to 1.5%. Benefits of integration of TEG in military vehicles include significant reduction in fuel consumption, increased electricity production and reduction of temperature of exhaust gasses.

Approach:

The team consists of: TARDEC – defining scope of design for military applications, BMW, an OEM representing the LDV market; Tenneco, a tier 1 exhaust system provider; Gentherm, a developer of thermoelectric devices and materials; and Caltech, an academic institution working on development of future thermoelectric materials. The role of NREL in this program is to act as a neutral party and perform device-level confirmatory tests. Gentherm is the project lead. The goal of this project is to develop a complete supply chain and demonstrate the ability to produce, integrate and test reliable waste heat recovery devices. In addition to development of the LDV device, a team consisting of Gentherm and Tenneco worked on development of the HDV device under contract with the Department of Energy and the U.S. Army Tank Automotive Research Development and Engineering Center (TARDEC). The goal of this part of the project was to demonstrate the ability to produce between 1kW and 2kW of electric power from the exhaust gas energy of a Bradley Fighting Vehicle (BFV). To reduce development time, both devices were designed based on a finned tube heat exchanger. The basic building block used in both devices is a thermoelectric cartridge: a power conversion device developed by Gentherm and shown here in Figure 1. Gentherm has developed methods of manufacturing these devices, test methodologies, and performance models. A combination of 1D and 3D models was used to evaluate performance and structural stability of the cartridge.

The role of the Tier 1 exhaust supplier, Tenneco, is to design and build the complete thermoelectric power generation unit, applying technologies developed in packaging catalytic converters, particulate filters and other exhaust components. Tenneco used 1D and 3D modeling tools to predict system level performance and to design structural components of the TEG. As the TEG is a new component, structural integrity was verified following protocols similar to those used in development of active exhaust components such as catalytic converters.

BMW is the only OEM in this program. The role of BMW was to define packaging space and provide advice on system level requirements. In the final stage of this program, BMW will perform light duty vehicle level tests and try to evaluate the effect of integration of the TEG on FEI.

TARDEC has participated in final confirmatory testing of performance of HDV TEG and has validated methodology used to test this device.

Results:

The program objectives can be divided in three groups: (1) development of low cost material processing methods, (2) development of highly efficient and reliable devices and (3) demonstration of device performance in vehicles.

In the development of the manufacturing process we focused on low-cost, high-yield technologies. Processing of thermoelectric materials requires fine control of ambient conditions and process parameters such as sintering temperatures. All thermoelectric materials are very sensitive to oxidation, contamination by impurities and phase separation. For this reason we have selected spark plasma sintering as our sintering process. As part of this project we have developed a process to manufacture net-shaped thermoelectric elements using materials from the Skutterudite family. Both p- and n-type materials are produced with highly repeatable physical properties such as electrical conductivity (σ), thermal conductivity (κ), and Seebeck coefficient (S). The thermoelectric figure of merit, $zT = (S^2.\sigma)/\kappa$, is the best indication of material quality as it directly correlates to the efficiency with which thermoelectric materials convert heat to electricity. Based on in-process sampling of materials produced at Gentherm, we have peak zT values of 0.8 to 0.9 for p-type materials and 0.9 to 1.1 for n-type materials. The range shows our observed deviation in material properties in past twelve months. Our manufacturing process is reliable, repeatable and results in very low material loss. Yields are as high as 80%. Further improvements and automation of equipment could bring yields in the range of 92-95%. To demonstrate our ability to produce materials at a high rate, Gentherm has developed and installed automated equipment capable of handling up to 1.2 tons of TE material per year.

Performance of thermoelectric devices is a strong function of the thermoelectric material properties, however even the best thermoelectric materials have very low potential to convert heat to electricity. Large gains in the performance of thermoelectric devices are not made by incrementally improving zT values but rather by closely integrating thermoelectric materials and heat exchangers. For efficient utilization of available heat, it is necessary to reduce thermal interface losses. To minimize the number of thermal interfaces, Gentherm has developed the cartridge shown in Figure 1. Details of the performance of this component were reported previously. A thermoelectric cartridge is a finned tube heat exchanger. There is a stainless steel heat exchanger on the outer, hot gas, side, and a smaller, liquid-cooled finned tube heat exchanger running down the center. Thermoelectric elements are in direct contact with heat exchangers via engineered thermal interfaces and electrical shunts. This thermoelectric cartridge is the basic building block used to design and manufacture larger Thermoelectric Generator Systems (TEG). In this program we have demonstrated two TEG systems, one designed for light duty vehicles (LDV) and a second designed for heavy duty vehicles (HDV).

The light duty vehicle TEG was designed in collaboration with Tenneco GMBH. One of the light duty vehicle devices is shown in Figure 2. A total of seven fully-functional systems were built for this program. Two systems were tested at Gentherm and Tenneco on hot gas flow benches. Independent verification of device performance was performed at the National Renewable Energy Lab on a hot gas burner bench. Peak power output is 200W under conditions representative of the flow and temperature of exhaust gas in a BMW X3 vehicle. The maximum measured power in flow bench tests was 250W. As part of this program, one device will be tested by BMW in an X3 vehicle and two additional devices will be tested by Gentherm in a Ford F350 truck. Vehicle level tests will be performed over the US06 cycle and these tests will be used to evaluate the device effect on FEI.

The heavy duty vehicle TEG was developed as part of an add-on program between the Department of Energy and the U.S. Army Tank Automotive Research Development and Engineering Center. For the purpose of device design, we have treated this portion of the project as development of a TEG device for heavy duty vehicle applications. This HDV TEG is designed to be attached to the exhaust of a 14.8L diesel engine before the after-treatment system. The device is designed to operate independent of the vehicle cooling system and to fit in a 2x2x4ft volume. The device consists of a radiator, a fan, a water pump, a coolant tank, manifolds, flow measurement system, and the active power generation unit (TEG) comprising 56 thermoelectric cartridges. The device is shown in Figure 3.

Effects of soot build-up were tested at Tenneco R&D labs in Grass Lake, Michigan, by evaluating soot buildup on a partial device. These tests show no significant soot build-up on heat exchanger fins for duration of this test. The complete device was tested on a gas burner bench at flow rates and temperatures equivalent to those measured in the exhaust of a 14.8L diesel engine. The gas burner was used instead of engine test to better control flow conditions.The measured power output is 1.8kW; a complete device operating map is shown in Figure 4.

Conclusions:

Team has demonstrated ability to merge development of devices for military and civilian applications. Device developed for Bradley Fighting Vehicle was designed using technologies developed for passenger vehicle applications. Partnership between Gentherm, TARDEC and Tenneco and resulted in demonstration of technology applicable for military applications. Device developed by Gentherm demonstrated ability to produce up to 20% of power required by BFW and to save over 5,000l;bs of fuel over the life of the vehicle.

Presentations:

- *IAA Frankfurt – Demonstration of TEG for Passenger Application.*
- *2015 High-Efficiency Truck Users Forum (HTUF) National Meeting and Technical Exchange Presentation of BFV TEG.*

Figures and Tables:

Figure 1. Thermoelectric Power Generation Cartridges.

Figure 2. Light Duty Vehicle TEG

Remainder of Page Intentionally Blank

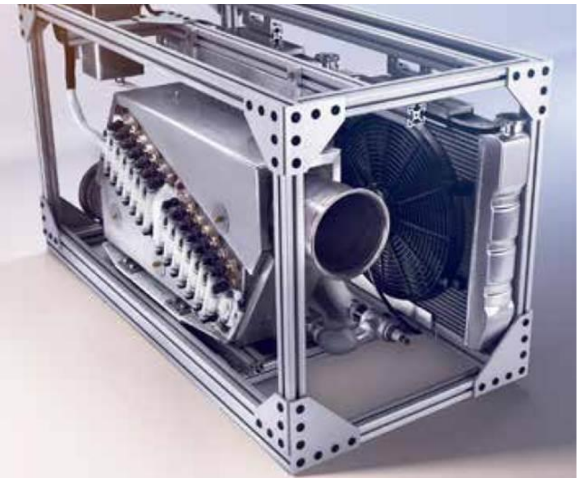

Figure 3. Thermoelectric Power Generation Device Designed for BFV

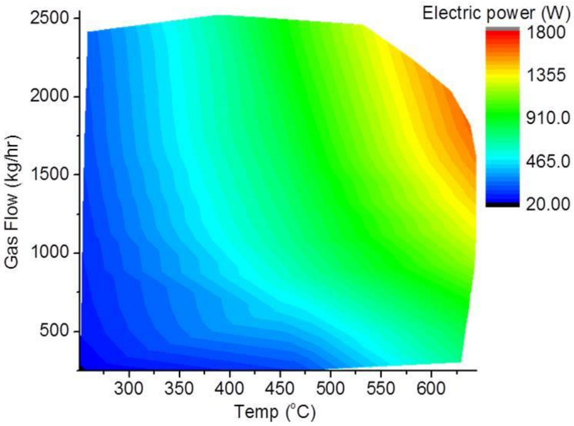

Figure 4. Measured Power Output Operating Map

Remainder of Page Intentionally Blank

AVPTA Technology Focus Area 4: Alternative Fuels & Lubricants

Lubricant Formulations to Enhance Fuel Efficiency
Polyalkylene Glygol (PAG) based Lubricant for Light & Medium Duty Axles

DOE-VTO TFA Lead: Kevin Stork
TARDEC TFA Lead: Dr. Jay Dusenbury

Principal Investigators:
Dr. Arup Gangopadhyay and
Chintin Ved

Affiliation:
Ford Motor Company
Research and Innovation Center
2101 Village Road
Dearborn, MI 48121

Project Start: 01/10/2013
Estimated Completion: Q4 FY16

Objective(s):

- Develop novel lubricant formulations that are expected to improve the fuel efficiency of medium-duty, commercial and military vehicles by at least 2%
- Develop engine, transmission and axle lubricant formulations, modeling and simulation

Strategic Context:

- This project aligns with TARDEC's LoE 1.4 and Army S&T Challenges to improve operational energy, as well as, DOE's mission to develop more energy-efficient and environmentally friendly technologies.

Accomplishments:

- Developed several candidate polyalkylene glycol (PAG) based axle lubricants. The lubricants have low viscosity and generally improved friction and wear results compared to fully formulated 75W-140 baseline oil.
- Seal compatibility and an industry standardized axle lubricant wear test (i.e., ASTM D6121) was completed on a PAG candidate. Some rebalancing of the additive package required to eliminate rippling issue.
- DOW developed a new oil soluble PAG (OSP) with improved extreme pressure properties and passing rust and copper corrosion test results.

Introduction:

The objective of this project is to develop novel lubricant formulations that are expected to improve the fuel efficiency of light, medium, heavy-duty, and military vehicles by at least 2% over Society of Automotive Engineers (SAE) 75W-140 axle lubricants (improvement based on comparative results from engine dynamometer testing, chassis dynamometer testing or test track, e.g., SAE J1321) without adverse impacts on vehicle performance or durability.

Approach:

The project objective will be met by completing the following: 1) Lubricant Formulation: Initiate work with the formulation of new polyalkylene glycol (PAG) based axle lubricants. Preliminary testing shall be conducted in an effort to identify those formulations with the greatest potential to meet project objectives. 2) Bench Testing: Evaluate fundamental properties of the new lubricant formulations, test to measure intrinsic properties, physical tests to determine performance characteristics in sliding and rolling friction and wear, micro-pitting, and analysis of lubricant additive-derived anti-wear films using surface sensitive analytical tools. In addition, oxidation and corrosion evaluations will be performed. 3) System and Vehicle Evaluation: Determine performance characteristics in system level (axle) test rigs to evaluate axle efficiency improvements and gear/bearing durability performance of lubricants. Vehicle fuel economy, and potential impact on emissions, will then be demonstrated on a chassis roll dynamometer.

Results and Discussion:

Ford in collaboration with DOW Chemical Company have successfully developed several candidate PAG based axle lubricants. Bench friction and wear testing has been completed at Argonne National Laboratory (ANL) and resulted in improved friction behavior, although ball-on-disc wear results have shown that most PAG candidates did not prevent wear as well as the fully formulated commercial 75W-140. The PAG candidate that showed equal results to the 75W-140 baseline had unacceptable rust test results. Modified PAG candidates were developed but testing showed these 2nd generation candidates resulted in significantly more wear. DOW developed an oil soluble PAG (OSP) candidate that had much improved wear compared to any of the 2nd generation PAG candidates. In addition, the OSP candidate passed both the rust prevention and copper corrosion test.

Conclusions:

Ford Motor Company is developing a polyalkylene glycol (PAG) based axle oil, taking advantage of PAG's natural lubricity, high viscosity index, and excellent oxidation and shear stability. In the coming year Ford will continue to identify, test, and evaluate 2nd generation and OSP candidates with additive pack modifications. They will complete extreme pressure and anti-wear additive chemistry optimization to address gear rippling issue and complete surface analysis at ANL with Ford axle system materials including specific gear steels and elastomer seal materials.

Lubricant Formulations to Enhance Fuel Efficiency
A Novel Lubricant Formulation Scheme for 2% Fuel Efficiency Improvement

DOE-VTO TFA Lead: Kevin Stork
TARDEC TFA Lead: Dr. Jay Dusenbury

Principal Investigator:
Dr. Q. Jane Wang

Affiliation:
Mechanical Engineering, Northwestern University
Tech A219, 2145 Sheridan Road
Evanston, IL 60208

Project Start: 01/10/2013
Estimated Completion: Q2 FY17

Objective(s):

- Develop novel lubricant formulations for improving the fuel efficiency of light-, medium-, heavy-duty, and/or military vehicles by at least 2% without adversely impacting vehicle performance or durability.

Strategic Context:

- This project aligns with TARDEC's LoE 1.4 and Army S&T Challenges to improve operational energy, as well as, DOE's mission to develop more energy-efficient and environmentally friendly technologies.

Accomplishments:

- Northwestern University has synthesized three major families of heterocyclic additives for boundary lubrication friction reduction.
- These compounds are sulfur and phosphorus free and have produced significant reductions in friction (20 – 40%) and wear (~95%) compared to base oils and fully formulated 5W-30 oil.
- Northwestern University has also developed a method to functionalize solid-state-lubricant nanoparticles (h-BN and B2O3) resulting in stable solutions in PAO. Scuffing resistance of the PAO base oil has been increased by a factor of three with 1wt% h-BN nanoparticle.

- Successful synthesis of target PMMA-PAO di-block copolymer, evidenced by NMR and GPC analyses.
- An ultra-thin film measurement system employed to evaluate boundary lubrication process.
- The results that at high temperatures, the heterocyclic FMs offer stronger enhancement of the boundary lubrication films than the based oil and the commercial products. Such film reinforcement is well in accord with our previous boundary friction test results
- Evidence of enhanced surface adsorption by heterocyclic molecules further confirmed by more MD simulations on an iron dioxide substrate.
- The synergistic effect that a further improved wear performance resulted from the mixture of capped nanoparticles and heterocyclic FMs.

Introduction:

Significant fuel economy benefits can be realized through optimized lubricant formulations utilizing new additive/base oil combinations to control friction, wear, and traction. Northwestern University is synthesizing new friction modifiers (FM) to reduce boundary and mixed lubrication regime friction to enhance the performance of low viscosity lubricants. Northwestern is developing temporary shear thinning viscosity modifiers, and functionalized nanoparticles which reduce friction and wear in the hydrodynamic and boundary lubrication regime respectively.

Approach:

The objective is to be achieved through: (1) reducing friction due to asperity rubbing in start-up and low-speed operations during which boundary friction controls energy dissipation, (2) temporarily reducing the lubricant viscosity (temporary shear-thinning) in medium- to high-speed cruise operations during which viscous loss is the dominant mechanism for energy dissipation, and (3) suppressing oil aeration or foaming responsible for lubrication breakdown in high-speed operations. The proposed research is expected to result not only in at least 2% fuel efficiency improvement, but also enhanced performance of the powertrain/drivetrain components.

Results and Discussion:

Nanoscratch tribometry had shown that substrates dip coated in the heterocyclic FM additive followed by washing were still able to reduce friction, meaning that there was an additive layer bound to the steel surface. The X-ray photoelectron spectroscopy (XPS) and X-ray reflectivity (XRR) have been used to confirm the presence of nitrogen in the adsorbed layer and determine the thickness of this adsorbed layer, which is likely a stack of molecules on the surface, rather than a monolayer. Surface roughness measurements indicate that the surface coverage is fairly even throughout and there were no spots without additive coverage.

MD simulations have shown that additive molecules are capable of strongly adsorbing to a surface. The alkyl chains introduce a large entropy to the system and sterically block the molecule from being bound to the surface; however they are necessary for solubility of the molecules in the base oil. If the number of alkyl chains can be reduced, while maintaining solubility, more strongly adsorbed layers may reduce friction further.

Lubricant film formations in different lubrication regimes were evaluated at 25 ºC, 75 ºC, and 125 ºC under pure rolling operations using an elastohydrodynamic lubrication (EHL) measurement system. Two commercial friction modifiers (FMs) including a fatty amine and a fatty diamine were studied for comparison with the heterocyclic additives. Variation of lubricant film thickness against the rolling speed were recorded during the EHL tests. For the pure rolling friction applications, only small amounts (i.e. 0.1 wt %) of heterocyclic FMs are needed for forming a significantly reinforced boundary lubrication film. Generally speaking, FMs play two principal roles in boundary lubrication regime: 1) reinforcement of the boundary lubrication film; and 2) enhancement of surface adsorption. Selected commercial FMs could improve surface adsorption only. The novel heterocyclic FMs developed in this research are able to improve both principal roles, which are believed to contribute to their unique capabilities of the continuous friction reduction at elevated temperatures. It is also such reinforced boundary lubrication films that effectively prevent the steel disks from wear damage by creating sufficient asperity spacing between the mating surfaces.

Boron oxide is commonly used as a solid phase anti-friction additive for extreme conditions. Functionalize boron oxide particles with alkyl chains have improved its solubility in a base oil. Investigation of the effect of different types of functional groups on the morphology of the final product and ultimately, the ability of these additives to reduce friction and wear is ongoing. It has been found that neither the capping agent nor the B2O3 nanoparticles alone have the same impact on reducing wear as the properly functionalized nanoparticle mixed in PAO4. Compared to the wear performance of PAO4 base oil testing, the capped nanoparticle effectively reduces wear by more than an order of magnitude.

Conclusions:

Northwestern University continues to make progress towards its stated goals. In the coming year they will finalize synthesis of the copolymer viscosity modifier, complete the development of a friction modifier package using the heterocyclic and nanoparticles additives, and develop a strategy for using heterocyclic additives, functionalized nanoparticles, and copolymer viscosity modifiers in a final lubricant formulation.

Remainder of Page Intentionally Blank

This Page Intentionally Blank

AVPTA Technology Focus Area 4: Alternative Fuels & Lubricants

Lubricant Formulations to Enhance Fuel Efficiency
Improved Fuel Economy through Formulation Design and Modeling

DOE-VTO TFA Lead: Kevin Stork
TARDEC TFA Lead: Dr. Jay Dusenbury

Principal Investigator:
Dr. Gefei Wu

Affiliation:
Valvoline, a Division of Ashland Inc.
3499 Blazer Parkway
Lexington, KY 40509-1850

Project Start: 01/10/2013
Estimated Completion: Q4 FY16

Objective(s):

- Develop novel lubricant formulations that are expected to improve the fuel efficiency of medium-duty, commercial and military vehicles by at least 2%.
- Develop engine, transmission and axle lubricant formulations, modeling and simulation.

Strategic Context:

- This project aligns with TARDEC's LoE 1.4 and Army S&T Challenges to improve operational energy, as well as, DOE's mission to develop more energy-efficient and environmentally friendly technologies.

Accomplishments:

- Valvoline has developed two candidate engine oils. Candidate 1 meets API commercial category PC-11 and is a 5W-30. Modeling results predict a 2.04% fuel economy improvement compared to baseline. Candidate 2 has a lower viscosity and uses a bio-base oil and friction modifier. Modeling predicts a 2.12% fuel economy improvement.
- Bench top boundary friction and wear results indicate that candidate 2 has lower overall friction and wear.
- Engine testing in an 8.9L heavy-duty diesel engine resulted in overall cycle averages of from 1% to 1.7% fuel economy improvement, while some operating points resulted in fuel economy improvements of almost 5%.

- Axle rig efficiency test results indicated that candidates performed better than the baseline in all test conditions. Temperature reductions of greater than 16°C, and efficiency improvement between 0.63% to 1.36% where measured under demanding conditions.

Introduction:

The objective of this project is to develop novel lubricant formulations that are expected to improve the fuel efficiency of medium -duty, commercial and military vehicles by at least 2% (improvement based on comparative results from engine dynamometer testing, chassis dynamometer testing or test track, e.g., SAE J1321) without adverse impacts on vehicle performance or durability. This will be accomplished through engine, transmission and axle lubricant formulation design, modeling and testing.

Approach:

Start with fundamental understanding of tribology, lubricant rheology, and oil formulations. Candidate formulations are optimized in the lab using bench tests and analysis led design (mathematical models). Candidate oils are then subjected to engine and/or mechanical testing. Oils with proven lab performance are taken to the field for final validation.

Results and Discussion:

Valvoline has been using their significant experience in lubricant formulation to develop optimized heavy duty diesel engine oil, transmission fluid, and axle oil formulations. Engine and axle dynamometer testing of candidate engine and axle oils have resulted in average fuel economy improvements of 1.7% and 1.36% respectively. A new low viscosity transmission fluid meeting Allison Transmission's TES-295 specification has been developed.

Conclusions:

Valvoline has successfully demonstrated significant fuel economy improvements in laboratory bench and dynamometer testing. In the final year of the project Valvoline will verify an overall fuel economy increase of greater than 2% in vehicle testing in accordance with SAE J1321.

Remainder of Page Intentionally Blank

AVPTA Technology Focus Area 4: Alternative Fuels & Lubricants

Lubricant Formulations to Enhance Fuel Efficiency
Modified Thermoresponsive Hyperbranched Polymers for Improved Viscosity and Enhanced Lubricity of Engine Oils

DOE-VTO TFA Lead: Kevin Stork
TARDEC TFA Lead: Dr. Jay Dusenbury

Principal Investigator:
Dr. Lelia Cosimbescu

Affiliation:
Pacific Northwest National Laboratory (PNNL)
902 Battelle Blvd.
P.O. Box 999, MSIN K2-44
Richland, WA 99352

Project Start: 01/10/2013
Estimated Completion: Q2 FY16

Objective:

- Develop novel lubricant formulations for improving the fuel efficiency of light-, medium-, heavy-duty, and/or military vehicles by at least 2% without adversely impacting vehicle performance or durability.

Strategic Context:

- This project aligns with TARDEC's LoE 1.4 and Army S&T Challenges to improve operational energy, as well as, DOE's mission to develop more energy-efficient and environmentally friendly technologies.

Accomplishments:

- PNNL has completed all of the tasks that involved synthesis and viscosity screening. All synthesized compounds were evaluated by room temperature fiction studies at ORNL.
- Three of hyperbranched viscosity modifier (VM) compounds were selected for further friction and wear evaluation at 100°C to provide a means for narrowing down to one candidate for scale-up.
- All blends, base stock with polymer additive, have a lower coefficient of friction (COF) than the base oil. The chosen candidate demonstrated a modest wear increase compared to benchmark additive, which is undesirable, but the COF was lower which should translate into greater fuel efficiency by reducing points of internal friction.

Introduction:

Significant fuel economy benefits can be realized through optimized lubricant formulations utilizing new additive/base oil combinations to control friction, wear, and traction. Transportation sources emitted 29% of all U.S. greenhouse gas (GHG) emissions in 2007 and have been the fastest-growing source of U.S. GHG emissions since 1990. Any steps taken towards more fuel efficient vehicles will reduce GHG emissions and by extension and facilitate a cleaner environment. PNNL has focused on designing additives that will lower engine friction and potentially drive train friction, by favorably modifying the lubricant viscosities at high temperatures.

Approach:

Develop and test novel polymers with a hyperbranched architecture as viscosity modifiers and lubricity enhancers to improve fuel efficiency, and ultimately impact fuel economy. The polymers will be engineered to change their molar volume upon heating, thereby increasing the viscosity of the oil, as well as providing terminal groups which will provide the desired lubrication at surface boundaries. The objective for the first component of the project is to design, synthesize and screen molecular structures with hyperbranched architectures for proof-of-concept experiments. This activity includes: 1) designing analogs with the most promising features and easiest to prepare; 2) synthesizing selected compounds; 3) performing screening tests to select the best candidates for further testing. Any design shortcomings will be addressed prior to the second component of the project, which is the tribological and engine testing portion.

Results and Discussion:

PNNL has successfully synthesized several candidate viscosity modifiers (VMs). Friction and wear studies have been completed by Oakridge National Laboratory (ORNL). All candidate VMs resulted in lower coefficient of friction then the base oil, but some also resulted in increased wear compared to a benchmark VM. Based on these results a final candidate VM has been selected for scale up. More than 1000 grams have been produced and will be used for further blend studies and engine testing. PNNL has been working with a major additive supplier to identify an appropriate detergent/inhibitor (DI) package for blending a fully formulated engine oil. A 0W-20 grade engine oil is being planned for final engine testing which will be conducted by ORNL.

Conclusions:

With the selection of a final candidate for engine testing, the project approaches its end. A final blend study is underway to narrow the concentration required to obtain a 0W-20 oil which then can be implemented in the final formulation for engine testing.

Remainder of Page Intentionally Blank

AVPTA Technology Focus Area 4: Alternative Fuels & Lubricants

Technology Development to Improve Fuel Efficiency through Friction Reduction

DOE-VTO TFA Lead: Mr. Kevin Stork
TARDEC TFA Lead: Dr. James Dusenbury

Principal Investigator:
Dr. Stephen Hsu

Affiliation:
George Washington University
GW Energy Initiative
Suite 323, room 323C
Exploration Hall, 20101 Academic Way
Ashburn, VA 20147

Project Start: 03/02/2015
Estimated Completion: Q1 FY 18

Objective:

- To develop friction reduction technology capable of improving fuel efficiency of legacy vehicles by at least 2% over the baseline technology using low viscosity lubricants and material technology options (surface textures, diamond-like carbon films, and bonded lubricant films) without sacrificing durability.

Strategic Context:

- Demonstrate a battlefield fuel reduction and reduce the logistics burden.
- Increase Power Density and Energy Efficiency resulting in increased vehicle range, endurance and operational tempo, while reducing the number of logistics convoys on the battlefield.
- Increasing fuel efficiency of ground vehicles to Reduce Life Cycle Costs.

Accomplishments:

- To develop a new low viscosity (GF-6 A/B) lubricant with 2% fuel economy gain over the baseline technology.
- To develop a time release microencapsulation technology ready to be used in new lubricant formulations to impart additional stability, friction and wear protection.

Introduction:

In lubricant formulations, base oils of various purities are the solvent and additives are the solute. Additives are added to the solution to impart various performance bench marks. Two types of additives are used, those that control the bulk property such as antioxidants, dispersants, detergents, viscosity modifier (VM), and antifoam; and those that control surface properties, such as antiwear, friction modifiers, corrosion inhibitors, rust inhibitors, and surface deactivators. The bulk property control agents are either neutrally charged or less polar than the surface active agents; the surface active agents have somewhat hierarchical polarity stacking order to arrange themselves against the sliding surfaces. The antiwear agent has to be able to adsorb and react with the metal surface to perform its antiwear function, so the decomposition products of the antiwear agent; ZDDP (zincdialkyl dithio-phosphate) have to react with the surface active sites (3). The formulation has to be delicately balanced to avoid precipitations and adverse additive-additive interactions rendering some or most of the additives non-functioning.

Over the decades, the basic lubricant chemistries have remained the same but modifications to the molecular structures and finer control have been made. The total amount of additives used, however, has grown steadily to accommodate increasing performance demands. Friction modifiers were introduced in the 1980s and a new engine dynamometer test Seq. VI was developed to measure their effectiveness.

Approach:

We propose four tasks to reach the goal (multiple lines of defense against friction deterioration and wear):

Task 1:

Valvoline will supply a commercial SAE 5W-30 GF-5 lubricant to GWU as the baseline formulation. GWU/Valvoline will work jointly to develop a next generation low viscosity fuel efficient lubricant formulation with at least 2% higher fuel efficiency as measured by Seq. VI engine test. GWU will screen new friction reduction chemistry and tougher antiwear film chemistry in bench tests to identify potential candidates. Valvoline will incorporate the successful candidates into the formulation for testing. The new formulation will be tested to see whether it achieves the fuel efficiency target (as measured by Seq. VI engine tests).

Task 2:

GWU will develop microencapsulation technique (encapsulation, release mechanism, and survivability through engine operation) to create the second line of defense to provide time-release of additives on demand as an option for task 1.

Task 3:

GWU will work with GMC on controlling engine component surface topography and fabricate surface textures to increase film thickness and enable more hydrodynamic lubrication mode in the most significant engine components (identified by GMC) to reduce friction throughout a selected engine model. When the specific engine component operation requires additional durability, GWU will deposit DLC film with bonded chemical film on the engine component to provide robust durability.

Task 4:

The team will integrate the improved engine component (friction surface technology in task 3) with the new energy efficient lubricant to evaluate the combined benefits and robustness of the system durability by bench scale simulation tests for a selected engine component. If the results warrant further testing and development, the industrial partners/and or DOE may consider further investment to commercialize the technology.

Results and Discussion:

The two oils, one GF-6A SAE 0W-20 and the baseline oil 2014 GF-5 Premium commercial oil, 5W-30 were tested for fuel economy gains against the test stand reference oil (a 20W-30 0il). The tests were conducted on a single engine, same engine test stand, back to back, the most reliable way of measuring fuel economy difference of two oils. Results are shown in Table 1. The tests were repeated to ensure that the measured fuel economy improvement results are reliable beyond the test variability. The % increase is against the test stand reference oil. For example, the new candidate oil has a FEI-1 of 1.84% and 2.13% gain over the test stand reference oil and the 2014 commercial oil which has a FEI-1 of 1.19% and 1.01% gain over the reference oil, so the net gain of fuel economy of the candidate oil over the 2014 baseline oil is (1.84%+2.13%)/2 - (1.19% +1.01)/2=0.89% for the candidate oil. FEI-2 is the results for the aged oil and therefore, the sum of the fuel economy gains is equal to FEI-1 + FEI-2. In this case, we have a net gain of 2.39%.

The Engine Seq. VI E test procedure was run according to the ASTM release VI E test protocol issued on July 14, 2014. The Seq. VI E test has not been finalized and the Multiple Test Acceptance Criteria has not been established. So the test results cannot be certified as a GF-6 test results yet. The test results reflect the latest fuel economy test procedure at this time.

The test stand will be referenced and certified when the Seq. VI E become the official. To avoid the potential issue of engine test variability statistics, the two oils were run on the same engine, the same test stand, and back to back sequence tests. This way, the test variability and the stand variability will not be a factor. Since this is a new test not yet formalized, we decided to conduct a repeat test on the 2014 commercial baseline oil to gauge the repeatability of the test. The test result was shown in Table 1, suggesting excellent repeatability.

Microencapsulation of antiwear additive poses special challenges compared to encapsulation of other additives. Antiwear additives such as ZDDP contain strong polar species such as phosphites and phosphates which often interfere with the emulsifiers used in the encapsulation processes. After extensive search and experimentations with various emulsifiers, we finally were able to successfully encapsulate ZDDP, the most common antiwear additive.

Conclusions:

These test results are valid engine test results. Officially the results cannot be considered as the GF-6 specification test results yet until the official GF-6 engine tests are finalized by voting.

Conclusion: the newly developed 0W-20 “GF-6A” prototype oil was successfully tested in the Seq. VI E tests and the results showed a 2.39% fuel economy over the baseline oil of 2014 GF-5 commercial 0W-30 oil.

The project is progressing on schedule. The search for supplemental antiwear additive combinations has shown reasonable candidates to boost the wear resistance in ultralow viscosity lubricants. Next quarter, we will conduct Sequence VI engine test to measure fuel economy of 0W-20 formulation to see whether it can achieve 2% fuel economy improvement. The optimization of friction modifier-antiwear additive combination to provide synergistic performance will continue into the 4th quarter. The surface texture design on the main shaft bearing will be finalized with additional inputs from GM. We have succeeded encapsulated antiwear additive and show that the encapsulated additive retains the same functionality.

Table on Next Page

Table:

	New Candidate	**New Candidate repeat**	**2014 commercial baseline oil**	**2014 commercial baseline oil repeat**	
Run No.	6-3-34-3	6-6-34-6	6-4-34-4	6-5-34-5	
EOT Date:	8/28/2015	10/28/2015	9/18/2015	10/13/2015	
Test stand	Number 6	Number 6	Number 6	Number 6	
Engine number	34	34	34	34	
EOT Engine Hours	887	1525	1100	1310	Improvement for Candidate (0W-20) Over Benchmark (5W-30)
Oil Code:	**JB1-105-1**	**JB1-113-1**	**JB1-106-1**	**X35951-017-01**	
Oil Vis-grade	**0W-20**	**0W-20**	**5W-30**	**5W-30**	
FEI-1 (new broken-in)	1.84%	2.13%	1.19 %	1.01%	0.89 %
FEI-2 (aged)	2.37%	2.28%	0.72 %	0.92%	1.51 %
FEI-SUM	4.21%	4.41%	1.91 %	1.93%	2.39 %

Table 1. Fuel economy increase as measured by Engine Dynamometer Seq. VI "E"

Remainder of Page Intentionally Blank

This Page Intentionally Blank

AVPTA Technology Focus Area 4: Alternative Fuels & Lubricants

Technology Development to Improve Fuel Efficiency through Friction Reduction

DOE-VTO TFA Lead: Mr. Kevin Stork
TARDEC TFA Lead: Dr. James Dusenbury

Principal Investigator:
Dr. Arup Gangopadhyay

Affiliation:
Ford Motor Company
2101 Village Road
Dearborn, MI 48121

Project Start: 01/23/2015
Estimated Completion: Q1 FY 18

Objective:

- To develop and demonstrate friction reduction technologies for light, and medium, vehicles that improve fuel efficiency of future vehicles by at least 4% without adverse impacts on engine durability.

Strategic Context:

- Demonstrate a battlefield fuel reduction and reduce the logistics burden.
- Increase Power Density and Energy Efficiency resulting in increased vehicle range, endurance and operational tempo, while reducing the number of logistics convoys on the battlefield.
- Increasing fuel efficiency of ground vehicles to Reduce Life Cycle Costs.

Accomplishments:

- Provided ANL with sample hardware, pistons and rings, to begin practice coating.
- ANL successfully produced samples of VN-Ni coating on to piston and rings with ~1 µm thickness and no signs of delamination. Further optimization of coating sample piston and rings will continue.
- ANL conducted preliminary screening of coatings using a benchtop friction and wear tester, High Frequency Reciprocating Rig (HFRR).

- Design of experiments and a workflow plan were developed between Ford and Comau Inc. to pursue PTWA Deposition development and validation.

Introduction:

In lubricant formulations, base oils of various purities are the solvent and additives are the solute. Additives are added to the solution to impart various performance bench marks. Two types of additives are used, those that control the bulk property such as antioxidants, dispersants, detergents, viscosity modifier (VM), and antifoam; and those that control surface properties, such as antiwear, friction modifiers, corrosion inhibitors, rust inhibitors, and surface deactivators. The bulk property control agents are either neutrally charged or less polar than the surface active agents; the surface active agents have somewhat hierarchical polarity stacking order to arrange themselves against the sliding surfaces. The antiwear agent has to be able to adsorb and react with the metal surface to perform its antiwear function, so the decomposition products of the antiwear agent; ZDDP (zincdialkyl dithio-phosphate) have to react with the surface active sites (3). The formulation has to be delicately balanced to avoid precipitations and adverse additive-additive interactions rendering some or most of the additives non-functioning.

Over the decades, the basic lubricant chemistries have remained the same but modifications to the molecular structures and finer control have been made. The total amount of additives used, however, has grown steadily to accommodate increasing performance demands. Friction modifiers were introduced in the 1980s and a new engine dynamometer test Seq. VI was developed to measure their effectiveness.

Approach:

Ford Motor Company (Ford) is investigating a novel way to surface texture engine components in Plasma Transferred Wire Arc (PTWA) coating. PTWA utilizes a cathode tube and plasma gas to sputter low carbon steel from a wire feedstock onto a surface. The scope of this effort includes altering the operating voltage and amperage of this apparatus to control the engine component surface porosity level. Highly porous surfaces could better entrain lubricant and hold it locally even under severe conditions.

Ford is also looking into a nanocomposite coating where a hard metal material (metal oxide or metal nitride) is incorporated into an array of a catalyst material. Argonne National Laboratory (ANL) will be involved for this role due to their expertise and knowledge on development and deposition of nanocomposite coatings on pistons and piston rings.

Results and Discussion:

Weekly meetings have been scheduled and conducted between Ford and Comau Inc. in order to review the progress of PTWA Deposition development and validation.

Conduct surface finish and dimensional inspection of liners in support of parameter development. Each liner is tracked by part and serial number through the manufacturing, coating deposition, honing and analysis steps, with liners being divided into Tier 1 and Tier 2 categories based on Aluminum substrate porosity after mechanical roughening. Liner Workflow Plan was developed and reviewed with Comau at 7-May-15 meeting. See Figure 1.0 below.

Using 83mm diameter cylinder bore liner samples, (4) L18 orthogonal arrays were proposed. Design of Experiments (DOE) was expected to start with air pressure, wire feed rate, percent H2, plasma gas flow as the control parameters and nozzle design and liner diameter as the noise factors. In order to reduce the number of samples needed and meet program timing, the DOE was reduced to an L9 and the PTWA Deposition development started. First batch of (20) roughened liners were delivered to Comau on 22-April-15. Initial trials with (3) different nozzle designs did not produce significant increase~~s~~ in porosity levels. Porosity level for all three designs was ~1%, leading to requirement for torch parameter and nozzle modification and further evaluations. With modifications to the following parameters, nozzle design (changes to plume geometry), traverse speed, wire feed and amperage increase (up to 100A), coatings with porosity levels ranging from 0.2 to 6.5% were achieved. Additionally, a new nozzle designed to reduce particle speed appears to have a positive effect on porosity. Levels of 3-10% were achieved in initial sample trials. Based on these results, DOE control parameters (3 levels) were modified to atomizing gas pressure (psi), wire feed rate (in/min), plasma gas flow and electrical current (Amps) and nozzle design (standard and new) and liner diameter as noise factors (83 and 92.5mm). To determine reproducibility of coating deposition and control parameter coupling effects for each nozzle design, a series of L4 coupon tests are being conducted at Comau. The first series of L4 samples show a strong correlation between atomizing gas pressure and porosity, slight correlation to wire feed rate and no correlation to traverse speed. Results of this analysis will enable the team to confirm control and noise factor levels and finalize L9 DOE. Agreement was made for Ford to develop process for cross lab porosity evaluation using 8 disk blind sampling process. These evaluations are to be completed prior to starting 83mm liner trials.

Conclusions:

The objectives for the project management portion of the work are to provide project planning, coordination, and reporting as required to successfully achieve the overall objectives of the project. The Recipient will maintain an up-to-date Project Management Plan designed to achieve the project objectives and cover the entire Project Period. The PMP will be updated and submitted as part of the continuation application prior to the initiation of each budget period as outlined in the deliverables section below. Monthly call in meetings with DOE Project Manager, Adrienne Riggi. Continue as scheduled. The project is progressing on schedule. A large amount of upfront planning was necessary to coordinate work efforts, but have been successfully completed. Laboratory benchtop testing has been initiated to screen different potential candidates to pursue.

Figures and Tables Start on Next Page

Figures and Tables:

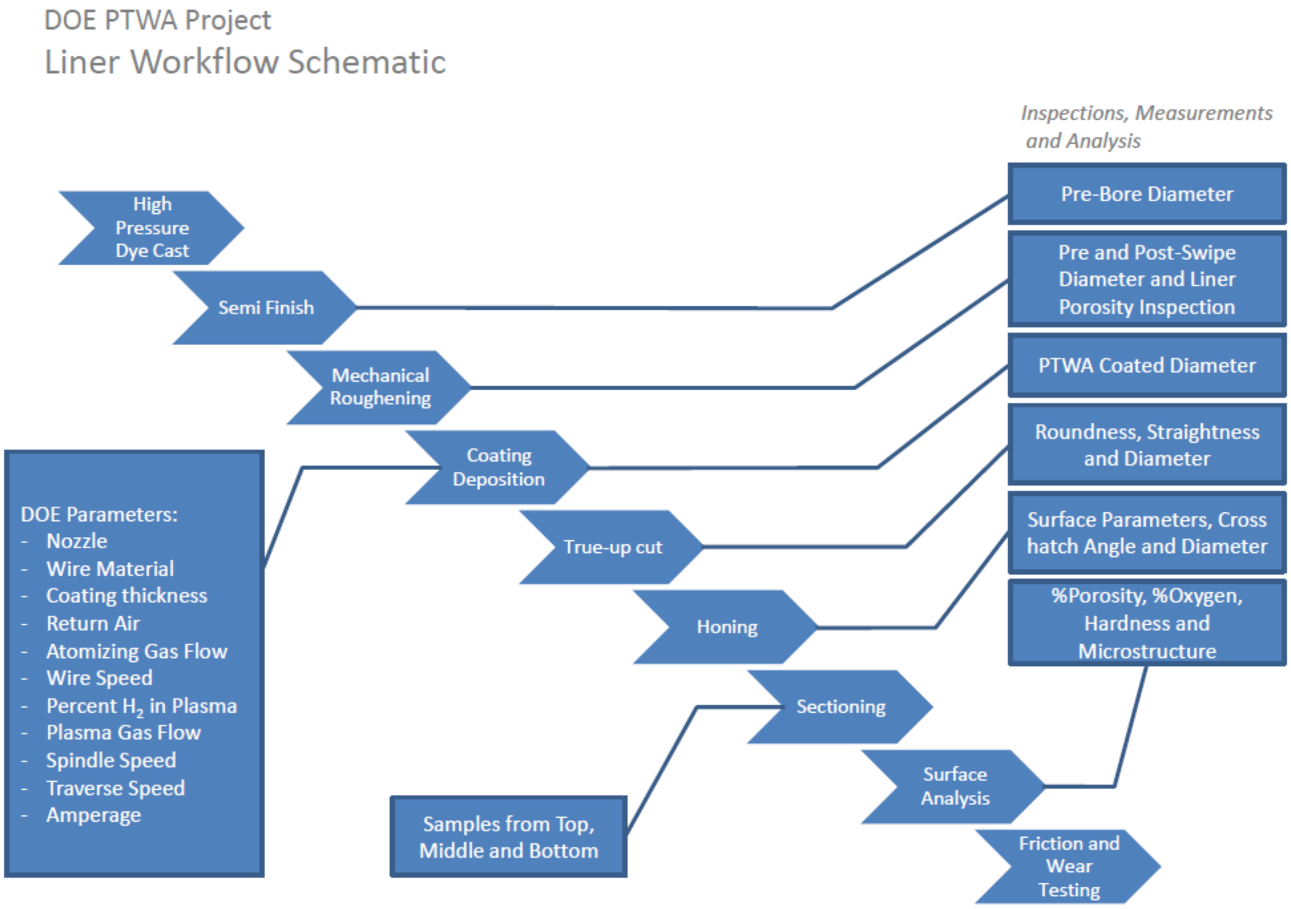

Figure 1. Linear Workflow Plan

Remainder of Page Intentionally Blank

Technology Development to Improve Fuel Efficiency through Friction Reduction

DOE-VTO TFA Lead: Mr. Kevin Stork
TARDEC TFA Lead: Dr. James Dusenbury

Principal Investigator:
Dr. Jun Qu

Affiliation:
Oak Ridge National Laboratory
1 Bethel Valley Road
Oak Ridge, TN 37831

Project Start: 08/03/2015
Estimated Completion: Q3 FY 18

Objectives:

- To further develop the ionic liquid-additized low viscosity engine oil meeting the GF-5/6 specifications and possessing superior lubricating characteristics.
- Expand the ionic liquid additive technology to rear axle lubricant to gain a combined 4% improvement in vehicle fuel economy.

Strategic Context:

- Demonstrate a battlefield fuel reduction and reduce the logistics burden.
- Increase Power Density and Energy Efficiency resulting in increased vehicle range, endurance and operational tempo, while reducing the number of logistics convoys on the battlefield.
- Increasing fuel efficiency of ground vehicles to Reduce Life Cycle Costs.

Accomplishments:

- No major accomplishments to date. Delayed start, but have successfully kicked off.

Introduction:

On 9/28/2013, the ORNL-GM team successfully concluded a 4-year joint project sponsored by DOE Vehicle Technologies Office (VTO) under a Cooperative Research and Development Agreement (CRADA) for developing ionic liquids as next-generation AW additives for engine lubrication. This team made a major breakthrough in developing new groups of oilmiscible ionic liquids (ILs)3-7, with high thermal stability, ashless, non-corrosiveness, and most importantly effective AW characteristics. Fundamental investigation has correlated the anti-wear and friction reduction mechanisms of IL additives to their physical (absorption) and chemical (tribofilm formation) interactions with the metallic bearing surfaces3-5. In addition, accelerated catalyst aging tests of the IL suggested potentially less adverse effects on three-way catalysts compared to ZDDP6. Working with Lubrizol, the team had developed a prototype IL-additized fully-formulated automotive engine oil (the first ever in the literature). The IL-additized engine oil has low-viscosity (comparable to the pending SAE grade 8) and has demonstrated promising lubricating performance6. High-temperature, high-load (HTHL) engine tests showed similar engine wear and oil aging behavior between the IL-additized low-viscosity engine oil and the Mobil 1 5W-30 engine oil6. Further, Sequence VID engine efficiency dynamometer tests of this prototype IL-additized engine oil demonstrated an improved fuel economy by 2.01% benchmarked against the Mobil 1 5W-30 engine oil6. The initial success of our ionic liquid additive technology has been highlighted at Inside Science8 and Green Car Congress9, and starts gaining interest from both academia and industry.

Approach:

There are a number of bearing components in an automotive vehicle. The second largest parasitic friction induced energy loss is the 3-5% at the rear axle (next to the 10-12% in the engine) 1, 2, and therefore is identified as the next application for the IL additive technology. GM's modeling predicts a potential recovery of 0.75-1.5% vehicle fuel economy by using a lower viscosity oil. This study proposes to apply ionic liquids to mitigate the challenge of wear protection induced by the reduced oil viscosity. The bearing interface for the rear axle is very different from that in the engine, therefore the IL chemistry will be tailored to better handle the much higher contact stress and longer oil service life required for the rear axle lubricant. This study will also provide us the opportunity to gain deeper fundamental understanding of ILs' anti-wear mechanism such as the roles of the cations and anions, and their advantages in surface absorption and tribofilm formation compared to conventional neutral AW additives. Such understanding will strengthen the scientific basis that we have been building for further material optimization and product development.

ORNL will be leading this joint project with main responsibilities for IL design and synthesis, tribological bench tests, tribofilm characterizations, lubrication modeling, and emission analysis. GM will work with Lubrizol to formulate IL-additized engine and rear axle lubricants. GM will conduct complementary tribological bench tests, multi-cylinder engine dynamometer tests, and vehicle tests.

Results and Discussion:

Awaiting first quarterly report.

Conclusions:

Awaiting first quarterly report.

AVPTA Technology Focus Area 4: Alternative Fuels & Lubricants

Technology Development to Improve Fuel Efficiency through Friction Reduction: Method to Measure, Predict and Relate Friction, Wear and Fuel Economy

DOE-VTO TFA Lead: Kevin Stork
TARDEC TFA Lead: Dr. Jay Dusenbury

Principal Investigator:
Dr. Steve Gravante

Affiliation:
Ricardo, Inc.
40000 Ricardo Drive
VanBuren Township, MI 48111

Project Start: 12/15/2014
Estimated Completion: Q2 FY16

Objectives:

- To provide the lab-scale fundamental data (open source), model correlations, and full scale verifications to enable more accurate predictions of friction coefficient and wear for a wider range of engines, lubricants, and operating conditions than currently exists.
- To extend the approach to sliding and rolling friction in gears.

Strategic Context:

- Demonstrate a battlefield fuel reduction and reduce the logistics burden.
- Increase Power Density and Energy Efficiency resulting in increased vehicle range, endurance and operational tempo, while reducing the number of logistics convoys on the battlefield.
- Increasing fuel efficiency of ground vehicles to Reduce Life Cycle Costs.

Accomplishments:

- A RINGPAK model was developed to simulate the reciprocating motion of lab-scale testing.
- Lab scale testing has been initiated using actual engine components to better simulate actual contact geometries.
- Stribeck mapping for an engine speed and load for a typical diesel engine.

Introduction:

Friction forces and wear performance in engines and other driveline components can be calculated from equations that capture the understanding of the fundamental physics involved. However, accuracy of the results is dependent on measurement or estimation of the friction coefficient used in the calculations. For contacting surfaces in any component system (piston ring or skirt and liner; bearings; gears, etc.) the friction coefficient is a function of lubricant viscosity, relative speed, surface properties and load, which is captured in a Stribeck curve.

For a given set of operating conditions the curve provides a friction coefficient which can be used to calculate FMEP (Friction Mean Effective Pressure). FMEP is a quantification of losses due to friction during engine operation. It combines all types of friction losses from asperity or boundary friction (caused by metal to metal contact) to hydrodynamic friction (caused by viscous losses) and mixed regimes between. Once FMEP is quantified, whether predicted or measured, it can be used to calculate friction impacts on fuel economy.

Approach:

In this program Ricardo will use existing computer models to specify relevant Stribeck conditions (speed and load) for light duty and heavy duty OEM engines (one or more of each). ANL and EMA will make careful measurements of friction and wear using high-precision lab-scale test rigs as a function of surface and lubricant properties over a range of operating temperatures, loads, and speeds typical of engine (or other) components. The data generated will be used, with some processing, as input to Ricardo‟s codes to improve correlations between model FMEP predictions and measurements of FMEP in full scale engine or driveline tests.

FMEP is equal to the difference between IMEP (Indicated Mean Effective Pressure), which is the theoretical amount of power the engine can produce from the amount of fuel burned, and BMEP (Brake Mean Effective Pressure), which is the amount of power delivered by the crankshaft. Because FMEP is the relatively small difference between two relatively large numbers, accuracy can be poor when determining FMEP by calculating IMEP and subtracting measured BMEP. It can be measured directly in motored tests, but they lack some of the physical realities (temperatures, combustion forces, etc.) of fired engines. Methods to calculate FMEP from well verified models are needed.

The “technology” developed in this project will be FMEP maps as a function of load and speed which, when coupled with IMEP, can be used with suitable weighting factors to predict fuel consumption for any user-specified driving cycle. The lab-scale rig data will be used to predict wear loads (cycle averaged as a function of speed and load) to compare with wear-load-sliding distance calculations. Lubricant effects will be evaluated in terms of both friction losses and wear performance. The models will be used to predict fuel savings and wear, as validated with engine dyno tests by Ricardo and Navistar using an off-the-shelf high viscosity lubricant and a friction-modified low-viscosity synthetic lubricant. Engine tear-down tests at INL will provide data on engine component wear in fleet-tested vehicles.

Results and Discussion:

A test matrix was developed for lab-scale testing to be conducted on actual engine components provided by a subcontractor. This testing will provide the needed data for subsequent tasks as well as facilitate comparison to full component lab-scale test results

Stribeck mapping has been initiated that entails the mapping of Stribeck parameter as a function of engine speed and load for a typical diesel engine. It will be used to identify the friction regime in which the engine is operating as a function of speed and load and guide the development of an appropriate test matrix for the lab-scale bench tests.

A ROL RINGPAK model has been developed and includes all of the essential engine geometries and typical material properties of the Isuzu engine that will be used in subsequent motored and fired dyno tests. The square wave prediction of RINGPAK needs to be understood and is currently under investigation. In addition, further development will include fine-tuning material surface properties, updating the analysis with new oil properties, and determination of ideal lubrication model and film thickness.

Conclusions:

The ROL RINGPAK model simulates the applied normal load (L) by controlling the ring tension, Fd. To replicate the sinusoidal motion of the ROL test rig within RINGPAK, a long crank coupled with a short crank throw is imposed on the RINGPAK model to provide a stroke comparable to ROL test rig (i.e., 20 mm). The model has been initially verified with further validation scheduled. The supporting stribeck mapping and engine component lab-scale testing have been verified.

Remainder of Page Intentionally Blank

This Page Intentionally Blank

AVPTA Technology Focus Area 4 Adjunct: Tire Efficiency

Improved Tire Efficiency through Elastomeric Polymers Enhanced with Carbon-based Nanostructured Materials

DOE-VTO TFA Lead: David Anderson
TARDEC TFA Lead: Dr. Jay Dusenbury

Principal Investigator:
Georgios Polyzos

Affiliation:
Oak Ridge National Laboratory (ORNL)
Oak Ridge, TN 37831-6054

Project Start: 4 Dec 2015
Estimated Completion: Ongoing

Objectives:

- Develop a novel surface-modified silica technology and demonstrate 4-6% improved fuel efficiency of truck and bus radial (TBR) tires built from the technology.
- Proposed fuel efficiency increase will be achieved while maintaining or improving tear strength and tread wear.

Strategic Context:

- Demonstrate a battlefield fuel reduction and reduce the logistics burden.
- Increase Power Density and Energy Efficiency resulting in increased vehicle range, endurance and operational tempo.
- Increase fuel efficiency of ground vehicles to Reduce Life Cycle Costs.
- Incorporate into Tactical Vehicles currently using commercial tires.
- Leverage technology to develop for military specific tires.

Accomplishments:

- Surface Energies of key rubbers were calculated at room temperatures.
- Twelve silica materials including controls were synthesized.
- Rubber compound testing was conducted on treated silicas.

Introduction:

Fuel-efficient silica fillers were adopted for passenger tires over 20 years ago. However, similar fuel-efficient benefits have not been realized for truck and bus radial tires. This project is focused on modifying silica to create an affinity for natural rubber as well as synthetic rubbers so that new, fuel-efficient truck and bus radial tires with optimized wear and tear properties result.

If half of the Class 8 vehicles on the road were to increase fuel efficiency by 4%, a potential 1.5 billion gallons of diesel, corresponding to $5.8B and 15 million metric tons of $C0_2$ emissions, could be saved.

Approach:

This project begins with the team systematically and thoroughly investigating the properties that enable uniform dispersion of silica in both natural and synthetic rubbers. This knowledge will drive custom silica synthesis. Once novel silicas are developed that can be uniformly dispersed throughout multiple rubber types, the team will develop new TBR tread compound formulas. The formulas will be tested at bench scale to predict performance with the best performers being built in actual tires so that on-tire testing can be completed. Two rounds of formulation and tire builds will be conducted during the project to confirm viability. At the conclusion of the project, the team will deliver prototype fuel-efficient tires and control tires. These tires will be evaluated at the Tank Automotive Research Development and Engineering Center (TARDEC).

This project will be conducted in close collaboration with Bridgestone Americas Tire Operations. Bridgestone's technical lead is Dr. Amy Randall, Manager of Advanced Materials.

Results and Discussion:

The surface energy/polarity measurements of rubber compounds were determined to provide a critical understanding of dispersion of fillers. (See Table 1).

Conclusion:

The Silica surface treatment in NR show a 47% reduction in rolling resistance indicator and an 18% improvement in abrasion resistance when compared to untreated control.

Ten treated silicas were synthesized with a variety of surface energies created.

Table on Next Page

Table:

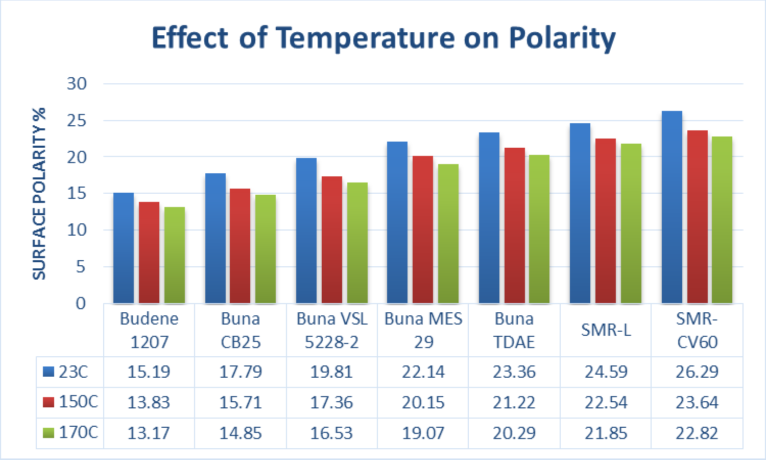

	Budene 1207	Buna CB25	Buna VSL 5228-2	Buna MES 29	Buna TDAE	SMR-L	SMR-CV60
🟦 23C	15.19	17.79	19.81	22.14	23.36	24.59	26.29
🟥 150C	13.83	15.71	17.36	20.15	21.22	22.54	23.64
🟩 170C	13.17	14.85	16.53	19.07	20.29	21.85	22.82

Table 1. Effect of Temperature on Polarity

Remainder of Page Intentionally Blank

This Page Intentionally Blank

AVPTA Technology Focus Area 5: Electrified Propulsion Systems

Non-Rare-Earth Integrated Starter Generator

DOE-VTO TFA Lead: Susan Rogers
TARDEC TFA Lead: Dean McGrew

Principal Investigators:
Joshua Tylenda and Joe Heuvers

Affiliation:
Ground Vehicle Power & Mobility
U.S Army TARDEC

Project Start: October 2012
Estimated Completion: Ongoing

Objectives:

- The TARDEC Advanced Propulsion Team, in collaboration with the DOE Vehicle Technologies Office, is working to develop and demonstrate two Integrated Starter Generators (ISG) without rare-earth permanent magnet materials suitable for onboard vehicle power generation.
- Most high-performance electric machines in hybrid electric applications use rare-earth magnets (NdFeB & SmCo) to achieve the required power and torque densities.
- This effort will additionally explore alternate electric machine topologies to achieve its goals.

Strategic Context:

Through the Non-Rare Earth ISG project, TARDEC's strategy is to develop the following:

- Ability of the motors to meet the specified performance without the use of rare-earth magnetic materials.
- Ability to perform according to schedule given issues and delays that have emerged.
- Ability to minimize audible noise signature of the Switched Reluctance (SR) generator topology.

To help manage risks, weekly status meetings are held to allow issues to be surfaced in a timely manner and mitigations put in place to resolve them in order to maintain schedule. Additional contract actions are planned to address audible noise of the SR topology.

Accomplishments:

- The Power Electronics & Electric Machinery Research group from Oak Ridge National Laboratory (ORNL) completed writing the control algorithms and software for the SR ISG and started testing the SR ISG with an inverter from Applied Power Systems (APS).
- The Spoke IPM testing and characterization was started at Remy's facility in Anderson, IN.
- GUI development for SR and Spoke IPM ISGs were completed by DCS.
- Work was started on controls optimization.
- Task 2 Preliminary design and Preliminary Design Review was completed.

Introduction:

The Non-Rare-Earth ISG project has the opportunity to reduce the cost of high-performance power generation hardware. This project seeks alternatives to rare earth designs in case of a supply disruption of rare-earth permanent magnet materials similar to events in 2010-2011. In July 2010, China cut its exports rare earth minerals by 72%. In September 2010, China temporarily cut rare earth exports to Japan due to a maritime dispute. In 2011, China had cut exports further and raised export tariffs for rare earths. The world remains almost completely dependent on China for rare earths.

In 2010, The Department of Energy had published a Critical Materials Strategy, ranking Neodymium and Dysprosium among the most critical from an importance and supply risk perspective. Both materials are used in the highest performance Neodymium Iron Boron (NdFeB) permanent magnets available today.

Approach:

This project commenced with trade studies to identify the two most promising ISG architectures without rare-earth permanent magnets and to identify permanent magnet materials which could be leveraged for this effort. The two ISG architectures which were down-selected include the Switched Reluctance (SR) and Spoke Interior Permanent Magnet (Spoke IPM). The SR architecture does not include permanent magnets. The Spoke IPM is leveraging ferrite magnets which have approximately 1/10 the energy product of high performance rare earth magnets.

A study on permanent magnets revealed that ferrite and Alnico permanent magnets are the only non-rare-earth permanent magnets available in sufficient quantities to achieve the program goals. Due to the low coercivity of Alnico magnets, ferrite was determined to be the most promising choice for the design.

The SR ISG has emerged as the more promising of the two designs evaluated and now being built under the effort. The SR topology is more cost effective than any other known generator architecture - approximately 1/3 the cost of comparable rare earth permanent magnet based designs.

Results and Discussion:

Performance projections for the two ISGs based on Finite Element Analysis are shown above. Tasks 1 & 2 were closed out, with SR ISG and Spoke IPM builds and optimizations completed. Testing of the SR motor was completed, and Spoke IPM is ongoing.

Phase I Deliverables included:

- Switched Reluctance (SR) ISG and ISG controller with associated software for operation, fixtures, couplings, mating connectors, plumbing interfaces, drawings, and documentation
- Spoke Interior Permanent Magnet (Spoke IPM) ISG and ISG controller with associated software for operation, fixtures, couplings, mating connectors, plumbing interfaces, drawings, and documentation

Optimized control algorithms to reduce the audible noise of the SR ISG was completed with submission of PDR materials.

Conclusions:

Debugging and verification of the GUI for both ISGs will be completed by DCS. SR & SIPM motors, inverters and GUI's should be ready for delivery in Q1FY2016. Engineering documentation and engineering analysis for each Preliminary Design will be delivered by subcontractor Remy.

Contractor DCS will identify a subcontractor to carry out Task 3 following the loss of subcontractor Remy from the Spoke IPM ISG development and testing in Task 2. Following

Figures and Tables Start on Next Page:

Figures and Tables:

	Objective	*Threshold*
Machine Dimensions		
Housing Outside Diameter	< 558 mm (22 inches)	
Overall Active Length	100 mm	120 mm
Power Supply		
Nominal Voltage:	600 V ± 35 V	
Thermal Requirements		
Liquid cooling	WEG / PWG	
Inlet Temperature	110°C	105°C
Cold Start Initial Condition	-50°C	
Maximum Flow Rate	< 30 LPM (8 GPM)	
Maximum Pressure Drop	16 PSI	
Operating Air Temperature	-50°C to 125°C	

Table 1. Technical Targets

Remainder of Page Intentionally Blank

	Objective	*Threshold*
Target performance		
Continuous Power	100 kW	
Max Operating Speed	4250 RPM	3200 RPM
Base (corner) Speed	800 RPM	1100 RPM
Continuous Torque (0-800 RPM)	1200 Nm	
Peak Torque (0-800 RPM)	1800 Nm	
Duration of Peak Torque	30 sec	
Torque Density		
Volumetric Torque Density	80 Nm/L	50 Nm/L
Gravimetric Torque Density	11 Nm/kg	7 Nm/kg
Power Density		
Volumetric Power Density	8 kW/L	5 kW/L
Gravimetric Power Density	1.2 kW/kg	0.8 kW/kg

Table 2. Performance Targets

Other
Compatible with SAE#1 Bell-housing. Designed for integration between Caterpillar C9 engine and Allison 3200SP transmission.
Waterproof (per 3.5.1.2 from MIL-S-3785E(AT))
Conform to MIL-STD-461F (EMC)
Resolver control hall-effect redundancy

Table 3. Other Specifications

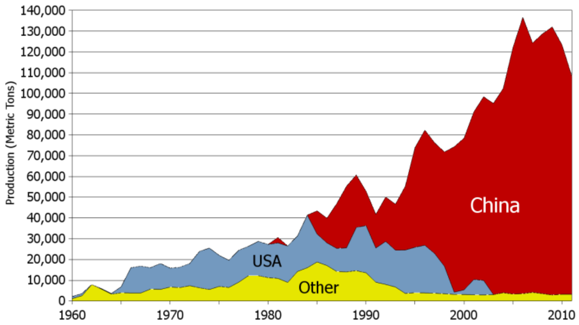

Figure 1. World-Wide Production of Rare-Earth Materials

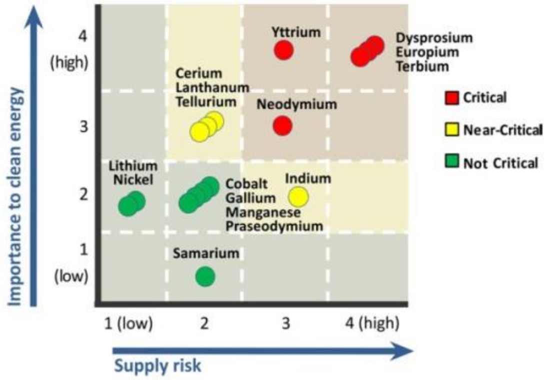

Figure 2. Department of Energy
Critical Materials Strategy

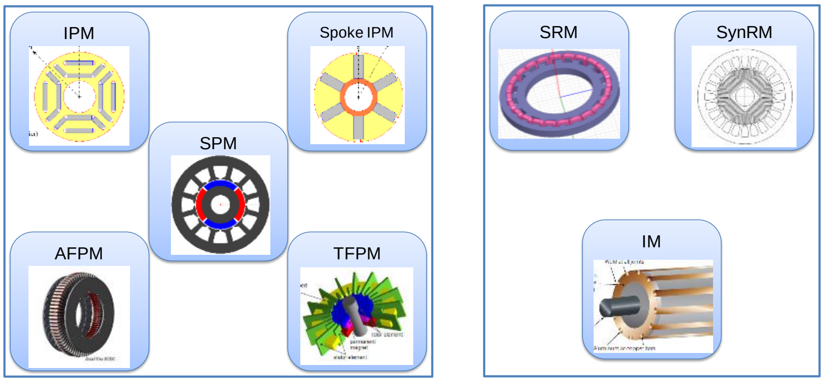

Figure 3. ISG Architectures

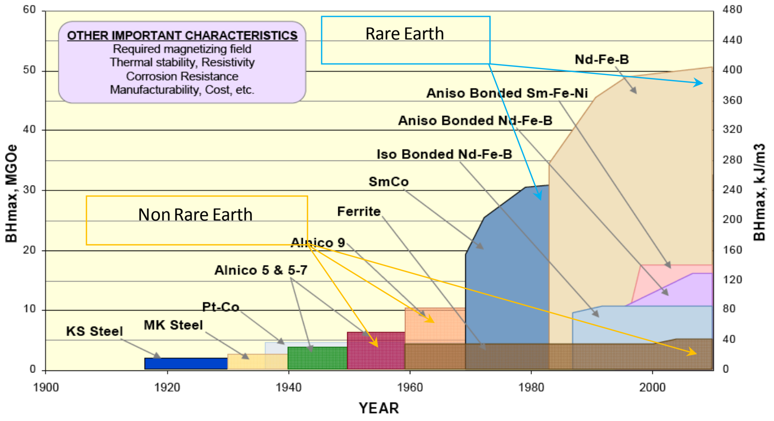

Figure 4. Non-Rare-Earth Permanent Magnet Quantities

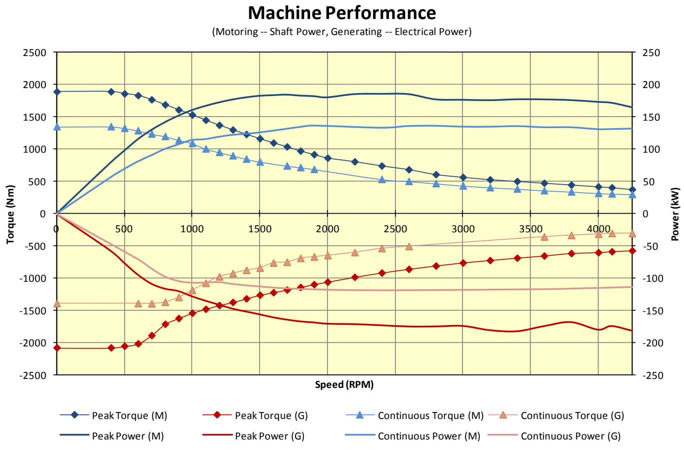

Figure 5. Characteristic Machine Performance

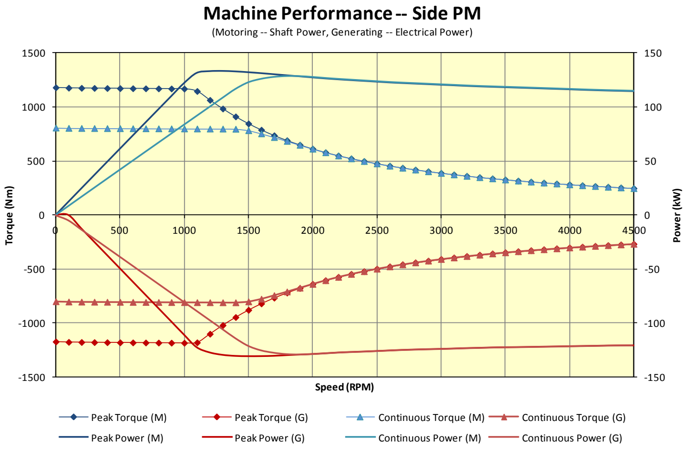

Figure 6. Side PM Machine Performance

This Page Intentionally Blank

Efficient Safety & Degradation Modeling of Automotive Li-Ion Cells & Packs

DOE-VTO TFA Lead: David Howell
TARDEC TFA Lead: Dr. Laurence Toomey

Principal Investigator:
Dr. Christian Shaffer

Affiliation:
EC Power, LLC
341 N. Science Park Rd.
State College, PA 16803

Project Start: 01/10/2013
Estimated Completion: 30/09/2016

Objectives:

- Develop an efficient & robust pack-level safety model.
- Develop abuse and refined life models.
- Perform life, abuse, and safety tests to acquire data for validation.
- Expand extensive materials database by characterizing and adding NCA material.
- Perform co-simulation of our software with structural mechanics software via the Open Architecture Standard (OAS).
- Support DOE CAEBAT activity.

Strategic Context:

- Key barriers to more widespread adoption of hybrid and electric platforms include challenges in the design of large-format Li-ion cells and packs related to performance, safety, life, and abuse.
- In this project, we are developing and refining commercial physics-based software tool that is directly aimed at helping cell manufacturers, the military, and automakers overcome these design challenges and barriers through an accurate and fast computer aided engineering tool.

Accomplishments:

- Completed all multi-cell safety testing, generating data for model validation.
- Completed abuse testing, generating data for model validation.

- Approximately 60 cells successfully fabricated for life testing.
- Life testing for ageing model validation approximately 50% complete.
- Validation of safety, abuse, and life models ongoing
- Successfully completed implementation of new performance and ageing model including effects of active material swelling (e.g. to simulate life of materials such as Si).
- NCA cathode active material characterization (-40°C < T < 60°C) complete and implemented in commercial software database.

Introduction:

The overarching objective of the ongoing work is to develop experimentally validated, robust, and easy-to-use computation models for Li-ion battery (a) pack-level safety and abuse simulation and (b) advanced and accurate degradation modeling. The commercial need for an efficient pack-level safety and abuse model is best highlighted by the Boeing 787 Li-ion battery pack fires, where there has been much debate as to the root cause of the fires, how the failure subsequently spread through the battery pack, and how to avoid such a scenario in the future via enhanced design. The pack-level safety model addresses precisely this type of scenario, yielding great insight as to how an initially local safety-related event such as nail penetration or internal short spreads throughout the pack both thermally and electrically/electrochemically. In addition to pack safety simulation, our team is developing additional chemistry-specific life and abuse models for simulation of Li-ion battery life and overcharge, for example. The models developed are being extensively validated by generating in-house data from a variety of advanced diagnostics tests. Finally, the team is experimentally characterizing commercially widely-used NCA cathode material (-40°C < T < 60°C) and adding material to the previously developed extensive material database.

Approach:

The EC Power-led team is working to develop physics-based Li-ion battery and pack design software, leveraging EC Power's demonstrated expertise in multi-physics modeling. This physic-based modeling approach results in a *predictive* design software focused on addressing life, safety, and performance barriers over automotive- and military-relevant wide-ranging operating conditions (e.g. -40°C < T < 60°C), which will lead to more widespread adoption of Li-ion batteries in this application. To ensure model accuracy, we also leverage the expertise of the Penn State University team in materials characterization, safety, and life testing, in order to validate the software developed.

Results and Discussion:

The work in the past year has focused largely on (a) refining our computational models for performance, life, and safety aspects of Li-ion batteries, (b) completing the characterization and subsequent implementation of NCA cathode material into the software materials database, and (c) carrying out a large number of tests to acquire data for life, safety, and abuse model validation.

Figure 1 gives an example of refined models implemented. This figure shows the cell voltage and SOC versus time for Li-ion cell with Silicon alloy based anode, with and without the swelling effect of the Si alloy incorporated into the model. These results imply that including the swelling effect of the Silicon material has a significant impact on the performance of the cell. We have likewise incorporated the swelling effect into our life models in the past year. The big picture impact of this work is that the refined models will allow more accurate assessment and screening of novel electrode materials in a cost-effective software tool.

Figure 2 highlights a small portion of our life modeling efforts through this work. Specifically, figure 2(a) shows the calendar life, and figure 2(b) the cycle life ageing of an LFP/graphite cell, as captured by the models implemented. Note that the physics-based models capture these battery life effects over a wide range of temperatures and states of charge. Our team is currently carrying out additional testing for additional Li-ion cells, and will validate all models in the coming year.

Figure 3 gives an example set of data from single cell and multiple cell nail penetration tests. In the past year, numerous repetitions of the nail penetration tests (both on the multi-cell and single-cell levels) have been performed to investigate reproducibility of the test data, which greatly enhances computational model validation. When the local temperature inside any cell reaches a dangerous level, thermal runaway will ensue, leading to a safety event such as fire or explosion. The predictive design software developed under this project allows users to quickly, cheaply, and safely iterate through various cell and pack designs to optimize safety before a cell is ever built, leading to a more refined and ultimately safer product. We expect this unprecedented capability of Li-ion battery cell and pack safety simulation will empower manufactures and automakers to reduce time and cost in developing safe Li-ion battery packs.

Conclusions:

EC Power has largely completed the core of the software implementation of the models developed under this project, including those related to safety, abuse, and life. EC Power has additionally fully implemented NCA material into the software materials database. By working with our partners at Penn State, we have also completed safety and abuse testing. In 2016 the project will largely focus on completing the life testing and wrapping up validation of the models. The ultimate goal at the conclusion of the project is to have refined commercial Li-ion battery design software that cuts cost and time from the design phase of automotive Li-ion batteries and packs.

References:

- 2015 DOE Annual Peer Review Meeting Presentation, June 9, 2015.
- Hasan, M.F., Chen, C.F., Shaffer, C.E. and Mukherjee, P.P. (2015). "Analysis of the Implications of Rapid Charging on Lithium-Ion Battery Performance," Journal of the Electrochemical Society, 162(7), A1382-A1395.
- Wang, Q., Shaffer, C.E. and Sinha, P.K. (2015). "Controlling factors of cell design on large-format Li-ion battery safety during nail penetration," Front. Energy Res., 3:35

Figures and Tables:

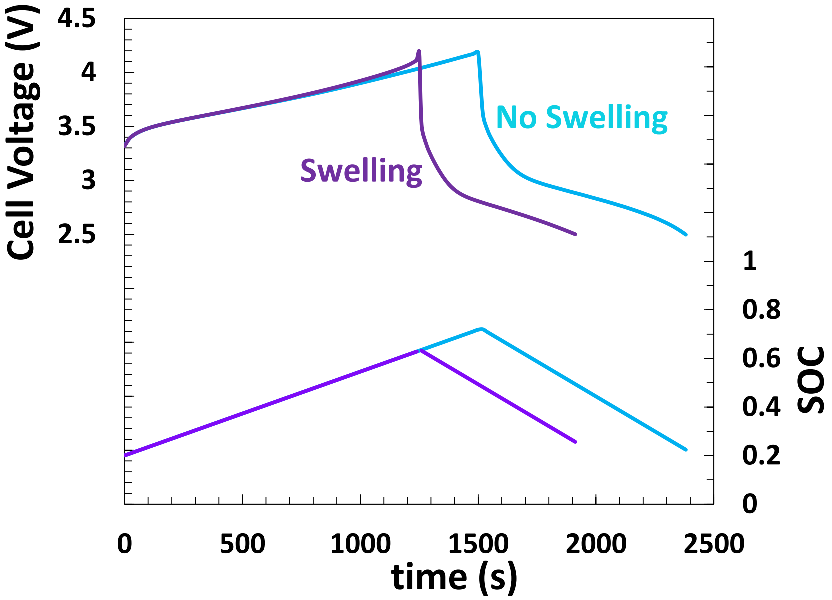

Figure 1. Charge Voltage and SOC of Li-ion Cell with Si Alloy-based Anode with and without Swelling Effect Accounted for in Computational Model.

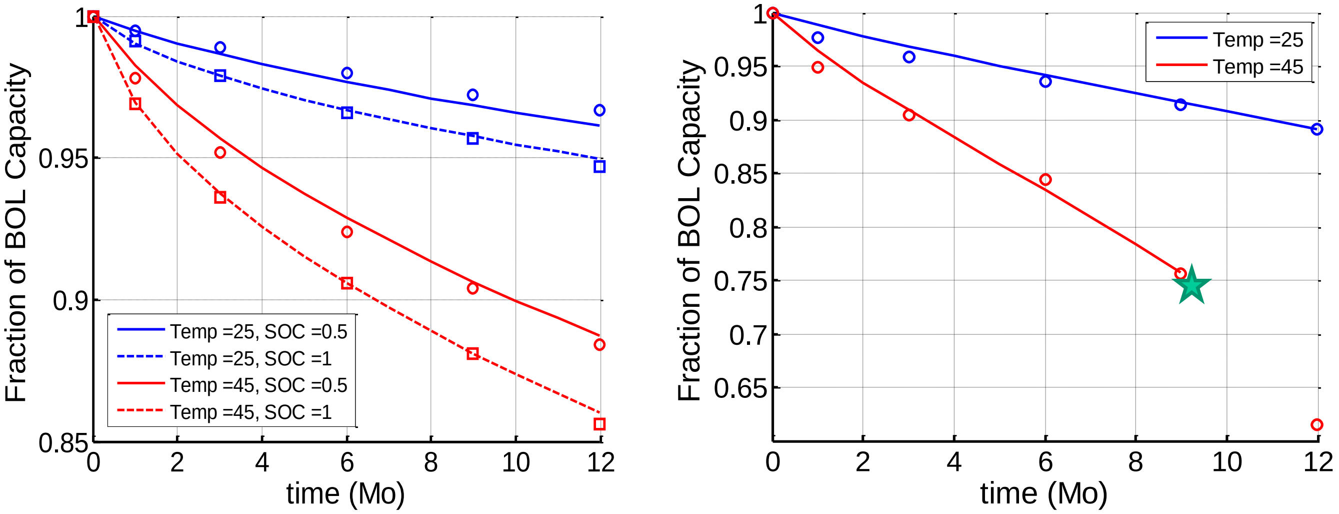

Figure 2. Calendar and Cycle Life Ageing of 26650 LFP/Graphite Cell with New Ageing Models (Temperature in Degrees Celsius); Data taken from Delacourt et al., *Journal of the Electrochemical Society*, 159 (8) A1283-A1291 (2012).

Remainder of Page Intentionally Blank

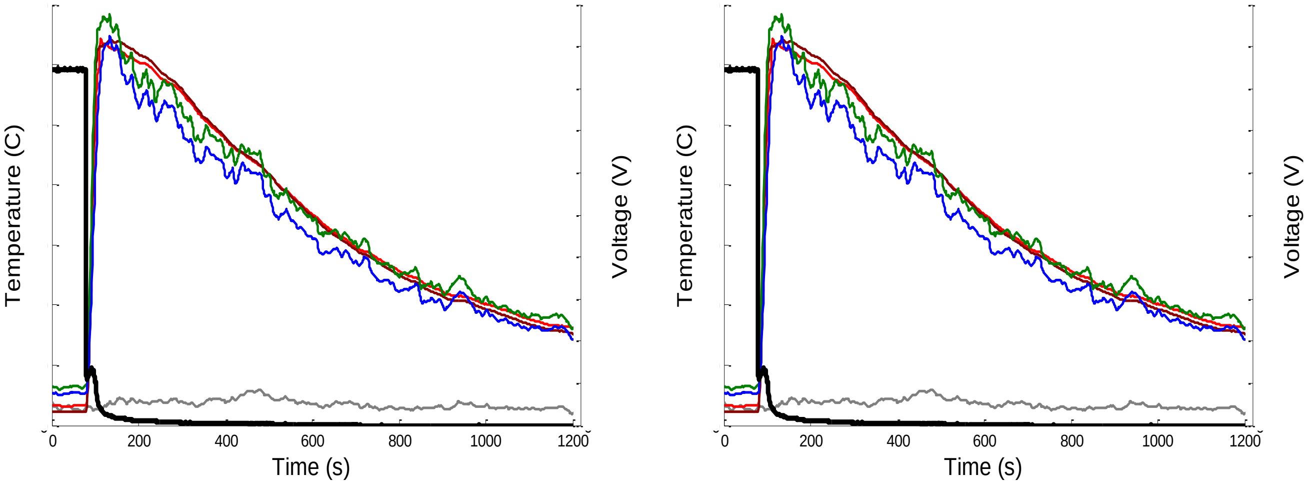

Figure 3. Nondimensional Temperature and Voltage Data Acquired from One Single Cell and One Multi-Cell Nail Penetration Tests; Data being used for Model Validation.

Remainder of Page Intentionally Blank

This Page Intentionally Blank

AVPTA Technology Focus Area 6: Energy Storage & Batteries

Significant Enhancement of Computational Efficiency in Nonlinear Multiscale Battery Model for Computer-Aided Engineering

DOE-VTO TFA Lead: David Howell
TARDEC TFA Lead: Dr. Laurence Toomey

Principal Investigator:
Dr. Gi-Heon Kim

Affiliation:
National Renewable Energy Laboratory
15013 Denver West Parkway, M/S 1633
Golden, CO 80401

Project Start: 01/10/2013
Estimated Completion: 31/12/2015

Objective:

- The objective of the project is to develop a computational methodology for a significant enhancement in computation speed of nonlinear multiscale modeling of plug-in electric vehicle (PEV) batteries while maintaining or improving the solution accuracy from the most advanced state-of-the art models.

Strategic Context:

- This project supports the need for advanced modeling and simulation capabilities for predicting the system-level performance, safety, and lifetime of ground vehicle batteries under both typical duty cycles and abuse conditions.
- In this project, a multiscale multidomain (MSMD) model is used to overcome challenges in modeling the highly nonlinear, multiphysics response of battery systems.

Accomplishments:

- Developed GH-MSMD, a new quasi-explicit, modular, extendable, tightly coupled, nonlinear framework in both the C++ and MATLAB platforms.
- Demonstrated that the new GH-MSMD speeds up computations by 1,000 times.
- Demonstrated implementation of GH-MSMD cell-domain model (CDM) in ANSYS/Fluent
- Built a custom graphical user interface (GUI) in ANSYS/Fluent for GH-MSMD simulation pre-processing.
- Compared options for an adaptive time-stepping algorithm in GH-MSMD versus the existing recursive method.

- Constructed the MSMD standard input file structure, facilitating its multiscale simulation.
- Refined the numerical method for the final version of the adaptive SVM (A-SVM) model.
- Validated and benchmarked A-SVM against other electrode domain model (EDM) MSMD models in MATLAB.
- Demonstrated that the A-SVM achieved 50x speed-up with accuracy better than 15 mV
- Developed a new time-domain ROM, Error-corrected Time-domain Series solution (ETS) for the solid-phase diffusion equation.
- Evaluated the computational speed and the solution accuracy of the ETS.
- Performed the first demonstration of wall-clock speed-up for POD/DEIM method for prototype electrolyte equation.
- Initiated the MSMD integration with vehicle simulator software.

Introduction:

NREL pioneered the multiscale multidomain (MSMD) model, overcoming challenges in modeling the highly nonlinear multiscale response of battery systems. The MSMD provides high extent flexibility and multiphysics expandability through its modularized architecture, as well as computational efficiency. However, further improvement of computational speed of the model is greatly desired to promote the application of the high fidelity multiphysics model in various battery engineering problems. In this project, we significantly improve the computation speed and stability of multiscale model framework by eliminating several layers of nested iteration through innovative multiscale coupling methodology, while still keeping the modular framework architecture, and provide a new reduced order model (ROM) that is adaptive to system evolution and identifiable with fewer compound parameters.

Approach:

Framework & Component:

The project target is achieved through complementary parallel efforts in framework efficiency improvement and component efficiency improvement. We developed a new quasi-explicit nonlinear multiscale model framework, GH-MSMD, using time-scale separation, variable decomposition, and partial linearization procedures (Figure 1). GH-MSMD eliminates several layers of nested iteration, significantly improve the speed and stability upon the original MSMD, and retain the modular framework architecture that is critical to battery behavior simulations. We also develop advanced ROMs for the component models. Computational time is often invested in advance to find a reduced order basis in a much lower dimension than that of the full ordinary differential equation systems derived from spatial discretization of the partial differential equation systems. The ROM basis is typically restricted to reuse in the system where its characteristics are evolving, such as the battery aging process. In this project, we developed the A-SVM, a new ROM that adapts to system evolution and identifiable with fewer compound parameters. For enhancing usability of the model, we constructed the MSMD-Fluent application programming interface for multiphysics integration of NREL’s custom model library in a commercial software environment – ANSYS/Fluent.

Results and Discussion:

The following progress was achieved:

New Model Speeds Up Computations by 1,000 Times:

Last year, NREL met the 100-fold computational speed-enhancement target for its multiscale multiphysics battery model (MSMD) one year ahead of schedule. In FY15, we significantly exceeded the projected target by further improving the code structure and by extending the model to a larger scale. Figure 2 presents the comparison of the electrical and thermal response of a battery for a mid-size sedan plug-in hybrid electric vehicle (PHEV10) on the US06 20-minute driving power profile. While the model outputs are shown to be very close to each other, the new quasi-explicit, modular, extendable, tightly coupled, nonlinear MSMD framework, GH-MSMD, demonstrates that the most efficient electrode-scale battery-cell model option can run a 1,200-second driving profile simulation in only 0.74 seconds using a personal computer—an approximate 1,000-fold improvement over previous capabilities. In contrast, the original MSMD runs the same simulation in 654 seconds. When the model is extended to its full-scale, three-dimensional, larger cell domain, the speed-enhancement factor reaches 1,000 to 10,000, depending on the choice of sub-model.

Figure 3 compares the model solution variables in each computational domain and the coupling variables exchanged between the adjacent length scale domains in MSMD (left) and in GH-MSMD (right). Even though the solution algorithms are significantly different between the two, the model structures are similar. This comparison signifies the modularity of model framework that the GH-MSMD inherited from the MSMD. The new GH-MSMD framework retains the flexibility needed for application to various lithium battery chemistries and designs. It still integrates a sophisticated particle model to address particulate morphology, size distribution, surface modification, contact resistances, and mixture composition of active particles. The model simulates all major cell form factors with variable electrode compositions and designs.

Reduced Order Electrochemical Model Becomes Adaptive:

NREL developed an accurate, computationally efficient realization of the Newman electrochemical model that runs 100 to 1,000 times faster than typical numerical solutions in modern commercial software. Although spectral model order-reduction techniques are available to achieve speed enhancement, previous efforts that applied these methods to the Newman model required a cumbersome preprocessing step to identify a model versus a few selected parameters of interest. To overcome this limitation, NREL eliminated the preprocessing step so that a simulation could run immediately, and NREL fully populated the ROM so that it is extendable to all possible lithium-ion porous electrode designs and states of health. This achievement will enable the rapid optimization of lithium-ion cell chemistries and the use of the model for aging studies. The new A-SVM was validated and benchmarked against other EDM MSMD models (two MSMD-EDMs and two GH-MSMD-EDMs) in MATLAB.

The compared MSMD EDM combinations are edLPD/pdPLLM, edPLM/edLPD, edSEG/pdPLM, and edSEG/pdSEG. Figure 4 presents the model output comparisons for a 5C and 10C pulse profile and constant current discharge in 1, 2, 5, and 10C. Accuracy is generally greater than 99%, and the speed-up factor of A-SVM against the highest-order segregated solver option is about 50. The unconditional stability of A-SVM enables a large time-step size, and additional speed-up is expected in practical situations. A-SVM shares the common input and output file structure with the MSMD/GH-MSMD.

Efforts to Promote Industry Access to New Models:

The successful development of GH-MSMD is expected to shift the paradigm in using a model for electric-drive vehicle battery system design and evaluation, potentially revolutionizing the standard development process for the entire industry. NREL's GH-MSMD baseline model codes are developed in both the MATLAB and C++ platforms. These NREL custom models are planned to be available to external users in the future. In the meantime, it is desired to implement GH-MSMD in commercial computer-aided engineering software to make it available immediately to a large number of users in the electric vehicle industry. In this regard, NREL developed a manual procedure for GH-MSMD implementation in ANSYS Fluent and built a GUI using scheme programing and the user codes. Figure 5 is a captured image of NREL's custom GUI of GH-MSMD. The current GUI is similar to that in the ANSYS/Fluent MSMD Battery Module. The customized GUI enables us to practice and test GH-MSMD implementation into Fluent. Unique features could be added for the GH-MSMD methodology to link different domain levels and improve simulation efficiency. NREL's implementation of the GH-MSMD CDM in Fluent has been verified by comparing the model outputs against the commercially available and existing MSMD model option in Fluent. The results are shown in Figure 6.

Conclusions:

We successfully accomplished the project goal and improved the computation speed of state-of-the-art nonlinear multiscale battery model by a factor of 100 while maintaining its solution accuracy. The new GH-MSMD demonstrates a 1,000-fold speed up compared with the original MSMD during vehicle driving profile benchmark simulation tests. The remaining challenges and the future directions that we expect to address in the third phase of the CAEBAT project are identified below.

Remaining Challenges

- GH-MSMD demonstrates significant speed up. The remaining challenge, however, is to enhance the applicability of the new model to various battery engineering problems.
- To address varied problems in the industry, interdisciplinary constituent models relating material/ design/ process/ operational parameters with physicochemical parameters of the GH- baseline models are needed.
- Electrochemical Impedance Spectroscopy is one of the frequently used methods for battery characterization and diagnostics. Since the current GH-MSMD has been developed in time-domain, it is difficult to utilize the information produced in frequency domain.
- The modular architecture of GH-MSMD facilitates participation of external expertise across the battery community. Independently developed sub-models can be plugged in the framework to extend the simulation capability. However, unlike the original MSMD, the GH-MSMD protocol is not intuitively understandable.

- Identification of a physics-based battery model is known to be difficult. This anticipated difficulty for development of a physics-based constituent model comes from the fact that characterization of a battery is intrinsically solving an under-determined problem.

Future Direction:

- There have been strong needs in the industry to use purely predictive physics-based models for design, evaluation, and control of batteries and systems. In the pursuit of providing such models, we will develop physics-based interdisciplinary constituent models working in the GH-MSMD framework.
- A frequency-domain GH-MSMD model will be developed from the identical governing equation sets used in the time-domain model, running with the standard input files.
- We will summarize the GH-MSMD principles and implementation and publicize them to encourage contributions from outside experts.
- We will develop sequential optimization procedures to break the under-determined parameter estimation problem of the whole system into a sequence of fully determined fits to subsets of the parameters and advanced model-based battery characterization.

References:

- G.-H. Kim et al., “Significant Enhancement of Computational Efficiency in Nonlinear Multiscale Battery Model for Computer Aided Engineering,” DOE Annual Merit Review, June, 2015, Washington DC.
- Annual Milestone Reports, September 2015.
- G.-H. Kim, C. Yang, A. Pesaran, “Integrated Multiscale Multiphysics Modeling of Dynamic Short Circuit Behavior in Large Lithium-ion Batteries,” 228th Electrochemical Society Meeting, October, 2015, Phoenix, AZ.
- C. Yang, G.-H. Kim, M. Keyser, A. Pesaran, “Numerically Characterizing Nail Penetration Testing for Safety Evaluation of Li-Ion Cells,” 228th Electrochemical Society Meeting, October, 2015, Phoenix, AZ.

Figures and Tables:

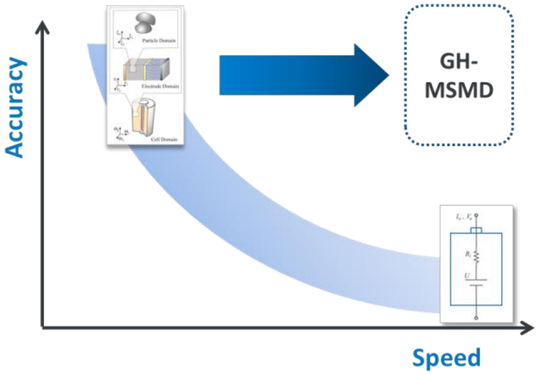

Figure 1. GH-MSMD Significantly Improves the Computational Speed of Nonlinear Multiscale Battery Model without Compromising Accuracy.

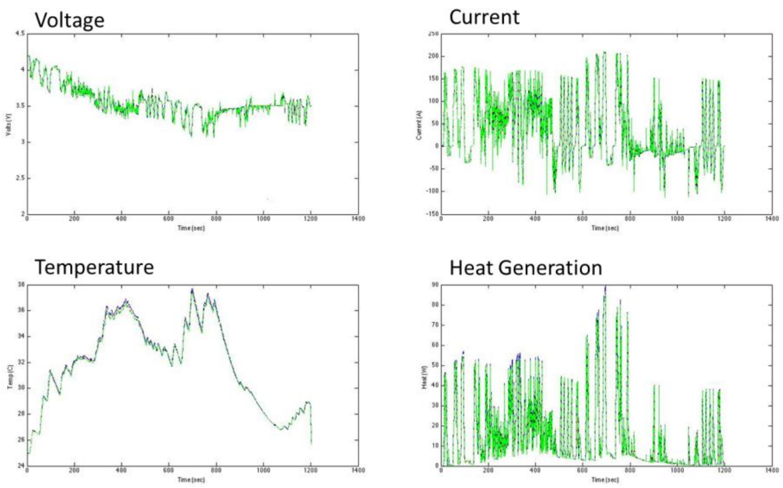

Figure 2. Comparison of Electrical and Thermal Response of a Battery for a Mid-Size Sedan Plug-in Hybrid Electric Vehicle (PHEV10) on the US06 20-minute Driving Power Profile from the GH-MSMD and the original MSMD.

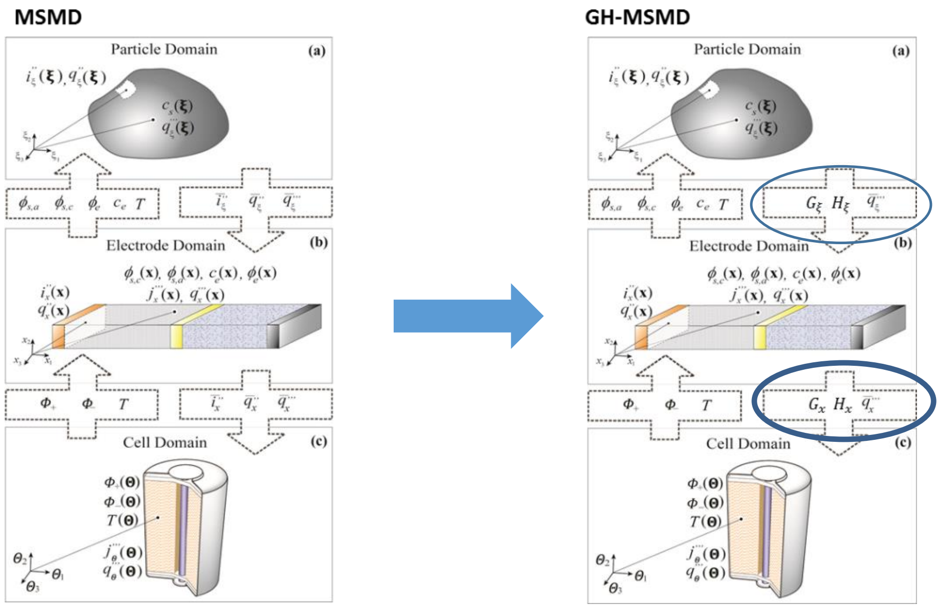

Figure 3. Comparison of the Original MSMD and the GH-MSMD Framework Structure and Main Changes in the GH-MSMD.

Remainder of Page Intentionally Blank

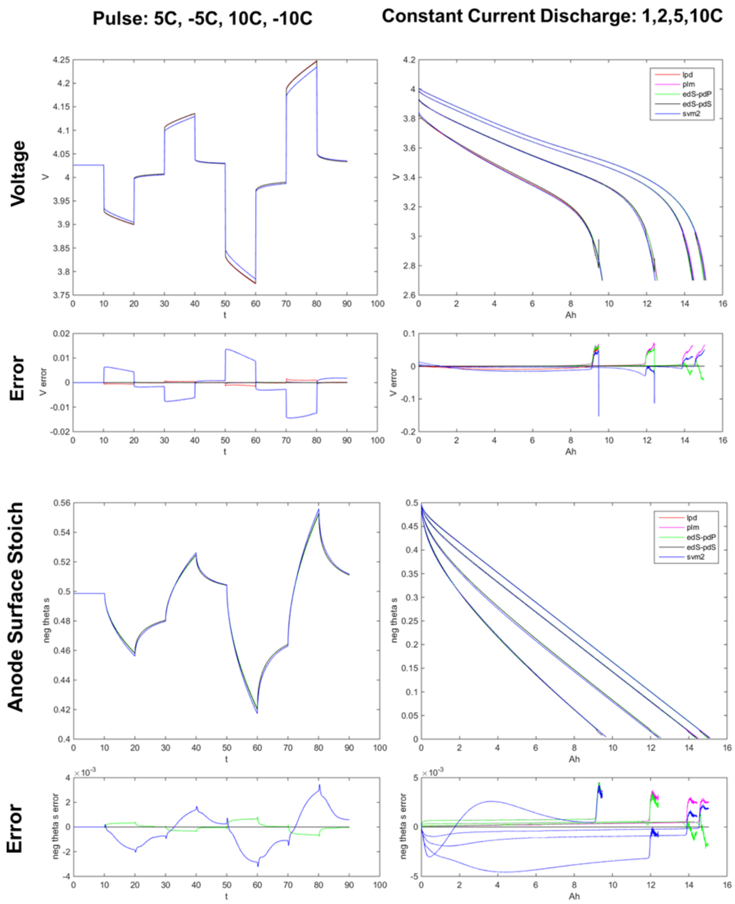

Figure 4. A-SVM Verification and Benchmark Results Against Various MSMD/GH-MSMD Models.

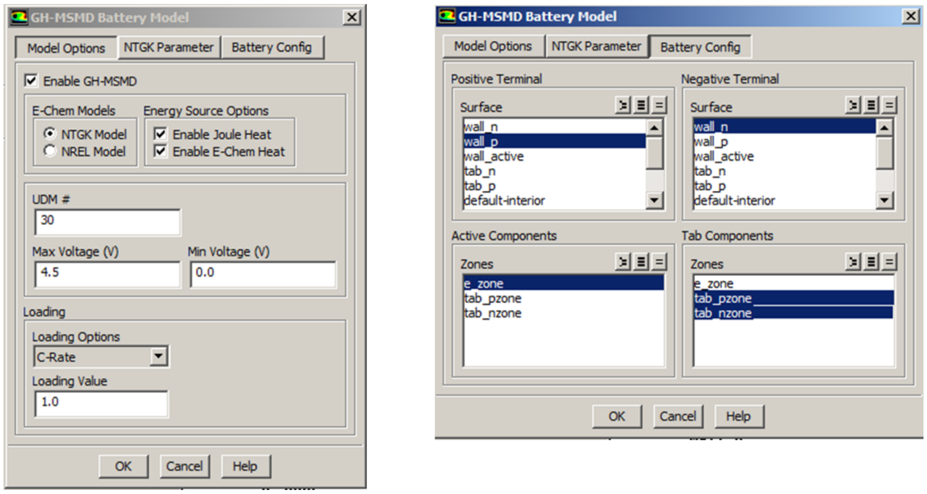

☑ Enable GH-MSMD

E-Chem Models
● NTGK Model
○ NREL Model

Energy Source Options
☑ Enable Joule Heat
☑ Enable E-Chem Heat

UDM # 30

Max Voltage (V) 4.5

Min Voltage (V) 0.0

Loading

Loading Options C-Rate

Loading Value 1.0

Positive Terminal

Surface: wall_n, wall_p, wall_active, tab_n, tab_p, default-interior

Negative Terminal

Surface: wall_n, wall_p, wall_active, tab_n, tab_p, default-interior

Active Components

Zones: e_zone, tab_pzone, tab_nzone

Tab Components

Zones: e_zone, tab_pzone, tab_nzone

Figure 5. Custom GUI of GH-MSMD set up in ANSYS/Fluent

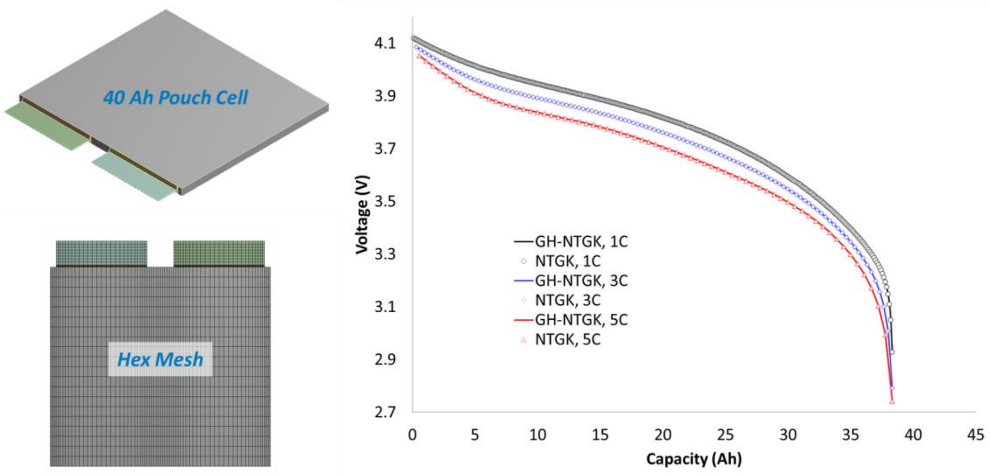

Figure 6. NREL's Custom Implementation of GH-MSMD in Fluent is Verified. Solid Lines are the Cell Voltage Response of NREL Custom GH-MSMD Model Simulations, and the Symbols are Corresponding Outputs from the Fluent MSMD Battery Simulation Module.

Remainder of Page Intentionally Blank

AVPTA Technology Focus Area 6: Energy Storage & Batteries

Beyond Li-Ion: Overcoming Interface Impedance in Solid-State Batteries

DOE-VTO TFA Lead: David Howell
TARDEC TFA Lead: Dr. Laurence Toomey

Principal Investigator:
Dr. Eric Wachsman

Affiliation:
University of Maryland
College Park, MD 20742
Phone: (301) 405 – 8193
E/M: ewach@umd.edu

Project Start: 01/10/2014
Estimated Completion: Q4FY17

Objective:

- Develop a multifaceted and integrated experimental and computational approach to solve the key issue in solid-state Li-ion batteries (SSLiBs), interfacial impedance. The research will focus on Garnet-based solid-state electrolytes (SSEs), but the knowledge can be applied to other SSE chemistries. The interfacial impedance in this proposal includes charge transfer, ionic and electronic transport, and interfacial structural/chemical stability over charge-discharge cycling. The developed low interface technique will be tested with solid state Li-NMC cell and Li-S cell testbeds that have 350-450 Wh/kg and 200 cycles.

Strategic Context:

- Generate a leap-ahead technology used for military vehicles to support the future power for TARDEC and the Army by enabling the development of advanced battery systems with significant increases in energy density
- Improve Battery safety characteristics to support vehicle silent watch and enable other high energy requiring applications.

Accomplishments:

- Developed computational models for garnet based interfaces.
- Characterized the interfacial impedance of garnet and LFMO electrodes by EIS.
- Demonstrated that 3D structures on the garnet surface can reduce the interfacial impedance.

- Unflammable PFPE solvent was prepared and PFPE/LiTFSI electrolyte was demonstrated to be electrochemically stable in the voltage region of 0-4.2V providing potential conformable low impedance interfacial layer.
- PVDF-HFP gel membrane was prepared and the stablilty and impedance of ionic liquid electrolyte in this gel membrane demonstrated providing potential conformable low impedance interfacial layer.

Introduction:

Solid state garnet-electrolyte lithium ion batteries have tremendous potential due to their inherent safety, high voltage stability, and reasonably high conductivity. However, the interfacial impedance between solid state electrolytes and electrode is currently too high. This work will focus on reducing the interfacial impedance, by making controlled structures on the garnet electrolyte surface, and introducing conductive and conformal interfacial layers between the garnet and the electrodes. These results will address the primary issue and significantly advance solid-state Li-battery technology.

Approach:

The objectives outlined above will be accomplished by optimizing the garnet surface structure and electrode material, and investigating high conductivity conformal interfacial layers.

Effect of Interfacial Structure on Impedance:

While we and others have made tremendous advances in understanding interfacial resistance in solid oxide fuel cells (SOFCs), to date no one has applied these techniques to SSLiBs. Therefore, we use SOFC techniques to develop a fundamental understanding of interfacial impedance in terms of intrinsic charge transfer rates, ionic and electronic transport, and effect of interfacial structure.

Electrochemical impedance spectroscopy (EIS) of solid electrolyte and electrode or interfacial layer pellets are being performed to identify the mechanistic frequency dependence of EIS response for each material as well as blocking electrode and DC measurements to separate out ionic vs.electronic conductivity for each material. Then bilayer electrolyte and electrode/interfacial layer pellets with smooth and controlled interfaces are being fabricated and tested with EIS.

This allows for determination of the specific interfacial impedance, as it will be resolved as an additional EIS frequency response. This interfacial impedance is then being used to calculate the charge transfer reaction rate across the electrolyte/electrode and electrolyte/interfacial layer interfaces. Bilayered pellets with tailored nano/micro-rod interfaces has been fabricated (by templated deposition and additive manufacturing) with different rod length to diameter aspect ratios. The EIS data from these cells is deconvoluted and compared with known ionic and electronic transport rates, and charge transfer rates, to create fundamental models of interfacial impedance as a function of 3-dimensional interfacial structure.

Investigate Interfacial Modifications and Cell Performance:

We are investigating two types of materials as interfacial layers in SSLiBs.

For Type 1, we use nonflammable organic electrolytes such as perfluoropolyethers (PFPE) based electrolytes. It has been confirmed that such organic electrolytes cannot catch fire and are intrinsically safe. Although, PFPE-based electrolytes have very low ionic conductivity (~ 10^{-5} S/cm) and can not meet the power density requirement in the FOA by itself, PFPE based organic electrolyte can greatly increase the interfaces across electrolyte grain boundaries, or electrolyte/electrode interface for enhancing the battery performance.

For Type 2, we also use a polymer electrolyte or gel electrolyte, which is Bis(trifluoromethane)sulfonimide lithium salt (LiTFSI) in Poly(vinylidene fluoride-co-hexafluoropropylene) (PVDF-HFP). Although the polymer or gel electrolyte has a much lower ionic conductivity, its thickness is small as an interface layer and thus its contribution in overall impedance is negligible. These soft electrolytes can largely improve the contacts between electrodes and electrolytes toward better charge transport and mechanical integrity.

For each approach, we are fabricating half cells to investigate interfacial impedance and their changes during cycling.

Results and Discussion:

The following progress has been achieved:

Characterization of Electrolyte/Cathode Interface Impedance:

We tested the impedance of LLCZN solid state electrolyte, and its interface impedance with LFMO electrodes. The LLCZN($Li_{6.8}(La_{2.95},Ca_{0.05})(Zr_{1.75},Nb_{0.25})O_{12}$) garnet was synthesized by conventional solid state reactions. The starting materials, Li(OH), $La(OH)_3$, $Ca(OH)_2$, ZrO_2, and Nb_2O_5 were mixed by planetary ball-milling, and then calcined at 700 °C for 48 h. The calcined LLZO-CaNb powder was mixed with additives (both Al_2O_3 and Li_3BO_3, only Al_2O_3 or only Li_3BO_3) by planetary ball-milling. The mixture was die-pressed at 10 MPa into a pellet and sintered at 790°C for 40 h in air. EIS of LLCZN electrolyte and LFMO cathode was tested with Solartron 1260 impedance analyzer at room temperature using gold paste current collectors. EIS plots were collected at 50 mV voltage signal over a frequency range of 10 Hz -20 MHz.

Figure 1 is the EIS curves of thick and thin LLCZN electrolyte samples. A semicircle and Warburg-type impedance appeared at high and low frequency regions, respectively. The high-frequency semicircle is the sum of bulk and grain boundary responses. The low-frequency tail corresponds to the capacitive behavior of gold blocking electrode. The total lithium-ion conductivity of LLCZN electrolyte is estimated from the intercepts from the semicircle at low frequency side. The thin pellet shows a slightly lower total conductivity than the thick pellet sample.

Figure 2 is the EIS curves of thick and thin LFMO cathode samples at initial state (0%SOC). The Nyquist plot contains one depressed semicircle in the high frequency and another semicircle in the medium frequency ascribed to the resistance of Li+ diffusion through the SEI layer and charge transfer reaction, respectively. The EIS plot indicates similar conductivity exhibited by both the thick and thin pellets of LFMO.

Knowing the frequency response of both LLCZN electrolyte and LFMO cathode we then analyzed the system consisting of electrolyte, cathode and their interface. Finely polished electrolyte and cathode with gold electrode on outer side were tightly pressed together. The electrolyte/cathode system was then characterized by EIS. Figure 3 shows the Nyquist plots of LLCZN electrolyte/LFMO cathode system. Both thick and thin pellet samples were examined to identify the interfacial effect in the system. The impedance arc is the total resistance of LLCZN electrolyte, LFMO cathode and their interface. The arc in the medium-low frequency range is the dominant interfacial resistance between LLCZN electrolyte and LFMO cathode. The high frequency response in the magnified plot is the sum of LLCZN electrolyte resistance and LFMO cathode resistance.

The garnet/cathode interface impedance was lowered by making structured garnet surfaces. Sintered dense garnet discs were sanded to 150 µm and polished. To make the column structures, polymer mesh was glued on disc surface as a template, after that a garnet slurry was drop coated to fill the open area. The coated sample was dried in oven and sintered at 800 ℃ for 2h. Figure 4 shows the structured garnet surface. The white shinning areas are the deposited column structures.

Symmetric cathode/electrolyte/cathode cells were made by screen printing thick cathode slurry on the garnet discs. LFMO cathode was sintered at 500 ℃ for 1h. Silver paste was used as current collector. Thickness of the cathode was about 20µm. EIS plots were collected at 50 mV voltage signal in a frequency range of 10 Hz -10 MHz at room temperature. Figure. 5 is the EIS response of cathode coated as-polished and structured garnet discs which exhibits lower interfacial resistance, compared to that with smooth surface due to the larger interfacial cathode/electrolyte contact area provided by the surface column structure.

Synthesis and Characterization of Gel and PFPE-based Electrolytes:

Nonflammable PFPE-based Electrolyte: PFPE-DMC was prepared from Fluorolink D10 and triethylamine in 1,1,1,3,3-pentafluorobutane at 0 °C under nitrogen atmosphere, followed by dropping a solution of methyl chloroformate in 1,1,1,3,3- pentafluorobutane. After the mixture was stirred at 25 °C for 12 h, the PFPE-DMC product was obtained by filtering and washing with water and brine, followed by evaporation under reduced atmosphere. The PFPE-DMC electrolyte was then produced by dissolving Lithium bis(Trifluoromethanesulfonyl)Imide into PFPE-DMC. The synthesis method of PFPE-DMC is shown in Figure 6.

A Li/PFPE/Ti structure in a CR2025 coin cell was used to tested cyclic voltammetry (CV) of the PFPE/LiTFSI electrolyte. The area of the cell is 1.98 cm^2 (radius=5/16 inch), and the area of Titanium cathode is 0.712 cm^2 (radius=5/32 inch). The voltage range was -0.3~4.2 V, and the voltage scan speed was 1mV/s.

The CV results are shown in Figure 7. The reaction current density is less than 0.002 mA in 0.3~4.2V region, which is very small. And after the first few cycles, the CV curve becomes stable. The two facts show that the PFPE electrolyte is electrochemically stable between 0-4V. Also, for the PFPE electrolyte, no obvious peaks appear in the voltage region of -0.3 ~ 4.2 V, which means that the Li stripping occurs at a higher voltage than 4.2 V, and the Li platting occurs at a lower voltage than -0.3 V. The electrochemical stability of PFPE/LiTFSI in the voltage range of 0~4.2 V ensures that this electrolyte is stable in the reactions of LLCZN garnet electrolyte lithium ion batteries, and can be used as the interfacial layer between garnet and cathode.

Gel-based Electrolyte: A PVDF-HFP based gel polymer was prepared (Figure 8) from 0.25 g PVDF-HFP dissolved into a mixture of 4.75 g acetone and 0.25 g DI water (95:5, m/m) under continuous stirring. The solution was cast onto an Al foil and the solvent evaporated at ambient temperature. After drying under vacuum at 100 °C a homogeneous free standing membrane was obtained. The as-prepared porous membrane was immersed into 1 M LiTFSI in a mixture of 1:1 volume ratio of tetraethylene glycol dimethyl ether and n-methyl-(n-butyl) pyrrolidinium bis(trifluoromethanesulfonyl)imide (Py14TFSI) at room temperature for 30 mins in an argon-filled glovebox.

CV testing cell was set up by sandwiching the gel electrolyte membrane between lithium and titanium disks and sealing the configuration in CR2032 coin cells. The CV (Figure 9) at a scan rate of 1 mV/s suggests a stable electrochemical window up to 4.2 V. The sharp peak at -0.2 V corresponds to the Li plating, while the peak around 0.1 V is due to the Li stripping.

Figure 10 shows the effect of gel polymer on reduction of impedance at the LLCZN electrolyte/LFMO cathode interface. The pristine LLCZN electrolyte/LFMO cathode reveals a huge resistance of 300 kΩ*cm^2, which consists of bulk resistance of electrolyte and cathode, as well as the significant interfacial resistance between electrolyte and cathode at medium and low frequency range. Introduction of the gel interfacial layer, which provides high Li-ion conduction path, conformal and elastic contact between electrolyte and cathode, results in great reduction of the interfacial resistance, as shown in the medium frequency range in the magnified plot. In addition, the EIS curve shows a different shape, consisting of Warburg-type impedance at low frequency, corresponding to the capacitive behavior of gold blocking electrode.

Computational Modeling of Garnet Interfaces:

First principles modeling of garnet solid electrolyte materials were performed on both tetraganoal and cubic LLZ phases. The ordering of Li was determined using computational methods, and the ground state ordering of Li was determined. The Li grand canonical phase diagram of the Li-La-Zr-O system based on first principles computation methods and electrochemical stability of garnet against Li metal was determined (Figure 11).

In addition, first principle models were constructed to evaluate the structure and energetics of the electrolyte-electrode interfaces between garnet and Li metal. We found that Li metal has a very weak interfacial binding with Li_2CO_3, which are found on the garnet surfaces, and Li metal binds strongly with oxide materials that may form on the garnet surfaces. The weak interface binding may lead to forming interfacial gaps and intervals, thus a low contact area and a high interfacial resistance. Stronger interface binding would lead to enhanced interfacial contacts with larger contact area and good interfacial conductance.

We developed a computational model for garnet-electrode interfaces (Figure 13). The comprehensive interface model is based on a large variety of inputs provided by a range of first principles computation and actual experimental parameters to model the interface properties. The interface model has been developed and demonstrated for garnet materials with electrode materials, such as $LiCoO_2$ and LFMO. The interphase layers between the garnet and the electrode were determined using grand potential phase diagram at the applied voltage of the battery at the input for the model. The formation of the interphase was found to be thermodynamically favorable for the interfaces of garnet with anode and cathode. In addition, the properties of the materials comprising the interphase, such as defect and migration energy, were also evaluated in first pricniples calculations. The effects of the space-charge layer were incorporated as a part of interface model. Using all these predicted input parameters, the conductivity and interfacial resistance of the interfacial layer were determined. The model is now ready to be applied to any composition of garnet solid electrolyte in contact with any electrode materials. The inputs for the interface model are generated by the first principles computation and experimental parameters. The model was able to demonstrate that a poor interfacial layer causes high interfacial resistance in all-solid-state batteries.

Conclusions:

We have made important progress on the interfacial impedance between solid state electrolyte and electrodes. The interfacial impedance between LLCZN garnet electrolyte and LFMO electrode was tested, and it was found that that extended 3D structures on the garnet surface can reduce the interfacial impedance.

PVDF-HFP gel membranes were fabricated, and their microstructure demonstrated by SEM. CV electrochemical tests have shown that the gel electrolyte is electrochemically stable between 0-4.2V and can thus be used as the interface layer between garnet electrolyte and various high voltage cathodes. The EIS of LLCZN/GEL/LFMO was tested and the total impedance decreased significantly compared with the LLCZN/LFMO system without the interfacial layer.

PFPE nonflammable electrolytes were also fabricated. The CV electrochemical tests of Li/PFPE/Ti shows that it is stable between 0-4.2v, which means that it can be used as the interface layer between garnet electrolyte and various high voltage cathodes.

Future work will focus on investigating the fundamentals of solid-solid interfacial impedance, and different kinds of interface layers by combining experiments and computations. The first task is to determine interfacial impedance in 3D controlled solid-state structures, and the second task is to finish the battery test using PFPE and gel based electrolyte interfacial layers to see if they can reduce the interfacial impedance, and start to research on other types of interfacial layers: Atomic layer deposition (ALD) based interlayers and β-Li3PS4 (LPS) based interlayers.

References:

1. Thangadurai, V.; Weppner, W., Ionics 2006, 12, 81-92.
2. Robertson, A. D.; West, A. R.; Ritchie, A. G., Solid State Ionics 1997, 104, 1-11.
3. Kamaya, N.; Homma, K.; Yamakawa, Y.; Hirayama, M.; Kanno, R.; Yonemura, M.; Kamiyama, T.; Kato, Y.; Hama, S.; Kawamoto, K.; Mitsui, A., Nature Materials 2011, 10, 682-686.

4. Thangadurai, V.; Kaack, H.; Weppner, W. J. F., Journal of the American Ceramic Society 2003, 86, 437-440.
5. Thangadurai, V.; Weppner, W., Advanced Functional Materials 2005, 15, 107-112.
6. Murugan, R.; Thangadurai, V.; Weppner, W., Angewandte Chemie-International Edition 2007, 46, 7778-7781.
7. Hitz, G. T.; Wachsman, E. D.; Thangadurai, V., Journal of the Electrochemical Society 2013, 160, A1248-A1255.
8. Rangasamy, E., Sahu, G., Keum, J., Rondinone, A., Dudney, N., Liang, C., Journal of Materials Chemistry A 2014, 2, 4111-4116.
9. Sakuda, A; Hayashi, A.; Tatsumisago, M. Scientific Report, 2013, 3, 2261-2265
10. Miara, L. J.; Ong, S. P.; Mo, Y.; Richards, W. D.; Park, Y.; Lee, J.-M.; Lee, H. S.; Ceder, G., Chemistry of Materials 2013, 25, 3048-3055.
11. Mo, Y.; Ong, S. P.; Ceder, G., Chemistry of Materials 2012, 24, 15-17.
12. Bruce, P. G.; Freunberger, S. A.; Hardwick, L. J.; Tarascon, J.-M., Nature Materials 2012, 11, 19-29.
13. DHC, W., PNAS: 2014, 111, 3327-3331.
14. Hu, L., Xu, K., PNAS: 2014, 111, 3205-3206.
15. Han, X.; Liu, Y.; Jia, Z.; Chen, Y.-C.; Wan, J.; Weadock, N.; Gaskell, K. J.; Li, T.; Hu, L., Nano Letter 2013, Accepted, Online.
16. Meng, X.; Yang, X.-Q.; Sun, X., Advanced Materials 2012, 24, 3589-3615.
17. Hu, L.; Wu, H.; Cui, Y., Metal nanogrids, nanowires, and nanofibers for transparent electrodes. Mrs Bulletin 2011, 36, 760-765.
18. Wu, H.; Hu, L.; Carney, T.; Ruan, Z.; Kong, D.; Yu, Z.; Yao, Y.; Cha, J. J.; Zhu, J.; Fan, S.; Cui, Y., Journal of the American Chemical Society 2011, 133, 27-29.

Figures and Tables:

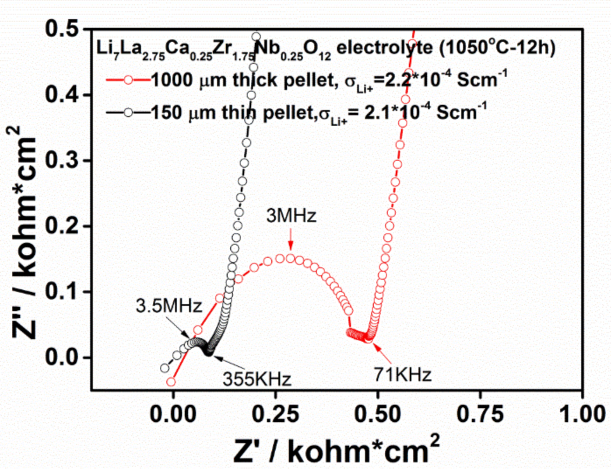

Figure 1. EIS of Thick and Thin LLCZN Pellets at Room Temperature.

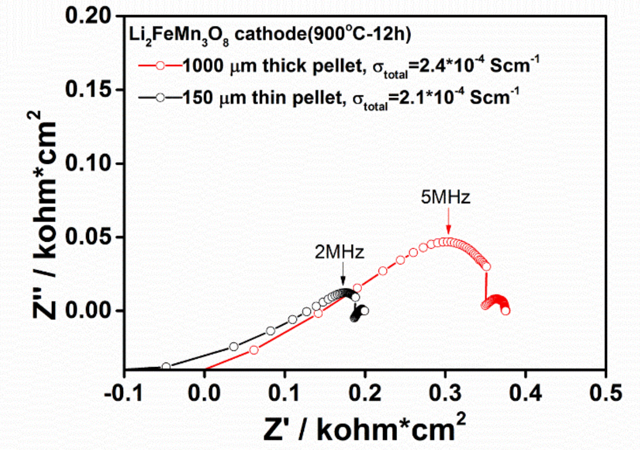

Figure 2. EIS of Thick and Thin LFMO pellets at Room Temperature.

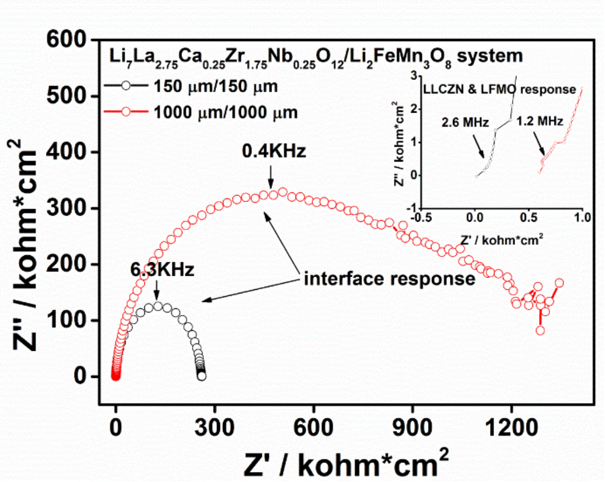

Figure 3. EIS Plot of LLCZN Electrolyte/LFMO Cathode System.

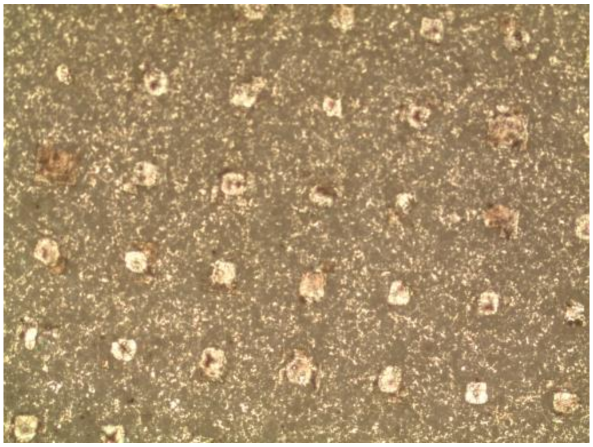

Figure 4. Structured Garnet Surface, White Shining Areas are Deposited Garnet Columns.

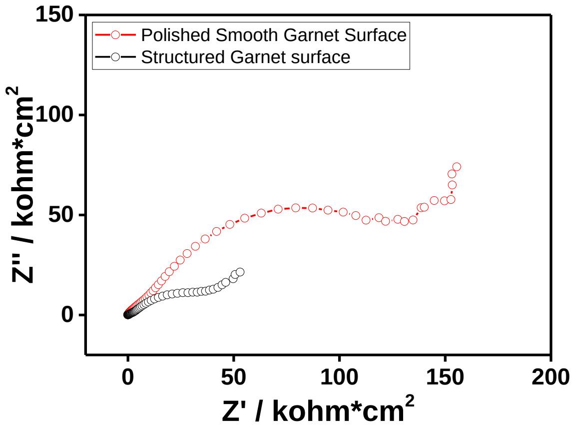

Figure 5. Impedance of Cathode on Smooth and Structured Garnet Electrolyte.

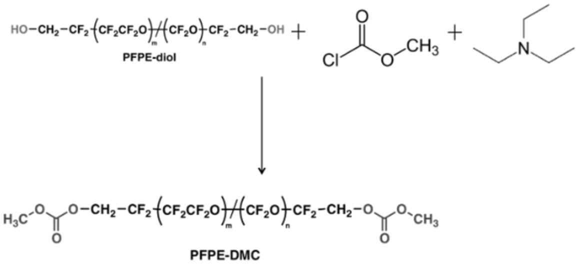

Figure 6. Synthesis Procedure of PFPE-DMC.

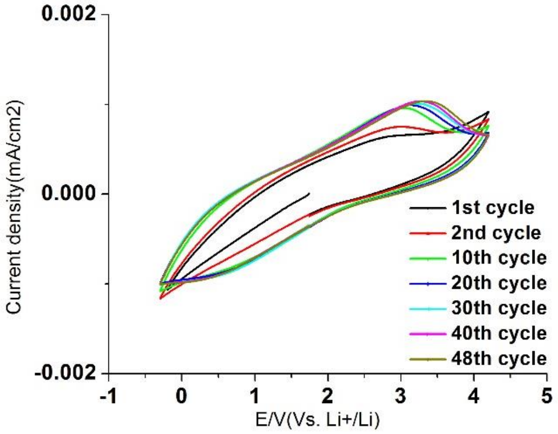

Figure 7. Cyclic Voltammetric Results for LiTFSI/PFPE.

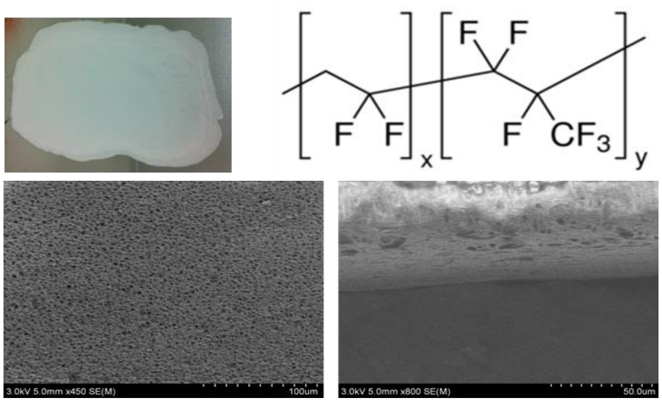

Figure 8. Photograph, Formula, and Top and Side SEM Images of PVDF-HFP Gel Membrane.

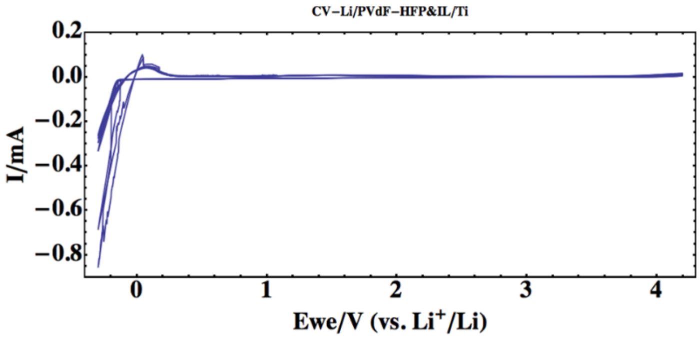

Figure 9. CV of Li/PVDF-HFP&IL/Ti System.

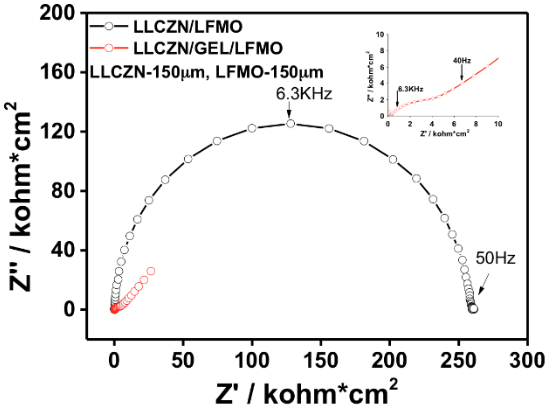

Figure 10. EIS of Garnet/Cathode and Garnet/Gel/Cathode.

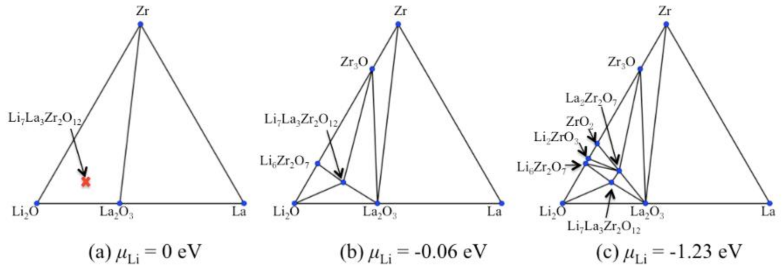

Figure 11. Li Grand Cannonical Phase Diagram of Li-La-Zr-O System.

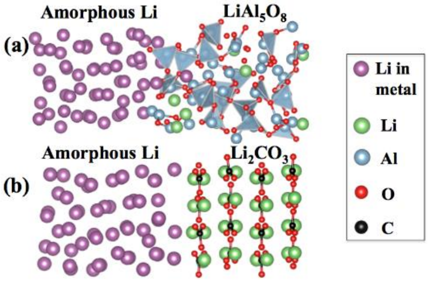

Figure 12. Models for the Interfaces between Li-Metal and Garnet Surface Materials.

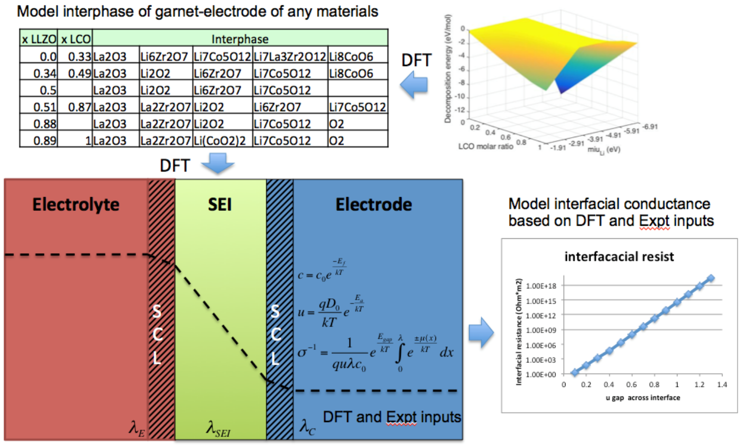
Model interphase of garnet-electrode of any materials

x LLZO	x LCO	Interphase				
0.0	0.33	La2O3	Li6Zr2O7	Li7Co5O12	Li7La3Zr2O12	Li8CoO6
0.34	0.49	La2O3	Li2O2	Li6Zr2O7	Li7Co5O12	Li8CoO6
0.5		La2O3	Li2O2	Li6Zr2O7	Li7Co5O12	
0.51	0.87	La2O3	La2Zr2O7	Li2O2	Li6Zr2O7	Li7Co5O12
0.88		La2O3	La2Zr2O7	Li2O2	Li7Co5O12	O2
0.89	1	La2O3	La2Zr2O7	Li(CoO2)2	Li7Co5O12	O2

$$c = c_0 e^{\frac{-E_f}{kT}}$$

$$u = \frac{qD_0}{kT} e^{-\frac{E_a}{kT}}$$

$$\sigma^{-1} = \frac{1}{qu\lambda c_0} e^{\frac{E_{gap}}{kT}} \int_0^{\lambda} e^{\frac{\pm\mu(x)}{kT}} dx$$

Model interfacial conductance based on DFT and Expt inputs

Figure 13. Model for Garnet-Electrode Interfaces, which take Inputs from First Principles Calculations and Experimental Condition Parameters.

This Page Intentionally Blank

AVPTA Technology Focus Area 6: Energy Storage & Batteries

Beyond Li-Ion: New Lamination and Doping Concepts for Enhanced Li-Sulfur Battery Performance

DOE-VTO TFA Lead: David Howell
TARDEC TFA Lead: Dr. Laurence Toomey

Principal Investigator:
Dr. Prashant N. Kumta

Affiliation:
University of Pittsburgh
123 University Place
Pittsburgh, PA 15213-2303
Phone: (412) 648 - 0223
E/M: pkumta@pitt.edu

Project Start: 01/10/2014
Estimated Completion: Q4FY17

Objective:

- To successfully demonstrate generation of novel sulfur cathodes for Li-S batteries meeting the targeted gravimetric energy densities ≥ 350 Wh/kg and ≥750Wh/l with a cost target $125/kWh and cycle life of at least 1000 cycles for meeting the EV everywhere blueprint. The proposed approach will yield sulfur cathodes with specific capacity ≥1400mAh/g, at ≥2.2V generating ~460Wh/kg, energy density higher than the target. Full cells meeting the required deliverables will also be made.

Strategic Context:

- Generate a leap-ahead technology used for military vehicles to support the future power for TARDEC and the Army by enabling the development of advanced battery systems with significant increases in energy density
- Improve Battery safety characteristics to support vehicle silent watch and enable other high energy requiring applications.

Accomplishments:

- Demonstrate synthesis of finely dispersed nanoparticles of sulfur (December 2014) – Completed
- Developed novel lithium-ion conducting (LIC) membrane systems using ab-initio methods displaying impermeability to sulfur diffusion (December 2014) – Completed

- Demonstrate capabilities for generation of novel sulfur 1-D, 2-D and 3-D morphologies exhibiting superior stability and capacity (June 2015) – Completed
- Identification and synthesis of LIC materials for use as coatings for sulfur cathodes (June 2015) – Completed
- Novel encapsulation and sheathing techniques and exploration of unique architectures and generation of 3-D composites displaying superior Li-ion conduction, reversible capacity and stability (June 2015) – Completed
- Identification of suitable dopants and dopant compositions to the improve electronic conductivity of sulfur (October 2015) – Completed
- Fundamental electrochemical studies to understand the reaction kinetics, mechanism and charge transfer kinetics (October 2015) – On-going
- Go/No-Go (October 2015) decision will be based on the ability to demonstrate improvement in cycling upon use of the LIC coating. – Completed

Introduction:

The increasing demand in the EV industry for low cost, light weight and high energy storage batteries to meet the EV everywhere grand challenge, the current focus of research has shifted towards the development of lithium sulfur (Li–S) batteries owing to the high theoretical specific capacity exhibited by sulfur compared to other cathode materials currently available. Li–S battery shows a theoretical capacity of 1675 mAh/g corresponding to the formation of Li_2S which makes sulfur a promising electrode to replace the layered transition metal oxides (~150 mAh/g) and $LiFePO_4$ (~170 mAh/g) deployed in present LIB systems. Moreover, the abundance of sulfur in the earth's crust, its ubiquitous availability as a byproduct in the extractive mineral and petrochemical industry, combined with ease of processing, makes it a more economical proposition compared to currently existing cathode materials.

Approach:

The objectives outlined above will be accomplished by engineering sulfur cathode materials primarily by laminating the electrodes with lithium ion conductor (LIC) coatings in order to prevent polysulfide dissolution and doping in order to improve the electronic and ionic conductivity. The following major technology innovations will be undertaken to accomplish the following objectives of this effort:

- *Phase – 1 (Year 1):* Synthesis, Characterization and Scale up of suitable LIC matrix materials and multilayer composite sulfur cathodes. This phase is completed.
- *Phase – 2 (Year 2):* Development of LIC coated sulfur nanoparticles, scale up of high capacity engineered LIC coated multilayer composite electrodes and doping strategies for improving the electronic conductivity of sulfur.
- *Phase-3 (Year 3):* Advanced high energy density, high rate, and extremely cyclable cell development.
- Identify novel LIC coating materials and morphology for composite multilayer sulfur cathode architectures exhibiting: Specific capacity ≥1000 mAh/g (≥8 mAh/cm^2), cyclability (~1000 cycles), loss per cycle ≤0.05% per cycle, Coulombic Efficiency (CE): ≥99.5%.

- Optimize the interface engineered multilayer composite LIC coated sulfur cathode architectures exhibiting: Specific capacity ≥1200 mAh/g (≥4 mAh/cm^2), cyclability (~1000 cycles), loss per cycle ≤0.01% per cycle, CE: ≥99.9%.
- Synthesize doped sulfur nanoparticles on gram scale and demonstrate improvement in performance, reflected as an increase in the sulfur weight percentage and improvement in rate capability of the electrodes.
- Tie together the three different trees of development i.e. coating development/sulfur particle development/CNT based exploration by identifying suitable configuration integrated electrode (I.E.) with maximum sulfur weight percentage demonstrating high capacity ≥1400 mAh/g, cyclability (~1000 cycles), loss per cycle ≤0.01% per cycle, CE: ≥99.99%.
- Assemble 4 mAh high energy density Li-S pouch cells and conduct performance testing.

Results and Discussion:

The aim of Phase-1 of this project was essentially to identify various materials that can act as lithium ion conductors (LICs) while preventing polysulfide transport and accompanying sulfur loss. The end of Q-4 has a Go/No-go point which is based on the ability to demonstrate that the working hypothesis is valid (i.e. LICs indeed improve Li-S battery cycle life). In order to achieve this target, 4 strategies were employed during Phase-1 of the project: (a) Use of inorganic LICs in the form of pellet coatings (Q1, Q2) (b) fabrication of flexible polymer-sulfur wires (Q2) (c) generation of gel polymer electrolyte (GPE) as an electrolyte medium (Q3) (d) use of complex framework materials (CFM) as trapping agents for sulfur species (Q4). The various strategies and progress achieved thus therein are described below:

High Areal Capacity Inorganic LIC-coated Sulfur Nanoparticulate Electrodes:

Research in the first quarter of Phase-1 involved identification of strategies to improve the characteristics of sulfur electrodes by pursuing a three-pronged approach:

1. Synthesis of nano-particles (NP) of sulfur in order to achieve higher capacities without significant increase in fade rate.
2. Use of solid state processing i.e. pellet pressing as an effective method to improve the capacity retention in lithium sulfur batteries in comparison to the conventional slurry casting procedure.
3. Coating of thin solid state lithium-ion conductive (LIC) layer for minimal contact of liquid electrolyte with sulfur preventing dissolution of the polysulfides formed during lithiation of sulfur, while at the same time not presenting problems observed with the use of purely solid state electrolytes.

Among the several approaches identified, the first was to synthesize sulfur nanoparticles (SNPs) size to increase the capacity approaching theoretical limits of sulfur (~1675 mAh/g-Sulfur). The synthesis procedure involved re-precipitation of sulfur dissolved in a basic media followed by acid-driven neutralization. Different concentrations of various molecular acids resulted in colloidal SNPs of various sizes determined by dynamic light scattering (DLS). The average particle size was observed to decrease with lower concentration of the dissolved sulfur solution and also with the decrease in the normality of the acid solution used for generating the colloidal SNPs. Among the various SNPs, particles of ~600 nm were found to have ideal electrochemical characteristics. Figure 1a, and Figure 1b show the SEM images of the nano-sulfur and commercial sulfur, respectively. The difference in particle size can be distinctly observed by comparing the two images. The nano-sulfur particles formed by the chemical re-precipitation procedure exhibit agglomerated particle sizes of ~500 nm-2 μm as seen in the SEM micrograph in Figure 1a. Commercially obtained sulfur particles used as precursors in the chemical re-precipitation reaction on the other hand, have a wide particle size distribution consisting of 20-150 micron particles as seen in Figure 1b. The fine particles of nano-sulfur are expected to have exceptional exposure to the lithium conducting (LIC) layer/conductive additive resulting in high capacity. Similar to the case of nanoparticle amorphous silicon anodes studied for Li-ion batteries, reversible expansion and contraction would not result in particle fracture and accompanying capacity fade. Figure 1c shows the morphology of the composite multilayer electrode assembled by the pellet pressing method. The pellet consists of a thin layer of lithium orthosilicate coating the mixture of sulfur and carbon. The uniformity of the coating and lack of macroscopic cracks are confirmed from the same. The inset images depict the disparate architecture existing within the orthosilicate layer and the sulfur-carbon layer. The orthosilicate layer consists of macroscopic particles fused together as a result of the mechanical pressing process. It can also be seen that the layer consists of macroscopic pores ideal for liquid electrolyte percolation. Short solid-state diffusion distances would thus result and the common issues typically experienced in solid electrolyte based lithium-sulfur batteries would thus be circumvented. The orthosilicate layer is a few microns thick ensuring that sulfur particles are not directly exposed to the liquid electrolyte thus serving to protect and prevent any dissolution of the polysulfides formed. The channel structure existing in the electrode would hence ensure minimal percolation of liquid electrolyte to sulfur particles. In addition to the protection offered by the orthosilicate layer, the pressing procedure ensures the formation of an elegant carbon coating on the sulfur particles. The carbon networks thus act both as electron conducting and lithium ion conducting (LIC) channels. Solid-state lithium ion diffusion through carbon is not hindered and should not pose as a barrier to the ensuing intercalation and de-intercalation processes. Evaluation of electrochemical performance of the various sulfur materials as cathodes was thus performed for the electrodes generated following two methods. Electrodes of sulfur-carbon (1:1) were prepared by either tape casting from the organic solvent based slurries or mechanically pressed pellets. Figure **2**a shows the 10th cycle charge-discharge profiles of the various sulfur-carbon materials. Characteristic plateaus corresponding to polysulfide formation and subsequent conversion to dilithium disulfide (Li_2S_2) and dilithium sulfide (Li_2S) are observed in all the materials. The composite multilayer electrode can be seen to exhibit however, the highest gravimetric capacity of the various materials after 10 cycles as a result of the high capacity yielded by the nano-sulfur morphology (as shown in Figure **2**b also). The nano-sulfur slurry electrode also displays a high capacity as compared to the commercial sulfur pellet and the slurry made from commercially obtained sulfur powder. The cycling stability of the various materials is plotted in Figure **2**b and Figure **2**c (specific gravimetric and areal capacity, respectively). Among the slurry cast electrodes, it can be seen that the nano-sulfur demonstrates the higher capacities and better fade characteristics in comparison to the commercially obtained sulfur. The improvement in capacity can be attributed to the change in particle size seen in Figure 1a, and Figure 1b. The higher surface area of the 0.3-2 μm particles (as confirmed by DLS) results in enhanced reactivity and thus better capacity. The improvement in cycling performance observed therein could be attributed to reduced particle stresses to be expected in smaller particles resulting in much reduced fracture and delamination. In addition, the fine particle size would ensure good contact with the conductive additive preventing the particles from becoming inactive over time as a result of the fracture. The crystalline nature of the fine nanoparticles would at the same time, ensure that the particles would not be completely insulating. The slurry cast nano-sulfur electrode thus has a high initial capacity of ~1125 mAh/g-S and a fade rate of 0.86%/cycle as seen in Figure **2**b. This superior performance indicates that sulfur behaves similar to silicon with respect to charge storage capability and cycling stability, in that the reduction in particle size of S aids both those characteristics. Furthermore, the nano-sulfur slurry cast electrode has a high initial areal capacity of 3.5 mAh/cm^2, stabilizing at ~1.4 mAh/cm^2, upon further cycling (Figure **2**c).

The improvement in charge storage as a result of utilizing the pellet-pressing procedure, especially the composite multilayer electrode architecture is together seen in Figure **2**b. The use of the pellet pressing procedure yields thicker electrodes, while at the same time allowing for better capacity retention. This results in the significantly higher areal capacities seen in Figure **2**c. The thick electrodes made from commercially obtained sulfur have an initial areal capacity of ~4 mAh/cm^2 while the composite multilayer electrode has an areal capacity of ~4.75 mAh/cm^2. These are values corresponding to the 5th cycle since these thick electrodes suffer from poor wetting in the initial cycles as would be expected. With further optimization, we believe we could improve the capacity and cyclability of these electrodes by ensuring that polysulfides would not contribute to loss of electrical contact and would thus get completely converted to Li_2S. Even so, the capacity observed at the 5th cycle is much higher than the current EERE-OVT (Office of Energy Efficiency & Renewable Energy-Office of Vehicle Technologies) target expectations for areal capacity of electrodes of 4 mAh/cm^2. It should be also noted that the areal capacities and sulfur loadings on the electrode exceed those previously reported though further optimization is ongoing to improve the overall sulfur weight percentage (to reduce overall electrode thickness) . Both electrodes exhibit superior cycling stability thus validating the hypothesis that the inorganic LIC materials aid in preventing polysulfide dissolution driven lithium-sulfur battery capacity loss hitherto seen.

First Principles Studies into Identification of High Ionic Conductivity LIC-coating Materials:

Improvement in LIC ionic conductivity and polysulfide filtration capability is to be achieved by first principles driven design and experimental development of suitable LIC materials with the aim of further improving cycling capability. Using the nudged elastic band method implemented in VASP (Vienna ab-initio simulation package), various Li-ion migration pathways have been considered and corresponding activation barriers Ea have been calculated. Corresponding results in Figure 3 indicate that the pathway (0-2) requires the lowest activation energy (~ 1 eV) for the Li-ion migration from the central position (0) to the Li-vacancy (2). All other pathways demonstrate higher activation barriers (up to 2.2 eV). Introduction of aliovalent dopants could create Li-ion vacancies as well as decrease the activation barriers for the ionic migration, thus improving the overall ionic mobility. The ionic conductivity of doped Li_4SiO_4 with Mg, Ca, V, Nb, and F has been studied from first principles calculations. Corresponding results shown in Figure 4 indicate that Mg^{2+} and Ca^{2+} substituting for Li^+-ion as well as F^- replacing O^{2-} ions help decrease the activation barriers for all corresponding Li-ion pathways in comparison to pure Li_4SiO_4. On the other hand, V and Nb substituting Si-ions slightly increase the E_a due to the larger ionic radii of V^{5+} and Nb^{5+} compared to Si^{4+}. However, the overall Li-ion conductivity is expected to be improved due to formation of Li^+ vacancies and thus, facilitating Li-ion hopping through the crystal lattice. In terms of structural and chemical stability, the calculated cohesive energies of the pure and doped orthosilicates indicate that V and Nb slightly decrease the stability, while Mg, Ca and F virtually render the stability invariant. Thus, the present theoretical study helped in identifying Mg, Ca, and F as prospective doping elements facilitating improvement in the Li-ion conductivity without sacrificing the overall structural and chemical stability of the LIC orthosilicate. An experimental validation of this conclusion will be conducted in the closest future and will be reported subsequently.

Flexible Polymer-sulfur Wires:

Following earlier studies demonstrating significant capacity and stability improvement in sulfur cathodes obtained by using a thin layer of lithium ion conductor (LIC) on sulfur nanoparticles, work in the second quarter involved identification of strategies to further improve the stability by tailoring the sulfur morphology. Towards this end, flexible sulfur wires (Flex-SWs) were generated using a simple polymer-handling method reported in Q2. The synthesis allows for a polymer-sulfur wire morphology (Figure 5) to be obtained with the polymer acting as a structural template as well as contributing to improving the cycling characteristics by facilitating polysulfide retention. Figure 6a and Figure 6b depict the scanning electron micrograph and corresponding sulfur map of the unique sulfur fiber (Flex-SW) morphology obtained for the first time rendering Flex-SW very amenable for use in compliant, flexible batteries. Figure 5 displays the yarn-like quality of the Flex-SWs opening the door for a multitude of unique applications. It can be seen from Figure 6b that sulfur is uniformly distributed over the entire length of the yarn with no obvious segregation. The unique synthesis procedure yields wires which are in-effect encapsulated in a polymer matrix thus directly addressing the primary problem of polysulfide dissolution typically solved by the ubiquitous chemically induced steric hindrance methods. Figure 7a shows the cycling response of the various sulfur electrodes including commercial sulfur cast (C-Sulfur:slurry) and pellet-pressed (C-Sulfur pellet); nano-sulfur pellet-pressed with an LIC layer (nano-Sulfur-LIC pellet); Flex-SWs with LIC (Flex-SW pellet-LIC) and void LIC (Flex-SW pellet) layers. The Flex-SW pellet demonstrates superior stability and minimal capacity fade over ~135 cycles (see Figure 7b). The Flex-SW pellet demonstrates an initial capacity of ~700 mAh/g which stabilizes to ~450-500 mAh/g over the first 5 cycles. Studies are on-going to understand this stabilization behavior which is a typical feature of Flex-SW materials. This 1st cycle irreversible loss behavior however, is circumvented by use of a thin LIC coating on Flex-SW as seen in Figure 7a wherein the FSW-LIC pellet maintains a stable capacity of ~650 mAh/g over 60 cycles (fade rate~0.003%/cycle). Further analysis and optimization is currently ongoing to improve the capacity and stability of the flexible sulfur-polymer wires. Further, stable areal capacity of the Flex-SW-pellet materials achieved thus far is ~2.5 mAh/cm^2. Optimization of sulfur weight percentage is needed to improve this number to achieve the targeted 4 mAh/cm^2. Research in this direction is on-going.

Polymeric LIC Materials (Gel-polymer electrolyes-GPEs):

In addition to inorganic LIC materials, polymer LIC (gel-polymer materials (GPE) containing lithium-ion conductor) materials were explored as a part of continuing studies into the same. These polymeric LIC materials were used to replace the conventional polymeric separator materials. Figure 8 depicts the improvement in cycling stability achieved by creating composite polymeric core-shell and layer-by-layer composite materials. In order to address the fade associated with the gel-polymer electrolyte materials, nanoparticulate oxide materials were used as fillers in the GPE matrix. Figure 9a shows the TEM images of the oxide nanoparticles used therein and Figure 9b depicts the improvement in cycling behavior achieved as a result of the same. Stability achieved by using doped oxide nanoparticles as filler materials in the polymer material results in a stable capacity of ~400 mAh/g seen up to 80 cycles. The polymer electrolyte materials with oxide tethering sites act both as polysulfide filters as well as restraining media ensuring improvement in cycling stability. Optimization work is ongoing involving the gel-polymer LIC electrolyte materials and will be reported in following reports.

Complex Framework Materials (CFM):

Research in Li – S batteries is mainly focused on three main aspects:(i) Improving the conductivity of Sulfur by using conductive coatings or composites and hence increasing the active material utilization, (ii) Modifying the liquid electrolyte – separator system using a gel – polymer or composite – polymer electrolyte to prevent polysulfide dissolution and (iii) Confining sulfur into porous matrices and hence, preventing polysulfide dissolution. Porous materials with pore size comparable to or less than the size of polysulfide species need to be devised in order to completely overcome the problem of polysulfide dissolution. Hence, the use of complex framework materials (CFM) as trapping agents for sulfur species has been explored. The CFM materials containing nanopores are ideal for entrapping the soluble polysulfide species formed during lithiation of sulfur. Figure 6 depicts the morphology of certain nanoporous CFMs acting as sulfur – hosts. There is a significant improvement in initial capacity and cycling stability achieved as a result of the use of sulfur-containing CFMs as Li-S battery cathodes and stable cycling up to 200 cycles has been demonstrated (Figure 10) thus-far (further cycling is ongoing). The CFM electrodes also exhibit a very low fade rate of ~0.01%/cycle following initial phase change. Work is on-going to understand the cause of the phase change while also developing approaches to overcome the initial loss due to this phase change.

Conclusions:

Table 1 summarizes the cycling characteristics of the various sulfur materials explored in Phase-1 of this project. The aim of Phase-1 was to establish methods to improve sulfur cycling characteristics by use of lamination approaches, especially in the form of LIC materials. It can clearly be observed that fade rates have been significantly reduced by using the 4 approaches in Phase-1 described above. Stable capacities of in excess of 600 mAh/g have been observed in two systems with stability for over 150 cycles, the flexible sulfur-polymer composite electrodes and the Sulfur CFM materials. Exceptionally low fade rates of ~0.003%/cycle have been observed which greatly supports the hypothesis of LIC-based engineering. In Phase-2 of the study, emphasis will be laid on improving capacity of these systems with the goal of achieving capacity excess of 1000 mAh/g for 1000 cycles. The primary driving force for this will be electronic conductivity improvement. In lieu of this, *ab-initio* calculations have been performed in Q4 to identify suitable doping strategies to achieve the same. First principles studies were conducted to understand the effect of dopants on the band-structure and density of electronic states (DOS) of sulfur (Figure 12). It can be seen that sulfur which is inherently an insulator following introduction of these dopants leads to sulfur exhibiting semiconducting properties upon the introduction of dopants into the sulfur lattice. Experimental synthesis of the doped sulfur followed by detailed evaluation forms a part of Phase-2 study of the project which will be initiated in year 2 and accordingly, reported in due course. Electronic and ionic conductivity optimization using various experimental strategies will be actively pursued towards generating high rate, high gravimetric and areal capacity sulfur cathodes with exceptional cycling stability. Results of these studies will be reported in due course.

References:

1. P. J. Hanumantha, B. Gattu, et al., Journal of The Electrochemical Society, 2014, 161, A1173-A1180.
2. P.J. Hanumantha, B. Gattu, P.M. Shanthi, P.N. Kumta, Provosional Patent, 2015, Application number: 62132014.
3. Jampani, P.H.; Shanthi, P.M.; Gattu, B.; Kumta, P.N. Novel Flexible Sulfur Wire Fabrics (FSF) for Lithium-Sulfur Batteries, The Electrochemical Society (Spring ‘15), Chicago, IL
4. Shanthi, P.M.; Jampani, P.H.; Gattu, B.; Velikokhatnyi, O.I.; Kumta, P.N. Effect of Coating and Particle Properties on the Cycling Stability of Li-Ion Conductor (LIC) Coated Sulfur Cathodes, The Electrochemical Society (Spring 2015), Chicago, IL
5. Jampani, P.H.; Gattu, B.; Shanthi, P.M.; Damle, S.S.; Basson, Z.; Bandi, R.; Datta, M.K.; Park, S.K.; Kumta, P.N. Flexible sulfur wires (Flex-SWs) – A Versatile platform for lithium-sulfur batteries, ChemElectrochem (2015), in press
6. Massalimov, A. R. Shainurova, A. N. Khusainov and A. G. Mustafin, Russ J Appl Chem, 2012, 85, 1832-1837.
7. J. Graetz, C. C. Ahn, R. Yazami and B. Fultz, Electrochemical and Solid State Letters, 2003, 6, A194-A197.
8. M. D. Levi and D. Aurbach, The Journal of Physical Chemistry B, 1997, 101, 4641-4647.
9. K. Zaghib, J. Shim, A. Guerfi, P. Charest and K. Striebel, Electrochemical and Solid-State Letters, 2005, 8, A207-A210.
10. Department of Energy, E. E. R. E.-Office of Vehicle Technologies Report, 2014.
11. T. Xu, J. Song, M. L. Gordin, H. Sohn, Z. Yu, S. Chen and D. Wang, ACS applied materials & interfaces, 2013, 5, 11355-11362.
12. S. Thieme, J. Brückner, I. Bauer, M. Oschatz, L. Borchardt, H. Althues and S. Kaskel, Journal of Materials Chemistry A, 2013, 1, 9225-9234.

Remainder of Page Intentionally Blank

Figures and Tables:

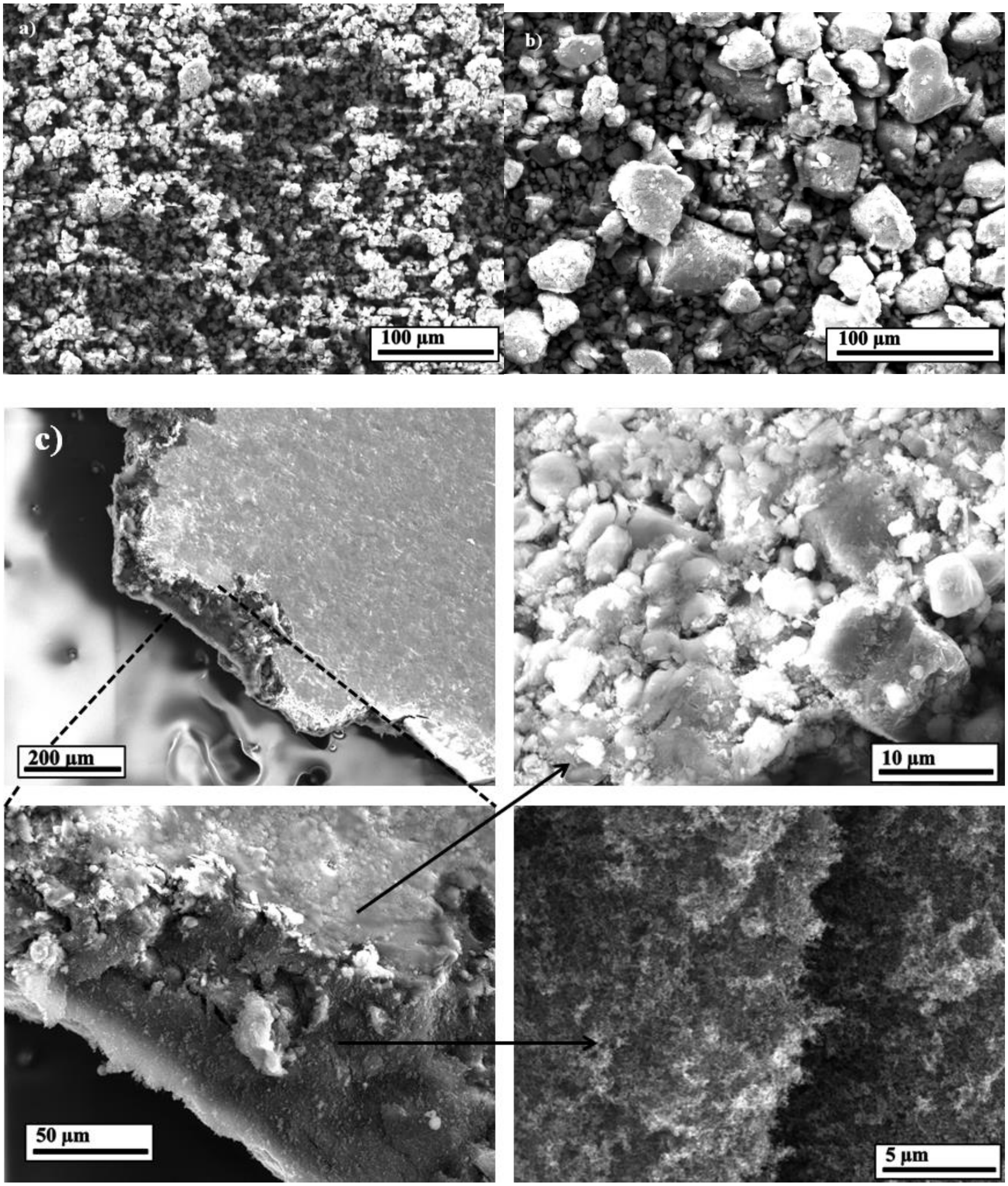

Figure 1. Scanning Electron Microscope Images of a) Chemically-derived Nano Sulfur; b) Commercially Procured Sulfur; c) Composite Multilayer Electrode Architecture with a Uniform Coating of Lithium Orthosilicate on a Sulfur-Carbon Mixture. The Layer Structure is Clearly Visible in the Inset Image. The Top Layer of Orthosilicate is Porous and Consists of Macroscopic Particles Fused as a Result of the Mechanical Pressing. The Soft Sulfur-Carbon Inner Layer Consists of much Finer Particles of Distinctly Different Morphology.

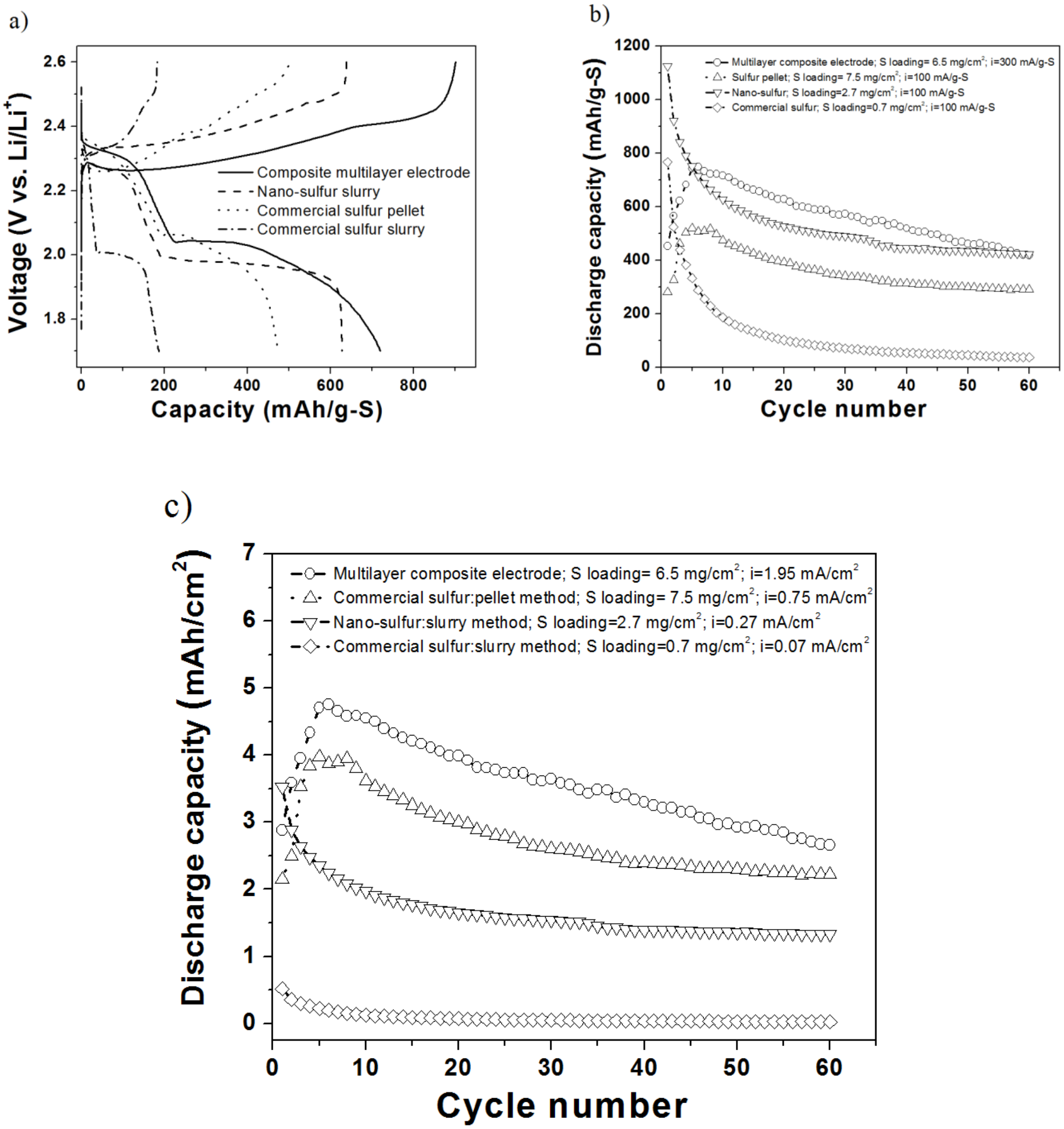

Figure 2. a) Charge-discharge Profiles (Sulfur Basis Gravimetric Capacity) of the Various Electrode Architectures; b) Comparison of Cycling Behavior of the Commercial Sulfur, Nano-sulfur Prepared by Slurry Method, Pellet Method and the Multilayer Composite Electrode; c) Comparison of Cycling Behavior (Overall Electrode Areal Capacity Basis) of the Various Electrodes.

Remainder of this Page Intentionally Blank

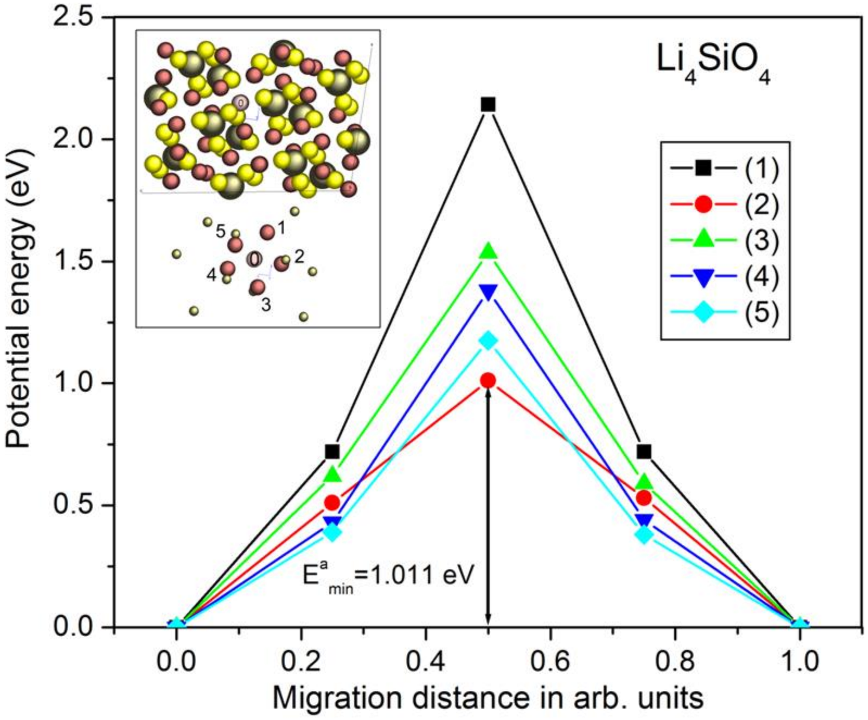

Figure 3. Activation Barriers for Different Migration Paths of Li-ions in Li$_4$SiO$_4$. Inset: Pink 0 - Li-ion Site; Red (1)-(5) – Li Vacancy Sites for Different Migration Pathways.

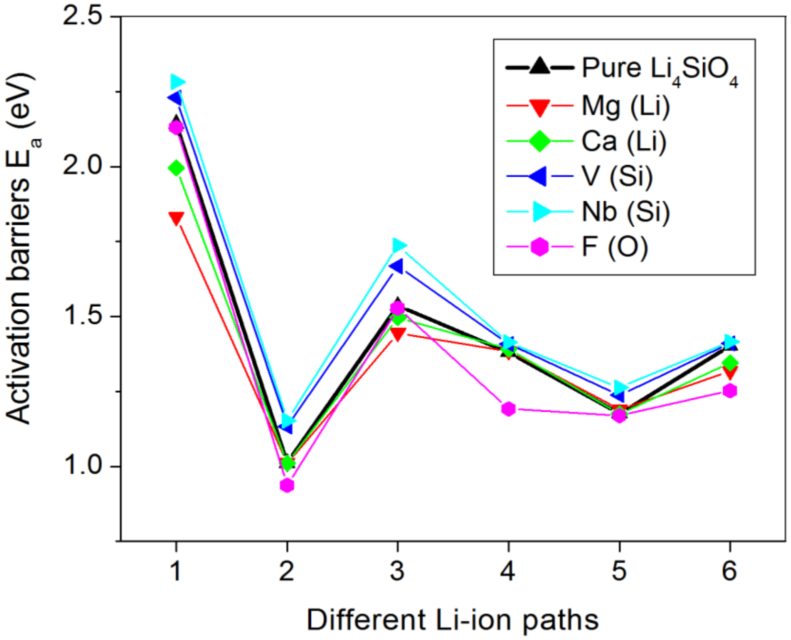

Figure 4. Activation Barriers E$_a$ for Different Migration Paths of Li-ions in Pure and Doped Li$_4$SiO$_4$.

Figure 5. Image Showing the Yarn-like Nature of the Flex – sulfur Wires (Flex-SWs).

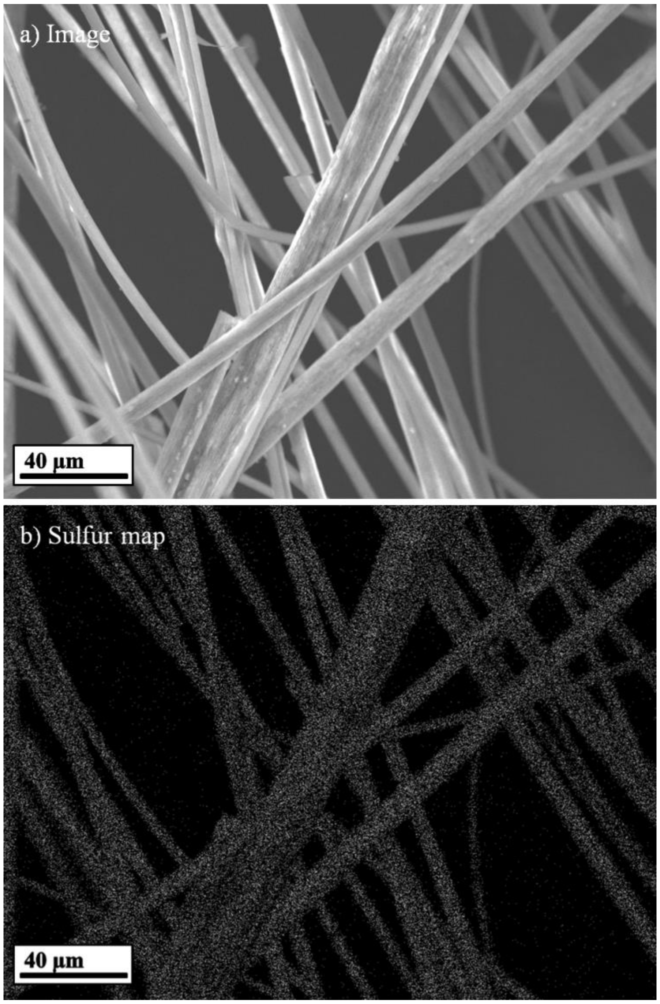

Figure 6. (a) SEM Image (b) EDAX Map of the Flexible Sulfur-polymer Morphology shown in Figure 5.

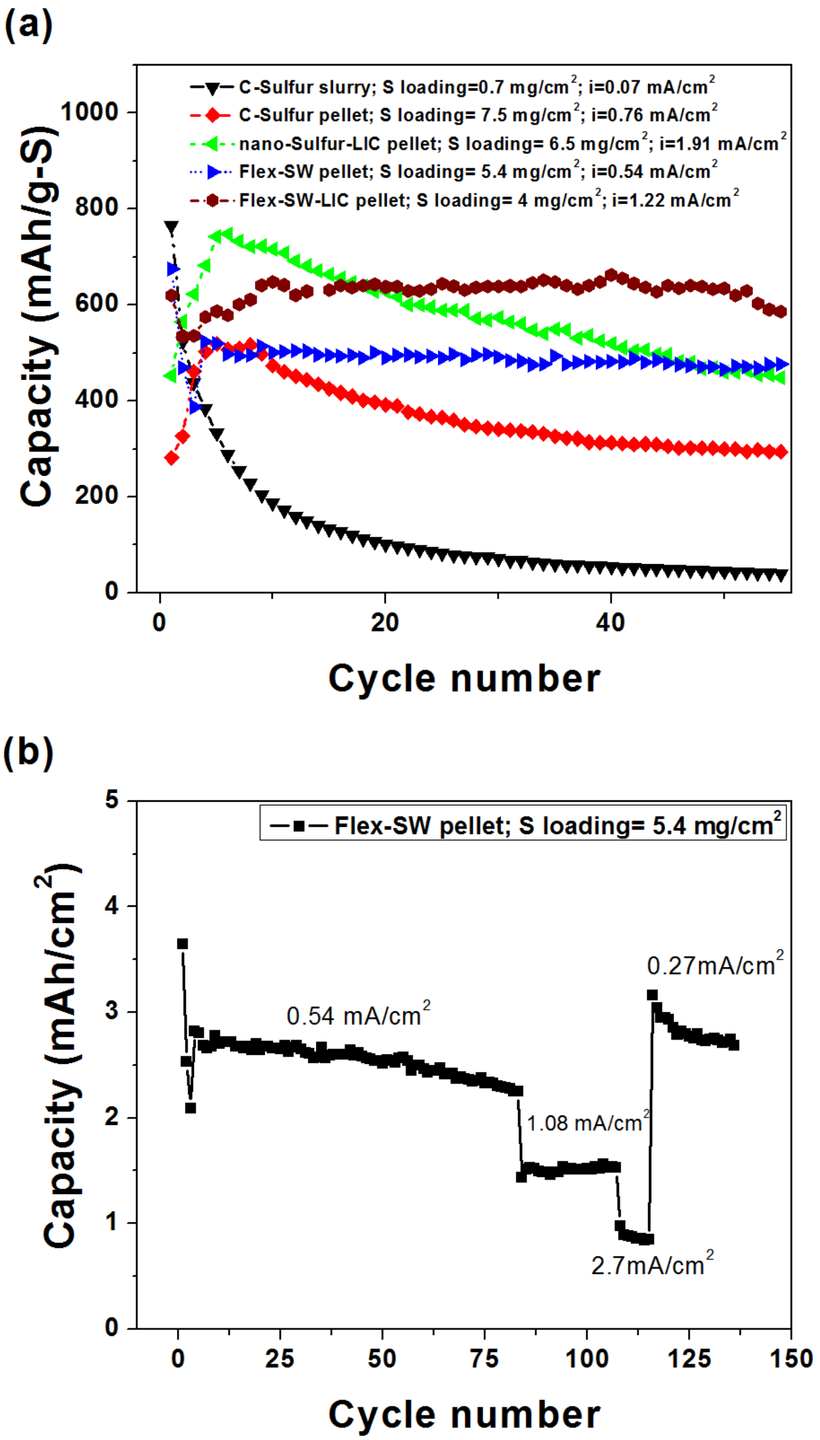

Figure 7. (a) Cycling Behavior of Various Sulfur Materials (b) Extended Cycling and Rate Dependence of Capacity in Flex-sulfur Wires seen in Figure 6.

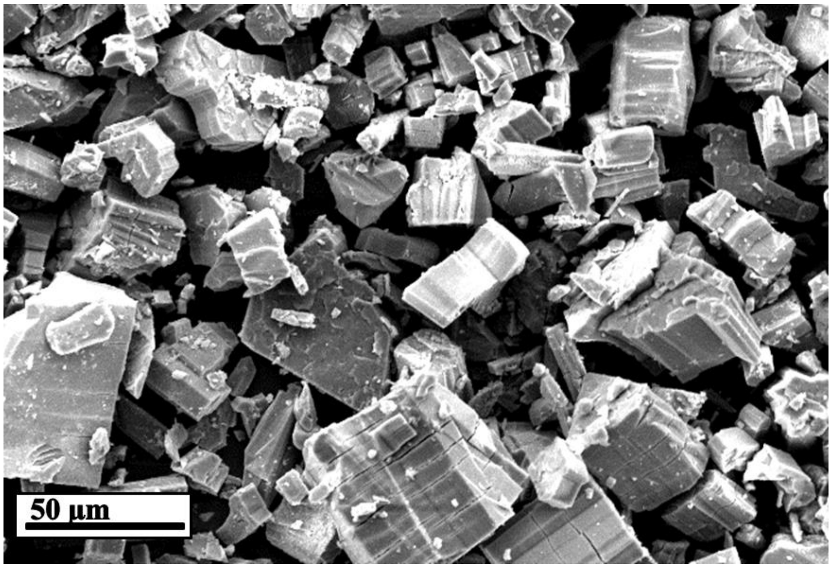

Figure 8. Comparison of Cycling Behavior of Various\
Polymeric LIC Electrolyte Materials.

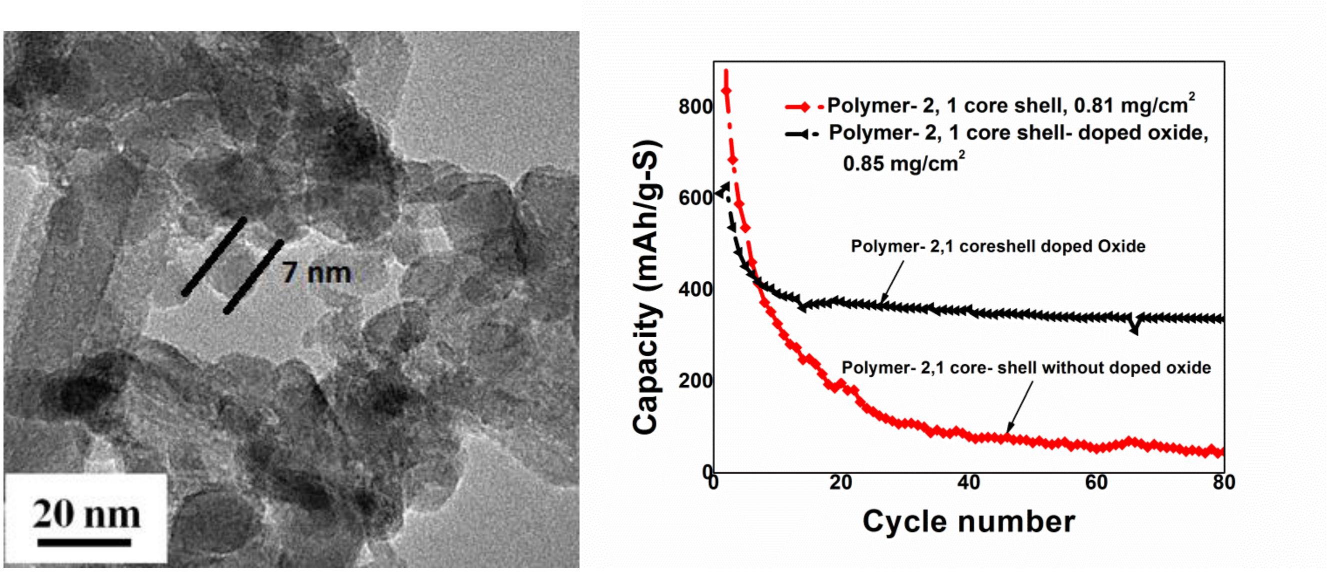

Figure 9. (a) Transmission Electron Microscope (TEM) (left Fig.) of Oxide Nanoparticles used as Fillers in the GPE Materials (b) Effect of Oxide Filler Material on Cycling Behavior in Polymer LIC Materials (right Fig.).

Remainder of Page Intentionally Blank

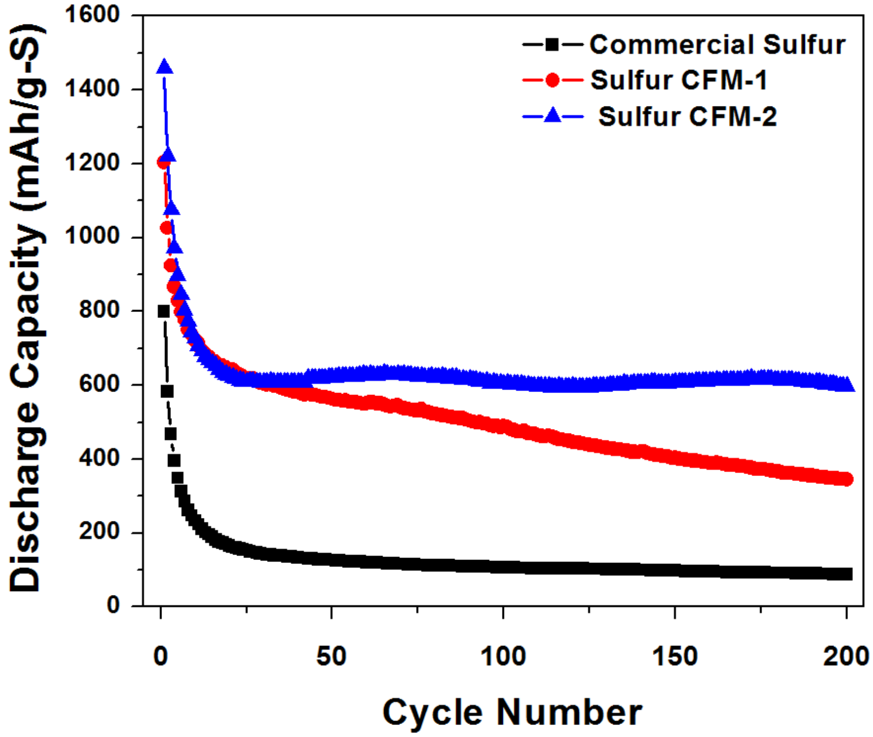

Figure 10. Improvement in Cycling Stability of Sulfur Cathodes by use of CFM Materials.

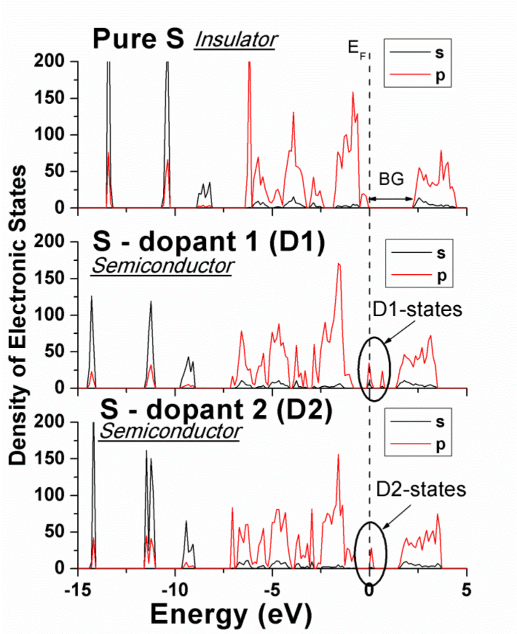

Figure 11. Effect of Doping on Electronic Conductivity of Sulfur.

Material	Initial discharge capacity (mAh/g-S)	Initial capacity fade[¥] (% capacity)	Fade rate[*] (% capacity/cycle)
C-Sulfur:slurry	766.3	56.53	1.76
C-Sulfur pellet	519.3[†]	N/A	0.87
nano-Sulfur-LIC pellet	748.2[†]	N/A	0.79
Flex-SW pellet	675.4	23.09	0.17
Flex-SW pellet-LIC	620.3	5.37	0.003
Polymer 2,1 core-shell-doped oxide	776.26	36.75	0.4
Sulfur CFM-2	1460.4[^]	54.79	0.01

[¥]Fade rate calculated on the basis of 1st cycle capacity and 5th cycle capacity.[*]Fade rate calculated on the basis of 5th cycle capacity and 55th cycle capacity. [†]Capacity reported at 5th cycle since there was an increase in capacity from 1st cycle due to gradual wetting of the electrode.[^]Stabilizes at 20th cycle and fade calculated upto 200th cycle.

Table 1. Cycling Characteristics of Various Sulfur Battery Systems Synthesized and Evaluated in this Work.

Remainder of Page Intentionally Blank

APPENDIX A

Memorandum of Understanding
Between
U. S. Department of Energy
And
U. S. Department of Defense

Concerning Cooperation in a Strategic Partnership to Enhance Energy Security

I. Purpose

The purpose of this Memorandum of Understanding (MOU) is to identify a framework for cooperation and partnership between the Department of Energy (DOE) and the Department of Defense (DOD), hereafter referred to as the Parties, to strengthen coordination of efforts to enhance national energy security, and demonstrate Federal Government leadership in transitioning America to a low carbon economy. This MOU covers, but is not limited to, efforts in the areas of energy efficiency, renewable energy, water efficiency, fossil fuels, alternative fuels, efficient transportation technologies and fueling infrastructure, grid security, smart grid, storage, waste-to-energy, basic science research, mobile/deployable power, small modular reactor nuclear energy, and related areas.

II. Legal Authority

DOE enters into this MOU under the authority of section 646 of the Department of Energy Organization Act (Pub. L. 95-91, as amended; 42 U.S.C. § 7256). DOD enters into this MOU under the authority of DOD Instruction 4000.19 "Inter-Service and Intra-Governmental Support" August 9, 1995.

III. Background

In the 2010 Quadrennial Defense Review, the DOD expressed an intent to partner with other U.S. agencies to research, develop, test, and evaluate new sustainable energy technologies. The DOD aims to speed innovative energy and conservation technologies from laboratories to military end users, and it uses military installations as a test bed to demonstrate and create a market for innovative energy efficiency and renewable energy technologies coming out of DOE laboratories, among other sources. The DOE is currently supporting a range of projects aimed at improving energy efficiency and renewable energy efforts across the military services.

Energy security for the DOD means having assured access to reliable supplies of energy and the ability to protect and deliver sufficient energy to meet operational and Installation energy needs. Energy efficiency can serve as a force multiplier, increasing the range and endurance of forces in the field while reducing the number of combat forces diverted to protect energy supply lines, as well as reducing long-term energy costs. DOD is also increasing its use of renewable energy supplies and reducing energy demand to improve energy security and operational effectiveness, reduce greenhouse gas (GHG) emissions in support of U.S. climate change initiatives, and protect the DOD from energy price fluctuations. Solving military challenges through innovation has the potential to yield spin-off technologies that benefit the civilian community as well.

The DOE is the lead Federal agency responsible for the development and deployment of advanced energy technologies, yet DOD will need to invest in many of these same energy technologies as well as other energy technologies which may be unique to DOD's operational requirements. Partnering with DOD provides DOE the opportunity to accelerate the deployment of its technologies and expertise toward the critical economic and energy security needs of the United States and to promote scientific and technological innovation.

The Parties acknowledge the significant positive collaboration that already exists between DOE and DOD and intend through this MOU to strengthen and broaden that cooperation.

IV. Activities

Specific activities covered under this MOU include, but are not limited to:

A. Evaluate energy systems and technology management solutions that meet DOD objectives including developing energy technologies that meet DOD energy requirements. Work collaboratively to identify a strategy for their development and deployment.

B. Maximize DOD access to DOE technical expertise and assistance through cooperation in the deployment and pilot testing of emerging energy technologies. Technology areas may include, but are not limited to, energy efficiency, renewable energy, water efficiency, fossil fuels, alternative fuels, efficient transportation technologies and fueling infrastructure, grid security (e.g., superconductivity, power, electronics, microgrids, cyber, EMP), smart grid, storage, waste-to-energy, basic science research, mobile/deployable power, small modular reactor nuclear energy, and related areas.

C. Expand cooperation related to energy management practices and knowledge exchange, working to ensure that Federal leadership is in compliance with all statutory and Executive Order goals and objectives, particularly in the area of GHG reductions. Encourage the sharing of data, including, but not limited to, data on internal energy management projects and technical assistance projects.

D. Collaborate on science and technology (S&T) projects at research institutions sponsored by either agency. Synchronize research and development (R&D) of new knowledge and technologies to expand complementary efforts.

E. Develop joint initiatives for major energy technology research, development and demonstration programs of mutual interest to DOD and DOE, such as pilot or demonstration facilities which address military needs and also may address national security needs that transcend military requirements. DOD installations may serve as test beds for such technical demonstrations.

F. Develop human capital within DOE and DOD through teaching and education. Work to integrate respective agency energy training and knowledge exchange practices.

G. Encourage professional exchanges and formal liaison relationships between all DOE and DOD components including, but not limited to, laboratory, headquarters, military installations, combatant command headquarters, and forward operating bases.

H. Collaborate on issues regarding nuclear power, except naval nuclear propulsion, including developing a business, licensing and regulatory strategy as appropriate, and evaluating the integration of energy technologies with other industrial applications that support DOD objectives for energy security and GHG reduction. Collaboration will include NRC review and licensing of nuclear power plants that are deployed for DOD purposes, and are located on or adjacent to DOD U.S. installations.

V. Implementation

DOE and DOD intend to develop and conduct cooperative activities relating to identified high priority energy strategic needs, where such cooperation contributes to the efficiency, productivity, and overall success of the activity. The Parties intend for the activities to be executed under the MOU to be established by a joint DOE/DOD senior-level Executive Committee. This Executive Committee will be co-chaired by a designee of the Under Secretary of Defense (Acquisition, Logistics and Technology) and a designee of the Deputy Secretary from DOE. The Executive Committee will be responsible for the operations and governance of this MOU. Under the direction of the Co-Chairs, the Committee will include representatives from each of the principal DOE offices, specifically, the Office of the Under Secretary for Science, the National Nuclear Security Administration, and the Office of the Under Secretary for Energy. From the Department of Defense representatives will include the Deputy Under Secretary of Defense (Installations and Environment) and the Director of Operational Energy Plans and Programs. Additional members from both Agencies that may be involved in issues or functions of this MOU may be added. Upon agreement of both Departments, the Co-Chairs will appoint a team to develop, within 60 days, a charter and operating structure, membership, products, and decision processes.

The Executive Committee may establish working groups of Federal employees to perform and execute necessary activities contemplated by this MOU at their discretion. The Executive Committee and its working groups may make consensus recommendations based on their collaboration.

The Executive Committee will determine an appropriate regular meeting schedule, not to be less than four times annually. The Co-Chairs will be responsible for the development and distribution of agendas, presentations, and minutes of each meeting. Action items will be clearly identified and tracked in the minutes.

The Co-Chairs will be responsible for any reporting to the appropriate Departmental Secretarial Officers and will outline accomplishments, issues, redirections, and change assessments. The reporting will be coordinated by the Co-Chairs as appropriate.

The Co-Chairs will be responsible for any reports or presentations that are requested by other organizations, subject to the necessary review of each Party.

VI. Funding

Each party intends to coordinate their individual funding and resource decisions in order to maximize the benefits of cooperation under this MOU. Any transfer of funds or sharing of resources between the parties will be pursuant to a separate or pre-existing agreement.

VII. General

Work under this MOU will be jointly planned and monitored by the DOD and DOE.

In the event any activity undertaken by the agencies to implement the purposes of this MOU involves access to and sharing or transfer of technology subject to patents or other intellectual property rights, such access and sharing or transfer will be provided on terms which recognize and are consistent with the adequate and effective protection of intellectual property rights.

This MOU is strictly for internal management purposes for each of the Parties. It is not legally enforceable and shall not be construed to create any legal obligation on the part of either Party. This MOU shall not be construed to provide a private right or cause of action for or by any person or entity.

This MOU in no way restricts either of the Parties from participating in any activity with other public or private agencies, organizations, or individuals.

This MOU is intended to complement, and not to duplicate, cooperation by the Parties under the Memorandum of Understanding between the Department of Energy (National Nuclear Security Administration)/(Office of Science)/(Office of the Under Secretary) and the Department of Defense (Acquisition, Technology and Logistics) concerning Cooperation in a Strategic Partnership to Enhance National Security of January 26, 2009.

All agreements herein are subject to, and will be carried out in compliance with, all Federal applicable laws, regulations and other legal requirements.

This MOU is neither a fiscal nor a funds obligation document. Nothing in this MOU authorizes or is intended to obligate the Parties to expend, exchange, or reimburse funds, services, or supplies, or transfer or receive anything of value.

VIII. Contacts/Designated Representatives

Under Secretary for Science
U.S. Department of Energy
Washington, DC 20585

Under Secretary for Energy
U.S. Department of Energy
Washington, DC 20585

Under Secretary for Nuclear Security
U.S. Department of Energy
Washington, DC 20585

Deputy Under Secretary of Defense
Installations and Environment
U.S. Department of Defense
Washington, DC 20301

Director of Operational Energy Plans and Programs
U.S. Department of Defense
Washington, DC 20301

Deputy Assistant to the Secretary of Defense for Nuclear Matters
U.S. Department of Defense
Washington, D.C. 20301-3050

IX. Duration of Agreement

This MOU is effective on the date of the final signature and will remain in effect until it is terminated by mutual agreement of the Parties or by either Party providing ninety days written notice to the other. This MOU may be modified at any time by written agreement of the Parties. Nothing in this MOU shall be interpreted to limit or otherwise affect any authorities, powers, rights, or privileges accorded to DOD or DOE or any of the officers, employees, or organizational units under any statute, rule, regulation, contract, or agreement.

Daniel B. Poneman
Deputy Secretary of Energy

JUL 22 2010
Date

William J. Lynn III
Deputy Secretary of Defense

JUL 22 2010
Date

APPENDIX B

The Deputy Secretary of Energy

and

The Under Secretary of the Army

CHARTER

Advanced Vehicle Power Technology Alliance

I. DESIGNATION

By authority of this charter and effective this date, the Advanced Vehicle Power Technology Alliance (AVPTA) is established. AVPTA shall be active until the charter is rescinded, repealed, terminated or suspended.

II. MISSION

The AVPTA will be a partnership between the Department of the Army (DA) and the Department of Energy (DOE) in accordance with Section IV. E of the Department of Defense (DoD) and DOE Memorandum Of Understanding Concerning Cooperating in a Strategic Partnership to Enhance Energy Security, for the establishment of a joint technology research initiative in the area of ground vehicle power technology research, development and transition. The six focus areas of science and technology are: (1) advanced combustion engines and transmissions; (2) lightweight structures and materials; (3) energy recovery and thermal management; (4) alternative fuels and lubricants; (5) hybrid propulsions systems (including batteries); and (6) analytical tools. Where requirements are common, the two Departments will leverage resources to improve transition of technologies into both the commercial and military marketplace. The Alliance will also leverage industrial research and development (IRAD) involving commercial automotive and defense ground vehicle manufacturers to transition technologies and increase precompetitive research and development.

III. RESPONSIBILITY

The AVPTA is designated as the Department of the Army's and Department of Energy's primary point of contact for automotive power technology in the six areas above. Consistent with applicable law, regulation and policy, the AVPTA may conduct its activities in accordance with such agreements as are deemed necessary for its efficient operation.

IV. AUTHORITY

The AVPTA is jointly led by the Director, U.S. Army Tank Automotive Research, Development and Engineering Center (hereinafter "Director"), and the Department of Energy Program Manager for Vehicle Technologies (hereinafter "Program Manager"). Both the Director and Program Manager maintain authorities over their respective budgets. The AVPTA conducts activities in accordance with the DOD-DOE Energy Security Memorandum of Understanding. DOE enters into this MOU under the authority of section 646 of the Department of Energy Organization Act (Pub. L. 95-91, as amended; 42 U.S.C. § The Army enters into this MOU under the authority of DOD Instruction 4000.19 "Inter-Service and Intra-Governmental Support" August 9, 1995. The Director and Program Manager are the principle and primary points of contact for the prioritization of automotive/ground vehicle power and energy technologies in the six areas above.

V. COORDINATION

The AVPTA shall, as appropriate, coordinate activities and actions with associated government agencies, industries and academia with a focus on efficient vehicle power systems. The DOE and DA leads will meet on a regular basis to coordinate science and technology (S&T) activities, and will align S&T projects and products where requirements are similar. A yearly meeting will be conducted to assess results, update requirements and determine new joint efforts. Results will be reported back to the Under Secretary of the Army and the Deputy Secretary of Energy.

VI. ADVISORY BOARD

The Director and Program Manager may establish a Senior Advisory Board with other government agencies to review strategic planning and make recommendations on future activities. All activities associated with the Senior Advisory Board will comply with the Federal Advisory Committee Act, 5 U.S.C. App. 2 (FACA) and implementing regulation and policy, as applicable. As authorized by law, regulation and policy, the Senior Advisory Board may seek the individual advice of non-Government employees (*e.g.,* individual members of industry or academia) to secure facts and other information to assist the Senior Advisory Board's review.

VII. LEGAL AUTHORITY

The Director and Program Manager will ensure that the activities of the AVPTA are conducted in a manner consistent with all applicable laws, regulations and policies. In particular, all interactions with industry, academia, or other non-governmental entities will be reviewed in advance by appropriate agency counsel to confirm that any necessary enabling authorities exist and to ensure compliance with the FACA and implementing regulations and policies.

VIII. TERMINATION AND REVIEW

This charter shall terminate automatically on the five-year anniversary date unless expressly approved for renewal by the undersigned. This charter will be reviewed by the Director and the Program Manager biannually on its anniversary date to ensure currency, completeness and adequacy. Changes to mission and/or responsibilities will require the review by and approval of the Secretary of the Army and the Secretary of Energy.

Daniel B. Poneman
Deputy Secretary of Energy

Joseph W. Westphal
Under Secretary of the Army

Dated: July 18, 2011

This Page Intentionally Blank